Double trouble: Structural basis of Guanylate Binding Proteins targeting pathogen membranes

Kuhm, T.I.

DOI
10.4233/uuid:602698f2-6f52-4080-883a-b20be9d0c6c7

Publication date
2024

Double trouble:
Structural basis of Guanylate Binding Proteins targeting pathogen membranes

Double trouble:
Structural basis of Guanylate Binding Proteins targeting pathogen membranes

Dissertation

for the purpose of obtaining the degree of doctor
at Delft University of Technology,
by the authority of the Rector Magnificus, Prof.dr.ir. T.H.J.J. van der Hagen,
chair of the Board for Doctorates to be defended publicly on
Wednesday 29th May 2024 at 12:30 o'clock

by

Tanja Isabell KUHM

Master of Science in Molecular Biotechnology,
Universität Heidelberg, Germany

born in Herrenberg, Germany

This dissertation has been approved by the promotor and the copromotor.

Composition of the doctoral committee:

Rector Magnificus	Chairperson
Prof. dr. A. M. Dogterom	Delft University of Technology, promotor
Dr. A. Jakobi	Delft University of Technology, copromotor
Independent members:	
Prof. dr. T. Sixma	NKI, Amsterdam and Erasmus MC, Rotterdam
Prof. dr. ir. S. J. J. Brouns	Delft University of Technology
Dr. ir. L. Laan	Delft University of Technology
Prof. dr. ir. S. J. Tans	Delft University of Technology and AMOLF Amsterdam
Prof. dr. C. Joo	Delft University of Technology, reserve member

Keywords: Cell-autonomous-immunity; Guanylate binding proteins; Cryo-EM; Lipopolysaccharides; Coatomers; SEC-MALS; Nanobodies

Printed by: Proefschriftspecialist

Front & Back: Cryo-EM tomogram of GBP1 coating lipid membranes, T. I. Kuhm

ISBN 978-94-6384-585-4

An electronic version of this dissertation will become available at
`http://repository.tudelft.nl/`.

Contents

1

General Introduction

1

1.1. Cell autonomous immunity

In vertebrates, the immune system is divided in two complementary lines of defense: First, the innate immunity which is a non-specific defence mechanism and second the adaptive immunity which is a specific defense mechanism that acts on pathogens memorised from a previous infection [1]. Both lines of defense are complementary and the innate immunity triggers processes that recruit specialised immune cells to the site of infection. From a pathogen side of view, individual cells are an attractive hiding place as well as a nutrient source. It is therefore not surprising that individual cells from all three domains of life have developed a repertoire of defense strategies to deal with intracellular pathogens called cell-autonomous immunity. [2–4] (Figure 1.1).

In order for cells to recognise an infection, distinguishing *self* from *non-self* is a critical characteristic. The recognition of exogenous components can be achieved via pattern recognition receptors (PRR) that are able to detect pathogen-associated molecular patterns (PAMPs), among others the bacterial flagellum, microbial DNA or lipopolysaccharides (LPS) which are part of the outer membrane of gram-negative bacteria [5]. After pathogen detection, ways to promote pathogen restriction and elimination have evolved (Figure 1.1).

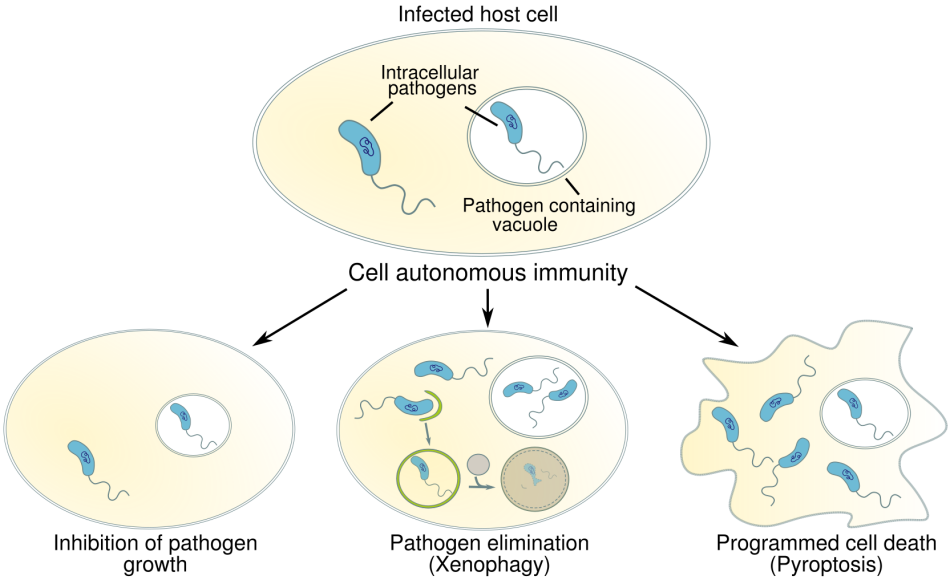

Figure 1.1: Schematic overview of cell-autonomous immunity. Different defense strategies of a cell to target either intracellular pathogens residing in the cytosol or within pathogen containing vacuoles are depicted. Cells can inhibit the growth of the pathogen (left), the pathogen can be selectively eliminated (middle) or the cell can enter an inflammatory type of programmed cell death called pyroptosis (right).

The inhibition of pathogen growth can be achieved by limiting essential nutrients, whereas a selective form of autophagy called xenophagy eliminates pathogens that have been marked for degradation [6–8]. Lastly, the host cell can decide to enter an inflammatory type of programmed cell death called pyroptosis, thereby destroying the growth

niche of the pathogen [9, 10]. Apart from functions within the cell, further strategies have evolved warning neighboring cells, for example by secreting cytokines, potentially inducing the expression of antimicrobial proteins.

1.2. Guanylate binding proteins (GBPs)

1.2.1. Discovery of interferon inducible human guanylate binding proteins.

In vertebrates, the expression of effector proteins involved in cell-autonomous immunity can be induced by cytokines such as interferons (IFN). One such class of effector proteins are called guanylate binding proteins (GBPs). GBPs have been identified 40 years ago in fibroblastic cells that had been stimulated with type II interferon (including interferon gamma (IFN-γ)), a cytokine with an immunomodulatory function [11]. Human GBPs (hGBPs) are strongly induced by interferons and levels of 3×10^5 molecules per human fibroblast cells have been reported after a 24 h treatment with IFN-γ [12]. Moreover, the name GBP originated from the capability to bind guanosine-5'-triphosphate (GTP), guanosine 5'-diphosphate (GDP) and guanosine 5'-monophosphate (GMP) [11]. The capability to bind to nucleotides, specifically guanylates was utilised for purification and enabled further protein characterisation [12]. In total seven GBPs have been identified in humans (hGBP1 to hGBP7), located in a cluster on chromosome 1 [13]. Besides in humans, GBPs have been found in many other species such as primates, mice, rats, but also in zebrafish and plants as for example *Arabidopsis thaliana* [4]. In recent years, the crucial role of GBPs in cell-autonomous immunity became apparent. Within the host cell, GBPs can assemble into large antimicrobial defense complexes targeting a wide range of pathogens including viruses, bacteria and parasitic protozoan [14–19]. Additionally, GBPs can serve as a signalling platform, recruiting downstream effectors important for pathogen restriction or elimination [20, 21].

1.2.2. Structure and domain architecture of human GBPs

The crystal structure of human GBP1 has been determined more than 20 years ago [22]. The hGBP1 monomer consists of a globular N-terminal large GTPase domain (LG domain, Figure 1.2a-b, dark blue) and a C-terminal α-helical domain. The C-terminal helical domain (CTHD) is again divided into a middle domain (MD; α7-α11, Figure 1.2 a,b in light-green) and a GTPase effector domain (GED; α12-α13, Figure 1.2 a,b in orange) [22].

In the absence of guanine nucleotides, GBP1 resides in its resting state with the GED folded back onto the MD making contact with the LG-domain (Figure 1.2 a,b). Nucleotide free GBP1 is 13 nm long and exhibits a rod-like shape. Additionally, the LG-domain of GBP1 has been shown to dimerise in a nucleotide dependent manner. To structurally investigate the LG-domain dimer a non hydrolysable GTP transition state mimic (GDP·AlF_3) was used to lock the protein in its dimeric conformation. The crystal structure of the GBP1 LG-domain dimer stabilised with GDP·AlF_3 revealed a large buried interface of approximately 3900 Å^2 with the nucleotide binding site closely located to the interface [23] (Figure 1.2 c, d).

Previous experiments using quantitative Förster resonance energy transfer (FRET) with full length GBP1 predicted major rearrangements of the α-helical stalk region in-

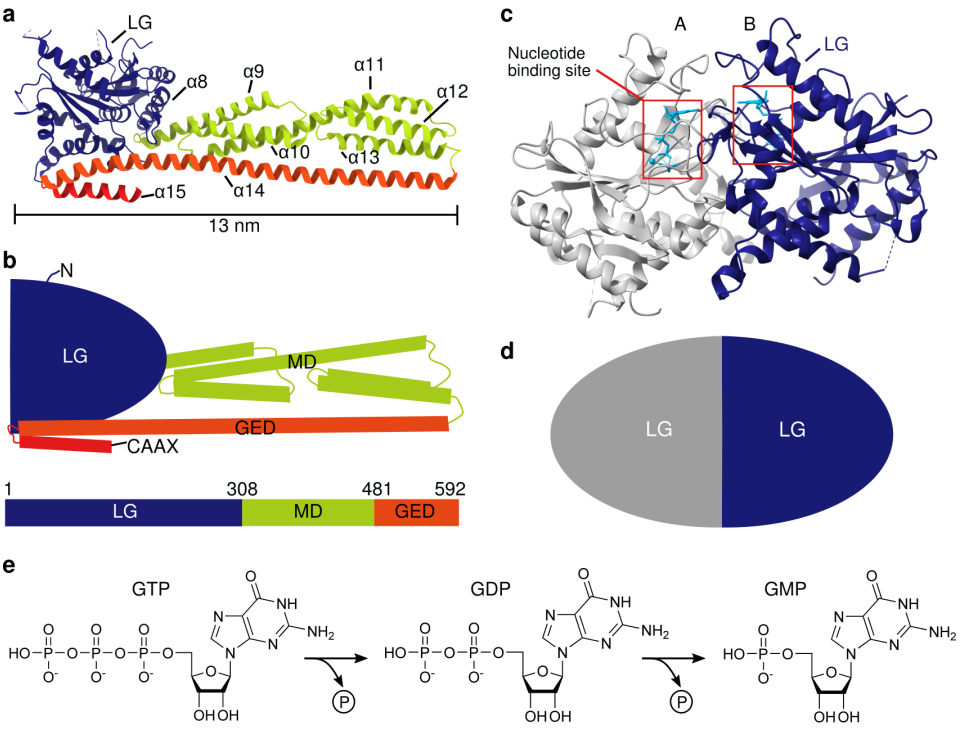

Figure 1.2: Domain architecture of GBP1 (a) Atomic model of monomeric GBP1 (PDB ID 1dg3) in cartoon representation [22]. Individual α-helices in the middle domain (green) and GTPase effector domain (orange and red) are numbered sequentially. (b) Schematic representation displaying the domain architecture. LG: Large GTPase domain (blue), MD: Middle domain (green), GED: GTPase effector domain (orange and red). CAAX represents a C-terminal sequence motif enabling the prenylation of GBP1. (c) Atomic model of the GDP·AlF_3 stabilised LG-domain dimer of GBP1 (PDB ID 2b92) in cartoon representation [23]. The bound nucleotide is highlighted in cyan. (d) Schematic representation of the LG-domain dimer displayed in (c). (e) GBP1 is able to hydrolyse guanosine-5'-triphosphate (GTP) to guanosine 5'-diphosphate (GDP) and further to guanosine 5'-monophosphate (GMP).

duced by nucleotide binding and hydrolysis of GTP to GDP and further to GMP (Figure 1.2e) [24].

1.2.3. GTP hydrolysis of GBPs

A remarkable feature of GBP1 is its ability to hydrolyse GTP to GDP and then further to GMP in a two-step reaction, successively cleaving a single phosphate group [23, 25] (Figure 1.2e). Whereas GBP2 is also able to convert GTP to GMP, although much less efficient resulting in ~10% GMP, GBP5 is only able to hydrolyse GTP to GDP [26, 27]. The high intrinsic GTPase rate of 80 min^{-1} is achieved independently from external GTPase-activating proteins but depends on a cooperative mechanism of GTP hydrolysis most likely achieved by multimerisation of GBP1 [22, 28, 29]. Important to note is that GTP-hydrolysis only occurs upon GBP dimerisation with the active site located at the interface formed between two LG-domain monomers (Figure 1.2c).

1.2.4. GBPs belong to the dynamin-like protein superfamily

Members of the dynamin-like protein superfamily share structural and biochemical properties that make them unique. GBPs together with other proteins such as dynamin, myxovirus resistance proteins (Mx), optic atrophy protein 1 (OPA1), mitofusin or atlastin belong to the superfamily of dynamin-like proteins [30, 31] (Figure 1.3). Functionally, members of the dynamin-like protein superfamily are involved in membrane-remodelling events as for example fission, fusion or membrane tethering [32, 33]. Other functions include organelle maintenance and responses to intracellular pathogens [33]. The function of dynamin-related proteins was often closely related with its ability to self-assemble into higher-order structures.

Structurally, the members of this protein family all contain a GTPase domain and an elongated α-helical bundle domain and have been described to self-assemble in a nucleotide dependent way (Figure 1.3). A common mechanism includes conformational changes of the α-helical domain induced by GTP hydrolysis in the LG domain [30, 34].

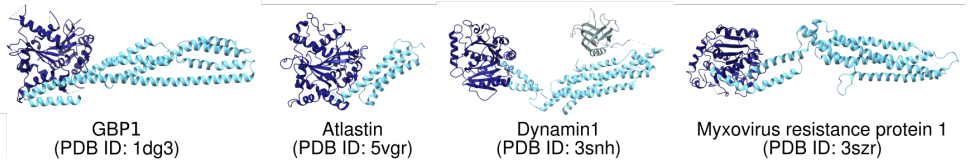

Figure 1.3: Structural comparison of members of the dynamin-like superfamily. Common structural features include a GTPase domain (dark blue) as well as a C-terminal helical part (light blue). Depicted are human GBP1 (PDB ID: 1dg3 [22]), human atlastin (PDB ID: 5vgr [35]), human dynamin 1, additionally containing a pleckstrin homology domain in grey (PDB ID: 3snh [36]) and human myxovirus resistance protein 1 (PDB ID: 3szr [37]).

Another common feature for members of the dynamin-like superfamily is their low affinity for guanine nucleotides (in the micro-molar range), caused by fast dissociation rates [30, 31]. Mechanistically, a cooperative mechanism including protein oligomerisation is underlying the GTP hydrolysis and the high intrinsic GTPase activity (kcat ~ 2 min^{-1} to 100 min^{-1}) is achieved without additional GTPase-activating proteins [30].

1.2.5. Isoprenylation and membrane binding of GBPs

Similar to other members of the dynamin-like protein superfamily, GBPs are also able to associate with membranes. In this case membrane association is achieved via a post-translational modification called isoprenylation that involves the attachment of either a C15 farnesyl group or a C20 geranylgeranyl group to the C-terminal cysteine of a protein [38–40]. The isoprenyl-group is highly hydrophobic and can therefore act as a lipid anchor. Out of the seven human GBPs, GBP1, GBP2 and GBP5 have been shown to either be farnesylated (GBP1) or geranylgeranylated (GBP2 and GBP5) [41, 42] (Figure 1.4a). The isoprenylation is catalysed by either a farnesyl transferase (FTase) or a geranylgeranyl transferase (GTase). Both enzymes are hetero-dimers consisting of either FNTA and FNTB for the FTase or of FNTA and PGGT1B for the GTase [43, 44]. Those transferases recognise a certain amino acid sequence called CaaX-box at the C-terminus of the target-protein which determines the type of isoprenylation [45]. The C in the CaaX-box corresponds to the cysteine that is able to get isoprenylated, followed by two aliphatic amino

acids (referring to the a in the CaaX-box). The amino acid representing the X determines the type of isoprenylation. While farnesyltransferases mainly recognise the CaaX-box, if the X corresponds to a methionine, serine, glutamine, alanine or cysteine, geranylgeranyl transferases preferentially recognise the CaaX box with X corresponding to a leucine or a glutamic acid [46].

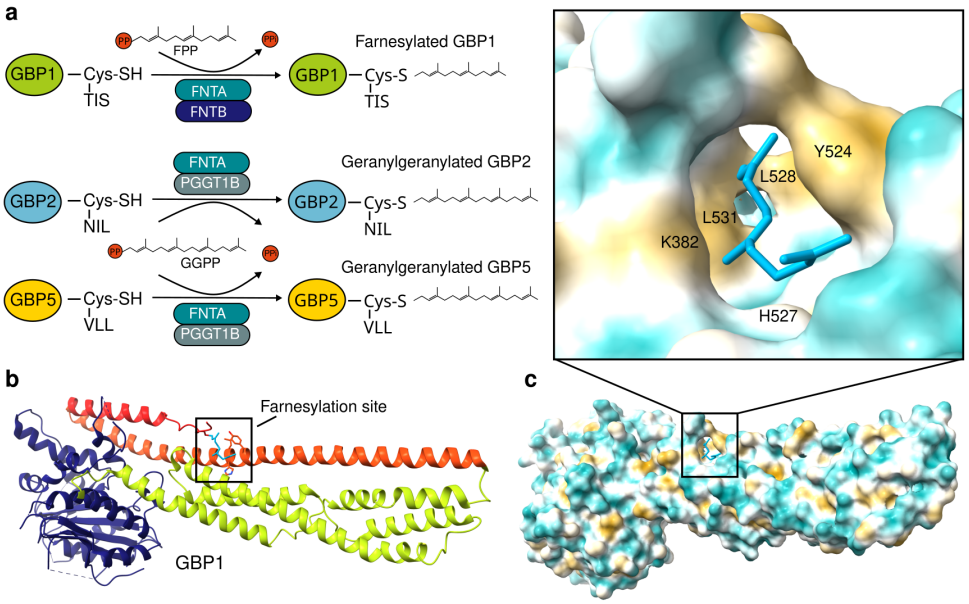

Figure 1.4: Isoprenylation of GBPs (a) Overview of isoprenylated GBPs. The C-terminal sequences, including the cysteine that can undergo isoprenylation, are depicted. (b) Atomic model of monomeric farnesylated GBP1 (PDB ID 6k1z) in cartoon representation [47]. The individual domains are color-coded and the farnesylation moiety is labelled in cyan. (c) Hydrophobic surface representation of (b) visualizing the hydrophobic pocket shielding the farnesyl moiety (cyan, stick representation) from the cytosol. Yellow corresponds to hydrophobic regions, turquoise to hydrophilic areas. Amino acids of GBP1 in close proximity to the farnesyl molecule are highlighted.

The C-terminal amino acid sequence of GBP1 is CTIS enabling farnesylation whereas the C-terminus of GBP2 (CNIL) and GBP5 (CVLL) are prone to get geranylgeranylated. Following the isoprenylation, proteins typically undergo two additional post-processing steps: proteolysis and methylation. The residues C-terminal of the prenylated cysteine are proteolytically cleaved off by a protein peptidase followed by a carboxyl methylation of the prenylated cysteine itself [39, 48–50]. The isoprenylation of a protein including the subsequent methylation increases its hydrophobicity. It can therefore be responsible for changes in the sub-cellular location of proteins, facilitating membrane interactions [42]. But membrane association of farnesylated GBP1 has been further shown to be dependent on GTP hydrolysis, most likely inducing a structural rearrangement of the protein that makes the prenylation site accessible [51]. In its nucleotide free form, the farnesyl moiety of GBP1 is shielded in a hydrophobic pocket which is mainly made up by amino acids located at the GED of the protein [47] (Figure 1.4 b,c).

Despite the fact that GBP1, GBP2 and GBP5 have been shown to be isoprenylated *in vivo* [42], GBP1 has been identified to be the first member of the GBP family associating with pathogens as well as with pathogen containing vacuoles. Subsequently to GBP1, membrane association of other GBP members gets initiated [20, 21, 52–55]. What precisely determines the ability of GBP1 to be the first member to be recruited to membranes is not yet fully understood. Multiple groups have proposed that a triple arginine motif at the C-terminus of GBP1 together with its farnesylation is necessary for the recruitment to membranes [56, 57]. Neither GBP2 nor GBP5 have this polybasic motif nearby their C-terminus. Interestingly, even non-prenylated GBP members can be redistributed to membranes in a hierarchical manner, potentially via hetero-interactions with isoprenylated GBPs [42].

1.2.6. Location in the cells

In the absence of activating signals, GBPs are typically expressed at low-to-medium basal levels. Upon IFN-γ induction, GBP1 has been found mainly in the cell cytosol displaying small granular patterns, despite its capability to be isoprenylated [42, 51]. The addition of GDP·AlF_3 induced a redistribution of GBP1 to membranes in IFN-γ treated cells, highlighting that membrane association of GBP1 does depend on its farnesylation as well as on nucleotide binding and hydrolysis [51, 58].

The other two isoprenylated GBP members have been observed associating with either the perinuclear membranes (GBP2) or the Golgi apparatus (GBP5) [42]. The non-prenylated members GBP3 and GBP4 are localised in the cytosol in a diffuse manner and are only able to bind to membranes when being recruited through hetero-interactions with isoprenylated GBP members [42, 51]. GBP6 and GBP7 are the least studied members of the GBP family. Unlike the other GBP members, they are only expressed in very specific cell types, namely the esophagus or the liver respectively [59, 60].

1.2.7. Evolutionary aspect of GBPs

As stated previously, guanylate binding proteins can be found in a broad range of organisms. Besides in vertebrates, GBPs have also been identified in plants and algae and thereby in organism lacking an IFN-inducible immune system [61]. A common feature in most species is that GBPs are chromosomally clustered as it has also been observed for human GBPs (clustering on chromosome 1) [13]. GBP genes are thought to have undergone gene conversions as well as duplications. While mice have eleven GBPs, *Arabidopsis thaliana* has three different GBPs and eight GBPs are found in zebrafish [4]. Interestingly, GBP3 and GBP4 from zebrafish additionally contain a caspase activation and recruitment domain (CARD) that can be found in human inflammasome-associated proteins such as caspase-4 or ASC (apoptosis-associated speck-like protein containing a CARD) [62]. Inflammasomes are large multi-protein complexes located in the cytoplasm that can recognize pathogen-associated molecular patterns and respond through the maturation of cytokines and pyroptotic cell death [63–65]. Potentially in humans, GBPs and CARD containing proteins have evolved into two separate proteins. Such evolutionary hints can help decipher potential roles of human GBPs regarding inflammasome activation.

1

1.2.8. Antimicrobial functions of GBPs

Following a cytokine induction, GBPs play an important role in cell-autonomous immunity targeting a wide range of pathogens. The first time GBPs were linked to an antiviral effect was against Encephaloymyocarditis virus (EMCV) and Vesicular stomatitis virus (VSV) [14] and has further been shown to among others target hepatitis C virus (HCV) and human immune deficiency virus (HIV) [15, 16]. A couple of years later, GBPs were also found to have an effect on protozoa like *Toxoplasma gondii* (Tg) and bacteria [17–19]. By now it is established that GBPs play an important role targeting many intracellular pathogens such as Shigella, Salmonella or *Mycobacterium tuberculosis* that are causing major health problems around the world [66, 67].

How GBPs are able to target such a wide variety of pathogens is still unclear. GBP1 has been shown to play a role in detecting and potentially disrupting the parasitophorous vacuole (PV) of Tg as well as the pathogen membrane itself [52, 53]. The parasitophorous vacuole is derived from the host plasma membrane when entering the host cell via endocytosis and can be used as a replication niche by certain pathogens. It thereby differs severely in membrane composition compared to the membrane of Tg itself. While only GBP1 was able to coat Tg, GBP2 and GBP5 were also shown to be up-regulated by IFN-γ contributing to Tg growth restriction independent of coat formation [68].

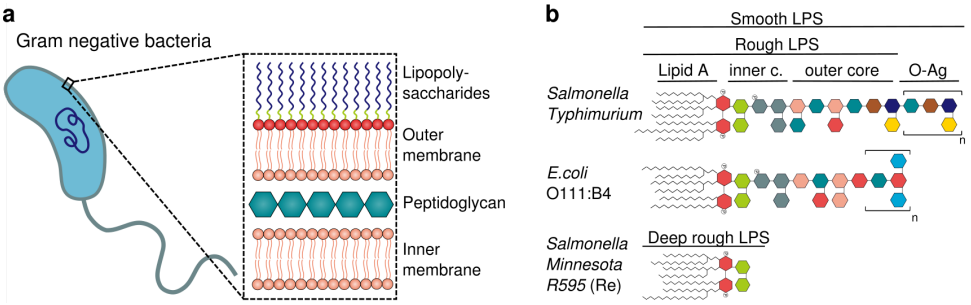

Figure 1.5: Overall structure of lipopolysaccharides (a) Schematic representation of the gram-negative bacterial cell envelope. (b) Schematic representation of different lipopolysaccharide strains differing in their overall length and polysaccharide composition (O-Ag: O-Antigen).

While farnesylated GBP1 has been shown to form a coat around gram-negative bacteria there has been no evidence so far that GBP1 can lead to membrane rupture of gram-negative bacteria [20, 21, 69]. The outer membrane of gram-negative bacteria consists of lipopolysaccharides (LPS) that play an important role in keeping the integrity of the outer membrane and maintaining its function as a barrier for detergents or toxins [70] (Figure 1.5 a). LPS molecules consist of an inner lipid A moiety, core sugars and variable repeating units of lipopolysaccharides called O-antigens (Figure 1.5 b) [71]. LPS lacking the O-antigen are referred to as rough LPS, whereas LPS containing the O-antigen are called smooth LPS, which originates from the morphology of the bacterial colonies.

Different modes of action have been proposed for GBPs to carry out their role in cell autonomous immunity. One mechanism that has been described before is the ability of GBP1 to interact directly with lipopolysaccharides (LPS), more precisely with the inner-

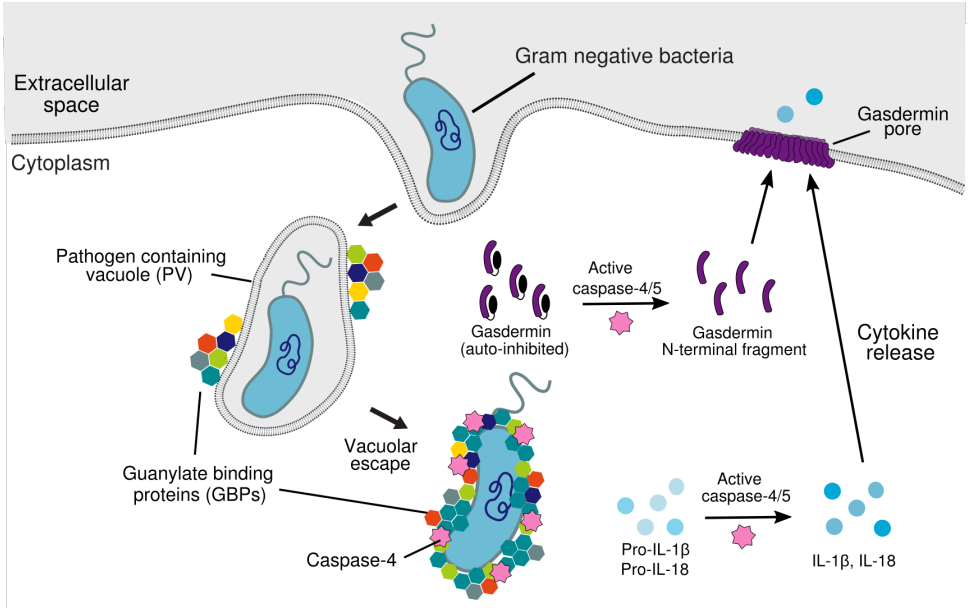

Figure 1.6: Overview of guanylate binding proteins targeting pathogen containing vacuoles as well as gram-negative bacteria. Pathogens can enter a cell via various strategies. Following an endocytic entry, the pathogens are enclosed in a pathogen containing vacuole (PV). GBPs have been shown to associate with some PVs and to bind directly to the LPS of gram negative bacteria. Certain GBP members are further able to activate caspase-4 which once activated induces the maturation of cytokine precursors IL-1β and IL-18 as well as gasdermin, resulting in pyroptosis.

most lipid-A moiety [69]. For gram-negative bacteria it is currently assumed that first GBP1 binds to LPS, which recruits other GBPs as well as caspase-4 to the bacterial membrane [20, 21]. Once activated, caspase-4 is then able to cleave and activate cytosolic gasdermin-D (GSDMD) [72], of which the N-terminal part oligomerises at the plasma membrane, forming ring-shaped pores causing pyroptosis and cytokine release [73, 74] (Figure 1.6). Another mode of action has been reported recently, where GBP1 has been shown to trigger LPS release after GBP1 coat formation [54]. Potentially, membrane remodelling capabilities of GBPs could result in LPS liberation, making the LPS available for caspase-4.

How and if GBPs interact with gram-positive bacteria is even less understood. Mouse GBPs have been shown to interact with the PV of gram-positive *Listeria monocytogenes* [66]. In contrast to gram-negative bacteria, multiple groups were unable to observe a coat of human GBP1 around gram-positive bacteria [54, 56, 69]. Puncta formation of GBP1 on *L. monocytogenes* was observed recently and was dependent on the endolysosomal damage of the PV [75]. Whether this binding of GBPs occurs directly on the bacteria itself or rather on the pathogen containing vacuole, needs further examination.

Important to note is that the cell type can have an effect on the ability of GBP1 to coat pathogen membranes as observed for human A549 epithelial cells where GBP1 failed to target Tg and *Chlamydia trachomatis* versus in human macrophages where co-

localisation of GBP1 with Tg and *Chlamydia trachomatis* was observed [52]. Additionally, GBPs preferentially target certain pathogens as shown in co-infected cells. In those experiments GBP1 preferentially targeted *S. flexneri* over *Francisella novicida* [55], but little is known what drives this preferential binding. The different types of LPS are one plausible explanation, but first structural information on how precisely GBPs interact with LPS needs to become available.

To counteract the targeting by GBPs, pathogens developed their own escape strategies. The pathogenic *S. flexneri* for example, possesses an E3 ubiquitin ligase (IpaH9.8) that is able to ubiquitinate several GBP members, marking it for proteasomal degradation, thus suppressing the host cells defense line [47, 67, 76, 77].

1.3. Cryogenic electron microscopy (cryo-EM)

In recent years the importance of GBPs in cell-autonomous immunity has become more and more apparent. While most studies have been performed using optical microscopy, less information about the molecular structure of GBPs is available. Therefore, we aimed to use cryogenic electron microscopy to study the structure of GBP dimers as well as GBP coats on membranes. The resolution of an optical microscope is determined by its diffraction limit. Whereas this limits the resolution to a range of hundreds of nanometres this is not sufficient to resolve protein structures that are a few nanometres in size. By using shorter wavelengths obtained from highly accelerated electrons (2 pm for 300 keV electrons), the resolution can be pushed further, enabling structure determination of individual proteins. As electrons are strongly scattered by air, the microscope column of an electron microscope needs to operate in vacuum which is not suited for aqueous biological samples since they would immediately evaporate in vacuum. To prevent evaporation, samples are handled in cryogenic conditions. Ice crystals on the other hand can damage the sample and alter the contrast of the image.

To overcome this issue, a method of sample vitrification was developed [78, 79]. By quickly freezing a thin biological sample on a support grid in liquid ethane (–180 °C), an amorphous glass like state called vitreous ice can be achieved which enables imaging of biological material in a close to native state on a (cryo) electron microscope (Figure 1.7 a,b). A massive progress in cryogenic electron microscopy (cryo-EM) resulted from the introduction of direct electron detectors (DED) in 2012 combined with a vast improvement of image processing algorithms [80]. Using DEDs made it possible to divide a single image into a movie of frames and subsequently correcting for the beam-induced motion [81].

Protein particles in vitreous ice imaged in focus do not have enough contrast to detect individual particles. While acquiring micrographs at a defocus helps to create phase contrast, it also alters the information of the image. That is the reason why after acquiring hundreds to thousands of images with multiple frames and subsequent motion correction, a typical single particle cryo-EM image processing workflow continues with the estimation of the contrast transfer function (CTF) [82, 83] (Figure 1.7c). The CTF estimation and correction is necessary, to correct for the alterations resulting from imaging at a defocus.

Another difficulty when performing cryo-EM of biological samples is the poor signal to noise ratio, resulting from the usage of an extremely low electron dose in order to pre-

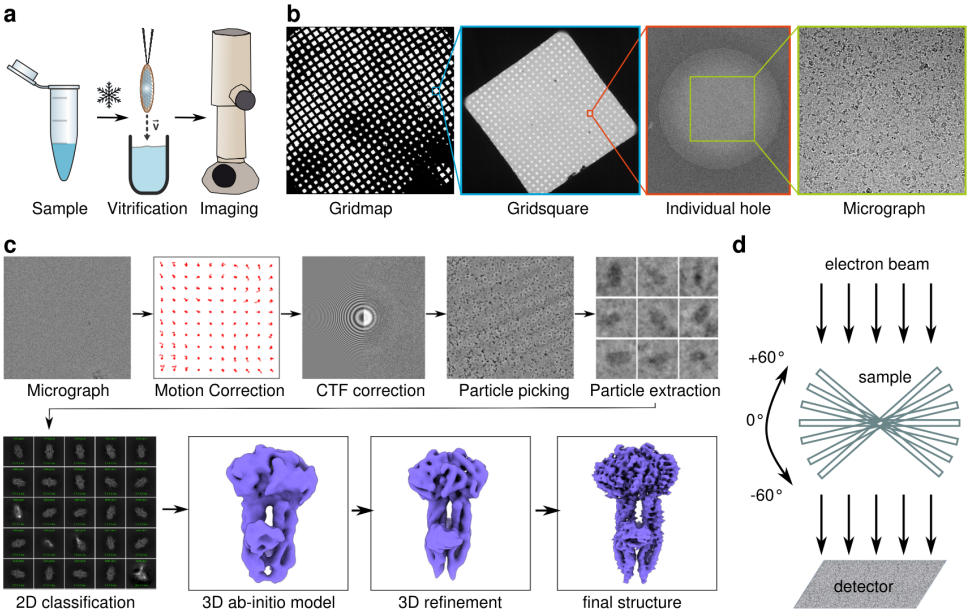

Figure 1.7: Overview of cryogenic electron microscopy (a) Schematic representation of sample vitrification. A thin biological sample on a support grid is flash frozen in liquid ethane, resulting in vitreous ice. The flash-cooled sample can be imaged on a cryogenic electron microscope. (b) Different magnifications within an EM grid, ranging from an overview image of the support grid (left), to an individual gridsquare, an individual hole, to an acquired micrograph (right). (c) Exemplary image processing workflow for single particle cryo-EM. (d) Schematic representation of the concept underlying cryo-electron tomography.

vent sample damage. That is why after particle picking and particle extraction, classifying particles into 2D averages is performed. The 2D classification increases the contrast and has the potential to sort different views and conformations of a protein. In a next step particles from multiple 2D classes are fed into a 3D reconstruction algorithm to obtain a 3D volume from 2D projection images [84]. After a first 3D initial model, multiple rounds of 3D refinement follow, before a final 3D EM reconstruction is achieved.

By now ~29,000 3D electron density maps have been deposited at the EM databank (August, 2023) and there is a clear trend that more and more structures are being solved by cryo-EM which becomes apparent when comparing the amount of submitted structures either solved by X-ray crystallography or cryo-EM. While the overall number of submitted PDB structures determined via X-ray crystallography stayed quite stable over the last 10 years (around 9,000 per year), the submitted cryo-EM structures have gone from 119 in 2013 to 4,582 structures in 2023, visualizing the vast growth that the field of cryo-EM has undergone (wwpdb.org) [85]. Moreover, the final resolution of the cryo-EM maps have improved. In 2023, 73 % of the entries in the electron microscopy data bank (EMDB) had a resolution better than 4 Å (Figure 1.8a). The highest resolution obtained by cryogenic EM so far has been achieved for apoferritin reaching an atomic resolution of 1.22 Å and 1.25 Å respectively [86, 87]. At such high resolution, individual atoms can be resolved and hydrogens are visible. Besides the great progress, most of the cryo-EM

structures found in the EMDB stay in a certain molecular weight range, namely between 100 kDa and 1000 kDa (~70 %) (Figure 1.8b).

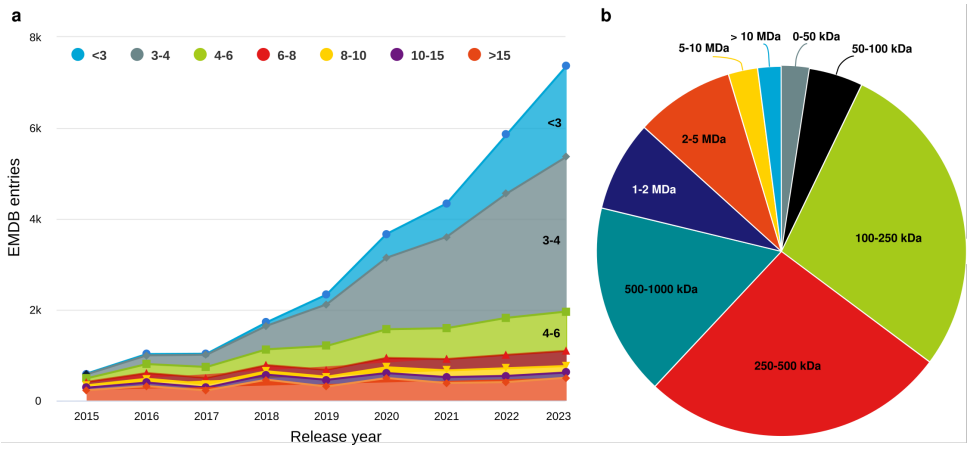

Figure 1.8: Statistics of cryo-EM structures deposited in the EMDB (a) Resolution of cryo-EM structures deposited in the EMDB in Å in the time period from 2015 to 2023. (b) Overview of the molecular weight of structures deposited at the EMDB (in 2023).

While cryogenic EM was originally especially suited for larger complexes since the amount of signal scales with the mass of the protein, the sizes of solved protein structures have become smaller and smaller and different research groups have managed to solve the structure of proteins that are even below 50 kDa [88].

Cryogenic electron microscopy offers advantages over techniques such as protein crystallography, notably in its ability to image flexible proteins in their instantaneous configurations. For objects with a unique conformation that prohibits signal averaging, cryo-electron tomography has been developed as an alternative imaging method. Instead of taking a single micrograph, the same field-of-view is imaged at a range of tilt angles which can subsequently be reconstructed into a 3D volume called a tomogram [89–91] (Figure 1.7d).

Disadvantages of cryogenic EM on the other hand are the low signal to noise ratio resulting from low-dose imaging which is used to reduce sample damage. In order to obtain enough information for a 3D reconstruction, usually a large number of particles from hundreds to thousands of micrographs are aligned. For small particles, the low contrast makes this alignment process challenging and it is thus more difficult to obtain a high resolution 3D reconstruction. Another reoccurring problem in many cryogenic EM projects is a strong preferred particle orientation. A thin ice layer is necessary in order for the electrons to penetrate. At the same time particles in this thin layer are more likely to interact with the air-water interface. A bias of particle orientation limits the angular information used to generate 3D maps and can make the interpretability of the obtained EM maps harder. There are different possibilities on how to approach preferred particle orientation [92]. Adding detergent can alter the properties of the air-water interface, aiding in the redistribution of particle orientations. Similarly, using EM grids coated with a thin carbon layer can sequester particles away from the air-water interface, achieving a

comparable effect. Another possibility is to acquire the dataset with different tilt angles in order to get a more complete coverage in particle distribution, but there are additional challenges that can arise from a tilted-stage acquisition [93]. Tilting the specimen stage can lead to an increase in beam-induced particle movement, a focus gradient across the micrograph as well as an increase in the apparent ice thickness, making the image processing of the sample more challenging. Finally, the addition of a binding partner can help in redistributing the particles in the ice by changing the propensities of the molecular surface, additionally increasing the size (and therefore the alignable mass) of the protein. An example of such a potential binding partner is discussed in the following paragraph.

1.4. Nanobodies

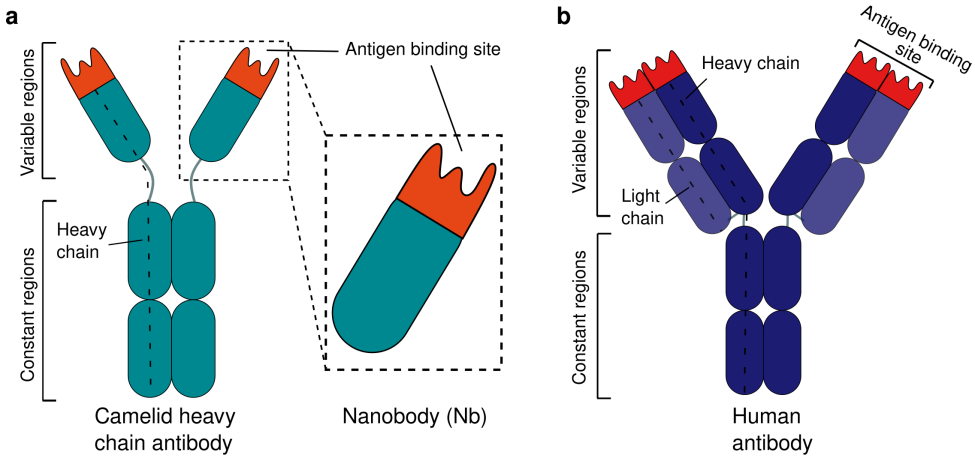

Figure 1.9: Schematic representation of Nanobodies (a) Nanobodies are single variable domains derived from heavy chain antibodies found in sera of camelidae (b) Schematic representation of a conventional human antibody consisting of heavy and light chains as comparison.

Nanobodies are single variable domains derived from heavy chain antibodies found in sera of *Camelidae* [94] (Figure 1.9 a). Compared to conventional antibodies the antigen binding site of nanobodies is made up by just a single variable domain (Figure 1.9 a, b) and thus nanobodies are only around 15 kDa in size (compared to 150 kDa for a conventional antibody). Their small size and potentially high target affinity make nanobodies a useful tool in structure determination. Besides increasing the overall mass of a complex (and thus the alignable mass), nanobodies have also been shown to stabilize proteins in certain conformational states [95–97]. Additionally, nanobodies are extremely stable regarding pH and temperature ranges and can even withstand reducing environments of eukaryotic cells without loosing target specificity [98]. These characteristics facilitate the expression of fluorescently labeled nanobodies, known as intrabodies, which track antigens within living cells [99, 100]. This approach effectively links structural studies with functional analysis.

1

1.5. Outlook of this thesis

In **Chapter 2** we characterise eight different nanobodies that were derived by immunizing llamas with either monomeric GBP1, farnesylated GBP1 or nucleotide stabilised dimeric GBP1. SEC-MALS experiments confirmed the ability of all eight nanobodies to bind to GBP1 and surface plasmon resonance was used to determine the affinity. We identified nanobodies that were only able to bind to dimeric GBP1 as well as two nanobodies preventing dimer formation. By using only the LG-domain of GBP1 we could further pin-point the binding site of the nanobodies. With the help of cryogenic electron microscopy we solved the structure of the GBP1 dimer bound to two different Nanobodies which helped us to describe the putative interface of the nanobodies. In this chapter we further show that some of the identified nanobodies specifically bind to GBP1 whereas they are unable to bind to GBP2. With this work we set the groundwork to utilise those nanobodies as intrabodies which could provide a powerful tool in targeting specific GBP members within cells, intracellularly localizing dimeric vs monomeric GBPs as well as studying the effect of coat formation and its disruption on downstream effects as for example caspase-4 activation.

In **Chapter 3** we use one of the nanobodies identified in Chapter 2 in order to solve the cryogenic EM structure of the nucleotide stabilised GBP1 dimer. A cross-over arrangement of the middle domain of GBP1 was observed, resulting in a parallel, outstretched configuration. This arrangement suggested that the potentially isoprenylated carboxyl-termini of the GBP1 dimer are oriented in the same direction, enabling a densely packed coatomer on membranes. Visualisation of this GBP1 coatomer was achieved on small unilamellar vesicles derived from brain polar lipid extract, as well as on three different types of LPS. We demonstrated that GBP1 dimers constitute the primary building blocks of the formed coat. Based on the obtained cryogenic EM structure, we introduce mutations located at the linker region between the large GTPase-domain and the middle domain and show reduced membrane binding. Finally, we show for the first time that farnesylated GBP1 is able to form tubular membrane protrusions which could be an important mechanism for destabilizing membranes or making LPS molecules accessible for caspase-4.

In **Chapter 4** we investigate the differences in their self-assembly properties of GBP1 and GBP2. To do so, we generated geranylgeranylated GBP2 as well as a GBP2-CTIS mutant that can be farnesylated. Successful isoprenylation was confirmed using liquid chromatography mass spectrometry. The effects of isoprenylation on the ability to dimerise and oligomerise were further investigated using size exclusion chromatography coupled to multi angle light scattering (SEC-MALS) as well as with electron microscopy techniques. While we could show for the first time that geranylgeranylated GBP2 formed similar micelle like structures as farnesylated GBP1, there was no coat formation observed. Farnesylated GBP2-CTIS on the other hand failed to self-oligomerise and coat membranes. Finally, we analyse the effects of isoprenylation on the GTPase activity of GBP2 and observe a reduced activity for geranylgeranylated GBP2 in contrast to an increased activity of farnesylated GBP1 and GBP2-CTIS.

References

[1] J. S. Marshall, R. Warrington, W. Watson, and H. L. Kim, *An introduction to immunology and immunopathology,* Allergy, Asthma & Clinical Immunology **14**, 1 (2018).

[2] B.-H. Kim, A. R. Shenoy, P. Kumar, C. J. Bradfield, and J. D. MacMicking, *Ifn-inducible gtpases in host cell defense,* Cell host & microbe **12**, 432 (2012).

[3] F. Randow, J. D. MacMicking, and L. C. James, *Cellular self-defense: how cell-autonomous immunity protects against pathogens,* Science **340**, 701 (2013).

[4] S. Huang, Q. Meng, A. Maminska, and J. D. MacMicking, *Cell-autonomous immunity by ifn-induced gbps in animals and plants,* Current opinion in immunology **60**, 71 (2019).

[5] S. Akira, S. Uematsu, and O. Takeuchi, *Pathogen recognition and innate immunity,* Cell **124**, 783 (2006).

[6] B. Levine, N. Mizushima, and H. W. Virgin, *Autophagy in immunity and inflammation,* Nature **469**, 323 (2011).

[7] J. D. MacMicking, *Interferon-inducible effector mechanisms in cell-autonomous immunity,* Nature Reviews Immunology **12**, 367 (2012).

[8] E.-K. Jo, J.-M. Yuk, D.-M. Shin, and C. Sasakawa, *Roles of autophagy in elimination of intracellular bacterial pathogens,* Frontiers in immunology **4**, 97 (2013).

[9] T. Bergsbaken, S. L. Fink, and B. T. Cookson, *Pyroptosis: host cell death and inflammation,* Nature Reviews Microbiology **7**, 99 (2009).

[10] P. Yu, X. Zhang, N. Liu, L. Tang, C. Peng, and X. Chen, *Pyroptosis: mechanisms and diseases,* Signal transduction and targeted therapy **6**, 128 (2021).

[11] Y. S. Cheng, R. J. Colonno, and F. H. Yin, *Interferon induction of fibroblast proteins with guanylate binding activity.* Journal of Biological Chemistry **258**, 7746 (1983).

[12] Y. Cheng, M. F. Becker-Manley, T. P. Chow, and D. C. Horan, *Affinity purification of an interferon-induced human guanylate-binding protein and its characterization.* Journal of Biological Chemistry **260**, 15834 (1985).

[13] M. A. Olszewski, J. Gray, and D. J. Vestal, *In silico genomic analysis of the human and murine guanylate-binding protein (gbp) gene clusters,* Journal of Interferon & Cytokine Research **26**, 328 (2006).

[14] S. L. Anderson, J. M. Carton, J. Lou, L. Xing, and B. Y. Rubin, *Interferon-induced guanylate binding protein-1 (gbp-1) mediates an antiviral effect against vesicular stomatitis virus and encephalomyocarditis virus,* Virology **256**, 8 (1999).

[15] Y. Itsui, N. Sakamoto, S. Kakinuma, M. Nakagawa, Y. Sekine-Osajima, M. Tasaka-Fujita, Y. Nishimura-Sakurai, G. Suda, Y. Karakama, K. Mishima, *et al.*, *Antiviral effects of the interferon-induced protein guanylate binding protein 1 and its interaction with the hepatitis c virus ns5b protein,* Hepatology **50**, 1727 (2009).

[16] C. Krapp, D. Hotter, A. Gawanbacht, P. J. McLaren, S. F. Kluge, C. M. Stürzel, K. Mack, E. Reith, S. Engelhart, A. Ciuffi, *et al.*, *Guanylate binding protein (gbp) 5 is an interferon-inducible inhibitor of hiv-1 infectivity,* Cell host & microbe **19**, 504 (2016).

[17] I. Tietzel, C. El-Haibi, and R. A. Carabeo, *Human guanylate binding proteins potentiate the anti-chlamydia effects of interferon-γ,* PloS one **4**, e6499 (2009).

[18] E. Braun, D. Hotter, L. Koepke, F. Zech, R. Groß, K. M. Sparrer, J. A. Müller, C. K. Pfaller, E. Heusinger, R. Wombacher, *et al.*, *Guanylate-binding proteins 2 and 5 exert broad antiviral activity by inhibiting furin-mediated processing of viral envelope proteins,* Cell Reports **27**, 2092 (2019).

[19] M. Yamamoto, M. Okuyama, J. S. Ma, T. Kimura, N. Kamiyama, H. Saiga, J. Ohshima, M. Sasai, H. Kayama, T. Okamoto, *et al.*, *A cluster of interferon-γ-inducible p65 gtpases plays a critical role in host defense against toxoplasma gondii,* Immunity **37**, 302 (2012).

[20] J. C. Santos, D. Boucher, L. K. Schneider, B. Demarco, M. Dilucca, K. Shkarina, R. Heilig, K. W. Chen, R. Y. Lim, and P. Broz, *Human gbp1 binds lps to initiate assembly of a caspase-4 activating platform on cytosolic bacteria,* Nature communications **11**, 3276 (2020).

[21] M. P. Wandel, B.-H. Kim, E.-S. Park, K. B. Boyle, K. Nayak, B. Lagrange, A. Herod, T. Henry, M. Zilbauer, J. Rohde, *et al.*, *Guanylate-binding proteins convert cytosolic bacteria into caspase-4 signaling platforms,* Nature immunology **21**, 880 (2020).

[22] B. Prakash, G. J. Praefcke, L. Renault, A. Wittinghofer, and C. Herrmann, *Structure of human guanylate-binding protein 1 representing a unique class of gtp-binding proteins,* Nature **403**, 567 (2000).

[23] A. Ghosh, G. J. Praefcke, L. Renault, A. Wittinghofer, and C. Herrmann, *How guanylate-binding proteins achieve assembly-stimulated processive cleavage of gtp to gmp,* Nature **440**, 101 (2006).

[24] T. Vöpel, C. S. Hengstenberg, T.-O. Peulen, Y. Ajaj, C. A. Seidel, C. Herrmann, and J. P. Klare, *Triphosphate induced dimerization of human guanylate binding protein 1 involves association of the c-terminal helices: a joint double electron–electron resonance and fret study,* Biochemistry **53**, 4590 (2014).

[25] M. Schwemmle and P. Staeheli, *The interferon-induced 67-kda guanylate-binding protein (hgbp1) is a gtpase that converts gtp to gmp,* Journal of Biological Chemistry **269**, 11299 (1994).

[26] R. Neun, M. F. Richter, P. Staeheli, and M. Schwemmle, *Gtpase properties of the interferon-induced human guanylate-binding protein 2,* FEBS letters **390**, 69 (1996).

[27] M. Wehner and C. Herrmann, *Biochemical properties of the human guanylate binding protein 5 and a tumor-specific truncated splice variant,* The FEBS journal **277**, 1597 (2010).

[28] G. J. Praefcke, M. Geyer, M. Schwemmle, H. R. Kalbitzer, and C. Herrmann, *Nucleotide-binding characteristics of human guanylate-binding protein 1 (hgbp1) and identification of the third gtp-binding motif,* Journal of molecular biology **292**, 321 (1999).

[29] G. J. Praefcke, S. Kloep, U. Benscheid, H. Lilie, B. Prakash, and C. Herrmann, *Identification of residues in the human guanylate-binding protein 1 critical for nucleotide binding and cooperative gtp hydrolysis,* Journal of molecular biology **344**, 257 (2004).

[30] G. J. Praefcke and H. T. McMahon, *The dynamin superfamily: universal membrane tubulation and fission molecules?* Nature reviews Molecular cell biology **5**, 133 (2004).

[31] R. Ramachandran and S. L. Schmid, *The dynamin superfamily,* Current Biology **28**, R411 (2018).

[32] O. Daumke and G. J. Praefcke, *Invited review: Mechanisms of gtp hydrolysis and conformational transitions in the dynamin superfamily,* Biopolymers **105**, 580 (2016).

[33] M. G. Ford and J. S. Chappie, *The structural biology of the dynamin-related proteins: New insights into a diverse, multitalented family,* Traffic **20**, 717 (2019).

[34] S. M. Ferguson and P. De Camilli, *Dynamin, a membrane-remodelling gtpase,* Nature reviews Molecular cell biology **13**, 75 (2012).

[35] J. P. O'Donnell, R. B. Cooley, C. M. Kelly, K. Miller, O. S. Andersen, R. Rusinova, and H. Sondermann, *Timing and reset mechanism of gtp hydrolysis-driven conformational changes of atlastin,* Structure **25**, 997 (2017).

[36] K. Faelber, Y. Posor, S. Gao, M. Held, Y. Roske, D. Schulze, V. Haucke, F. Noé, and O. Daumke, *Crystal structure of nucleotide-free dynamin,* Nature **477**, 556 (2011).

[37] S. Gao, A. von der Malsburg, A. Dick, K. Faelber, G. F. Schröder, O. Haller, G. Kochs, and O. Daumke, *Structure of myxovirus resistance protein a reveals intra-and intermolecular domain interactions required for the antiviral function,* Immunity **35**, 514 (2011).

[38] P. J. Casey, J. A. Thissen, and J. F. Moomaw, *Enzymatic modification of proteins with a geranylgeranyl isoprenoid.* Proceedings of the National Academy of Sciences **88**, 8631 (1991).

[39] S. Clarke, *Protein isoprenylation and methylation at carboxyl-terminal cysteine residues,* Annual review of biochemistry **61**, 355 (1992).

[40] P. J. Casey, *Biochemistry of protein prenylation.* Journal of lipid research **33**, 1731 (1992).

[41] D. E. Nantais, M. Schwemmle, J. T. Stickney, D. J. Vestal, and J. E. Buss, *Prenylation of an interferon-γ-induced gtp-binding protein: the human guanylate binding protein, hugbp1,* Journal of leukocyte biology **60**, 423 (1996).

[42] N. Britzen-Laurent, M. Bauer, V. Berton, N. Fischer, A. Syguda, S. Reipschläger, E. Naschberger, C. Herrmann, and M. Stürzl, *Intracellular trafficking of guanylate-binding proteins is regulated by heterodimerization in a hierarchical manner,* PloS one **5**, e14246 (2010).

[43] Y. Reiss, J. L. Goldstein, M. C. Seabra, P. J. Casey, and M. S. Brown, *Inhibition of purified p21ras farnesyl: protein transferase by cys-aax tetrapeptides,* Cell **62**, 81 (1990).

[44] P. J. Casey and M. C. Seabra, *Protein prenyltransferases,* Journal of Biological Chemistry **271**, 5289 (1996).

[45] S. L. Moores, M. D. Schaber, S. D. Mosser, E. Rands, M. B. O'Hara, V. M. Garsky, M. S. Marshall, D. L. Pompliano, and J. Gibbs, *Sequence dependence of protein isoprenylation,* Journal of Biological Chemistry **266**, 14603 (1991).

[46] N. Baumann and A. Menon, *Chapter 2. lipid modifications of proteins,* NEW COMPREHENSIVE BIOCHEMISTRY **36**, 37 (2002).

[47] C. Ji, S. Du, P. Li, Q. Zhu, X. Yang, C. Long, J. Yu, F. Shao, and J. Xiao, *Structural mechanism for guanylate-binding proteins (gbps) targeting by the shigella e3 ligase ipah9. 8,* PLoS pathogens **15**, e1007876 (2019).

[48] M. R. Philips, M. H. Pillinger, R. Staud, C. Volker, M. G. Rosenfeld, G. Weissmann, and J. B. Stock, *Carboxyl methylation of ras-related proteins during signal transduction in neutrophils,* Science **259**, 977 (1993).

[49] V. L. Boyartchuk, M. N. Ashby, and J. Rine, *Modulation of ras and a-factor function by carboxyl-terminal proteolysis,* Science **275**, 1796 (1997).

[50] J. Gao, J. Liao, and G.-Y. Yang, *Caax-box protein, prenylation process and carcinogenesis,* American journal of translational research **1**, 312 (2009).

[51] P. Tripal, M. Bauer, E. Naschberger, T. Mörtinger, C. Hohenadl, E. Cornali, M. Thurau, and M. Stürzl, *Unique features of different members of the human guanylate-binding protein family,* Journal of interferon & cytokine research **27**, 44 (2007).

[52] D. Fisch, H. Bando, B. Clough, V. Hornung, M. Yamamoto, A. R. Shenoy, and E.-M. Frickel, *Human gbp 1 is a microbe-specific gatekeeper of macrophage apoptosis and pyroptosis,* The EMBO journal **38**, e100926 (2019).

[53] D. Fisch, B. Clough, M.-C. Domart, V. Encheva, H. Bando, A. P. Snijders, L. M. Collinson, M. Yamamoto, A. R. Shenoy, and E.-M. Frickel, *Human gbp1 differentially targets salmonella and toxoplasma to license recognition of microbial ligands and caspase-mediated death,* Cell reports **32**, 108008 (2020).

[54] S. Zhu, C. J. Bradfield, A. Mamińska, E.-S. Park, B.-H. Kim, P. Kumar, S. Huang, Y. Zhang, J. Bewersdorf, and J. D. MacMicking, *Cryo-et of a human gbp coatomer governing cell-autonomous innate immunity to infection,* Biorxiv , 2021 (2021).

[55] S. V. Valeva, M. Degabriel, F. Michal, G. Gay, J. R. Rohde, F. Randow, B. Lagrange, and T. Henry, *Comparative study of gbp recruitment on two cytosol-dwelling pathogens, francisella novicida and shigella flexneri highlights differences in gbp repertoire and in gbp1 motif requirements,* Pathogens and Disease **81**, ftad005 (2023).

[56] A. S. Piro, D. Hernandez, S. Luoma, E. M. Feeley, R. Finethy, A. Yirga, E. M. Frickel, C. F. Lesser, and J. Coers, *Detection of cytosolic shigella flexneri via a c-terminal triple-arginine motif of gbp1 inhibits actin-based motility,* MBio **8**, 10 (2017).

[57] K. M. Kohler, M. Kutsch, A. S. Piro, G. D. Wallace, J. Coers, and M. F. Barber, *A rapidly evolving polybasic motif modulates bacterial detection by guanylate binding proteins,* MBio **11**, 10 (2020).

[58] N. Modiano, Y. E. Lu, and P. Cresswell, *Golgi targeting of human guanylate-binding protein-1 requires nucleotide binding, isoprenylation, and an ifn-γ-inducible cofactor,* Proceedings of the National Academy of Sciences **102**, 8680 (2005).

[59] L. Fagerberg, B. M. Hallström, P. Oksvold, C. Kampf, D. Djureinovic, J. Odeberg, M. Habuka, S. Tahmasebpoor, A. Danielsson, K. Edlund, *et al.*, *Analysis of the human tissue-specific expression by genome-wide integration of transcriptomics and antibody-based proteomics,* Molecular & cellular proteomics **13**, 397 (2014).

[60] M. Uhlén, L. Fagerberg, B. M. Hallström, C. Lindskog, P. Oksvold, A. Mardinoglu, Å. Sivertsson, C. Kampf, E. Sjöstedt, A. Asplund, *et al.*, *Tissue-based map of the human proteome,* Science **347**, 1260419 (2015).

[61] K. Tretina, E.-S. Park, A. Maminska, and J. D. MacMicking, *Interferon-induced guanylate-binding proteins: Guardians of host defense in health and disease,* Journal of Experimental Medicine **216**, 482 (2019).

[62] T. Jin, M. Huang, P. Smith, J. Jiang, and T. S. Xiao, *Structure of the caspase-recruitment domain from a zebrafish guanylate-binding protein,* Acta Crystallographica Section F: Structural Biology and Crystallization Communications **69**, 855 (2013).

[63] K. S. Schneider, C. J. Groß, R. F. Dreier, B. S. Saller, R. Mishra, O. Gorka, R. Heilig, E. Meunier, M. S. Dick, T. Ćiković, *et al.*, *The inflammasome drives gsdmd-independent secondary pyroptosis and il-1 release in the absence of caspase-1 protease activity,* Cell reports **21**, 3846 (2017).

[64] D. Zheng, T. Liwinski, and E. Elinav, *Inflammasome activation and regulation: toward a better understanding of complex mechanisms,* Cell discovery **6**, 36 (2020).

[65] Y. Dai, J. Zhou, and C. Shi, *Inflammasome: structure, biological functions, and therapeutic targets,* MedComm **4**, e391 (2023).

[66] B.-H. Kim, A. R. Shenoy, P. Kumar, R. Das, S. Tiwari, and J. D. MacMicking, *A family of ifn-γ–inducible 65-kd gtpases protects against bacterial infection,* Science **332**, 717 (2011).

[67] M. P. Wandel, C. Pathe, E. I. Werner, C. J. Ellison, K. B. Boyle, A. von der Malsburg, J. Rohde, and F. Randow, *Gbps inhibit motility of shigella flexneri but are targeted for degradation by the bacterial ubiquitin ligase ipah9. 8,* Cell host & microbe **22**, 507 (2017).

[68] D. Fisch, B. Clough, R. Khan, L. Healy, and E.-M. Frickel, *Toxoplasma-proximal and distal control by gbps in human macrophages,* Pathogens and disease **79**, ftab058 (2021).

[69] M. Kutsch, L. Sistemich, C. F. Lesser, M. B. Goldberg, C. Herrmann, and J. Coers, *Direct binding of polymeric gbp1 to lps disrupts bacterial cell envelope functions,* The EMBO journal **39**, e104926 (2020).

[70] M. Osborn, J. Gander, E. Parisi, and J. Carson, *Mechanism of assembly of the outer membrane of salmonella typhimurium: isolation and characterization of cytoplasmic and outer membrane,* Journal of Biological Chemistry **247**, 3962 (1972).

[71] A. E. Gauthier, R. D. Rotjan, and J. C. Kagan, *Lipopolysaccharide detection by the innate immune system may be an uncommon defence strategy used in nature,* Open Biology **12**, 220146 (2022).

[72] J. Shi, Y. Zhao, K. Wang, X. Shi, Y. Wang, H. Huang, Y. Zhuang, T. Cai, F. Wang, and F. Shao, *Cleavage of gsdmd by inflammatory caspases determines pyroptotic cell death,* Nature **526**, 660 (2015).

[73] X. Liu, Z. Zhang, J. Ruan, Y. Pan, V. G. Magupalli, H. Wu, and J. Lieberman, *Inflammasome-activated gasdermin d causes pyroptosis by forming membrane pores,* Nature **535**, 153 (2016).

[74] C. L. Evavold, J. Ruan, Y. Tan, S. Xia, H. Wu, and J. C. Kagan, *The pore-forming protein gasdermin d regulates interleukin-1 secretion from living macrophages,* Immunity **48**, 35 (2018).

[75] H. Buijze, V. Brinkmann, R. Hurwitz, A. Dorhoi, S. H. Kaufmann, and G. Pei, *Human gbp1 is involved in the repair of damaged phagosomes/endolysosomes,* International Journal of Molecular Sciences **24**, 9701 (2023).

[76] P. Li, W. Jiang, Q. Yu, W. Liu, P. Zhou, J. Li, J. Xu, B. Xu, F. Wang, and F. Shao, *Ubiquitination and degradation of gbps by a shigella effector to suppress host defence,* Nature **551**, 378 (2017).

[77] L. Goers, K. Kim, T. C. Stedman, P. J. Canning, X. Mou, N. H. Ernst, J. Coers, and C. F. Lesser, *Shigella ipah9. 8 limits gbp1-dependent lps release from intracytosolic bacteria to suppress caspase-4 activation,* Proceedings of the National Academy of Sciences **120**, e2218469120 (2023).

[78] M. Adrian, J. Dubochet, J. Lepault, and A. W. McDowall, *Cryo-electron microscopy of viruses,* Nature **308**, 32 (1984).

[79] J. Dubochet, M. Adrian, J.-J. Chang, J.-C. Homo, J. Lepault, A. W. McDowall, and P. Schultz, *Cryo-electron microscopy of vitrified specimens,* Quarterly reviews of biophysics **21**, 129 (1988).

[80] A. F. Brilot, J. Z. Chen, A. Cheng, J. Pan, S. C. Harrison, C. S. Potter, B. Carragher, R. Henderson, and N. Grigorieff, *Beam-induced motion of vitrified specimen on holey carbon film,* Journal of structural biology **177**, 630 (2012).

[81] S. Q. Zheng, E. Palovcak, J.-P. Armache, K. A. Verba, Y. Cheng, and D. A. Agard, *Motioncor2: anisotropic correction of beam-induced motion for improved cryo-electron microscopy,* Nature methods **14**, 331 (2017).

[82] H. Erickson and A. Klug, *Measurement and compensation of defocusing and aberrations by fourier processing of electron micrographs,* Philosophical Transactions of the Royal Society of London. B, Biological Sciences **261**, 105 (1971).

[83] A. Rohou and N. Grigorieff, *Ctffind4: Fast and accurate defocus estimation from electron micrographs,* Journal of structural biology **192**, 216 (2015).

[84] M. Van Heel and J. Frank, *Use of multivariates statistics in analysing the images of biological macromolecules,* Ultramicroscopy **6**, 187 (1981).

[85] H. Berman, K. Henrick, and H. Nakamura, *Announcing the worldwide protein data bank,* Nature structural & molecular biology **10**, 980 (2003).

[86] T. Nakane, A. Kotecha, A. Sente, G. McMullan, S. Masiulis, P. M. Brown, I. T. Grigoras, L. Malinauskaite, T. Malinauskas, J. Miehling, *et al.*, *Single-particle cryo-em at atomic resolution,* Nature **587**, 152 (2020).

[87] K. M. Yip, N. Fischer, E. Paknia, A. Chari, and H. Stark, *Atomic-resolution protein structure determination by cryo-em,* Nature **587**, 157 (2020).

[88] M. A. Herzik Jr, M. Wu, and G. C. Lander, *High-resolution structure determination of sub-100 kda complexes using conventional cryo-em,* Nature communications **10**, 1032 (2019).

[89] K. Dierksen, D. Typke, R. Hegerl, J. Walz, E. Sackmann, and W. Baumeister, *Three-dimensional structure of lipid vesicles embedded in vitreous ice and investigated by automated electron tomography,* Biophysical Journal **68**, 1416 (1995).

[90] A. Steven and D. Belnap, *Electron microscopy and image processing: an essential tool for structural analysis of macromolecules,* Current Protocols in Protein Science **42**, 17 (2005).

[91] R. I. Koning, A. J. Koster, and T. H. Sharp, *Advances in cryo-electron tomography for biology and medicine,* Annals of Anatomy-Anatomischer Anzeiger **217**, 82 (2018).

[92] I. Drulyte, R. M. Johnson, E. L. Hesketh, D. L. Hurdiss, C. A. Scarff, S. A. Porav, N. A. Ranson, S. P. Muench, and R. F. Thompson, *Approaches to altering particle distributions in cryo-electron microscopy sample preparation,* Acta Crystallographica Section D: Structural Biology **74**, 560 (2018).

[93] Y. Z. Tan, P. R. Baldwin, J. H. Davis, J. R. Williamson, C. S. Potter, B. Carragher, and D. Lyumkis, *Addressing preferred specimen orientation in single-particle cryo-em through tilting,* Nature methods **14**, 793 (2017).

[94] C. Hamers-Casterman, T. Atarhouch, S. a. Muyldermans, G. Robinson, C. Hammers, E. B. Songa, N. Bendahman, and R. Hammers, *Naturally occurring antibodies devoid of light chains,* Nature **363**, 446 (1993).

[95] C. McMahon, A. S. Baier, R. Pascolutti, M. Wegrecki, S. Zheng, J. X. Ong, S. C. Erlandson, D. Hilger, S. G. Rasmussen, A. M. Ring, *et al., Yeast surface display platform for rapid discovery of conformationally selective nanobodies,* Nature structural & molecular biology **25**, 289 (2018).

[96] H. Kaur, J.-B. Hartmann, R. P. Jakob, M. Zahn, I. Zimmermann, T. Maier, M. A. Seeger, and S. Hiller, *Identification of conformation-selective nanobodies against the membrane protein insertase bama by an integrated structural biology approach,* Journal of biomolecular NMR **73**, 375 (2019).

[97] T. Uchański, E. Pardon, and J. Steyaert, *Nanobodies to study protein conformational states,* Current opinion in structural biology **60**, 117 (2020).

[98] R. Van der Linden, L. Frenken, B. De Geus, M. Harmsen, R. Ruuls, W. Stok, L. De Ron, S. Wilson, P. Davis, and C. Verrips, *Comparison of physical chemical properties of llama vhh antibody fragments and mouse monoclonal antibodies,* Biochimica et Biophysica Acta (BBA)-Protein Structure and Molecular Enzymology **1431**, 37 (1999).

[99] U. Rothbauer, K. Zolghadr, S. Tillib, D. Nowak, L. Schermelleh, A. Gahl, N. Backmann, K. Conrath, S. Muyldermans, M. C. Cardoso, *et al., Targeting and tracing antigens in live cells with fluorescent nanobodies,* Nature methods **3**, 887 (2006).

[100] B. Traenkle and U. Rothbauer, *Under the microscope: single-domain antibodies for live-cell imaging and super-resolution microscopy,* Frontiers in immunology **8**, 1030 (2017).

2

A nanobody toolbox for GBP1

Guanylate binding protein 1 (GBP1) is a large guanosine triphosphatase (GTPase) of the dynamin superfamily, able to promote interferon inducible cell-autonomous immunity and cell death. Structurally, GBP1 consists of an N-terminal large GTPase domain and an extended α-helical C-terminal domain. While the crystal structure of the GBP1 monomer has been determined, the nucleotide-induced GBP1 dimer has resisted crystallisation. A high degree of structural flexibility and low molecular weight also pose challenges for structure determination by cryogenic electron microscopy (cryo-EM). In order to increase the effective molecular weight and to stabilise certain conformational states of GBP1, we explored the possibility to utilise conformation-specific nanobodies. Here, we present and characterise eight GBP1-binding nanobodies (Nbs) derived from llama immunisation with conformationally stabilised GBP1 preparations. We evaluated their specificity for GBP1 over its closest homolog GBP2 using size exclusion chromatography coupled to multi-angle light scattering (SEC-MALS) and determined their affinities by surface plasmon resonance (SPR). For a subset of Nbs we also characterised the GBP1 binding site by cryo-EM. To mechanistically study the effect Nbs can have on the ability of GBP1 to coat membranes, we set up a fluorescence microscopy experiment. With this set of newly identified Nbs, we open up the possibility to structurally stabilise the GBP1 dimer, facilitating structure determination. Moreover, it enabled us to structurally and functionally investigate the relevance of certain structural states essential for coat formation.

This chapter has not been published. Contributions to the work have been made by Tanja Kuhm, Lennart Pagani, Cecilia de Agrela Pinto, Alex Fish, Els Pardon and Arjen J. Jakobi

2.1. Introduction

Over the last decade guanylate binding proteins (GBPs) have emerged as important players in cell-autonomous immunity [1, 2]. Following a cytokine induction, they have been linked to defend the host against cytosolic and vacuole-resident bacteria as well as parasites and viruses. [3–10]. While the exact mechanism of action remains incompletely understood, GBPs have been shown to restrict pathogen replication [11–13]. Although guanylate binding protein 1 (GBP1) has been shown to be actively involved in the lysis of *toxoplasma gondii* (Tg) containing vacuoles as well as the pathogen membrane itself, GBP1 induced membrane rupture of other pathogen membranes has not been observed yet [10].

Notably, GBP1 directly interacts with lipopolysaccharides (LPS) on the outer membrane of gram-negative bacteria [9, 14, 15], forming supramolecular complexes that can coat the entire bacterial surface [9, 14, 15]. This interaction initiates the assembly of other GBP family members (GBP2-GBP4), leading to the recruitment and activation of caspase-4 [15]. Activated caspase-4 subsequently cleaves gasdermin D, triggering an inflammatory type of programmed cell death known as pyroptosis [16, 17]. Given GBP1's role as the primary member recruited to pathogens and pathogen-containing vacuoles, this chapter primarily focuses on GBP1.

Structurally, GBP1 comprises an N-terminal large GTPase (LG) domain and an extended purely α-helical C-terminal domain, which can be subdivided into a middle domain (MD) and a GTPase effector domain (GED) [18]. In addition, GBP1 possesses a prenylation motif, allowing farnesylation of a cysteine residue at the C-terminus [19]. Prenylation enables recruitment of GBP1 to intracellular membranes [20]. Although crystal structures of monomeric GBP1 and the nucleotide-dependent dimer of the LG domain are available [18, 21], high-resolution structures of the full-length GBP1 dimer and its detailed organisation on membranes remain elusive. Different models of potential GBP1-dimer structures have been postulated [22, 23] but lack experimental verification.

A high degree of structural flexibility and low molecular weight of the GBP1 dimer (130 kDa) make cryo-EM structure determination challenging [22]. One strategy to limit protein flexibility in structural biology is the use of conformational stabilisers. A widely applicable strategy uses chemical cross-linking which unspecifically introduces covalent bonds between two close reactive amino-acid residues [24–26]. Disadvantages of cross-linking include the possibility to favor the most compact configuration over other conformations as well as the possibility to introduce artificial interactions [27]. Besides, establishing a suitable cross-linking protocol can require extensive rounds of optimisation. Another approach to limit conformational flexibility of proteins includes the binding of either immunoglobulin derivatives such as antibodies or nanobodies or non-immunoglobulin binders [28]. Non-immunoglobulin binders comprise of a scaffolding protein forming the structural core, while target-specific binder sequences are generated by directed evolution [28]. Such binders include affibodies, anticalins, DARPins or monobodies [29–32]. The main advantages of such non-immunoglobulin binders is that it circumvents the need of animal immunization, besides other advantages such as low production costs, high solubility and thermal stability [33].

Nanobodies on the other hand are an immunoglobulin derivative type of stabiliser [34, 35]. They consist of a single variable domain derived from heavy chain antibodies found in sera of Camelidae [36]. Compared to antibodies, they are small in size (~ 15 kDa) and are therefore well suited to specifically recognise, bind and stabilise a particular conformational state of the protein. The combination of high target affinity and conformational specific binding makes Nbs a useful tool in structure determination using cryo-electron microscopy or crystallography [35, 37–39].

Nbs contain three hyper-variable complementarity determining regions (CDRs) responsible for antigen binding. The CDR3 loop of most Nbs is longer compared to conventional antibodies and is able to adapt a finger-like structure that can recognise and strongly bind to small clefts and active sites of enzymes. [37, 40]. Nbs have the potential to decrease protein flexibility by locking the target proteins in a specific conformation [38, 39, 41]. Among the attractive properties of Nbs are, that they can be expressed in bacteria, their good solubility and their extraordinary stability regarding temperature or pH [42–45]. As Nbs are able to even withstand reducing environments of eukaryotic cells without losing target specificity, they can be expressed as fluorescently labelled intrabodies, specifically marking antigens inside living cells [46, 47], enabling the coupling of structural data and functional data.

Here, we were interested to identify Nbs stabilising the full length GBP1 dimer to aid structure determination by cryo-EM. More precisely, we sought for Nbs that are specific for monomeric GBP1, dimeric GBP1 or farnesylated GBP1 in order to establish a comprehensive toolkit that allows discriminating between different structural and oligomeric states of GBP1 for mechanistic studies *in vitro* and in the cell.

We present eight different Nbs that were raised either against monomeric GBP1, farnesylated GBP1 or nucleotide stabilised dimeric GBP1. We characterise their ability to bind GBP1 using SEC-MALS experiments and determine their affinity by surface plasmon resonance (SPR). To probe the specificity of our Nbs for GBP1, we also tested whether the Nbs were able to bind to GBP2, the most closely related member of the human GBP family. We further structurally mapped the binding site of selected Nbs on recombinantly produced GBP1 by cryo-EM. Our nanobody toolkit will allow addressing important outstanding structural and mechanistic questions related to GBP1 function in cell-autonomous immunity.

2.2. Results

Discovery of conformation-specific Nbs for GBP1.

In this chapter, we explore Nb discovery to identify binders that stabilise specific conformational states of GBP1 to support structural and functional studies. Our primary goal is to identify Nbs which will enable structure determination of the GBP1 dimer. However, the identification of Nbs specifically targeting monomeric or dimeric and farnesylated or non-farnesylated GBP1 could enable us to better understand the conformational and oligomeric states GBP1 has to undergo in order for its antimicrobial function to be effective. We therefore immunised llamas with either monomeric GBP1 with/without C-

terminal farnesylation or unmodified dimeric GBP1 (Figure 2.1).

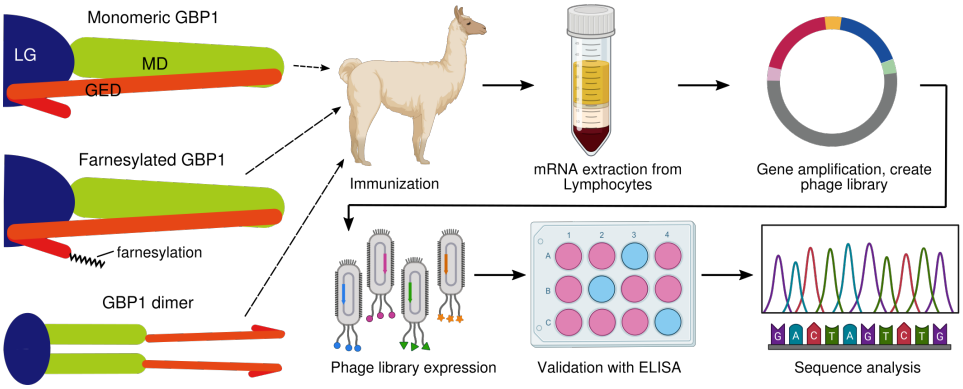

Figure 2.1: Generation of conformation-specific Nbs for GBP1. Left: Schematic representation of the domain architecture of GBP1. LG: Large GTPase domain (blue), MD: Middle domain (green), GED: GTPase effector domain (orange and red). A schematic representation of farnesylated GBP and a potential GBP1-dimer is also shown. Right: Overview of Nb generation, selection and validation. Blood samples are taken from a previously immunised llama, RNA is extracted from blood lymphocytes, reverse-transcribed into cDNA, PCR-amplified and cloned into a phage display library. Clones are validated using enzyme-linked immunosorbent assay (ELISA) and sequences of binding Nbs are further analysed to cluster Nb families. The figure was partly generated with BioRender.

We identified a total of 71 Nbs raised against farnesylated monomeric GBP1 (12 Nbs), GDP·AlF_3-stabilised dimeric GBP1 (42 Nbs) or non-farnesylated monomeric GBP1 (17 Nbs) belonging to 36 different families (Table 2.1). A nanobody family is defined by a high degree of amino acid sequence identity in their CDR3 loop (identical length and >80% sequence identity), typically indicating that they recognise similar epitopes [48]. Whereas Nbs that were raised against farnesylated GBP1 and dimeric GBP1 show clustering into distinct CDR families, nine out of the 17 Nbs raised against the non-farnesylated, monomeric GBP1 cluster into CDR families also identified for Nbs raised against GDP·AlF_3-stabilised dimeric GBP1, namely family 11, 12 and 14 (Table 2.1).

Table 2.1: Summary of identified Nbs that were raised against farnesylated GBP1, GDP·AlF_3-stabilised dimeric GBP1 and monomeric GBP1

Raised against	**No of Nbs**	**No of families**	**Family names**	**No of Nbs per family**	**Nbs in this study**
Farnesylated GBP1	12	10	1 2 - 10	3 one each	**Nb74**
GDP·AlF_3 stabilised dimer	42	18	11 12 13-28	14 12 one each	**Nb77** **Nb76** and **Nb202** **Nb193** (family 18) **Nb195** (family 14) **Nb196** (family 25)
Monomer	17	11	11 12 14 29 - 36	6 2 1 one each	 **Nb75** (family 29)

Selection and purification of eight Nbs that were raised against GBP1.

The sequences of the obtained Nbs were analysed by multiple sequence alignment (MSA) showing large differences in the three complementarity-determining regions of the sequences (CDRs) as expected (Figure 2.2, Supplementary Figure 2.20 and Supplementary Figure 2.21).

For this study, we selected eight different Nbs that were raised against either farnesylated monomeric GBP1 ($GBP1_F$), non-farnesylated monomeric GBP1 or unmodified dimeric GBP1-GDP·AlF_3 (Table 2.1). We chose one Nb (Nb74) that was raised against $GBP1_F$, six Nbs that were raised against GDP·AlF_3-stabilised dimeric GBP1 and one Nb (Nb75) that was raised against monomeric GBP1 (Table 2.1). Nb74 was raised against $GBP1_F$ and belongs to family 1. It was selected for this study because it belongs to a family with multiple members. Having multiple Nbs in one family can be of advantage if expression or stability of the Nb is poor, as single amino acid mutation can potentially improve those properties [48]. The same reasoning was used when choosing Nbs that were raised against GDP·AlF_3-stabilised dimeric GBP1. We chose Nb77 from family 11 as well as Nb76 and Nb202, both belonging to family 12, only differing in two individual amino acids (Figure 2.2a, Figure 2.10c). To increase the probability to target different eipitopes, we also chose Nbs from different families that had only one member per family (Nb193 from family 18, Nb195 from family 14 and Nb196 from family 25) as well as Nb75 that was raised against monomeric GBP1 and belongs to family 29 (Table 2.1).

In a first step, Nbs were successfully expressed and purified, which was verified by an SDS-PAGE revealing a single band without visible contaminants indicating high purity at a molecular weight around 10 kDa (Figure 2.2b,c).

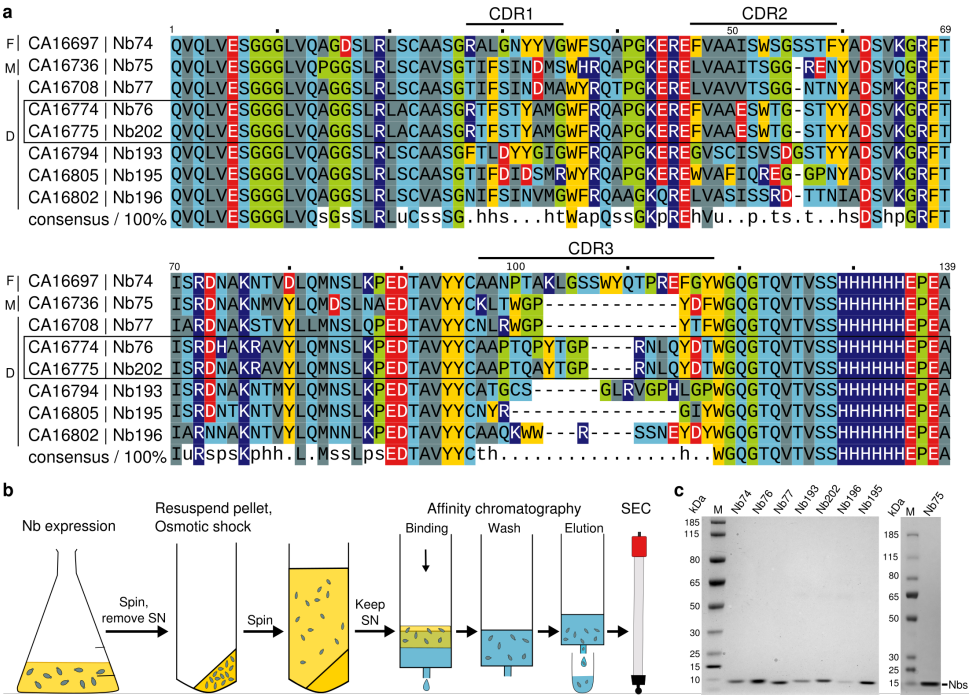

Figure 2.2: Multiple sequence alignment and Nb expression and purification schematic. (a) Multiple sequence alignment (MSA) of Nbs used in this chapter. Primary sequences were used as input for Clustal Omega [49]. The three complementarity-determining regions of the sequences (CDRs) are highlighted above the MSA. The letters F, M or D indicate whether the Nbs were discovered using monomeric farnesylated GBP1 (F), non-farnesylated monomeric GBP1 (M) or unmodified dimeric GBP1-GDP·AlF_3 (D). The box around Nb76 and Nb202 indicates that they belong to the same family. Residues are coloured by physicochemical property of the side chain (grey: hydrophobic, light blue: polar, red: negatively charged, dark blue: positively charged, yellow: aromatic, green: special cases). The consensus sequence (100 %) is shown below the alignment together with conserved physicochemical classes (l: aliphatic, a: aromatic, c: charged, h: hydrophobic, -: negative, p: polar, +: positive, s: small, u: tiny, t: turn-like). (b) Schematic of Nb expression and purification. After expression and centrifugation, the supernatant (SN) was removed. The pellet was resuspended, before performing an osmotic shock. The supernatant of a following centrifugation step was used as input for an ion metal affinity chromatography (IMAC). In a final step a size exclusion chromatography (SEC) was performed. (c) Representative SDS-PAGE analysis of purified Nbs with a pure protein band around 10 kDa corresponding to the size of the Nbs.

Selected Nbs show specificity for conformational and oligomeric states of GBP1

We next probed Nb selectivity for monomeric or dimeric GBP1 via size exclusion chromatography coupled to multi-angle light scattering (SEC-MALS). SEC-MALS experiments identified two Nbs (Nb74 and Nb76) that were able to bind monomeric GBP1 as observed from the shift in molecular weight (M_W) by roughly 13 kDa, consistent with the molecular weight of a 1:1 complex of GBP1 with Nb74 or Nb76. To test whether Nb74 and Nb76 also bind the GBP1 dimer, we repeated the experiments with the GDP·AlF_3-stabilised dimer preparations of GBP1 (Figure 2.3a,b). We observed the molecular weight to increase by ~26 kDa confirming a 2:2 stochiometry and that Nb74/Nb76 binding does not interfere with GBP1 dimerisation. For Nb76 we observed an additional peak with a M_W of 178 kDa (Figure 2.3b) indicating that the binding stochiometry between Nb76 and GBP1 is not always strictly 2:2. Although we have not resolved the exact composition of this additional peak, the shift to higher elution volumes is an indication for a more compact conformation and the observed behaviour was reproducible (Supplementary Figure 2.22a).

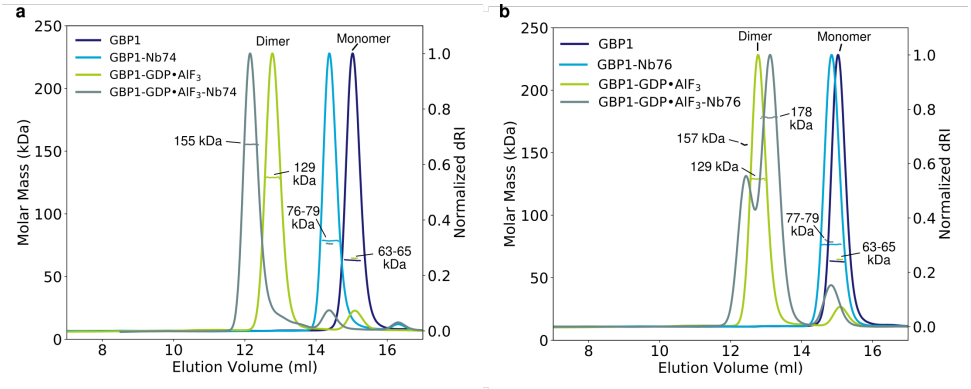

Figure 2.3: Nb74 and Nb76 bind to monomeric and dimeric GBP1. (a-b) SEC-MALS profiles showing that Nb74 and Nb76 bind to monomeric and GDP·AlF_3-stabilised dimeric GBP1 shifting the molecular weight by roughly 13 kDa for the monomer or by 26 kDa for the dimer. The M_W of the Nb is ~12 kDa, consistent with a 1:1 and 2:2 binding stochiometry with the GBP1 monomer and dimer, respectively (b) The binding of Nb76 to dimeric GBP1 results in an additional peak with an estimated M_W of 178 kDa. This 178 kDa peak is shifted to the right relative to the 157 kDa peak indicating a more compact conformation.

Contrary to Nb74 and Nb76 which are not selective toward the oligomerisation state of GBP1, we also identified four Nbs (Nb193, Nb195, Nb196 and Nb202) that exclusively bind the GDP·AlF_3-stabilised dimer of GBP1 and not monomeric GBP1. This suggests that this Nb subset binds an epitope located at the dimerisation interface of two GBP1 molecules. Depending on the Nb, the molecular weight of the GBP1 dimer (M_W = 129 kDa) shifted by 7 kDa for Nb196 (Figure 2.4c) up to 26 kDa for Nb195 (Figure 2.4b). With an estimated molecular weight of 12 kDa per Nb, the shift in molecular weight indicate that these Nbs bind with either 1:2 or 2:2 stochiometry. Steric hindrance resulting from two Nbs binding could be one reason of why we only observe one Nb binding to the LG domain dimer. The crystal structure of GBP1-LG has been shown to be C2 symmetric

[21], which we assumed to be true for the full-length GBP1 dimer as well. The binding of only one Nb to the GBP1 dimer could be an indication that the full-length GBP1-dimer is in fact not C2 symmetric or that the binding of one Nb causes a conformational change of the GBP1-dimer preventing the second Nb from binding.

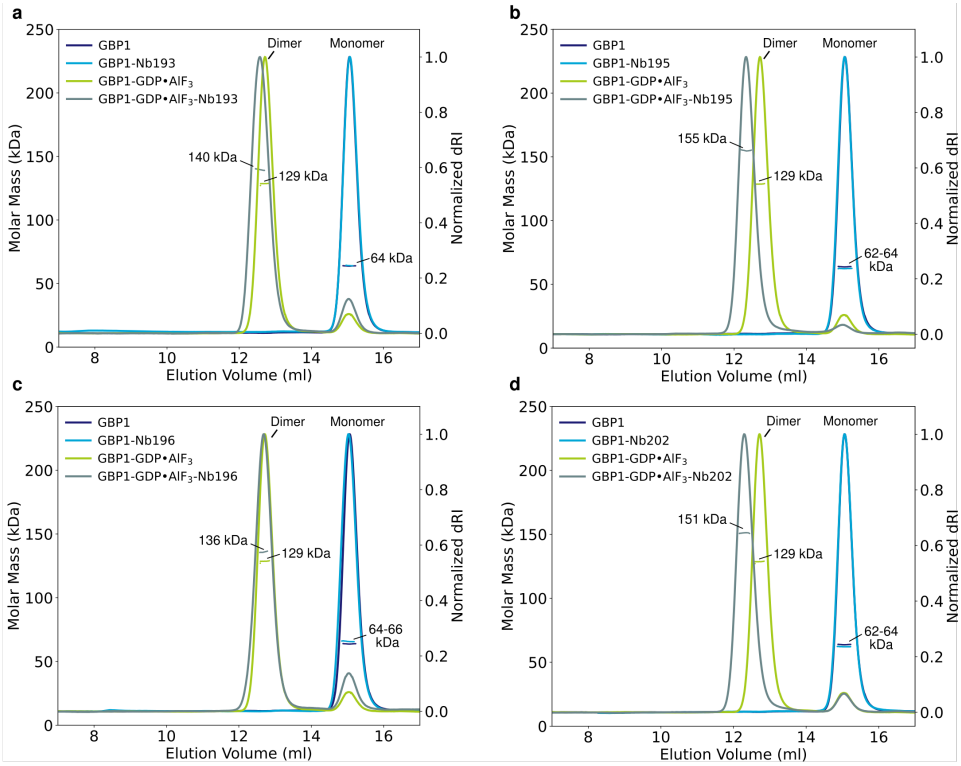

Figure 2.4: Nb193, Nb195, Nb196 and Nb202 bind to dimeric GBP1. (a-d) The addition of 2:1 molar excess of Nb193, Nb195, Nb196 and Nb202 shifts the molecular weight of GDP·AlF_3-stabilised dimeric GBP1 (M_W = 129 kDa) by 7 kDa (Nb196) up to 26 kDa (Nb195) indicating the binding of 1-2 Nbs per GBP1-dimer. None of the four Nbs binds monomeric GBP1 (M_W = 64 kDa).

Surprisingly, we also found two Nbs (Nb75 and Nb77) which entirely disrupt the pre-formed GDP·AlF_3-stabilised GBP1 dimer. Instead, our SEC-MALS data revealed a peak with M_W of 77 kDa, consistent with a 1:1 complex of monomeric GBP1 with Nb75 or Nb77 (Figure 2.5a,b). In accordance, when incubated with monomeric GBP1 we found equivalent peaks, confirming Nb75 and Nb77 bind the GBP1 monomer in a 1:1 complex. These results suggest that Nb75 and Nb77 recognise and compete for an epitope relevant for GBP1 dimerisation. Consistently, we find 1:1 GBP1/Nb complexes irrespective of whether we add the Nb to a pre-formed GBP1 dimer or whether we attempt to form GBP1 dimers after pre-incubation of monomeric GBP1 with Nb75 or 77 (Supplementary Figure 2.22b).

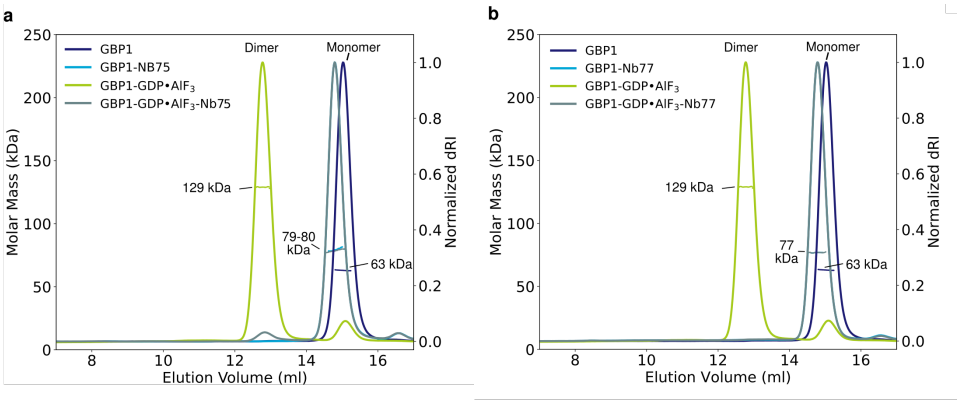

Figure 2.5: Nb75 and Nb77 compete with GDP·AlF$_3$-induced dimerisation of GBP1. (a-b) SEC-MALS profiles of monomeric GBP1 and Nb75 or Nb77 (1:2 molar excess) show a molecular weight shift of approximately 15 kDa relative to the molecular weight of monomeric GBP1 alone, consistent with formation of a 1:1 GBP1:Nb complex. Incubation of Nbs with preformed GDP·AlF$_3$-stabilised GBP1 dimer lead to dissociation of GBP1 dimers and formation of 1:1 GBP1:Nb complexes.

GBP1-specific Nbs have affinities in the picomolar to nanomolar range.

Most relevant applications of Nbs require high target affinity. When using Nbs for structure determination, high affinity binders facilitate complex purification and reduce unspecific background. In applications involving nanobody-based intrabodies, cellular expression levels of intrabodies are limited to avoid cell stress, requiring high affinity for target binding in the cell.

To determine the affinity and specificity of our Nbs for GBP1 we used surface plasmon resonance (SPR) (Figure 2.6a). To facilitate GBP immobilisation on the SPR chip, we expressed and purified GBP1 containing a C-terminal Avi-tag, a 15 amino acid peptide tag that allows biotinylation at a single lysine residue contained within its sequence using the bacterial biotin ligase BirA [50]. To confirm biotinylation of GBP1, we used a gel shift assay with the tetrameric bacterial biotin receptor streptavidin. The interaction of biotin and streptavidin is very strong ($K_D \sim 10^{-14}$ mol/L) and can withstand the denaturing condition of an SDS-PAGE [51]. The characteristic ladder pattern of high-molecular weight species on SDS-PAGE, resulting from the formation of streptavidin complexes with biotinylated substrates, confirmed successful biotinylation of GBP1 (Figure 2.6c).

After biotinylation, GDP·AlF$_3$ stabilised dimeric GBP1 was immobilised onto SPR chips coated with DNA oligonucleotide duplexes carrying streptavidin (Figure 2.6b). Nbs were injected into the sensor chip with increasing concentrations ranging from 1 nM to 256 nM and SPR sensorgrams were recorded (Figure 2.6d). From the sensorgrams, association rates (k_{on}), dissociation rates (k_{off}) and dissociation constants (k_D) were determined (summarised in Figure 2.6e). The k_Ds range from 63 pM for the strongest binder (Nb195) to 4.5 nM for the weakest binder (Nb193). With k_Ds in the picomolar to nanomolar range all Nbs can be considered strong binders. Consistent with SEC-MALS experiments, Nb75 and Nb77 were unable to bind to dimeric GBP1 (Supplementary Figure 2.23).

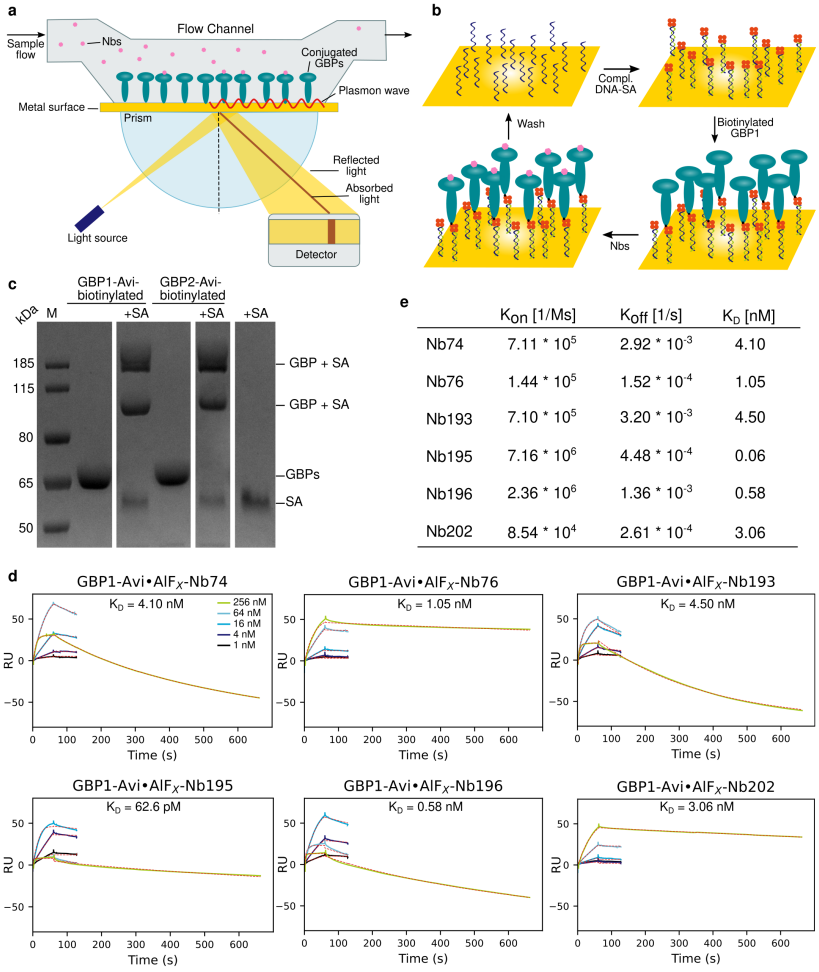

	K_{on} [1/Ms]	K_{off} [1/s]	K_D [nM]
Nb74	$7.11 * 10^5$	$2.92 * 10^{-3}$	4.10
Nb76	$1.44 * 10^5$	$1.52 * 10^{-4}$	1.05
Nb193	$7.10 * 10^5$	$3.20 * 10^{-3}$	4.50
Nb195	$7.16 * 10^6$	$4.48 * 10^{-4}$	0.06
Nb196	$2.36 * 10^6$	$1.36 * 10^{-3}$	0.58
Nb202	$8.54 * 10^4$	$2.61 * 10^{-4}$	3.06

Figure 2.6: Surface plasmon resonance (SPR) experiments to determine the affinity between GBP1 and different Nbs. (a) Schematic representation of an SPR experiment (b) and of the chip used for immobilising biotinylated GBP1 onto complementary DNA oligonucleotides coupled to streptavidin (SA). (c) SDS-PAGE analysis of GBP1 and GBP2 biotinylation. Bands containing GBP1 and GBP2 shift to higher order molecular weight species indicating complete biotinylation. (d) SPR sensorgrams showing the kinetics of Nb74, Nb76, Nb193, Nb195, Nb196 and Nb202 binding to the GDP·AlF_3-stabilised dimer of GBP1-Avi. Increasing concentrations of Nbs (ranging from 1 nM to 256 nM) were injected into the sensor chip containing the immobilised dimer of GBP1-Avi. (e) Summary of the association rates (k_{on}), dissociation rates (k_{off}) as well as dissociation constants (k_D).

Previously, SEC-MALS experiments showed that Nb75 and Nb77 are able to dissociate the GBP1 dimer (Figure 2.5) by forming stable 1:1 complexes with monomeric GBP1. The results of the SPR experiment indicate that the Nbs were unable to dissociate the GBP1 dimer immobilised on the SPR chip. One potential explanation lies in the fact that biotinylated GBP1 is immobilised on the SPR chip, preventing conformational states of GBP1 necessary for Nb75 and Nb77 to bind. Another explanation could result from the immobilisation process itself, which massively increases the local GBP1 concentration and hence the probability of self-interaction might outcompete Nb binding. In order to determine the k_D of Nb75 and Nb77 the SPR experiments will need to be repeated with immobilising monomeric GBP1 onto the chip.

A subset of selected Nbs binds to the large GTPase domain of GBP1

To narrow down the epitopes more precisely, we cloned and purified the large GTPase domain (LG) of GBP1 (amino acid residues 1-311) (Supplementary Figure 2.19c). Similar to full length GBP1, the LG domain of GBP1 has been shown to dimerise in a nucleotide dependant manner [21]. SEC-MALS experiments revealed that Nb193, Nb195, Nb196 and Nb202 all bind to the GDP·AlF_3 stabilised LG domain dimer, shifting its molecular weight (M_W = 69 kDa) by 16 kDa (for Nb196) up to 26 kDa (for Nb195) (Figure 2.7a-d).

These molecular weight shifts follow a similar trend as observed for full length GBP1 (Figure 2.4) indicating 2:2 or 1:2 stochiometries of Nb:LG complexes for different Nbs. In accordance with previous experiments, we do not observe binding of Nb193, Nb195, Nb196 and Nb202 to the LG domain monomer which under these condition elutes in a peak with a molecular weight of ~36 kDa corresponding to the LG domain monomer alone (Figure 2.7a-d).

To test if the Nbs that are able to bind the LG domain dimer compete for the same binding site, we first incubated the LG domain dimer with Nb195, followed by another incubation step with either Nb193 or Nb202 prior to the SEC-MALS experiment. We observed a shift in molecular weight by ~26 kDa when adding Nb195 consistent with a 2:2 complex (M_W = 96 kDa). The molecular weight does not increase further when we incubate the GDP·AlF_3-stabilised LG domain of GBP1 with a second Nb, indicating that Nb193 and Nb202 bind at a similar location as Nb195, sterically preventing the other Nb to bind (Figure 2.8a).

Conversely, when adding Nb195 and Nb74 simultaneously to the GBP1 dimer, we observed an upward shift in molecular weight by 44 kDa to an absolute molecular weight of the complex of 173 kDa, indicating the binding of three to four Nbs (Figure 2.8b). We therefore conclude that Nb195 and Nb74 bind non-competitively to different epitopes on the GBP1-dimer.

To determine whether Nb75 and Nb77 would also be able to dissociate the GBP1 LG domain dimer, we performed SEC-MALS experiments and realised that they do not bind the LG domain (Figure 2.9a,b). The LG domain dimer also remained intact after addition of Nb75 or Nb77 with a SEC-MALS peak and associated molecular weight of 70 kDa corresponding to an LG dimer with no Nb bound. Equivalently, Nb75 and Nb77 did not bind the LG monomer.

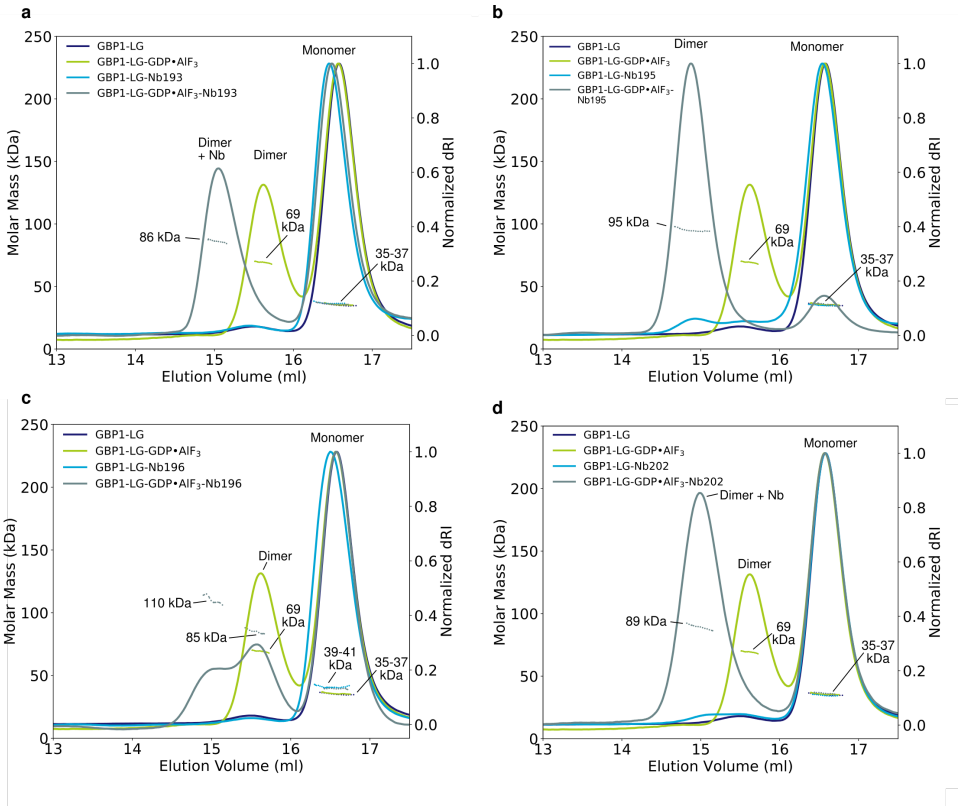

Figure 2.7: Nb193, Nb195, Nb196 and Nb202 bind to the GDP·AlF$_3$-stabilised LG domain of GBP1. (a-d) SEC-MALS experiments revealed that Nb193, Nb195, Nb196 and Nb202 bind to the GDP·AlF$_3$-stabilised LG domain of GBP1 shifting the molecular weight by 16 kDa (Nb196) up to 26 kDa (Nb195). The Nbs did not bind to the monomeric LG domain of GBP1.

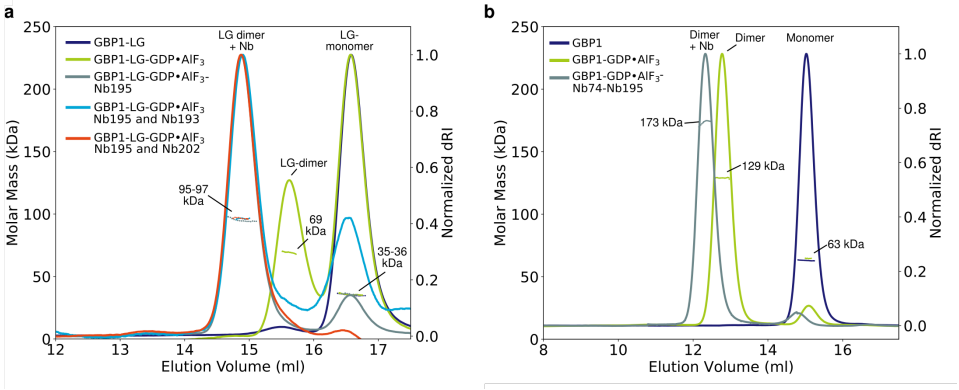

Figure 2.8: Adding multiple Nbs to GBP1 or GBP1-LG. (a) Nb 193, Nb195 and Nb202 are unable to bind simultaneously to the GDP·AlF_3-stabilised LG domain of GBP1 resulting in a molecular weight of ~96 kDa corresponding to an LG domain dimer with two Nbs bound. (b) SEC-MALS experiments show that multiple Nbs (Nb74 and Nb195) can bind to GBP1 simultaneously. The molecular weight shifts by 44 kDa compared to the GDP·AlF_3-stabilised dimeric GBP1, corresponding to three to four bound Nbs.

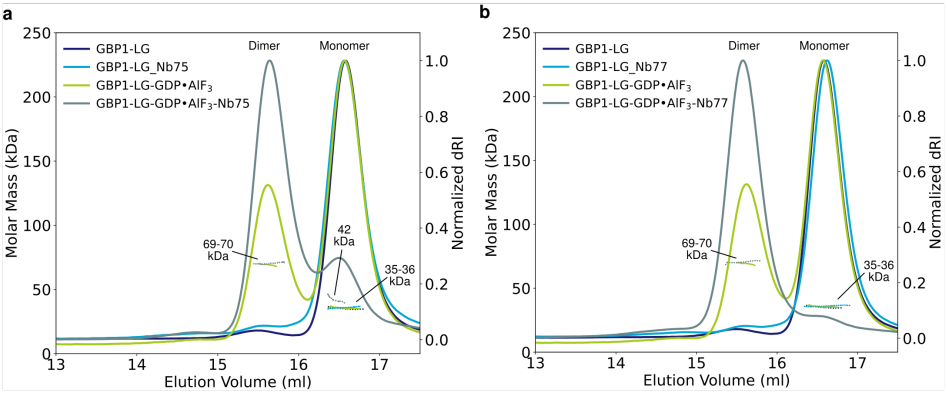

Figure 2.9: Nb75 and Nb77 do not interact with the LG domain of GBP1. SEC-MALS profiles of Nb75 and Nb77 with GBP1 LG domain showing no complex formation with either monomeric (36 kDa) or dimeric (70 kDa) LG domain of GBP1.

Nbs of the same family cluster demonstrate different binding behaviours.

In view of the broadly different binding characteristics observed in our experiments, we wanted to probe whether Nbs from the same family (i.e. with high sequence identity) share consistent interaction properties. We therefore investigated Nb76 and Nb202 which were both raised against dimeric GBP1 and only differ in two amino acid positions (out of 133 amino acid positions in total) (Figure 2.10a, indicated with a star).

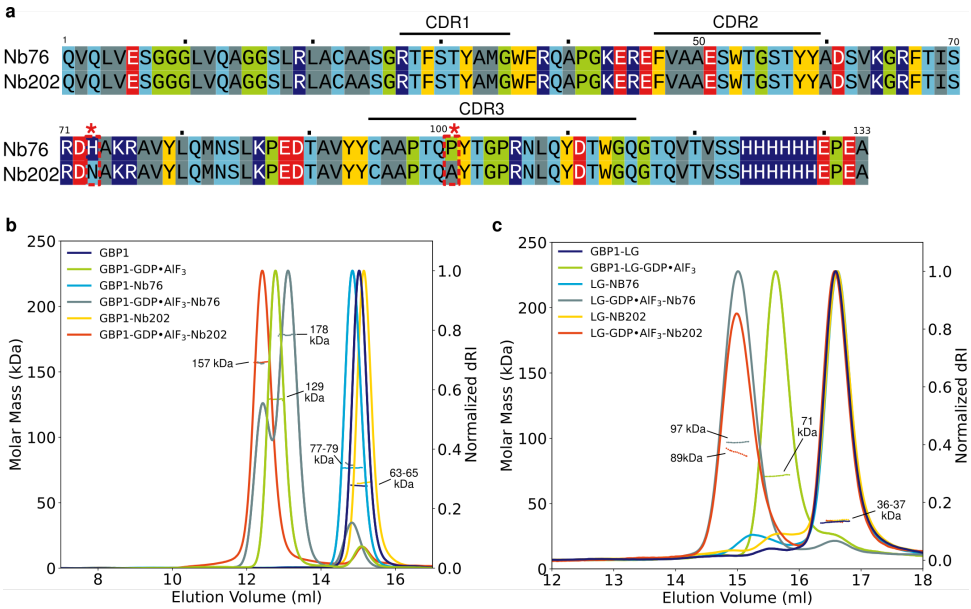

Figure 2.10: Nb76 and Nb202 share high sequence identity, but display different binding characteristics towards GBP1. (a) Pairwise sequence alignment of Nb76 and Nb202. Primary sequences were used as input for Clustal Omega [49]. Residues are coloured by physicochemical property of the side chain (grey: hydrophobic, light blue: polar, red: negatively charged, dark blue: positively charged, yellow: aromatic, green: special cases). The two differing residue positions (73 and 101) are highlighted with a red asterisk. (b) SEC-MALS profiles show that while Nb76 binds both monomeric GBP1 and GDP·AlF_3-stabilised dimeric GBP1, Nb202 exclusively binds the GBP1-dimer. Of note, binding of Nb76 to the GBP1 dimer results in an additional peak of 178 kDa which is absent for Nb202. (c) Nb76 and Nb202 both only bind to the GDP·AlF_3-stabilised dimeric LG domain and not to the monomeric LG domain.

SEC-MALS analysis revealed different binding behaviours for Nb76 and Nb202 with GBP1. While Nb76 formed a complex with monomeric GBP1 resulting in an upward M_W shift from 63 kDa to 77 kDa, Nb202 does not bind monomeric GBP1 (Figure 2.7d and Figure 2.10b). Both Nb202 and Nb76 on the other hand bind to GDP·AlF_3-stabilised dimeric GBP1. Unlike for Nb76, the binding of Nb202 did not result in an additional peak around 178 kDa. To further understand where the Nbs bind on GBP1, we studied the interaction of Nb76 and Nb202 with the monomeric and GDP·AlF_3-stabilised dimeric LG domain of GBP1. Both Nbs were able to bind to the dimeric LG domain of GBP1, but unable to bind to the monomeric LG domain (Figure 2.10c). This suggests that Nb76 needs additional binding sites outside of the LG domain enabling it to bind to monomeric full-length

GBP1. Together, these observations suggest that despite the high sequence identity of both Nbs, they recognise different epitopes.

A subset of selected Nbs are able to differentiate between GBP1 and GBP2.

The human genome encodes seven GBPs (GBP1-GBP7) which are highly similar in primary sequence. Among the human GBPs, GBP1 and GBP2 are most closely related. Both proteins reveal a high sequence similarity and when comparing the crystal structures of monomeric GBP1 and monomeric GBP2, the structures reveal an almost identical fold with a backbone root mean square deviation (r.m.s.d) of 3.1 Å over 572 residues (Figure 2.11 a,b). Since we were aiming for Nbs specific for GBP1, we tested cross-reactivity with GBP2.

To test this we repeated the SEC-MALS based interaction assays with monomeric and GDP·AlF_3-stabilised dimeric GBP2. In the presence of Nb74 or Nb76, GBP2 still eluted in a peak corresponding to a molecular weight of the monomeric GBP2 (65 kDa, Figure 2.11c,d, dark-blue and cyan) or dimeric GBP2 (126 kDa, Figure 2.11c, d, light-green and grey). These experiments demonstrate that Nb74 and Nb76 did not bind to GBP2 and hence are specific for GBP1 (Figure 2.11c,d and Table 2.2). Having identified Nbs that are specific for GBP1 provides us with a tool to differentiate between GBP1 from other closely related GBPs. Likewise, SEC-MALS experiments with Nb193, Nb195, Nb196 and Nb202 and GBP2 showed no binding of Nbs to GBP2, indicating that these Nbs are also specific for GBP1 (Supplementary Figure 2.24 and Table 2.2).

Although some Nbs seem to be highly specific for GBP1 we also identified two Nbs (Nb75 and Nb77) that are able to bind both monomeric GBP1 and GBP2 (compare Figure 2.12a,b and Figure 2.5a,b). As for GBP1, Nb75 and Nb77 are able to disrupt the previously formed GDP·AlF_3-stabilised dimer of GBP2 resulting in a 1:1 Nb:GBP2 complex. The ability to disrupt the GBP2 dimer was slightly reduced for Nb77 resulting in a residual dimer peak with associated molecular weight of ~129 kDa (Figure 2.12b, grey).

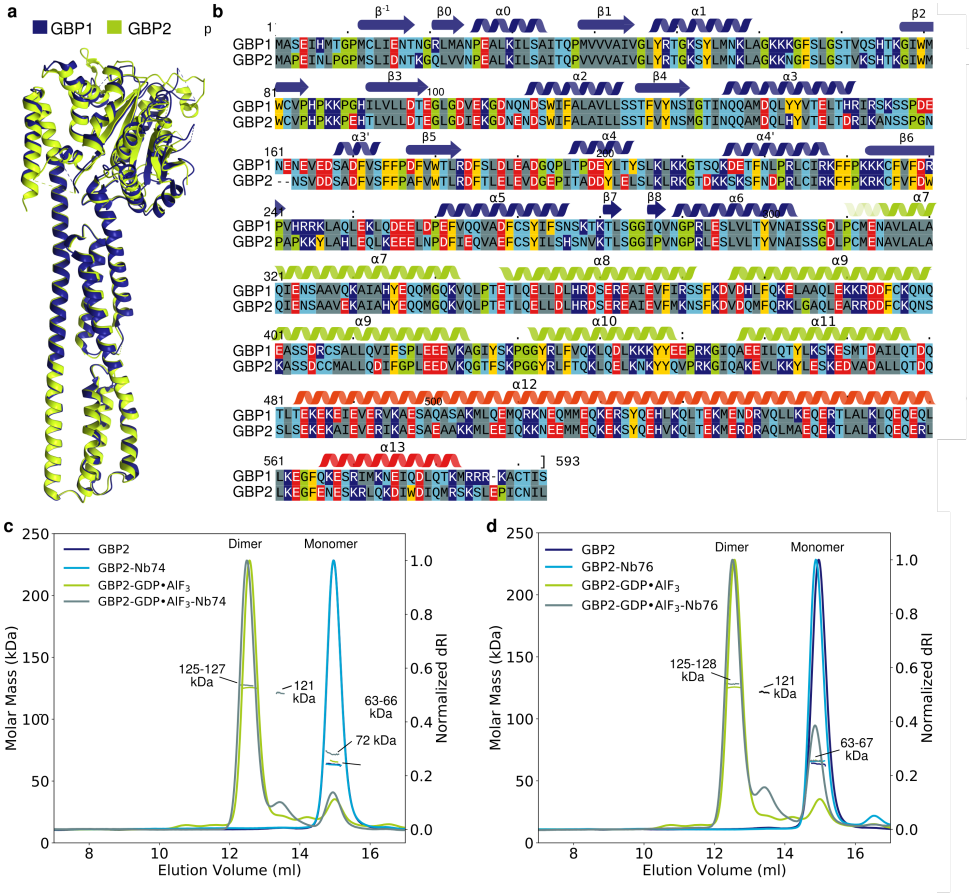

Figure 2.11: Nb74 and Nb76 are specific for GBP1. (a) Structural comparison of monomeric GBP1 and GBP2. The crystal structures of GBP1 (PDB ID: 1dg3 [18]) and GBP2 (PDB ID: 7e58 [52]) in their monomeric form are overlayed to display the high degree of structural similarity. (b) Pairwise sequence alignment of human GBP1 (UniProt: P32455) and human GBP2 (UniProt: P32456). Primary sequences were used as input for Clustal Omega [49]. Secondary structure elements for GBP1 [18] are displayed for guidance. The colour of the alpha-helices and beta-sheets correspond to the domain architecture of GBP1 shown in Figure 2.1 and used throughout the text (blue: Large GTPase domain, green: Middle domain (MD), orange/red: GTPase effector domain). Residues are coloured by physicochemical property of the side chain (grey: hydrophobic, light blue: polar, red: negatively charged, dark blue: positively charged, yellow: aromatic, green: special cases). (c-d) SEC-MALS experiments show that Nb74 and Nb76 do not bind to monomeric or GDP·AlF_3-stabilised dimeric GBP2 contrary to equivalent experiments with monomeric and dimeric GBP1 (as displayed in Figure 2.3).

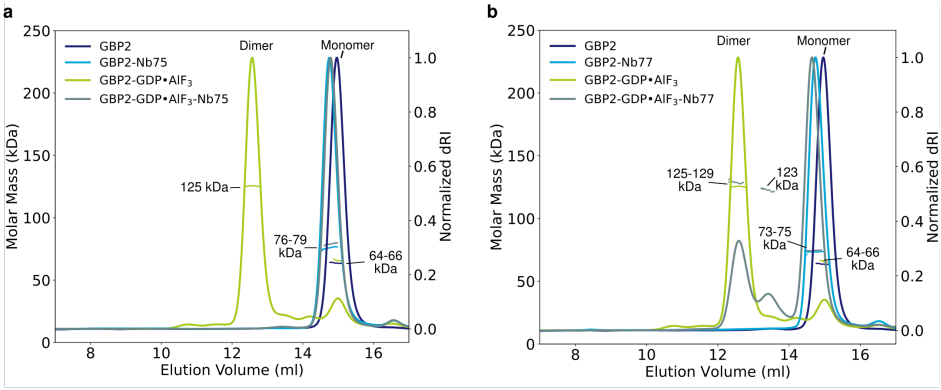

Figure 2.12: Nb75 and Nb77 dissociate the GDP·AlF$_3$-stabilised dimer of GBP2. (a-b) SEC-MALS profiles showing that Nb75 or Nb77 (in 2:1 molar excess) dissociate the pre-formed GDP·AlF$_3$-stabilised dimer of GBP2, equivalent to observations with GBP1 (see Figure 2.5). The profiles are consistent with 1:1 Nb:GBP2 complexes with an upward molecular weight shift of ~13 kDa relative to monomeric GBP2.

Table 2.2: Summary of SEC-MALS data obtained with different Nbs and monomeric or GDP·AlF$_3$-stabilised dimeric GBP1, GBP1 LG domain or GBP2. *: Indicates the presence of another peak of unknown stochiometry with a molecular weight of 180 kDa (Supplementary Figure 2.22a).

Nano-body	Raised against	Fam-ily	GBP1 mon.	GBP1 dimer	LG mon.	LG dimer	GBP2 mon.	GBP2 dimer
Nb74	farnes. GBP1	1	Yes	Yes	No	No	No	No
Nb75	mon. GBP1	29	Yes	Breaks dimer	No	No	Yes	Breaks dimer
Nb76	dim. GBP1	12	Yes	Yes *	No	Yes	No	No
Nb77	dim. GBP1	11	Yes	Breaks dimer	No	No	Yes	Breaks dimer
Nb193	dim. GBP1	18	No	Yes	No	Yes	No	No
Nb195	dim. GBP1	14	No	Yes	No	Yes	No	No
Nb196	dim. GBP1	25	No	Yes	No	Yes	No	No
Nb202	dim. GBP1	12	No	Yes	No	Yes	No	No

2.2.1. SPR experiments confirm the specificity of Nbs towards GBP1

In order to confirm that six out of the eight Nbs were indeed specific for GBP1 and do not bind GBP2, we performed SPR experiments. As for GBP1, we immobilised dimeric biotinylated GBP2 onto an SPR chip (Figure 2.6b, c). Different to the experiments for dimeric GBP1 for which no interaction with Nb75 and 77 could be established, we did observe binding of GBP2 to Nb75 or Nb77 (k_D of 37.4 nM and 88.2 nM) (Figure 2.13, upper row), potentially resulting from incomplete dimer formation of GBP2 on the sensor chip. Consistent with this interpretation, SEC-MALS profiles with biotinylated GBP1-Avi and GBP2-Avi in their GDP·AlF_3 stabilised dimeric states confirmed a larger monomer fraction in the GBP2-Avi sample compared to GBP1-Avi (Supplementary Figure 2.25). All the other Nbs were unable to bind to GBP2 consistent with our SEC-MALS experiments and the above stated k_D for GBP2 binding to Nb75 or Nb77 need to be considered carefully, as the fits were not reliable (Figure 2.13).

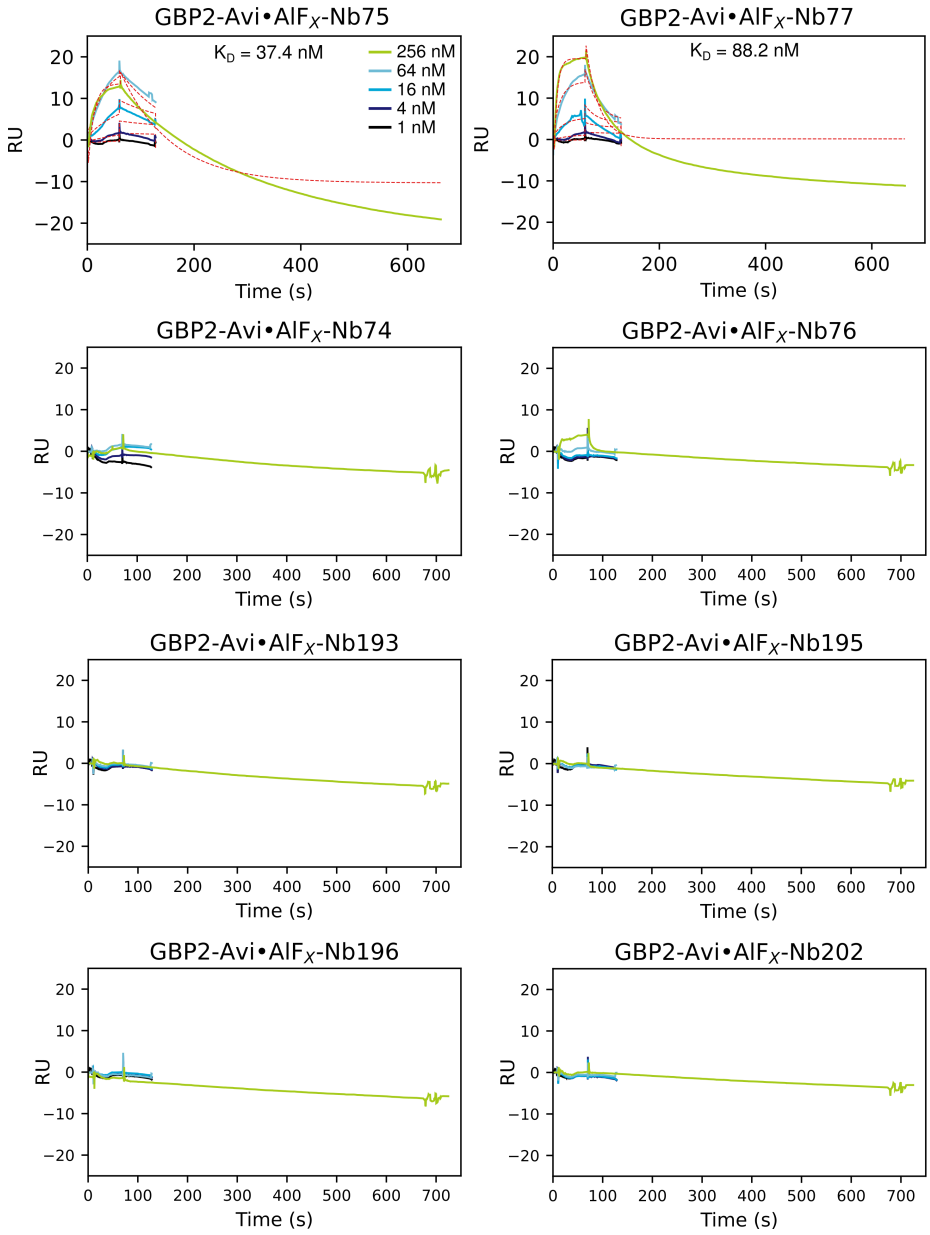

Figure 2.13: Surface plasmon resonance (SPR) experiments to determine the affinity between dimeric GBP2 and different Nbs. SPR sensorgrams showing the binding kinetics of GBP2 with different Nbs. Increasing concentrations of Nbs (ranging from 1 nM to 256 nM) were injected into the sensor chip containing immobilised GBP2. Nb75 and Nb77 bind to GBP2 (upper panel) enabling the determination of dissociation constants (k_D of 37.4 nM for Nb75 and 88.2 nM for Nb77, uppermost panel). Other tested Nbs did not bind to GBP2 (lower three panels).

2.2.2. Nb75 interferes with coat formation of farnesylated GBP1

Farnesylated and nucleotide-activated GBP1 has previously been shown to be able to bind to giant unilamellar vesicles (GUVs) using fluorescence microscopy [53]. To understand whether disrupting the GBP1 dimer has an effect on coat formation of purified farnesylated GBP1 ($GBP1_F$) (Supplementary Figure 2.19d, e), we used fluorescently labelled $GBP1_F$ ($GBP1_F$-Q577C-AF647) and Texas Red DHPE labelled brain polar lipid extract (BPLE)-derived GUVs.

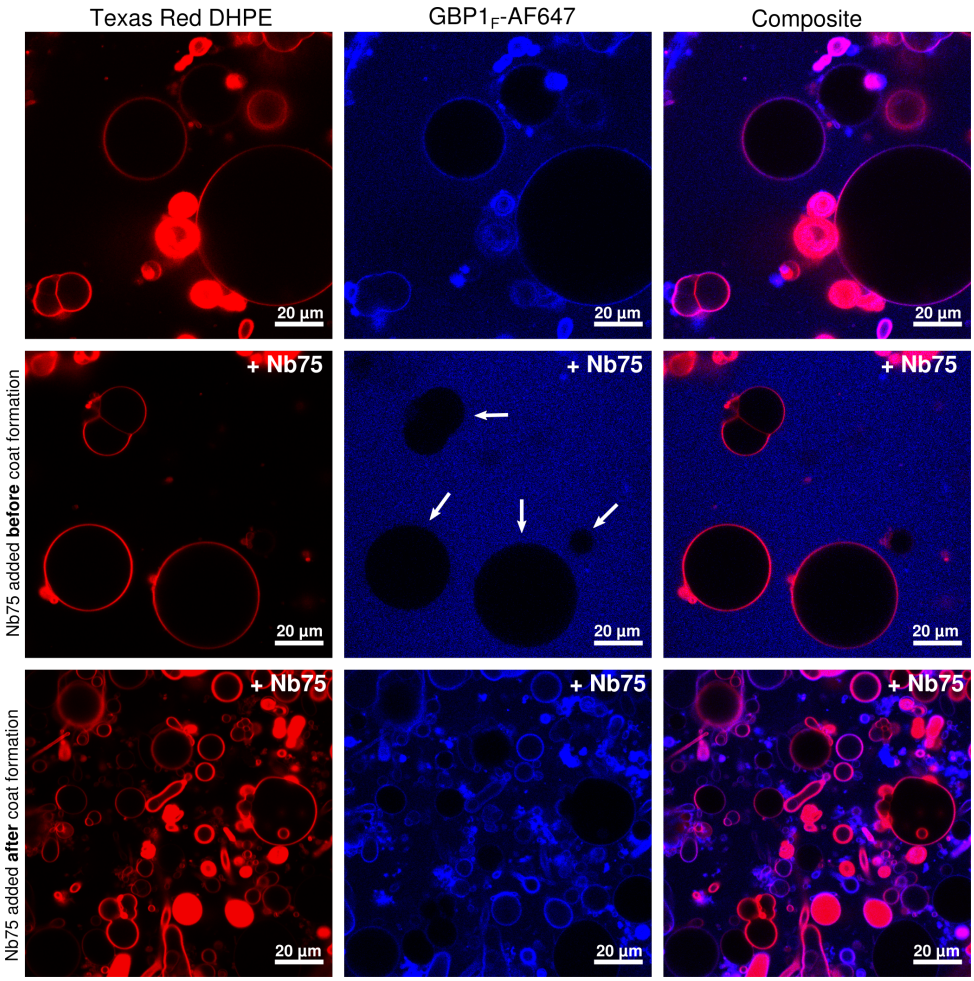

Figure 2.14: Confocal fluorescence imaging of $GBP1_F$ on GUVs with Nb75. $GBP1_F$-Q577C-AF647 shows weak binding to Texas Red DHPE labelled GUVs when adding GDP·AlF_3 (top panel). When Nb75 was bound to $GBP1_F$-Q577C-AF647 before addition to the GUVs, coat formation of GBP1 is completely lost (middle panel, white arrows). The addition of Nb75 after coat formation, had no effect on $GBP1_F$-Q577C-AF647 binding to GUVs (lower panel).

When $GBP1_F$ is activated by GDP·AlF_3 it uniformly stains the GUVs (Figure 2.14 up-

per row). Incubation of GBP1$_F$ with Nb75 for 1h at RT prior to nucleotide activation completely abolishes GBP1$_F$ coat formation on GUVs, indicating that Nb75 interferes with coat formation (Figure 2.14 middle row). Together with our observation that Nb75 prevents GBP1-dimer formation, this suggests that GBP1 dimerisation is a prerequisite for GBP1 coat formation.

To test if Nb75 is also able to disrupt a pre-formed GBP1$_F$ coat on GUVs, we incubated the GBP1$_F$-coated GUVs for 50 min with Nb75 while imaging in regular intervals. Different to the SEC-MALS experiments where Nb75 was able to dissociate pre-formed GBP1-dimers, Nb75 was not able to break the GBP1$_F$ coat (Figure 2.14 bottom row). Possibly, the Nb75 epitope is no longer accessible in the pre-formed GBP1 coat. Alternatively, coat formation could be energetically favorable and inter-coat interactions may out-compete Nb75 binding.

2.2.3. Cryo-EM single-particle analysis of GDP·AlF$_3$ stabilised GBP1 dimer only resolves the LG domains

One primary goal of this thesis is to obtain the 3D structure of the full-length GBP1 dimer, which has so far remained elusive. To this end, we employed cryo-EM single particle analysis of highly purified nucleotide-bound GBP1. Cryo-EM analysis of the GDP·AlF$_3$ stabilised GBP1 dimer resulted in 2D classes with strong preferred orientation (Figure 2.15a,b). Most classes showed one particular orientation (Figure 2.15b, top two panels) consistent with the projection of the dimerised LG domains and resulting in a low resolution 3D reconstruction with strong directional resolution anisotropy. Fitting of a previously solved atomic structure of the GBP1 LG domain dimer (PDB-ID: 2b92, [21]) into the obtained cryo-EM map revealed that the middle domain and the C-terminal GTPase effector domain were absent in our 3D reconstruction (Figure 2.15c,d).

The inability to resolve those domains is most likely due to a high degree of flexibility resulting from a linker region in close proximity to the LG domain between the α6 helix and the α7 helix (Figure 2.11b). Nbs have the potential to decrease protein flexibility by stabilising specific target conformations [38, 39, 41]. Exploiting those characteristics, we incubated different Nbs with a GDP·AlF$_3$ stabilised GBP1 dimer prior to vitrification. Since our aim was to stabilise the MD and GED in a conformation suitable for structure determination by cryo-EM, we excluded Nbs that we previously found to bind the LG domain. We converged on Nb74 for our subsequent cryo-EM experiments. Single-particle analysis of cryo-EM micrographs obtained with the GBP1 dimer in complex with Nb74 resulted in 2D class averages displaying a more diverse set of particle orientations that showed promise for cryo-EM structure determination (Figure 2.15e). These results will be further discussed in chapter 3.

2.2.4. Nb195 and Nb196 bind to the GDP·AlF$_3$ stabilised dimeric LG domain of GBP1.

Our SEC-MALS analysis already indicated that Nb195 and Nb196 putatively bind at the interface between two LG domains in the GBP1 dimer. To test this hypothesis, we used cryo-EM single-particle analysis to structurally map the epitopes of Nb195 and Nb196

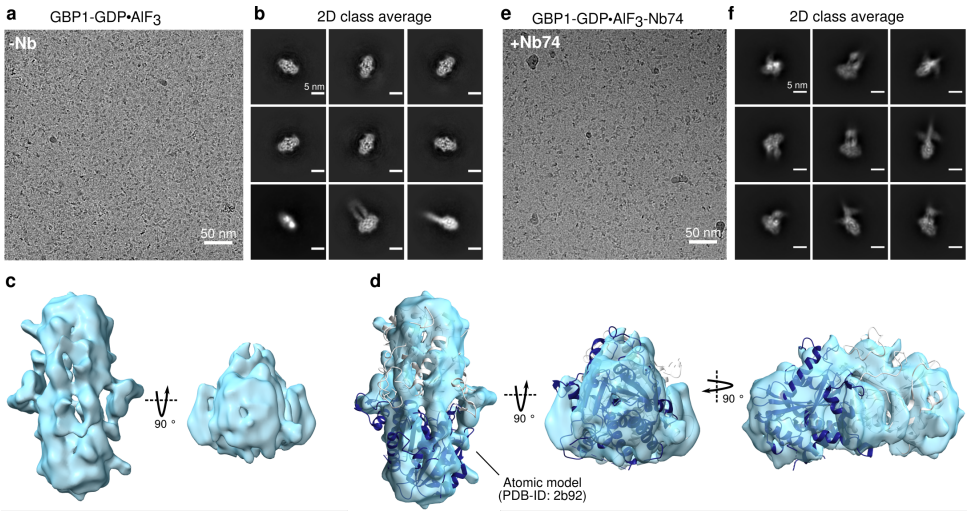

Figure 2.15: Cryo-EM structure of GBP1-GDP·AlF$_3$ only resolves LG domains. (a) Representative cryo-EM micrograph (b) 2D class averages and (c) 3D cryo-EM density map of the GDP·AlF$_3$-stabilised GBP1-dimer. (d) The atomic model of the GDP·AlF$_3$ stabilised GBP1 LG domain (PDB-ID: 2b92, [21]) fitted into the 3D cryo-EM density map. (e) Cryo-EM micrograph of GBP1-GDP·AlF$_3$-Nb74 (f) and the associated 2D class averages.

on the GDP·AlF$_3$ stabilised GBP1-dimer (Figure 2.16a and Figure 2.17).

For Nb195, the 2D class averages and density map from a low-resolution 3D reconstruction show two Nbs binding at the interface of the LG domain dimer (Figure 2.16b,c). The 2D class averages indicate preferred particle orientation and the middle domain (MD) and GTPase effector domain (GED) of GBP1 are not visible in the 3D reconstruction similar to the results from single-particle analysis of the GBP1-dimer alone (compare to Figure 2.15d). The atomic model of the GDP·AlF$_3$ stabilised GBP1-LG domain (PDB-ID: 2b92, [21]) fits well into the EM density map, highlighting that Nb195 indeed binds at the interface between the two LG domain monomers colored in grey and dark blue (Figure 2.16d). Consistent with the 2D classes, a comparison of the cryo-EM density map of GBP1:Nb195 to that obtained with the GDP·AlF$_3$-stabilised GBP1 dimer alone reveals the absence of interpretable density for the MD and GED (Figure 2.16e and Figure 2.15c,d).

2D class averages of the GBP1-dimer incubated with Nb196 also showed strong preferred particle orientation (Figure 2.17b). Different to Nb195, we only observe one single Nb binding in this case which is in accordance to SEC-MALS experiments displaying a molecular weight shift of 7 kDa upon addition of Nb196 compared to 26 kDa for Nb195 (Figure 2.4b,c). This difference could be due to a lower affinity of Nb196 (0.58 nM for Nb196 compared to 0.06 nM for Nb195 (Figure 2.6e)). Alternatively, Nb196 might bind to elements of the GBP1-dimer that are not following the C2 symmetry of the LG-domain dimer, potentially explaining why Nb196 only bind with 1:2 stochiometry. Again, the MD and GED were absent in our 3D reconstruction. (Figure 2.17c,d). When comparing both structures, the most prominent difference is that we can only visualise Nb196 bound to one side of the GBP1-dimer and instead of a Nb binding orientation perpendicular to the short axis of the LG domain dimer, it appears tilted by a ~ 45° angle (Figure 2.17e)

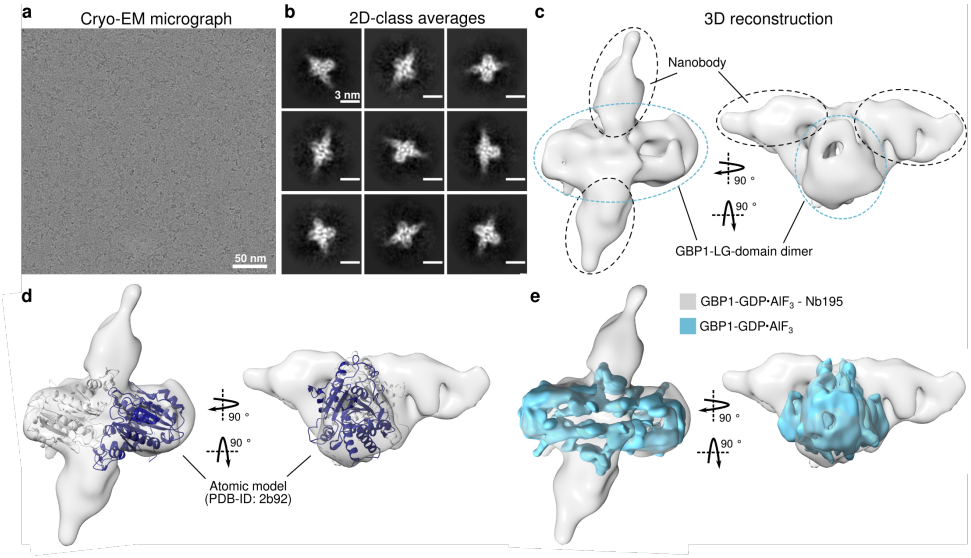

Figure 2.16: Cryo-EM structure of GBP1-GDP·AlF$_3$ with Nb195. (a) Representative cryo-EM micrograph (b) 2D class averages and (c) 3D cryo-EM density map of the GDP·AlF$_3$-stabilised GBP1-dimer bound to Nb195. (d) The atomic model of the GDP·AlF$_3$ stabilised GBP1 LG domain (PDB-ID: 2b92, [21]) fitted into the 3D cryo-EM density map. (e) Comparison of the 3D cryo-EM density map of GDP·AlF$_3$-stabilised GBP1-dimer obtained in the presence or absence of Nb195.

relative to the LG dimer.

To rationalise why Nb195 and Nb196 exclusively bind GBP1 and not GBP2, we examined the interface between the Nbs and the GDP·AlF$_3$-stabilised LG domain of GBP1 based on our 3D reconstructions. We performed a sequence alignment between GBP1 and GBP2 and plotted the sequence identity onto the LG domain dimer (Figure 2.18a-c). While the limited resolution of our reconstructions do not allow a conclusive description of the interaction interfaces, from crude patch mapping of the segment intersections of the LG and Nb densities, we identified a number of residues potentially interacting with Nb195 (Figure 2.18b). Nb195 binds at the interface of two LG domains with amino acids from both molecules contributing to the interface (Figure 2.18b, orange or black). This explains why Nb195 only binds to dimeric GBP1 but not to the monomer. To further rationalise the specificity that Nb195 displays for GBP1 over GBP2, we also examined residues at the interface that differ between both sequences (corresponding residues for GBP2 are in parentheses) and identified Q72 (K72), D188 (E186), Q194 (E192), R244 (K242), R245 (K243), K246 (Y244), Q249 (H247) and K252 (Q250) as putative candidates.

The residues at the interface between GBP1 and Nb196 are all located on one of LG monomers (Figure 2.18c). As for Nb195 we identified a number of residues differing between GBP1 and GBP2 (in parentheses), namely D188 (E186), Q194 (E192), E200 (D198), E261 (D259), Q264 (E262), D268 (E266) that were positioned at the interface putatively contributing to the specificity of Nb196 towards GBP1. To rationalise why Nb196 does not bind the monomeric LG domain, we compared the structures of the dimeric LG do-

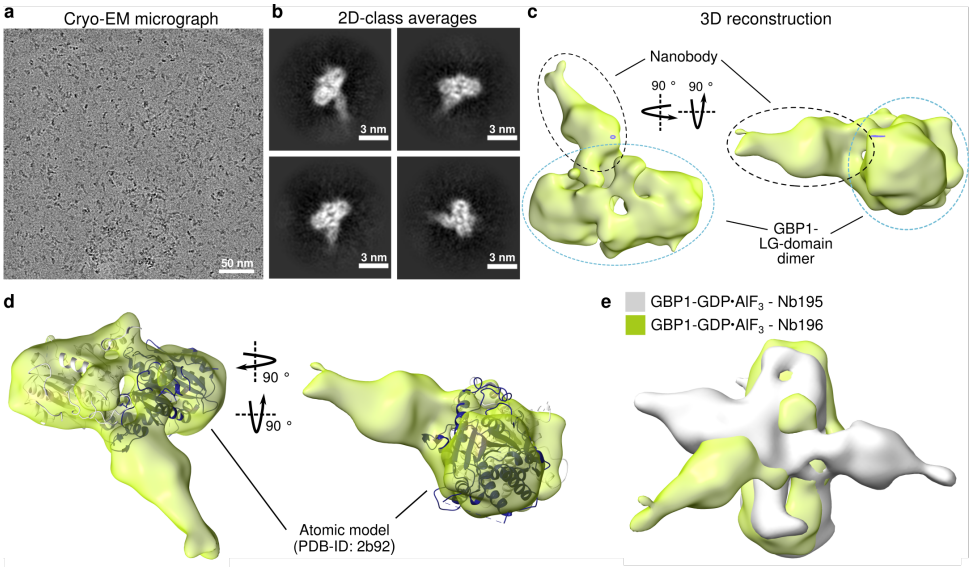

Figure 2.17: Cryo-EM structure of GBP1-GDP·AlF$_3$ with Nb196. (a) Representative cryo-EM micrograph (b) 2D class averages and (c) 3D cryo-EM density map of the GDP·AlF$_3$-stabilised GBP1-dimer bound to Nb196. (d) The atomic model of the GDP·AlF$_3$ stabilised GBP1 LG domain (PDB-ID: 2b92, [21]) fitted into the 3D cryo-EM density map. (e) Comparison of the 3D cryo-EM density map of GDP·AlF$_3$-stabilised GBP1-dimer obtained in the presence of Nb195 or Nb196.

main (PDB:2b92) with the LG domain of monomeric GBP1 (PDB:1dg3) (Figure 2.18d). Although the crystal structure of the GBP1 monomer lacks tracing of residues 189-194, we could still observe structural differences in areas close to the interface with Nb196, which may affect binding of Nb196 to monomeric GBP1. Interestingly, when comparing all publicly available structures of human GBP LG domains, we realised that the GDP·AlF$_3$ stabilised dimeric structures all had this loop region resolved (Figure 2.18e, left panel). Additionally, the loop was also resolved in the GBP2 monomer although slightly shifted in position compared to the dimeric structures of GBP1-LG and GBP5. Contrary, the loop was not resolved in the crystal structures of monomeric GBP1 (PDB ID: 1dg3), GBP1$_F$ (PDB ID: 6k1z) and GBP5 (PDB ID: 7e59) indicating structural flexibility in this region (Figure 2.18e, right panel).

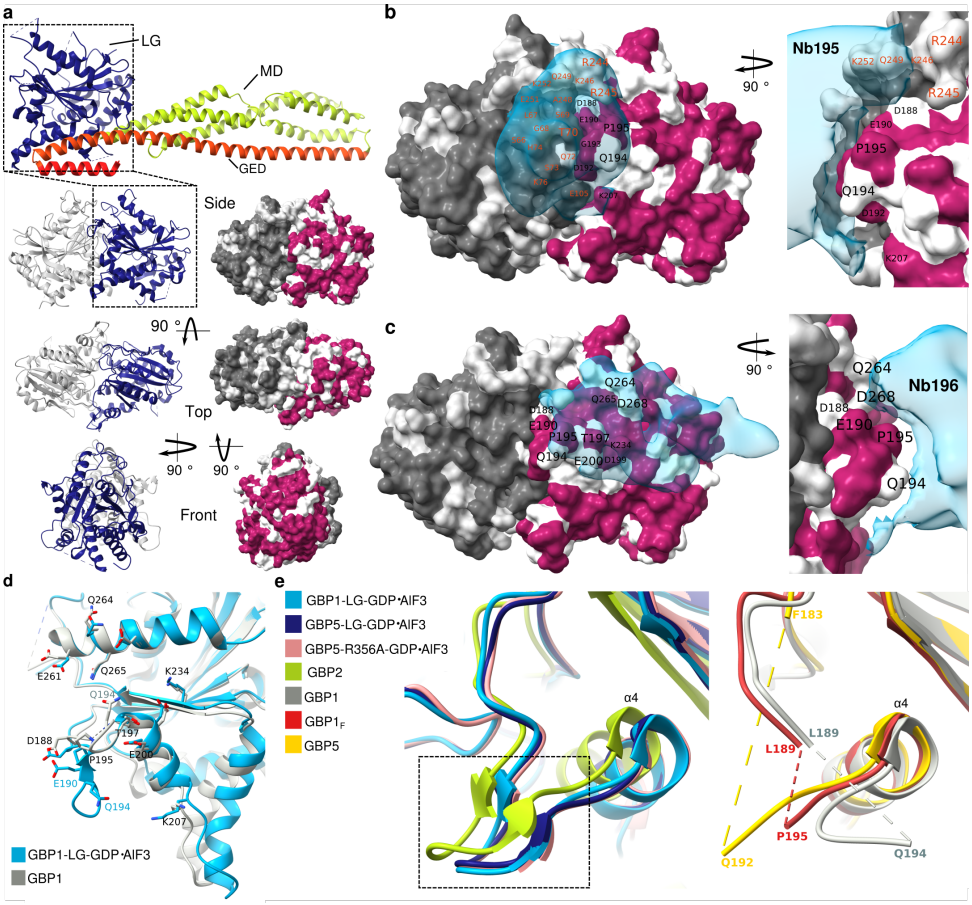

Figure 2.18: Close-up of the putative interface of Nb195/Nb196 and GBP1 (a) Atomic model of monomeric GBP1 (PDB ID: 1dg3) in cartoon representation (LG: Large GTPase domain (blue), MD: Middle domain (green), GED: GTPase effector domain (orange and red)) as well as side-by-side display of atomic model and surface representation of the GDP·AlF_3 stabilised dimeric GBP1 LG domain (PDB ID: 2b92). The color coding of the surface representation corresponds to the sequence identity between GBP1 and GBP2. Magenta or dark grey refers to an identical sequence between GBP1 and GBP2 whereas white or light grey represents a difference in primary sequence between GBP1 and GBP2. (b) Potential amino acid residues of GBP1 involved in binding Nb195 are highlighted. Nb195 binds at the interface between two GBP1-LG domains. Residues belonging to the same LG domain are either labelled in orange or black. (c) Residues of GBP1 likely to be involved in binding Nb196 are highlighted. (d) Structural comparison between the GDP·AlF_3 stabilised dimeric LG domain of GBP1 (PDB ID: 2b92) in cyan superposed with the LG domain of monomeric GBP1 (PDB-ID: 1dg3) in grey. Residues located at the interface between GBP1 and Nb196 are represented as sticks. (e) Comparison of available structures of GBPs in the loop region between amino acid position 189 and 197. The loop region is resolved for the GBP1-LG-dimer (PDB ID: 2b92, in cyan), GBP5-LG-dimer (PDB ID: 7ckf, in dark blue), GBP5-R356A-dimer (1-487) (PDB ID: 7e5a, pink) and the GBP2 monomer (PDB ID: 7e58, in light green). The same sequence is not resolved in the structures available for the monomer of GBP1 (PDB ID: 1dg3, in grey), farnesylated GBP1 (PDB ID: 6k1z, in red) and GBP5 (PDB ID: 7e59, in yellow) indicating structural flexibility in the loop region.

2.3. Discussion

GBP1 is a key player in cell-autonomous immunity. It has been shown to form a coat functioning as a signalling platform on gram-negative cytosolic bacteria as well as on pathogen-containing vacuoles and promotes caspase-4 induced cell death [14, 15]. The conformational changes that GBP1 has to undergo in order to dimerise and oligomerise to form a membrane-associated coat remain unsolved. In our study we generated and characterised eight different Nbs that are able to interact with GBP1 to establish a molecular toolbox to further structurally and functionally characterise GBP1 by structural techniques such as cryo-EM/cryo-ET, but also by utilising those Nbs as intrabodies for cellular studies.

We identified two Nbs (Nb74 and Nb76) that are able to specifically bind to the GBP1 monomer and GBP1 dimer. Importantly, these Nbs show high specificity for GBP1 over its closest homolog GBP2 despite their high degree of sequence identity. Both Nbs could be very useful for structural investigation of GBP hetero-dimers that have been postulated previously [20, 54].

SEC-MALS analysis showed that Nb75 and Nb77 are able to dissociate GBP1 and GBP2 dimers. It will be interesting to investigate if those Nbs are also able to dissociate other GBP dimers and to map their epitopes. The Nb binding site is not exclusively located at the LG dimer interface as determined by SEC-MALS experiments. When using the LG domain of GBP1, Nb75 and Nb77 were unable to interact and to dissociate the dimer. This is surprising as the LG domain dimer forms a large contact surface [21]. The observation that Nb75 was able to inhibit coat formation, but unable to disrupt a preformed GBP1 coat, could result from a densely packed GBP1-coat hindering Nb75 binding. This could also explain why Nb75 and Nb77 are unable to bind to immobilised GBP1 on an SPR chip. Either there was sterical hindrance for the Nbs to bind, or by having the dimers immobilised on its C-terminus they could not undergo a conformational change necessary for the dimers to break apart facilitating Nb binding. Lastly, it could also be that the Nb concentration range that we used in the SPR experiment (1 nM to 256 nM) was too low to break the GBP1 dimer apart. For GBP2, it could be a possibility that the GBP2 dimer formation was not complete explaining why we do observe binding of Nb75 and Nb77 to GBP2. In order to correctly determine the k_D of Nb75 and Nb77 to GBP1 or GBP2, it is necessary to perform an SPR experiment having monomeric GBP1 or GBP2 immobilised onto the chip.

Structural analysis of the GDP·AlF_3 stabilised dimer of GBP1 could not resolve the middle domain and the C-terminal GTPase effector domain (GED) of GBP1 indicating a high degree of flexibility of those regions. Additionally, the particle distribution of the GBP1-dimer showed strong preferred orientation. Together with a relatively low molecular weight (~ 130 kDa) for cryo-EM, resolving the cryo-EM structure of the GBP1-dimer appeared challenging. In a first attempt, we ended up with a 3D reconstruction only containing interpretable density for the LG domain dimer. The addition of Nb74 to the GBP1-dimer resulted in a better particle distribution and more diverse 2D classes also comprising the MD. Our findings regarding the cryo-EM structure of GDP·AlF_3 with Nb74 will be discussed in detail in chapter 3.

For Nb195 and Nb196 we obtained cryo-EM reconstructions visualising the binding of the Nbs to the LG domain and confirming the results from SEC-MALS analysis. Whether the GBP1-dimer is only able to bind one Nb196 as observed in the cryo-EM reconstruction and in SEC-MALS experiments or whether this is a concentration and affinity dependent observation is still under investigation. There is also the possibility that the binding of Nb196 to the GBP1-dimer induces a small structural rearrangement preventing the binding of a second Nb.

When analysing the interface between Nb195 and Nb196 with GBP1, we observed a number of residues located at the interface that differ between GBP1 and GBP2 explaining why both Nbs specifically bind to GBP1. We also took a closer look at the loop between amino acid position 189 and 197 involved in the binding of Nb196. We realised that Nb196 only binds to one LG-monomer and not like Nb195 at the interface of two LG domains. Surprisingly, Nb196 was unable to bind to the LG domain monomer, indicating structural changes between the monomer and the dimer of GBP1 in this loop region. Unfortunately the loop was not resolved in the available crystal structures of the GBP1 monomer (PDB-ID:1dg3) as well as the farnesylated GBP1 monomer (PDB-ID:6k1z) indicating a high degree of structural flexibility when being monomeric. Interestingly, we also observed the same loop missing in the monomeric GBP5 structure, whereas it was present for the GBP2-monomer, although slightly shifted compared to the structure of the GBP1-LG-dimer or the GBP5-dimer.

2.4. Conclusions and Outlook

Taken together, we characterised eight different Nbs on their abilities to interact with GBP1 or GBP2, determined the affinity and further described the interfaces of two Nbs using cryo-electron microscopy. By utilising those Nbs as intrabodies it might be possible to address important and so far unanswered questions regarding the precise role of GBP1 and GBP2 within cells as well as investigating the importance of coat formation of GBPs for downstream mechanistic effects like caspase-4. Using Nb74 or Nb76 that are only able to bind GBP1, but not GBP2 as fluorescently labelled intrabodies could be a powerful tool to follow native, non labelled GBP1 in cells. The identification of Nbs that are specific for GBP1 while being unable to bind GBP2, further enables differentiation between a GBP1 homo-dimer and a GBP1-GBP2 hetero-dimer *in vitro* which could be used for structural studies. By having identified a set of Nbs that only bind to the GBP1-dimer but not the GBP1-monomer, we would be able to differentiate between oligomeric states within cells and study the importance of it. Additionally, the discovery of Nbs that are able to break the GBP1 and GBP2 dimer apart set the foundation for future experiments. By utilising those Nbs as intrabodies it will enable us to study the relationship between GBP dimers, the ability to coat membranes and the biological role of GBPs to function as a signalling platform for caspase-4. The identified Nbs can also be used to increase the molecular weight and thereby the signal to noise ratio when utilising cryo-EM for structure determination of the 130 kDa small GBP1 dimer. Adding multiple Nbs that can bind simultaneously to GBP1 could further increase the contrast in cryo-EM and might help stabilising flexible regions of the protein that are otherwise difficult to visualise.

Author contributions
TK, LP, CP purified proteins. TK and CP performed fluorescence imaging. TK and LP conducted biophysical experiments, prepared cryo-EM samples, collected cryo-EM data and processed cryo-EM data. EP initiated Nb generation. AF performed SPR data acquisition. TK wrote the chapter. AJ revised the chapter as well as conceptualised and supervised the study.

Acknowledgements
We thank Roland Kieffer and Jeremie Capulade for help with fluorescence imaging and Wiel Evers for help with cryo-EM data collection. We acknowledge Instruct-ERIC (PID 7267), part of the European Strategy Forum on Research Infrastructures (ESFRI), and the Research Foundation - Flanders (FWO) for their support and use of resources, as well as Alison Lundqvist for technical assistance during Nb discovery. We also acknowledge Instruct-ERIC (PID 24937) and the Nederlands Kanker Instituut (NKI) for providing access to SPR instrumentation. Cryo-EM data collection benefited from access to the Netherlands Centre for Electron Nanoscopy (NeCEN) with financial support from the Dutch Roadmap Grant NEMI (NWO.GWI.184.034.014). This work was supported by the European Research Council (ERC-StG-852880 to AJ), the Dutch Research Council (NWO.STU.018-2.007 to AJ) and the Kavli Institute of Nanoscience Delft.

2.5. Materials and Methods

Plasmid construction

GBP1 and GBP2
Codon-optimised synthetic DNA encoding human GBP1 (UniProt accession P32455) and human GBP2 (UniProt accession P32456) was cloned into the NcoI/NotI linearised pETM14 vector containing an N-terminal His_6 tag and 3C cleavage site, yielding pETM14-GBP1 (AJLD0030) or pETM14-GBP2 (AJLD0036) (Table 2.5).

GBP1-LG domain
The hGBP1-LG domain consists of an N-terminal 6xHis-tag and an HRV-3C cleavage site. The hGBP1 construct (AJLD0030) and pETM14 vector (AJLV0009) were amplified in DH5α and isolated by plasmid preparation (Promega) according the manufactures instructions. The hGBP1-LG domain was amplified by PCR from pETM14-hGBP1 (AJLD-0030) utilising primers AJLO030 and AJL0257 (Table 2.3). Both the PCR product and vector were cut/digested with NotI and NcoI. The cleaned PCR product was ligated into the dephosphorylated vector and the correct plasmid (AJLD0217) was confirmed via DNA sequencing (Macrogen).

GBP1-Avi
The Avi-tag (GLNDIFEAQKIEWHE) was introduced at the C-terminus of GBP1 by PCR amplification using the primers AJLO-0002 and AJLO-0058 (Table 2.3). GBP1-Avi was cut with NotI and BsaI and cloned into the NcoI/NotI linearised pETM14 vector containing an N-terminal His_6 tag and 3C cleavage site, yielding pETM14-GBP1-Avi (AJLD0040) (Table 2.5).

GBP2-Avi
Fragment amplification of the insert was performed using the primers AJLO-0110 and AJLO-011 (Table 2.3) introducing the Avi-tag (GLNDIFEAQKIEWHE) at the C-terminus of GBP2 as well as creating overhang sequences. The backbone (AJLV009) was amplified with the primers AJLO-012 and AJLO-013 (Table 2.3). The resulting Gibson assembly fragments were confirmed by gel electrophoresis using a 1 % agarose gel. The Gibson assembly reaction was carried out using NEB Gibson Assembly Master Mix where the fragments were combined at 0.5 pmol of DNA and incubated at 50°C for 1h. After the assembly, the reaction was transformed into DH5α chemically competent cells.

Protein expression and purification

GBP1 and GBP2
Proteins were expressed in *E.coli* BL21(DE3) (Supplementary Table 2.4) using auto induction in lactose-containing media. Pre-cultures were grown in LB-medium o/n at 37°C. For protein expression, ZYP5052 medium was inoculated at 1/50 (v/v) with pre-culture and cells were grown at 37°C at 180 rpm for 3-4 h before lowering the temperature to 20°C for 15-20 h. Cells were harvested by centrifugation at 4°C and 4000 rpm and the cell pellet was resuspended in lysis buffer (50 mM HEPES pH 7.8, 500 mM NaCl, 0.1 % Triton X-100) on ice. The cells were disrupted by three successive freeze-thaw cycles. To digest genomic DNA, 1-10 ug/ml DNAseI was added and incubated on a rotating wheel for 1-2 hours at 4°C. To separate cell debris, the lysate was centrifuged at 20,000 x g for 40 min at 4°C. The supernatant was applied to TALON (Takara) affinity resin. The bound fraction was washed with 20 column volumes (cv) of wash-buffer (50 mM sodium phosphate, 300 mM NaCl, 10 mM imidazole, pH 7.4) and eluted in the same buffer containing 150 mM imidazole. The eluent was dialysed into 3C cleavage buffer (50 mM HEPES pH 7.4, 150 mM NaCl, 0.5 mM DTT) and incubated with 1:100 mol/mol 3C protease o/n at 4°C. Following cleavage, the proteins were further purified via size exclusion chromatography using a GE Superdex200 Increase 10/300 GL column (GE Healthcare) in running buffer (50 mM HEPES pH 7.4, 150 mM NaCl, 0.5 mM DTT).

GBP1-LG domain
Protein expression, cell harvesting and bacterial lysis was performed as described for GBP1. To separate cell debris, the lysate was centrifuged at 30,000 x g for 30 min at 4°C. The supernatant was applied to Ni-NTA affinity resin. The bound fraction was washed with 20 cv of wash buffer (50 mM HEPES pH 7.4, 500 mM NaCl) and eluted in the same buffer containing 300 mM imidazole. The proteins were further purified via size exclusion chromatography using a GE Superdex200 Increase 10/300 GL column (GE Healthcare) in running buffer (50 mM HEPES pH 7.4, 150 mM NaCl, 0.5 mM DTT).

GBP1-Avi and GBP2-Avi
C43(DE3) cells transformed with pCDFDuet-BirA (AJLD0192) were transformed with either GBP1-avi (AJLD0040) or GBP2-avi (AJLD0078) (Table 2.5). Pre-cultures were grown in LB-medium o/n at 37°C. For protein expression, TB medium was inoculated with 1/166 (v/v) with pre-culture and cells were grown until an OD of one at 180 rpm. Protein expression was induced with 0.5 mM IPTG and biotin was added to a final concentration

of 0.1 mM, before lowering the temperature to 22°C for o/n expression at 180 rpm. The harvesting and protein purification was done as described for GBP1. The biotinylation of GBP1-avi and GBP2-avi was confirmed by performing an SDS-page analysis. Protein samples were heated to 95°C. After letting the sample cool down to RT again, streptavidin was incubated with the protein sample for 5 min before loading the sample onto an SDS-PAGE. By analysing the shift in M_W to higher molecular weight species, the overall degree of biotinylation can be determined.

Nb generation, selection and purification

Nb generation

Llamas were immunised either with purified monomeric GBP1, farnesylated GBP1 or GDP·AlF_3-stabilised dimeric GBP1. From each llama a blood sample was taken and the peripheral blood lymphocytes were isolated followed by the purification of RNA and synthesis of cDNA. Nb coding sequences were then PCR-amplified and cloned into a phage display library, creating libraries with > 10^8 independent clones.

Nb selection

For phage display selections, farnesylated, monomeric or GDP·AlF_3-stabilised dimeric GBP1 was solid phase coated in 50 mM HEPES pH 7.4, 150 mM NaCl, 0.5 mM DTT and selections were performed in the same buffer. To identify GBP1-specific Nbs, the His-tag was detected by an anti-His monoclonal antibody followed by the addition of an anti-mouse-antibody conjugated to alkaline phosphatase. As a substrate for alkaline phosphatase conjugates, 2 mg/ml of 4-Nitrophenyl phosphate disodium salt hexahydrate (pNPP) was used. In total 78 clones were found positive for the dimeric GBP1-GDP·AlF_3, 26 on $GBP1_F$ and 33 clones for monomeric GBP1. We selected Nbs from different families and performed SEC-MALS analysis to investigate the binding behaviour.

Expression and purification

Nbs were expressed in *E.coli* WK6 (su-) cells. Pre-cultures were grown overnight in LB medium containing 100 µg/ml ampicillin, 2 % glucose and 1 mM $MgCl_2$. TB medium (2.4 % yeast extract, 2 % tryptone, 0.4 % glycerol, 17 mM KH_2PO_4, 72 mM K_2HPO_4), supplemented with 100 µg/ml ampicillin, 0.1 % glucose and 2 mM $MgCl_2$ was inoculated with a 1:50 (v/v) dilution of the pre-culture and cells were grown at 37 °C with 190 rpm. Protein expression was induced with 1 mM IPTG at an OD_{600nm} between 0.7-1.2, before lowering the temperature to 25 °C for 18 hours of expression. Cells were harvested by centrifugation at 4 °C and 4000 x g for 20 min. For lysis, by osmotic shock, a pellet of a 1 l culture (with OD600 nm = 25) was resuspended with 10 ml TES buffer (0.2 M Tris pH 8, 0.5 mM EDTA, 0.5 M sucrose) for 2 hours on a rotating wheel. Next, 30 ml TES/4 buffer (TES buffer, four times diluted in H_2O) was added and left on a rotating wheel for 1 h.

The resuspended cell lysate was centrifuged for 30 min at 8000 x g and the supernatant was kept. Approximately 1 ml of Ni-NTA agarose (Qiagen) was utilised for purification of the lysate resulting from 1 l culture. Pre-equilibrated Ni-NTA agarose beads, in 50 mM sodium phosphate, 1 M NaCl, pH 7, were added to the supernatant and left to incubate on a rotating wheel for 1 h at room temperature. Following incubation the beads were washed with 20 ml of 50 mM sodium phosphate, 1 M NaCl, 10 mM imidazole, pH

7 and protein was eluted with 2.5 ml 50 mM sodium phosphate, 150 mM NaCl, 300 mM imidazole, pH 7. The elution fractions were dialysed (Spectra/Por 3, 3.5 kDa cut-off) over night against 50 mM HEPES, 150 mM NaCl pH 7.5 and subsequently concentrated (Amicon, 3 kDa cut-off) to concentrations between 150 µM to 500 µM prior to storage at –80 °C.

Preparation of GDP·AlF_3-stabilised GBP1/GBP2 or GBP1-LG dimers

15 µM of full length GBP1/GBP2 or GBP1-LG was incubated with 200 µM GDP, 10 mM NaF, 300 µM $AlCl_3$, 5 mM $MgCl_2$ and 1 mM DTT for 10 min at RT.

SEC-MALS

GBP1, GBP1-LG, GBP2 and Nbs were analysed using analytical size exclusion chromatography coupled to multi-angle light scattering (SEC-MALS). Purified protein samples were resolved on a Superdex200 Increase 10/300 GL column (GE Healthcare) connected to a high-performance liquid chromatography (HPLC) unit (1260 Infinity II, Agilent) running in series with an online UV detector (1260 Infinity II VWD, Agilent), an 8-angle static light scattering detector (DAWN HELEOS 8+; Wyatt Technology), and a refractometer (Optilab T-rEX; Wyatt Technology).

For SEC-MALS measurements, full length GBP1/GBP2 and GBP1-LG were diluted to a final concentration of 15 µM in SEC buffer (50 mM HEPES pH 7.4, 150 mM NaCl, 0.5 mM TCEP or DTT) with or without the GTP transition state mimic. Depending on the experiments Nbs were added prior to nucleotide dependent dimer formation or afterwards in either an equimolar ratio or in a 2:1 molar excess. On the basis of the measured Rayleigh scattering at different angles and the established differential refractive index increment of value of 0.185 ml*g^{-1} for proteins in solution with respect to the change in protein concentration (dn/dc) , weight-averaged molar masses for each species were calculated using ASTRA software (Wyatt Technology; v.7.3.1).

Surface plasmon resonance (SPR)

SPR experiments were carried out on a BIAcore T200 system (GE Healthcare) at 25°C. Avi-tag biotinylated GBP1 and Avi-tag biotinylated GBP2 were immobilised on SPR sensor chips (Biotin capture Kit series S, GE Healthcare). All binding studies, as well as dilutions, were performed in SPR running buffer (50 mM HEPES pH 7.4, 150 mM NaCl, 0.5 mM TCEP, 0.005 % (v/v) Tween-20). Dilution series of Nbs (1 nM to 256 nM) were injected at a flow rate of 50 µl/min for 60 s and the dissociation time was set to 60 s. The last dissociation step was 600 s for a reliable determination of k_{off}. The chip surface was regenerated after every Nb with 6 M guanidinium hydrochloride dissolved in 250 mM sodium hydroxide. Data from the reference flow cell was subtracted for all runs and kinetic parameters were evaluated using BIAcore T200 evaluation software (version 3.2).

GUV preparation

Per experimental condition, 30 µl of 10 mg/ml BPLE (Avanti Polar Lipids), was added to 10 µl of 0.1 mg/mL Texas Red 1,2-Dihexadecanoyl-sn-Glycero-3-Phosphoethanolamine, Triethylammonium (Texas Red DHPE, Invitrogen) and 4 µl of 10 mg/mL DSPE-PEG(2000)-biotin (Sigma Aldrich). 30 µl of this solution was carefully aspirated and spread onto a

Polyvinyl alcohol (PVA) coated glass cover slide (5 % PVA was prepared in water, dried on a 22x22 mm cover slide for 30 min at 50 °C), prior to an additional 30 min in a desiccator connected to a vacuum pump. To the dried lipid film 250 µl of inside buffer (50 mM HEPES (pH 7.5), 150 mM NaCl, 50 mM sucrose) were added and lipids were allowed to swell in the dark for 15 min with gentle shaking. The giant unilamellar vesicles (GUVs) were collected and freshly used.

Confocal fluorescence microscopy

Preparation of the imaging chamber

Glass coverslips (22x40 mm) were attached with UV resin, to a home-made pre-drilled piece of plexiglass, to form the imaging chambers. The chambers were flushed with 2 mg/mL BSA-biotin, containing 3 moles of biotin per mole of BSA (BioVision). After removal of Biotin, the chambers were washed with buffer (50 mM HEPES (pH 7.5), 150 mM NaCl) and incubated further 5 minutes with 1 mg/mL Avidin (Thermo Fisher) prior to addition of the GUVs for imaging.

Maleimide labelling of GBP1$_F$-Q577C

Alexa Fluor 647 (Thermo Fisher) dissolved in DMSO to a final concentration of 10 mM was added drop-wise to the protein until a 20x molar excess was achieved. Prior to addition of the fluorophore, the protein was reduced for 5 min with 0.5 mM TCEP. After addition, the sample was incubated 2 h at room temperature. Separation of the labelled protein from excess dye was performed according to the manufacturer using a desalting column (5 ml, HiTrap Desalting, Cytiva) in 50 mM HEPES pH 7.4, 150 mM NaCl and 0.5 mM.

Mixing of GBP1$_F$-GDP·AlF$_3$ with GUVs

5 µl of protein solution consisting of 18.5 µM GBP1$_F$-GDP·AlF$_3$ and 1.5 µM of GBP1$_F$-Q577C-GDP·AlF$_3$, labelled with Alexa 647-C2-maleimide was either pre-incubated with Nb75 in a 1:5 molar excess for 60 min at RT or Nb75 was added after mixing GUVs with GBP1. 20 µl of Texas Red DHPE labelled GUVs were mixed with 5 µl protein solution resulting in a final protein concentration of 4 µM.

Confocal microscopy

Imaging was performed on a Nikon A1R confocal microscope using a Nikon SR Apo TIRF 100x oil/1.49 NA objective. The excitation wavelength of the lasers was 561 nm (for Texas Red DHPE) and 640 nm (for GBP1-AF647). Images were processed with Fiji software.

Single particle cryo-EM

GBP1-GDP·AlF$_3$ dataset

A total of 3.0 µL of 0.7 mg/ml GBP1-GDP·AlF$_3$ was applied to glow-discharged Quantifoil grids (QF-1.2/1.3, 300-mesh holey carbon on copper) on a Leica GP2 vitrification robot at 99 % humidity and a temperature of 22 °C. The sample was blotted for 4 s from the carbon side of the grid and immediately flash-cooled in liquid ethane. Micrographs were acquired on a FEI Titan Krios (Thermo Fisher Scientific) operated at 300 kV. Images were recorded on a K2 Summit direct electron detector (Gatan) with a pixel size of

1.09 Å. Image acquisition was performed with EPU Software (Thermo Fisher Scientific), and micrographs were collected at an underfocus varying between –3.5 µm and –0.5 µm. We collected a total of 48 frames accumulating to a total exposure of 60 $e^-/Å^2$. In total, 1,193 micrographs were acquired.

GBP1-GDP·AlF_3-Nb74 dataset
GBP1 was incubated in a 1:1 molar ratio with Nb74 for 70 min at RT, before adding GDP·AlF_3 and incubating additionally for 10 min at RT. Vitrification was performed as described for GBP1-GDP·AlF_3. Micrographs were acquired on a FEI Titan Krios (Thermo Fisher Scientific) operated at 300 kV. Images were recorded on a K3 Summit direct electron detector (Gatan) at a magnification of 105kx, corresponding to a pixel size of 0.834 Å at the specimen level. Image acquisition was performed with EPU 2.8.1 Software (Thermo Fisher Scientific), and micrographs were collected at an underfocus varying between –2.2 µm and –0.6 µm. We collected a total of 50 frames accumulating to a total electron exposure of 60 $e^-/Å^2$. In total, 5,214 micrographs were acquired.

GBP1-GDP·AlF_3-Nb195 dataset
GBP1-GDP·AlF_3 was incubated with Nb195 in a 1:3 molar excess for 30 min at RT. A total of 3.6 µL of 0.6 mg/ml GBP1-GDP·AlF_3-Nb195 was applied to glow-discharged Quantifoil grids (QF-1.2/1.3, 300-mesh holey carbon on copper) on a Leica GP2 vitrification robot at 99 % humidity and a temperature of 20 °C. The sample was blotted for 10 s from the carbon side of the grid and immediately flash-cooled in liquid ethane. Micrographs were acquired on a JEM 3200FSC TEM (JEOL) operated at 200 kV. Images were recorded on a K2 Summit direct electron detector (Gatan) at a magnification of 40kx, corresponding to a pixel size of 0.94 Å at the specimen level. Image acquisition was performed with SerialEM, and micrographs were collected at an underfocus varying between –2.5 µm and –0.5 µm. We collected a total of 53 frames accumulating to a total electron exposure of 60 $e^-/Å^2$. In total, 195 micrographs were acquired.

GBP1-GDP·AlF_3-Nb196 dataset
GBP1-GDP·AlF_3 was incubated with Nb196 in a 1:4 molar excess for 30 min at RT. Vitrification and data acquisition was performed as described for GBP1-GDP·AlF_3-Nb195. 45 frames accumulating to a total electron exposure of 60 $e^-/Å^2$ were collected. In total, 436 micrographs were acquired.

Single-particle image processing

GBP1-GDP·AlF_3
1,193 movies of GBP1-GDP·AlF_3 were processed in cryoSPARC v3.1 [55]. Patch-motion correction and patched CTF estimation were followed by manual particle picking [56, 57]. Those manual picks were used to train a Topaz model [58] from which 240,487 particles were extracted. After multiple rounds of 2D classification, particles assigned to classes displaying secondary structure were used as an input to perform *ab initio* reconstruction to generate 5 different models (67,197 particles). Three classes were used for heterogeneous refinement imposing C2 symmetry. A final non-uniform refinement [59] consisting of 35,715 particles resulted in a 4.9 Å resolution structure that only covered the LG domain of GBP1.

GBP1-GDP·AlF_3-Nb74
The GBP1-GDP·AlF_3-Nb74 dataset was processed using cryoSPARC v3.3.2 [55]. The in-built patch-motion correction [56] routine in cryoSPARC was used to correct for stage drift and beam-induced specimen movement over the acquired frames. 5,208 micrographs were selected for further processing and patched contrast transfer function (CTF) determination [57] was performed in cryoSPARC. Using a blob-based particle picker, 2,171,521 particles were extracted and cleaned via multiple rounds of 2D classification, each consisting of 50 - 100 classes.

GBP1-GDP·AlF_3-Nb195
195 movies of GBP1-GDP·AlF_3-Nb195 were processed in cryoSPARC v4.2.1 [55]. Patch-motion correction and patched CTF estimation were followed by particle picking with a blob picker [56, 57]. 2D class averages resulting from those picks were used to train a Topaz model [58] from which 46,492 particles were extracted. After multiple rounds of 2D classification, particles displaying distinct particle features were used as input for *ab initio* reconstruction to generate 3 different models (11,427 particles). Two classes were used for heterogeneous refinement without imposing symmetry resulting in a 10.4 Å resolution structure only covering the LG domain of GBP1 bound to Nb195 which is displayed in Figure 2.16c containing 7200 particles.

GBP1-GDP·AlF_3-Nb196
436 movies of GBP1-GDP·AlF_3-Nb195 were processed as described for GBP1-GDP·AlF_3-Nb195. 47,750 particles were extracted from a trained Topaz model [58]. After multiple rounds of 2D classification, particles displaying distinct particle features were used as input for *ab initio* reconstruction to generate one model (10,281 particles). The model was further used as input for homogeneous refinement without imposing symmetry resulting in a 9 Å resolution structure. The EM map only covers the LG domain of GBP1 bound to one Nb196 which is displayed in Figure 2.17c.

Bioinformatic analysis

Multiple sequence alignment
The sequences of Nb74, Nb76, Nb77, Nb193, Nb195, Nb196 and Nb202 were used as input for Clustal Omega [49]. The resulting sequence alignment was displayed and consensus sequences computed in MView [60].

References

[1] B.-H. Kim, A. R. Shenoy, P. Kumar, C. J. Bradfield, and J. D. MacMicking, *Ifn-inducible gtpases in host cell defense,* Cell host & microbe **12**, 432 (2012).

[2] F. Randow, J. D. MacMicking, and L. C. James, *Cellular self-defense: how cell-autonomous immunity protects against pathogens,* Science **340**, 701 (2013).

[3] S. L. Anderson, J. M. Carton, J. Lou, L. Xing, and B. Y. Rubin, *Interferon-induced guanylate binding protein-1 (gbp-1) mediates an antiviral effect against vesicular stomatitis virus and encephalomyocarditis virus,* Virology **256**, 8 (1999).

[4] Y. Itsui, N. Sakamoto, S. Kakinuma, M. Nakagawa, Y. Sekine-Osajima, M. Tasaka-Fujita, Y. Nishimura-Sakurai, G. Suda, Y. Karakama, K. Mishima, *et al.*, *Antiviral effects of the interferon-induced protein guanylate binding protein 1 and its interaction with the hepatitis c virus ns5b protein,* Hepatology **50**, 1727 (2009).

[5] I. Tietzel, C. El-Haibi, and R. A. Carabeo, *Human guanylate binding proteins potentiate the anti-chlamydia effects of interferon-γ,* PloS one **4**, e6499 (2009).

[6] M. Yamamoto, M. Okuyama, J. S. Ma, T. Kimura, N. Kamiyama, H. Saiga, J. Ohshima, M. Sasai, H. Kayama, T. Okamoto, *et al.*, *A cluster of interferon-γ-inducible p65 gtpases plays a critical role in host defense against toxoplasma gondii,* Immunity **37**, 302 (2012).

[7] C. Krapp, D. Hotter, A. Gawanbacht, P. J. McLaren, S. F. Kluge, C. M. Stürzel, K. Mack, E. Reith, S. Engelhart, A. Ciuffi, *et al.*, *Guanylate binding protein (gbp) 5 is an interferon-inducible inhibitor of hiv-1 infectivity,* Cell host & microbe **19**, 504 (2016).

[8] E. Braun, D. Hotter, L. Koepke, F. Zech, R. Groß, K. M. Sparrer, J. A. Müller, C. K. Pfaller, E. Heusinger, R. Wombacher, *et al.*, *Guanylate-binding proteins 2 and 5 exert broad antiviral activity by inhibiting furin-mediated processing of viral envelope proteins,* Cell Reports **27**, 2092 (2019).

[9] M. Kutsch, L. Sistemich, C. F. Lesser, M. B. Goldberg, C. Herrmann, and J. Coers, *Direct binding of polymeric gbp1 to lps disrupts bacterial cell envelope functions,* The EMBO journal **39**, e104926 (2020).

[10] D. Fisch, B. Clough, M.-C. Domart, V. Encheva, H. Bando, A. P. Snijders, L. M. Collinson, M. Yamamoto, A. R. Shenoy, and E.-M. Frickel, *Human gbp1 differentially targets salmonella and toxoplasma to license recognition of microbial ligands and caspase-mediated death,* Cell reports **32**, 108008 (2020).

[11] E. Meunier, M. S. Dick, R. F. Dreier, N. Schürmann, D. K. Broz, S. Warming, M. Roose-Girma, D. Bumann, N. Kayagaki, K. Takeda, *et al.*, *Caspase-11 activation requires lysis of pathogen-containing vacuoles by ifn-induced gtpases,* Nature **509**, 366 (2014).

[12] E. Meunier, P. Wallet, R. F. Dreier, S. Costanzo, L. Anton, S. Rühl, S. Dussurgey, M. S. Dick, A. Kistner, M. Rigard, *et al.*, *Guanylate-binding proteins promote activation of the aim2 inflammasome during infection with francisella novicida,* Nature immunology **16**, 476 (2015).

[13] E. Kravets, D. Degrandi, Q. Ma, T.-O. Peulen, V. Kluempers, S. Felekyan, R. Kuehnemuth, S. Weidtkamp-Peters, C. A. Seidel, and K. Pfeffer, *Guanylate binding proteins directly attack toxoplasma gondii via supramolecular complexes,* Elife **5**, e11479 (2016).

[14] J. C. Santos, D. Boucher, L. K. Schneider, B. Demarco, M. Dilucca, K. Shkarina, R. Heilig, K. W. Chen, R. Y. Lim, and P. Broz, *Human gbp1 binds lps to initiate assembly of a caspase-4 activating platform on cytosolic bacteria,* Nature communications **11**, 3276 (2020).

[15] M. P. Wandel, B.-H. Kim, E.-S. Park, K. B. Boyle, K. Nayak, B. Lagrange, A. Herod, T. Henry, M. Zilbauer, J. Rohde, *et al.*, *Guanylate-binding proteins convert cytosolic bacteria into caspase-4 signaling platforms,* Nature immunology **21**, 880 (2020).

[16] J. Shi, Y. Zhao, K. Wang, X. Shi, Y. Wang, H. Huang, Y. Zhuang, T. Cai, F. Wang, and F. Shao, *Cleavage of gsdmd by inflammatory caspases determines pyroptotic cell death,* Nature **526**, 660 (2015).

[17] X. Liu, Z. Zhang, J. Ruan, Y. Pan, V. G. Magupalli, H. Wu, and J. Lieberman, *Inflammasome-activated gasdermin d causes pyroptosis by forming membrane pores,* Nature **535**, 153 (2016).

[18] B. Prakash, G. J. Praefcke, L. Renault, A. Wittinghofer, and C. Herrmann, *Structure of human guanylate-binding protein 1 representing a unique class of gtp-binding proteins,* Nature **403**, 567 (2000).

[19] D. E. Nantais, M. Schwemmle, J. T. Stickney, D. J. Vestal, and J. E. Buss, *Prenylation of an interferon-γ-induced gtp-binding protein: the human guanylate binding protein, hugbp1,* Journal of leukocyte biology **60**, 423 (1996).

[20] N. Britzen-Laurent, M. Bauer, V. Berton, N. Fischer, A. Syguda, S. Reipschläger, E. Naschberger, C. Herrmann, and M. Stürzl, *Intracellular trafficking of guanylate-binding proteins is regulated by heterodimerization in a hierarchical manner,* PloS one **5**, e14246 (2010).

[21] A. Ghosh, G. J. Praefcke, L. Renault, A. Wittinghofer, and C. Herrmann, *How guanylate-binding proteins achieve assembly-stimulated processive cleavage of gtp to gmp,* Nature **440**, 101 (2006).

[22] T. Vopel, C. S. Hengstenberg, T.-O. Peulen, Y. Ajaj, C. A. Seidel, C. Herrmann, and J. P. Klare, *Triphosphate induced dimerization of human guanylate binding protein 1 involves association of the c-terminal helices: a joint double electron–electron resonance and fret study,* Biochemistry **53**, 4590 (2014).

[23] B. Barz, J. Loschwitz, and B. Strodel, *Large-scale, dynamin-like motions of the human guanylate binding protein 1 revealed by multi-resolution simulations,* PLoS Computational Biology **15**, e1007193 (2019).

[24] H. Stark, *Grafix: stabilization of fragile macromolecular complexes for single particle cryo-em,* in *Methods in enzymology*, Vol. 481 (Elsevier, 2010) pp. 109–126.

[25] F. Chu, D. T. Thornton, and H. T. Nguyen, *Chemical cross-linking in the structural analysis of protein assemblies,* Methods **144**, 53 (2018).

[26] B. Jayachandran, T. N. Parvin, M. M. Alam, K. Chanda, and B. Mm, *Insights on chemical crosslinking strategies for proteins,* Molecules **27**, 8124 (2022).

[27] E. Nwanochie and V. N. Uversky, *Structure determination by single-particle cryo-electron microscopy: only the sky (and intrinsic disorder) is the limit,* International journal of molecular sciences **20**, 4186 (2019).

[28] J. Helma, M. C. Cardoso, S. Muyldermans, and H. Leonhardt, *Nanobodies and recombinant binders in cell biology,* Journal of Cell Biology **209**, 633 (2015).

[29] K. Nord, E. Gunneriusson, J. Ringdahl, S. Ståhl, M. Uhlén, and P.-Å. Nygren, *Binding proteins selected from combinatorial libraries of an α-helical bacterial receptor domain,* Nature biotechnology **15**, 772 (1997).

[30] A. Koide, C. W. Bailey, X. Huang, and S. Koide, *The fibronectin type iii domain as a scaffold for novel binding proteins,* Journal of molecular biology **284**, 1141 (1998).

[31] G. Beste, F. S. Schmidt, T. Stibora, and A. Skerra, *Small antibody-like proteins with prescribed ligand specificities derived from the lipocalin fold,* Proceedings of the National Academy of Sciences **96**, 1898 (1999).

[32] P. Forrer, M. T. Stumpp, H. K. Binz, and A. Plückthun, *A novel strategy to design binding molecules harnessing the modular nature of repeat proteins,* FEBS letters **539**, 2 (2003).

[33] S. Hober, S. Lindbo, and J. Nilvebrant, *Bispecific applications of non-immunoglobulin scaffold binders,* Methods **154**, 143 (2019).

[34] S. G. Rasmussen, H.-J. Choi, J. J. Fung, E. Pardon, P. Casarosa, P. S. Chae, B. T. DeVree, D. M. Rosenbaum, F. S. Thian, T. S. Kobilka, *et al., Structure of a nanobody-stabilized active state of the β2 adrenoceptor,* Nature **469**, 175 (2011).

[35] J. Steyaert and B. K. Kobilka, *Nanobody stabilization of g protein-coupled receptor conformational states,* Current opinion in structural biology **21**, 567 (2011).

[36] C. Hamers-Casterman, T. Atarhouch, S. a. Muyldermans, G. Robinson, C. Hammers, E. B. Songa, N. Bendahman, and R. Hammers, *Naturally occurring antibodies devoid of light chains,* Nature **363**, 446 (1993).

[37] E. De Genst, K. Silence, K. Decanniere, K. Conrath, R. Loris, J. Kinne, S. Muyldermans, and L. Wyns, *Molecular basis for the preferential cleft recognition by dromedary heavy-chain antibodies,* Proceedings of the National Academy of Sciences **103**, 4586 (2006).

[38] H. Kaur, J.-B. Hartmann, R. P. Jakob, M. Zahn, I. Zimmermann, T. Maier, M. A. Seeger, and S. Hiller, *Identification of conformation-selective nanobodies against the membrane protein insertase bama by an integrated structural biology approach,* Journal of biomolecular NMR **73**, 375 (2019).

[39] T. Uchański, E. Pardon, and J. Steyaert, *Nanobodies to study protein conformational states,* Current opinion in structural biology **60**, 117 (2020).

[40] I. Jovčevska and S. Muyldermans, *The therapeutic potential of nanobodies,* BioDrugs **34**, 11 (2020).

[41] C. McMahon, A. S. Baier, R. Pascolutti, M. Wegrecki, S. Zheng, J. X. Ong, S. C. Erlandson, D. Hilger, S. G. Rasmussen, A. M. Ring, *et al.*, *Yeast surface display platform for rapid discovery of conformationally selective nanobodies,* Nature structural & molecular biology **25**, 289 (2018).

[42] R. Van der Linden, L. Frenken, B. De Geus, M. Harmsen, R. Ruuls, W. Stok, L. De Ron, S. Wilson, P. Davis, and C. Verrips, *Comparison of physical chemical properties of llama vhh antibody fragments and mouse monoclonal antibodies,* Biochimica et Biophysica Acta (BBA)-Protein Structure and Molecular Enzymology **1431**, 37 (1999).

[43] M. Dumoulin, K. Conrath, A. Van Meirhaeghe, F. Meersman, K. Heremans, L. G. Frenken, S. Muyldermans, L. Wyns, and A. Matagne, *Single-domain antibody fragments with high conformational stability,* Protein Science **11**, 500 (2002).

[44] C. Vincke, C. Gutiérrez, U. Wernery, N. Devoogdt, G. Hassanzadeh-Ghassabeh, and S. Muyldermans, *Generation of single domain antibody fragments derived from camelids and generation of manifold constructs,* Antibody Engineering: Methods and Protocols, Second Edition , 145 (2012).

[45] P. Kunz, K. Zinner, N. Mücke, T. Bartoschik, S. Muyldermans, and J. D. Hoheisel, *The structural basis of nanobody unfolding reversibility and thermoresistance,* Scientific reports **8**, 7934 (2018).

[46] U. Rothbauer, K. Zolghadr, S. Tillib, D. Nowak, L. Schermelleh, A. Gahl, N. Backmann, K. Conrath, S. Muyldermans, M. C. Cardoso, *et al.*, *Targeting and tracing antigens in live cells with fluorescent nanobodies,* Nature methods **3**, 887 (2006).

[47] B. Traenkle and U. Rothbauer, *Under the microscope: single-domain antibodies for live-cell imaging and super-resolution microscopy,* Frontiers in immunology **8**, 1030 (2017).

[48] E. Pardon, T. Laeremans, S. Triest, S. G. Rasmussen, A. Wohlkönig, A. Ruf, S. Muyldermans, W. G. Hol, B. K. Kobilka, and J. Steyaert, *A general protocol for the generation of nanobodies for structural biology,* Nature protocols **9**, 674 (2014).

[49] F. Madeira, Y. M. Park, J. Lee, N. Buso, T. Gur, N. Madhusoodanan, P. Basutkar, A. R. Tivey, S. C. Potter, R. D. Finn, *et al.*, *The embl-ebi search and sequence analysis tools apis in 2019,* Nucleic acids research **47**, W636 (2019).

[50] M. Fairhead and M. Howarth, *Site-specific biotinylation of purified proteins using bira,* Site-Specific Protein Labeling: Methods and Protocols , 171 (2015).

[51] N. M. Green, *[5] avidin and streptavidin,* in *Methods in enzymology*, Vol. 184 (Elsevier, 1990) pp. 51–67.

[52] W. Cui, E. Braun, W. Wang, J. Tang, Y. Zheng, B. Slater, N. Li, C. Chen, Q. Liu, B. Wang, *et al.*, *Structural basis for gtp-induced dimerization and antiviral function of guanylate-binding proteins,* Proceedings of the National Academy of Sciences **118**, e2022269118 (2021).

[53] S. Shydlovskyi, A. Y. Zienert, S. Ince, C. Dovengerds, A. Hohendahl, J. M. Dargazanli, A. Blum, S. D. Günther, N. Kladt, M. Stürzl, *et al.*, *Nucleotide-dependent farnesyl switch orchestrates polymerization and membrane binding of human guanylate-binding protein 1,* Proceedings of the National Academy of Sciences **114**, E5559 (2017).

[54] M. Kutsch, S. Ince, and C. Herrmann, *Homo and hetero dimerisation of the human guanylate-binding proteins hgbp-1 and hgbp-5 characterised by affinities and kinetics,* The FEBS Journal **285**, 2019 (2018).

[55] A. Punjani, J. L. Rubinstein, D. J. Fleet, and M. A. Brubaker, *cryosparc: algorithms for rapid unsupervised cryo-em structure determination,* Nature methods **14**, 290 (2017).

[56] S. Q. Zheng, E. Palovcak, J.-P. Armache, K. A. Verba, Y. Cheng, and D. A. Agard, *Motioncor2: anisotropic correction of beam-induced motion for improved cryo-electron microscopy,* Nature methods **14**, 331 (2017).

[57] A. Rohou and N. Grigorieff, *Ctffind4: Fast and accurate defocus estimation from electron micrographs,* Journal of structural biology **192**, 216 (2015).

[58] T. Bepler, A. Morin, M. Rapp, J. Brasch, L. Shapiro, A. J. Noble, and B. Berger, *Positive-unlabeled convolutional neural networks for particle picking in cryo-electron micrographs,* Nature methods **16**, 1153 (2019).

[59] A. Punjani, H. Zhang, and D. J. Fleet, *Non-uniform refinement: adaptive regularization improves single-particle cryo-em reconstruction,* Nature methods **17**, 1214 (2020).

[60] N. P. Brown, C. Leroy, and C. Sander, *Mview: a web-compatible database search or multiple alignment viewer.* Bioinformatics (Oxford, England) **14**, 380 (1998).

[61] F. Studier and B. A. Moffatt, *Use of bacteriophage t7 rna polymerase to direct selective high-level expression of cloned genes,* Journal of Molecular Biology **189**, 113 (1986).

[62] R. Zell and H.-J. Fritz, *Dna mismatch-repair in escherichia coli counteracting the hydrolytic deamination of 5-methyl-cytosine residues.* The EMBO Journal **6**, 1809 (1987).

[63] A. Dümmler, A.-M. Lawrence, and A. De Marco, *Simplified screening for the detection of soluble fusion constructs expressed in e. coli using a modular set of vectors,* Microbial cell factories **4**, 1 (2005).

[64] M. van Dijk and A. M. Bonvin, *3d-dart: a dna structure modelling server,* Nucleic acids research **37**, W235 (2009).

2.6. Supplementary

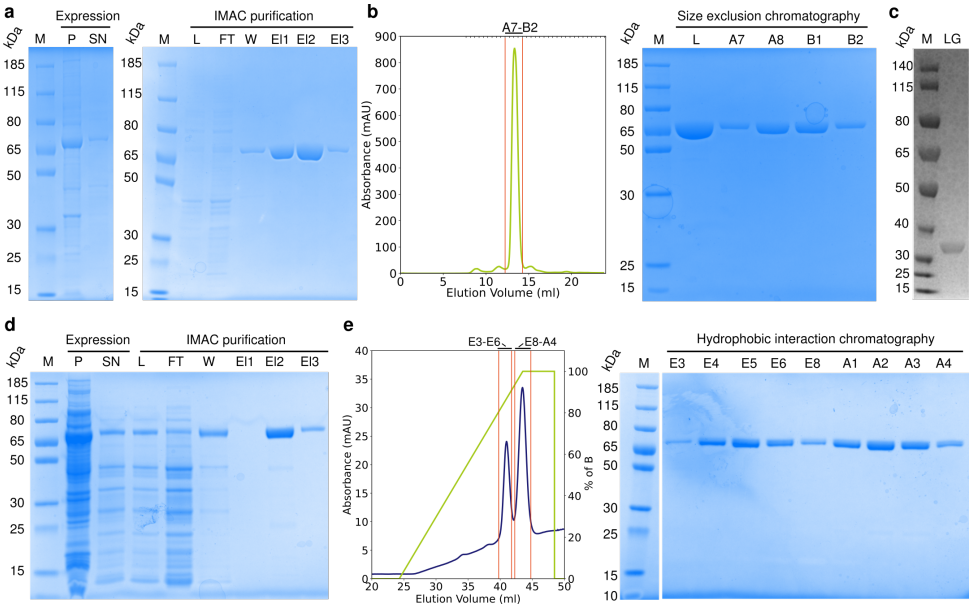

Figure 2.19: Expression and purification of GBP1, GBP1$_F$ and GBP1-LG. (a) Expression of GBP1 from BL21(DE3) cells (P: Pellet, SN: Supernatant) and ion metal affinity chromatography (IMAC) visualised on an SDS-Page (L: Load, FT: Flow through, W: Wash, El: Elution). GBP1 has a molecular weight of 67 kDa. (b) Size exclusion chromatography profile of GBP1 as well as the corresponding fractions visualised on an SDS-PAGE. (c) SDS-PAGE of purified GBP1-LG with an expected molecular weight of 35 kDa. (d) Expression of farnesylated GBP1 from BL21(DE3) cells (P: Pellet, SN: Supernatant) and ion metal affinity chromatography (IMAC) visualised on an SDS-Page (L: Load, FT: Flow through, W: Wash, El: Elution). (e) Hydrophobic interaction chromatography (HIC) profile to separate farnesylated GBP1 (first peak) from non-farnesylated GBP1 (second peak) together with the corresponding fractions visualised by SDS-PAGE.

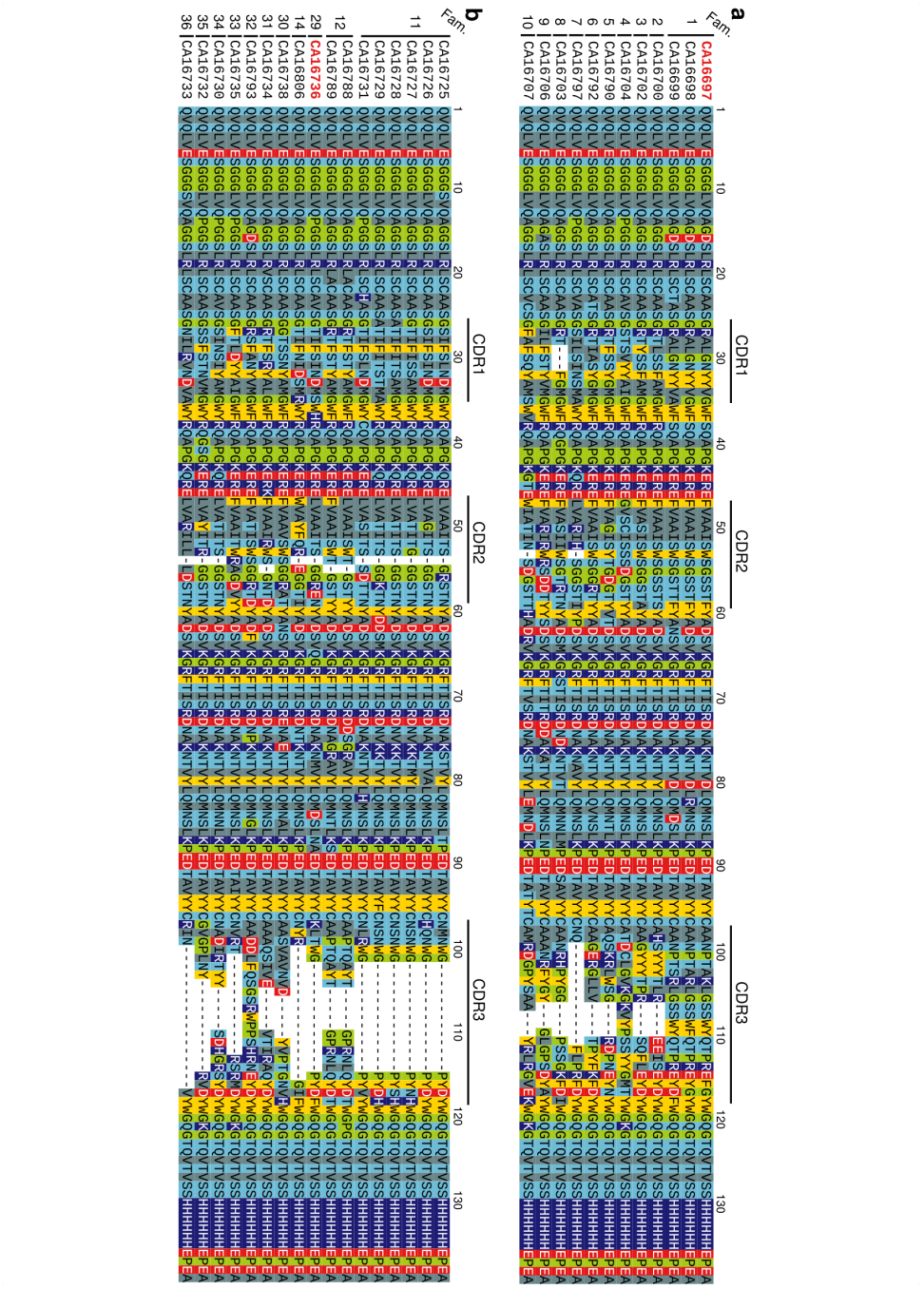

Figure 2.20: Multiple sequence alignment of Nbs that were raised against (a) farnesylated GBP1 or (b) monomeric GBP1. Primary sequences were used as input for Clustal Omega [49]. The three complementarity-determining regions of the sequences (CDRs) are emphasised above. The Nbs characterised in this study are emphasised in red (Nb74: CA16697 and Nb75: CA16736) and the corresponding Nb families are highlighted on the very left of the alignment. Residues are coloured by physicochemical property of the side chain (grey: hydrophobic, light blue: polar, red: negatively charged, dark blue: positively charged, yellow: aromatic, green: special cases).

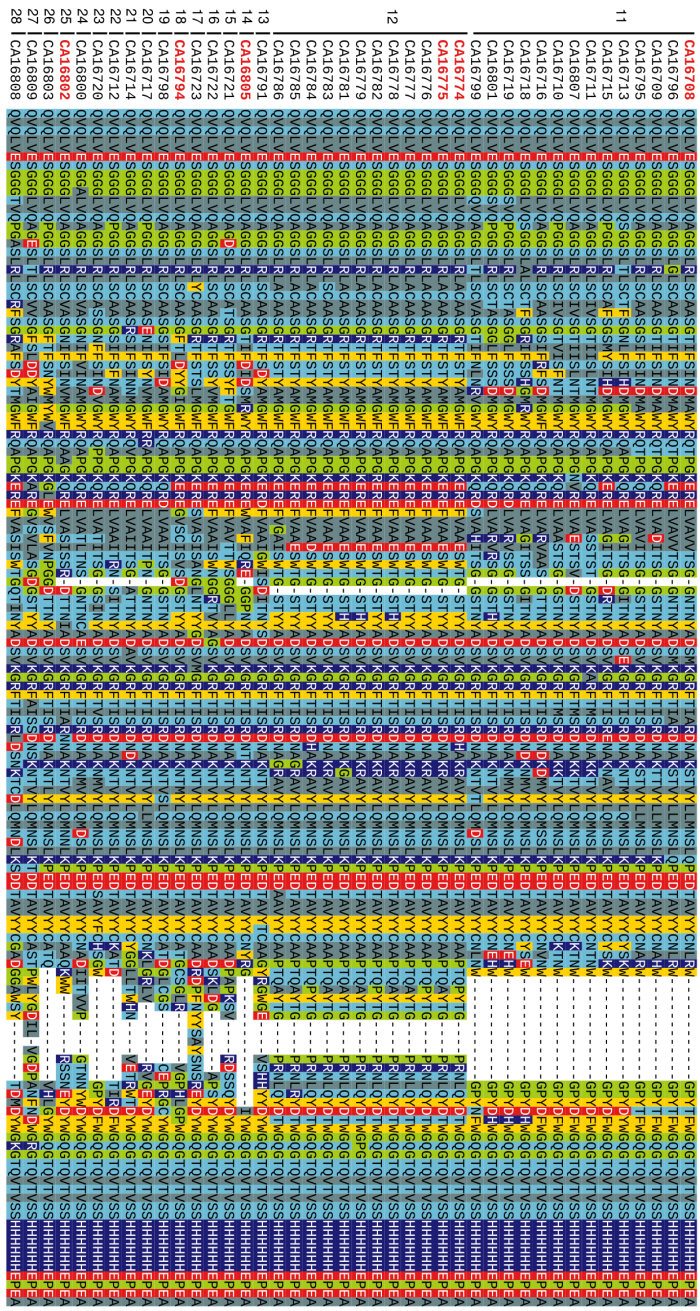

Figure 2.21: Multiple sequence alignment of Nbs that were raised against GDP·AlF_3 stabilised dimeric GBP1. Primary sequences were used as input for Clustal Omega [49]. The three complementarity-determining regions of the sequences (CDRs) are emphasised above. The Nbs characterised in this study are emphasised in red (Nb76: CA16774, Nb77: CA16708, Nb193: CA16794, Nb195: CA16805, Nb196: CA16802, Nb202: CA16775) and the corresponding Nb families are highlighted on the very left of the alignment. Residues are coloured by physicochemical property of the side chain (grey: hydrophobic, light blue: polar, red: negatively charged, dark blue: positively charged, yellow: aromatic, green: special cases).

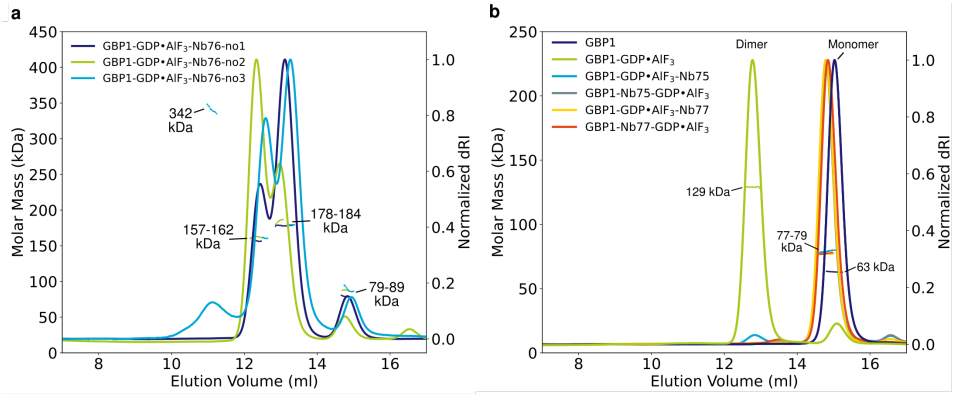

Figure 2.22: Binding of Nb75, Nb76 and Nb77 to GDP·AlF$_3$ stabilised dimeric GBP1. (a) SEC-MALS experiments reveal that the behaviour of Nb76 binding to GDP·AlF$_3$ stabilised dimeric GBP1 is reproducible as shown with three different experiments. Additionally to the expected molecular weight of a GBP1-dimer with two bound Nbs (around 160 kDa), we observe another peak with a molecular weight around 180 kDa which is shifted to the right indicating a more compact shape of the molecule. The composition of this 180 kDa complex is still unclear. (b) SEC-MALS experiments show that binding of Nb75 or Nb77 to GBP1 before adding GDP·AlF$_3$ prevents dimer formation completely (grey and orange). Moreover, a previously GDP·AlF$_3$ stabilised GBP1 dimer can be broken apart, when adding Nb75 or Nb77 (cyan and yellow) resulting in a peak with a molecular weight around 78 kDa corresponding to monomeric GBP1 with one Nb bound.

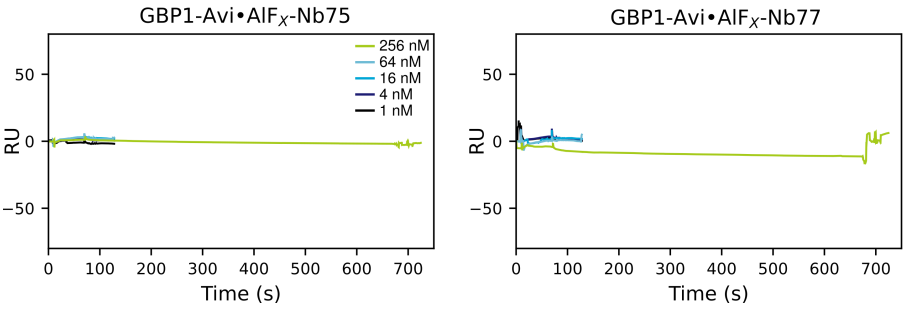

Figure 2.23: Surface plasmon resonance (SPR) experiments show no binding of Nb75 and Nb77 to GDP·AlF$_3$ stabilised dimeric biotinylated GBP1. SPR sensorgrams of Nb75 and Nb77 with dimeric GBP1-Avi. Increasing concentrations of Nbs (ranging from 1 nM to 256 nM) were injected into the sensor chip to which dimeric biotinylated GBP1 was immobilised. The sensorgrams show no interaction between Nb75 or Nb77 and dimeric GBP1.

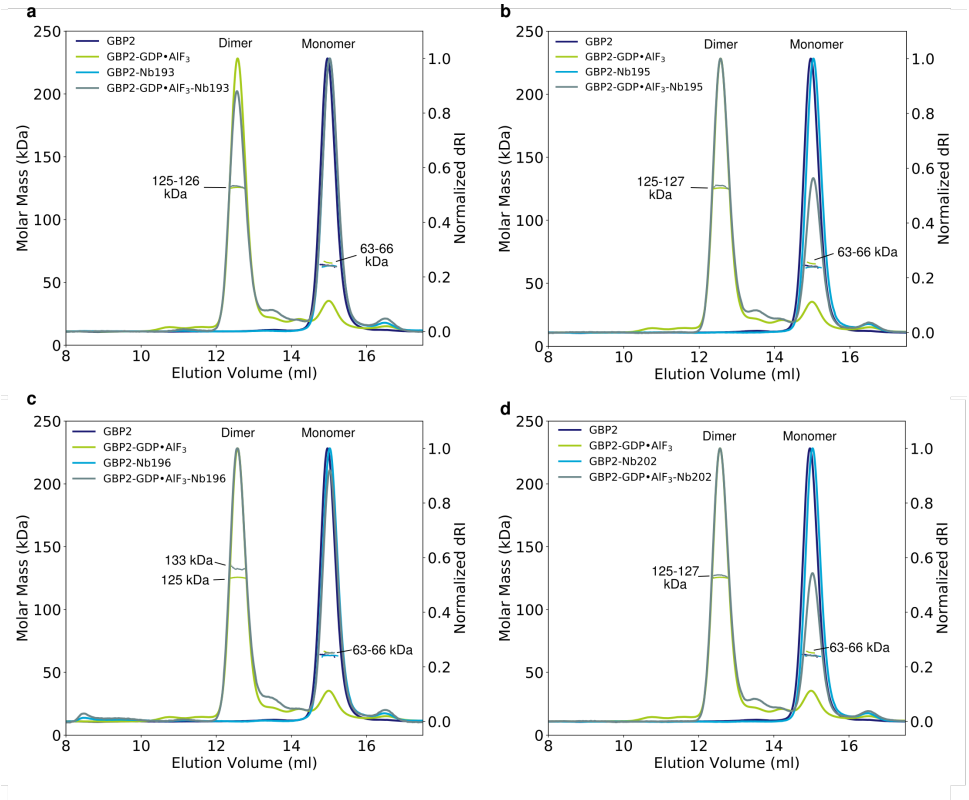

Figure 2.24: SEC-MALS experiments show that Nb193, Nb195, Nb196 and Nb202 do not bind GBP2. The Nbs 193, 195, 196 and 202 which are capable of binding to the GDP·AlF_3 stabilised LG domain dimer of GBP1 (see Figure 2.7) are unable to bind monomeric GBP2 or GDP·AlF_3 stabilised dimeric GBP2, highlighting the ability of those Nbs to bind specifically to GBP1.

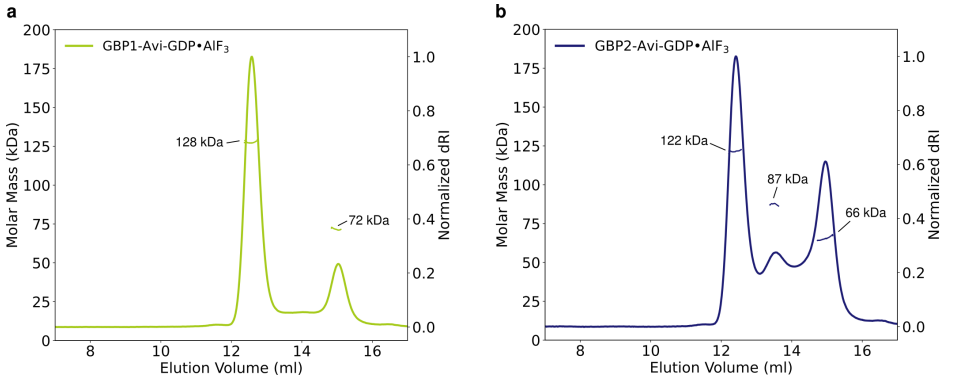

Figure 2.25: SEC-MALS experiments of GDP·AlF_3 stabilised biotinylated GBP1-Avi and GBP2-Avi. (a-b) Biotinylated GBP1-Avi and GBP2-Avi are able to form GDP·AlF_3 stabilised dimers with a molecular weight around 128 and 122 kDa. For GBP2-Avi the ratio of monomeric GBP2-Avi (66 kDa) is larger compared to GBP1-Avi.

Table 2.3: Primer sequences used in this manuscript.

Oligo name	Description	Sequence
AJLO-0002	pUC57-hGBP1-fw	ggtctcccatggcgagcgagatccacatg
AJLO-0004	pUC57-hGBP1-rev	ggtctccggccgcttattagctg
AJLO-0006	pUC57-hGBP2-fw	ggtctcccatggcgccggaaatcaacctgc
AJLO-0007	pUC57-hGBP2-rev	ggtctccggccgcttattacagaatg
AJLO-0030	T7-promotor-fw	taatacgactcactataggg
AJLO-0058	pUC57-hGBP1-Avi-rev	gggggggcggccgcttattcatgccattcaattttctgcg cttcaaaaatatcgttcaggccgctgatggtgcacgcctt
AJLO-0110	pETM14-hGBP2-Avi-gibson-fw	tgttccaggggcccatggcgccggaaatcaacc
AJLO-0111	pETM14-hGBP2-Avi-gibson-rev	tggtggtgctcgagtttattcatgccattcaattttctg cgcttcaaaaatatcgttcaggccgctgcccagaatgttgca
AJLO-0112	pETM14-gibson-fw	ggttgatttccggcgccatgggcccctggaaca
AJLO-0113	pETM14-gibson-rev	tgcaacattctgggcagcggcctgaacgatat ttttgaagcgcagaaaattgaatggcatgaataaactc-gagcaccacca
AJLO-0257	hGBP1-LG-rev	gcggccgcttattagcacggcaggtca

Table 2.4: Bacterial host strains used in this chapter.

Strain	Description	Reference
E.coli DH5α	Cloning host	Invitrogen
E.coli BL21(DE3)	Expression host for GBPs	Thermo Fisher Scientific [61]
E.coli WK6	Expression host for Nbs	Zell & Fritz, 1987 [62]
E.coli C43(DE3)	Expression host for pCDFDuet-BirA with GBP1-avi or GBP2-avi	Immunosource

Table 2.5: Vectors and Constructs used in this manuscript.

Name	Description	Source/ Reference
AJLV0009	pETM14: *E.coli* expression vector (KanR)	[63]
AJLV0038	pCDFDuet: *E.coli* expression vector (SmR)	Merck Millipore (Novagen)
AJLD0001	pUC57-hGBP1: Subcloning vector pUC57 with synthetic gene of hGBP1 optimised for *E.coli* expression (AmpR)	GenScript
AJLD0002	pUC57-hGBP2: Subcloning vector pUC57 with synthetic gene of hGBP2 optimised for *E.coli* expression (AmpR)	GenScript
AJLD0030	pETM14-hGBP1: *E.coli* expression vector (KanR) with hGBP1	Derived from AJLV0009 and AJLD0001
AJLD0036	pETM14-hGBP2: *E.coli* expression vector (KanR) with hGBP2	Derived from AJLV0009 and AJLD0002
AJLD0039	pUC57-hGBP1-Avi	Derived from AJLD0001
AJLD0040	pETM14-hGBP1-Avi: *E.coli* expression vector (KanR) with hGBP1-avi	Derived from AJLV0009 and AJLD0039
AJLD0042	pOPINJ-BirA: *E.coli* expression vector (AmpR) containing N-His6-GST-BirA	Derived from addgene (plasmid 26045) [64]
AJLD0074	pMES4y-CA16697: C-His6-tagged Nb (Nb74) raised against farnesylated GBP1	Instruct-ERIC (PID7267)
AJLD0075	pMES4y-CA16736: C-His6-tagged Nb (Nb75) raised against monomeric GBP1	Instruct-ERIC (PID7267)
AJLD0076	pMES4y-CA16774: C-His6-tagged Nb (Nb76) raised against dimeric GBP1	Instruct-ERIC (PID7267)
AJLD0077	pMES4y-CA16708: C-His6-tagged Nb (Nb77) raised against dimeric GBP1	Instruct-ERIC (PID7267)
AJLD0078	pETM14-hGBP2-Avi: *E.coli* expression vector (KanR) with hGBP2-avi	Derived from AJLV0009 and AJLD0002
AJLD0192	pCDFDuet-BirA: *E.coli* expression vector (SmR)	Derived from AJLD0042 and AJLV0038
AJLD0193	pMES4y-CA16794: C-His6-tagged Nb (Nb193) raised against dimeric GBP1	Instruct-ERIC (PID7267)
AJLD0195	pMES4y-CA16805: C-His6-tagged Nb (Nb195) raised against dimeric GBP1	Instruct-ERIC (PID7267)
AJLD0196	pMES4y-CA16802: C-His6-tagged Nb (Nb196) raised against dimeric GBP1	Instruct-ERIC (PID7267)
AJLD0202	pMES4y-CA16775: C-His6-tagged Nb (Nb202) raised against dimeric GBP1	Instruct-ERIC (PID7267)
AJLD0217	pETM14-hGBP1-LG: *E.coli* expression vector (KanR) with large GTPase domain of hGBP1	Derived from AJLD0030

3

Structural basis of membrane targeting and coatomer assembly by human GBP1

Guanylate-Binding Proteins (GBPs) are interferon-inducible guanosine triphosphate hydrolases (GTPases) that mediate immune effector functions against intracellular pathogens. A key step for the antimicrobial activity of GBPs is the formation of homo- and hetero-oligomeric complexes on the membrane of pathogen-associated compartments or cytosol-invasive bacteria. Similar to other large GTPases of the dynamin family, oligomerisation and membrane association of GBPs depend on their GTPase activity. How nucleotide binding and hydrolysis prime GBPs for membrane targeting and coatomer formation remains unclear. Here, we report the cryo-EM structure of the full-length human GBP1 dimer in its guanine nucleotide-bound state and resolve the molecular ultrastructure of GBP1 coatomer assemblies on liposomes and bacterial lipopolysaccharide membranes. We show how nucleotide binding promotes large-scale conformational changes of the middle and GTPase effector domains that expose the isoprenylated carboxyl-terminus for association with lipid membranes. Our structure reveals how the α-helical stalks of the middle domain form a parallel arrangement firmly held in a unique cross-over arrangement by intermolecular contacts between adjacent monomers. This conformation is critical for GBP1 dimers to assemble into densely packed coatomers on target membranes. The extended α-helix of the effector domain is flexible and permits intercalation into the dense lipopolysaccharide layer on the outer membrane of gram-negative bacterial pathogens. We show that nucleotide-dependent oligomerisation and GTP hydrolysis yield GBP1 membrane scaffolds with contractile abilities that promote the formation of tubular membrane protrusions and membrane fragmentation. Collectively, our data provide

This chapter is available as a preprint on *bioRxiv* (https://doi.org/10.1101/2023.03.28.534355) and has been accepted in Nature Structural & Molecular Biology. Contributions to the work have been made by Tanja Kuhm, Clémence Taisne, Cecilia de Agrela Pinto, Luca Gross, Stefan T. Huber, Evdokia A. Giannopoulou, Els Pardon, Jan Steyaert, Sander J. Tans, Arjen J. Jakobi.

a structural and mechanistic framework for interrogating the molecular basis for GBP1 effector functions in intracellular immunity.

3.1. Introduction

Robust mechanisms for recognition and elimination of microbial pathogens are essential for maintaining the integrity of mammalian organisms. These are the central tasks of the innate immune system and the humoral arm of the adaptive immune system, which cooperate to ensure that a rapid response is formed to eliminate pathogens from extracellular spaces. Yet, many clinically relevant microbes have developed strategies to breach this barrier by surviving and replicating inside host cells [1]. As a response, mammalian cells have evolved molecular machinery that elicits effector mechanisms to combat intracellular microbes at the level of individual cells [2]. These include pathogen elimination by autophagy, effector immune activation by interferon (IFN) cytokines and the activation of inflammasome complexes [3–7]. To subvert cytosolic surveillance, some intracellular pathogens co-opt the host cell endomembrane system to remain sequestered in customised pathogen-associated vacuoles [1, 8]. Other pathogens actively disrupt this compartment to replicate in the cytosol [9–11]. In either case, the machinery of cell-autonomous immunity forms the last line of defense against such pathogens.

One of the most potent effector systems in cell-autonomous immunity leads to the release of type I and type II interferon cytokines and expression of IFN-stimulated genes. Among the most strongly induced genes is a conserved superfamily of dynamin-like guanosine triphosphatases (GTPases) including the family of Guanylate-Binding Proteins (GBPs) [12, 13]. Over the past decade, GBPs have been recognised as key players in mediating host defense against intracellular vacuole-resident and cytosolic bacteria, but also parasites and viruses [14–17]. GBPs have been proposed to be recruited to the membrane of some PCVs to form sensory platforms [4, 7], affect vacuolar integrity [6, 18], or to engage with the membrane of cytosolic gram-negative bacteria and parasites directly [16, 18–21].

The human genome encodes seven GBP paralogs sharing similarities with other members of the dynamin-like GTPase superfamily that undergo guanine nucleotide-dependent oligomerisation and mediate diverse biological functions in promoting membrane fusion or fission [22]. GBPs have a high intrinsic GTPase activity for hydrolysis of guanosine-5'-triphosphate (GTP) to guanosine-5'-diphosphate (GDP) without the requirement for auxiliary GTPase activating proteins or guanine nucleotide exchange factors [23–25]. The enzymology of GBPs is unique among the dynamin superfamily in that some GBPs can also bind GDP with high affinity to produce guanosine-5'-monophosphate (GMP) [26, 27], which can affect bacterial growth and inflammamatory signaling [28]. In the absence of infection, GBPs mainly localise to the cytosol, and some associate with endogenous membranes [29]. Upon interferon induction, GBPs are recruited to and rapidly assemble into supramolecular coatomers on pathogen-enclosing compartments (PCVs) [18]. Recent studies showed that GBPs can also encapsulate cytosolic gram-negative bacteria. In this case, co-recruitment of other effectors and release of lipopolysaccharides (LPS), a glycosylated lipid component of the outer membrane of gram-negative bacteria, activate the non-canonical inflammasome pathway leading to caspase-4 dependent cleavage of gasdermin D and pyroptosis [6, 20, 21, 30]. GTPase activity-dependent GBP recruitment to endogenous, PCV or microbial membranes relies on post-translational modifications of a CaaX isoprenylation motif at the carboxyl-

terminus. Three members of the human GBP family contain CaaX motifs that lead to covalent attachment of 20-carbon geranylgeranyl (GBP2 and GBP5) or 15-carbon farnesyl moiety (GBP1) and mediate membrane association *in vivo* [29, 31]. In its nucleotide-free resting state the farnesyl moiety of GBP1 is buried in a hydrophobic pocket and requires GTP binding to be released [32]. The associated conformational changes promote accessibility of its farnesyl anchor for engagement with lipid membranes and can mediate self-oligomerisation into micellar structures in the absence of lipids [33, 34]. All reported antimicrobial functions of GBPs are critically dependent on GBP1 isoprenylation, rendering mechanistic insight into the conformational changes that facilitate physical engagement with membranes important for our understanding of their role in cytosolic host defense. In the absence of high-resolution structural data on full-length GBP1 in its activated state, or of native state structures of membrane-associated GBP assemblies, important mechanistic questions related to their mode of action remain unclear.

Here, we determined the cryo-EM structure of the full-length nucleotide-bound dimer of human GBP1. Our structure reveals large scale conformational changes of the α-helical middle domains and GTPase effector domains that stabilise the GBP1 dimer in an extended conformation suitable for association with biological membranes. In vitro biochemical analysis and electron tomography of membrane-assembled farnesylated GBP1 oligomers suggest a critical role of this conformation in GBP coatomer formation on endogenous and bacterial membranes. Importantly, we show that membrane-associated GBP1 assemblies possess GTPase-dependent membrane remodelling capacity that may underlie observations reporting GBP-dependent modulation of membrane integrity and LPS release. Our data provide a structural framework for further studies aiming at unravelling the molecular mechanism of antimicrobial and antiviral activities of GBPs.

3.2. Results

Cryo-EM structure of the GBP1 dimer

GBP1 is a multidomain protein consisting of an N-terminal large GTPase (LG) domain and a C-terminal α-helical region (C-terminal helical domain, CTHD), which can be further subdivided into a middle domain (MD; α7-α11) and an elongated C-terminal GTPase effector domain (GED; α12-α13) [Figure 3.1a] [35]. In the absence of guanine nucleotides, the GED folds back onto the MD to span the entire GBP1 molecule and makes extensive interactions with the LG domain and the MD, which are important to maintain GBP1 in the resting state. Quantitative Förster resonance energy transfer (FRET) experiments previously predicted that nucleotide binding and hydrolysis induce major rearrangements of the α-helical stalk region by liberating a latch mediating interaction of α12 with the LG domain [36]. This rearrangement results in an extended conformation that releases the C-terminal C15-farnesyl moiety required to reversibly associate with membranes. To map these conformational changes on a structural level we used cryogenic electron microscopy (cryo-EM) to solve the structure of human GBP1 bound to GDP·AlF_3, a compound assumed to represent the transition state of GTP hydrolysis [37]. Unlike the isolated LG domain that readily dimerises under several guanine nucleotide conditions [37], full-length GBP1 forms stable dimers only in the presence of GDP·AlF_3 [Figure 3.1b,c, Supplementary Data Figure 3.8]. 2D class averages of the

GDP·AlF_3-stabilised GBP1 dimer showed one predominant class [Figure 3.1d, top panel] making up 92 percent of the total particle set. Only a small subset of classes showed signatures of densities that we assigned to the α-helical stalk [Figure 3.1d, middle and lower panel]. Consistently, 3D reconstructions from this data set converged on the LG domain dimer, with no visible density for the stalks comprising MD and GED, and an angular distribution of particles that was indicative of strong preferred orientation [Supplementary Data Figure 3.9]. We hypothesised that the stalks are either highly flexible, or engage in preferential interactions at the air-water interface. To mitigate these effects, we sought to identify strategies to limit the structural heterogeneity by stabilising the extended conformation.

A novel nanobody specific for the GBP1 middle domain

We raised camelid antibodies (nanobodies) specific for human GBP1 by immunising llamas with recombinant GBP1. We then constructed a phage display library from mRNA isolated from peripheral lymphocytes [38] and selected nanobodies specific for GBP1 by panning, which were confirmed by ELISA using immobilised GBP1. We next tested a subset of nanobodies from different complementarity-determining region (CDR) clusters on their ability to bind the GDP·AlF_3-stabilised GBP1 dimer using SEC-MALS and mass photometry. Of several candidates, we selected one nanobody (Nb74) that bound both GBP1 monomers and dimers in an apparent 1:1 molar ratio [Figure 3.1e, Supplementary Data Figure 3.10, Supplementary Table 3.2]. To confirm whether Nb74 binds the extended stalk, we acquired cryo-EM micrographs of GDP·AlF_3 stabilised GBP1 dimer in the presence of Nb74. 2D class averages revealed pronounced density protruding from the LG dimer, suggestive of better preservation of the α-helical stalk in this sample. Several 2D classes also showed additional density in close proximity to the MD, indicating that Nb74 selectively binds the α-helical region in the extended conformation [Figure 3.1f-g].

Large conformational changes induce a cross-over arrangement of the MDs in nucleotide-bound GBP1

We next determined the 3D structure of Nb74-bound GBP1 dimers in complex with GDP·AlF_3, yielding a pseudo-C2 symmetric 3D reconstruction at a nominal resolution of 3.7 Å [Figure 3.1h-i, Supplementary Data Figure 3.11]. We found better resolved density in the stalk region when not imposing C2 symmetry, suggesting some residual structural flexibility of the MD and GED in the dimer which was supported by local resolution analysis and flexible refinement [Supplementary Data Figure 3.11, Figure 3.12 and Supplementary Data Movie SM1].

GBP1 associates into dimers via the LG domains, with additional contacts formed between the MDs. The Nb74 nanobody binds the MD at the junction formed by helices α7-8 and α10-11 [Figure 3.1h]. In the dimer the MDs form a cross-over arrangement in which the linker regions Gly^{307}- Val^{316} connecting LG domain and MD cross each other, such that the MDs associate with the LG domain of the respective pairing monomer and extend in parallel from the LG dimer. The GED (residues 481-592) is likely flexible and not visible in our structure. The LG dimer interface is stabilised by a large contact surface formed across the A-face of the GTPase domain, induced by cross-monomer coor-

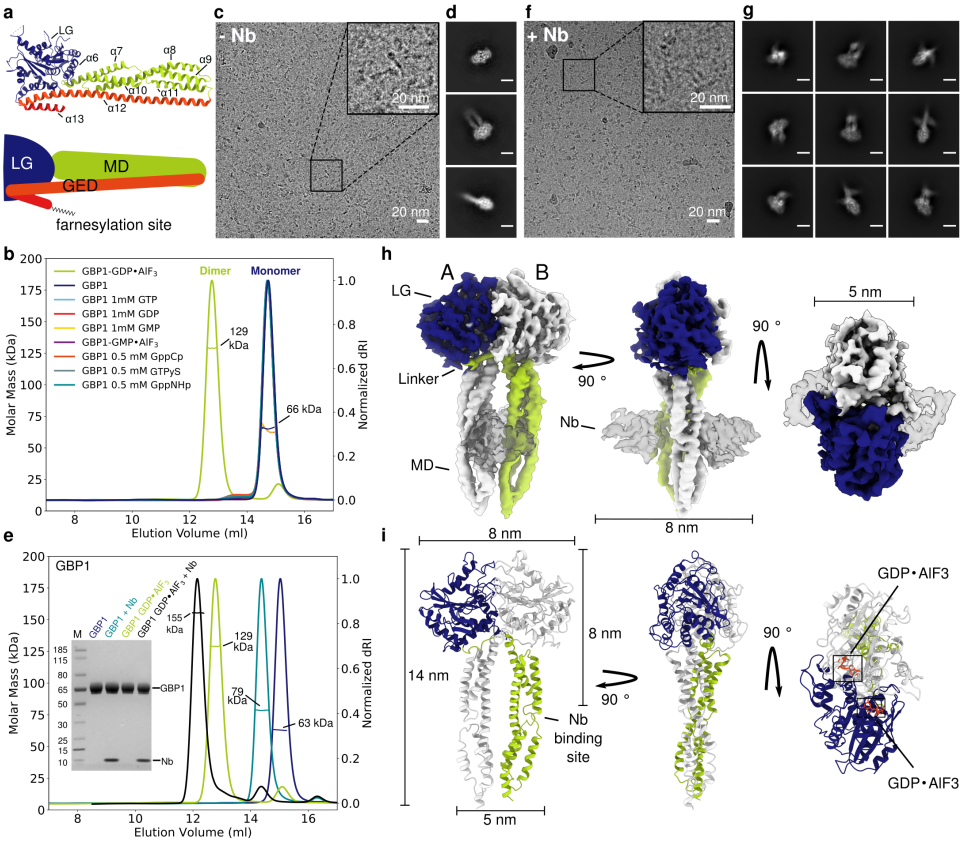

Figure 3.1: Cryo-EM structure of the GDP·AlF$_3$ stabilised GBP1 dimer. (a) Atomic model of monomeric GBP1 (PDB ID 1dg3) in cartoon representation alongside a schematic representation displaying the domain architecture. LG: Large GTPase domain (blue), MD: Middle domain (green), GED: GTPase effector domain (orange and red). Individual α-helices in the MD and GED are numbered sequentially. (b) Size-exclusion chromatogram and multi-angle laser light scattering (SEC-MALS) analysis of GBP1 with different nucleotides. GBP1 appears monomeric on SEC-MALS in the presence of GTP, GDP, GMP, GMP·AlF$_3$, GppCp, GTPγS or GppNHp, while a dimer peak emerges in the presence of GDP·AlF$_3$. The experimentally determined molecular weight is plotted across the chromatographic peak and is reported in kDa. (c) Representative cryo-EM micrograph and (d) 2D class averages of GBP1-GDP·AlF$_3$. Scale bar in (d) is 5 nm. (e) Size-exclusion chromatogram and MALS analysis of recombinant GBP1:Nb74 complex in the presence and absence of GDP·AlF$_3$. An SDS-PAGE analysis of peak fractions is also shown (molecular marker in leftmost lane, in kDa). (f) Cryo-EM micrograph and (g) 2D class averages of GBP1-GDP·AlF$_3$-Nb74 (scale bar 5 nm). (h) 3D cryo-EM density map of the GDP·AlF$_3$-stabilised GBP1-dimer bound to Nb74. (i) Refined atomic model of the GBP1-dimer as derived from fitting into the cryo-EM density in (h). The nucleotide binding sites located at the LG dimer interface are highlighted in orange.

dination of the GDP·AlF_3 ligand [Supplementary Data Figure 3.13] and is consistent with crystal structures of the nucleotide-bound LG domain dimer [37]. The conformational change induced by nucleotide binding leads to partial unraveling of the C-terminal part of helix α6 (Ile^{304}-Ser^{306}) and the N-terminal end of helix α7 (Cys^{310} - Val^{316}) to form the linker region of the domain cross-over in which the MD swings out to form a new interface with the respective pairing monomer in the GBP1 dimer [Figure 3.2a-d]. This interface is primarily formed by a hydrophobic patch between the LG domain of one monomer and an aliphatic stretch of residues at the C-terminal end of the linker region and helix α7 (residues Ala^{315} - Ile^{322}) in the other monomer [Figure 3.2c,d]. While the MDs undergo a large spatial transformation relative to the resting state, their overall conformation of helices α7-α11 remains essentially unchanged with a root mean square deviation (r.m.s.d) of 2.03 Å relative to the nucleotide-free resting state after superimposing Cα atoms of the MD (residues 327-481). The parallel arrangement of the MD is stabilised by a series of charged residues along helices α9-α11 that form an electrostatic zipper across the protruding stalks [Supplementary Data Figure 3.14]. Towards the C-terminal end of the MD, helices α11 of both monomers come into close proximity and form an additional contact site. While the EM density at this location was not of sufficient quality to identify individual interactions contributing to this interface, it appears

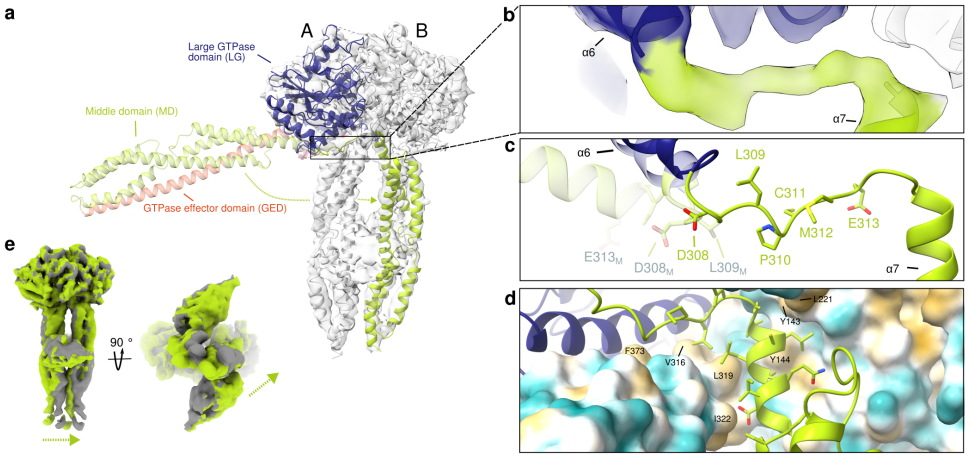

Figure 3.2: Structural details of the GDP·AlF_3 stabilised GBP1 dimer. (a) The full-length nucleotide-free GBP1 monomer (pale colours; PDB ID 1dg3) is superposed onto one of the monomers in the GDP·AlF_3 stabilised GBP1 dimer (bright colours) by least-squares superposition of their LG domains. Dimer formation involves a large conformational rearrangement in which the α-helical MDs swing across each other to form a parallel arrangement protruding from the LG domains. (b-d) Close-up of the cross-over region (in cartoon representation, superposed on the EM density) formed by a linker region Gly^{307}-Val^{316} originating from partially unravelled helices α6 and α7. (c) Residues 307–316 which are part of a linker connecting α6 and α7 need to flip by 180° when changing from the monomer into the dimer conformation. Relevant residues in the nucleotide-free conformation are labelled in grey. (d) The dimer conformation is stabilised by a hydrophobic pocket formed by residues located on α3, α4' and α7 (highlighted in yellow), interacting with an aliphatic stretch encompassing residues Ala^{315}–Ile^{322} on helix α7 of the second monomer. (e) Flexibility of the α-helical MD, visualised through flexible refinement. End points of the density morph along one exemplary latent space dimension are displayed (green and gray densities). The arrow indicates the direction of movement.

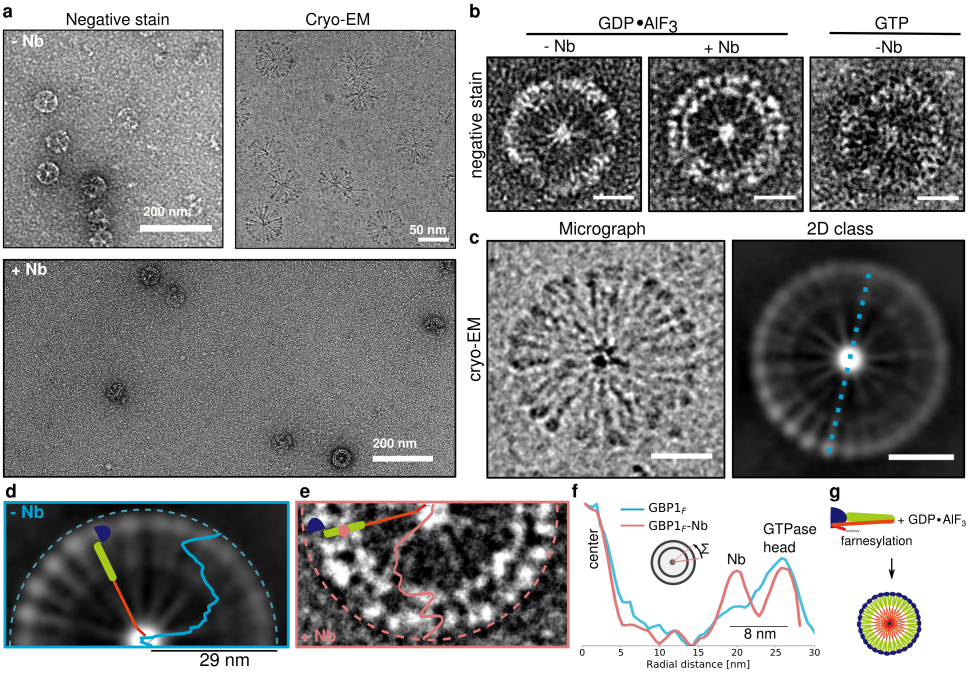

Figure 3.3: Micellar self-assembly by GBP1$_F$-GDP·AlF$_3$ (a) Negative stain images (top left) and cryo EM images (top right) of GBP1$_F$-GDP·AlF$_3$ as well as negative stain images of GBP1$_F$-GDP·AlF$_3$ with Nb74 (bottom) showing abundant formation of flower-like GBP1 micelles. (b) Close-up of individual GBP1$_F$-GDP·AlF$_3$ micelles formed by GBP1$_F$ alone or in the presence of Nb74 (GBP1$_F$:Nb74). A GBP1$_F$ micelle formed in the presence of GTP is also shown (scale bar 20 nm). (c) Close-up of a cryo-EM micrograph with a GBP1$_F$-GDP·AlF$_3$ flower showing discernible repetitive elements (left panel). Cryo-EM 2D class average of GBP1 micelles (right panel) highlighting spherical densities at the perimeter and spokes pointing towards the particle center (scale bar 20 nm). (d-e) Radially averaged intensity profiles of GBP1 micelles plotted on top of a cryo-EM 2D class average of GBP1$_F$-GDP·AlF$_3$ micelle (top panel) or on top of a negative stain image of a GBP1$_F$-GDP·AlF$_3$ micelle formed with Nb74. A second ring of globular density is visible at 8 nm distance from the perimeter. (f) Schematic representation of GBP1$_F$-GDP·AlF$_3$ micelle formation.

to provide additional stabilisation to the pseudo-symmetric parallel MD arrangement. This interpretation is supported by 3D flexible refinement [Figure 3.2e, Supplementary Data movie SM1], which shows that both MDs undergo concerted motion relative to the LG domains. Close inspection of the EM map revealed additional weak density interspersed between helix α3 and α3' in the LG domain, and protruding beyond the apical end of the MD. To visualise these map regions, we used a model-independent implementation of local density sharpening [39, 40] to improve scaling of weak densities relative to the better resolved parts. This allowed tracing the α3-α3' loop (residues 156-167) [Supplementary Data Figure 3.15a]. In addition, we observed tubular density protruding from helices α11, which likely corresponds to the N-terminal end of the flexible helices α12 of the GEDs [Supplementary Data Figure 3.15a,b].

Farnesylated GBP1 forms micellar structures upon nucleotide binding

Our structure of the GDP·AlF_3-stabilised dimer was obtained with recombinant protein devoid of the farnesyl modification at the C-terminal CTIS motif normally required for association with membranes [41]. In our structure, the MDs point away from the LG domains as parallel stalks, compatible with a model in which nucleotide binding primes both farnesyl anchors to insert into the membrane. To test this hypothesis, we co-expressed GBP1 together with the human farnesyl transferase machinery to purify natively farnesylated GBP1 ($GBP1_F$). Unexpectedly, size-exclusion chromatography of $GBP1_F$ in the presence of GDP·AlF_3 did not yield GBP1 dimers as observed for unmodified GBP1 [Figure 3.1b]. Instead, in a subset of our SEC-MALS experiments we noted an additional peak corresponding to higher molecular weight species [Supplementary Data Figure 3.10]. Negative stain imaging of this peak fraction revealed circular particles of 58 nm diameter, reminiscent of flowers consisting of discernible petals with a dense spherical perimeter and spoke-like protrusions towards the particle center [Figure 3.3a,b]. These structures are consistent with previous observations [33] and were present in higher occurrences if no size-exclusion separation was performed before the imaging experiments.

To test whether these structures are exclusively formed with transition-state stabilised GBP1 or more generally occur with actively hydrolysing GBP1, we also prepared samples in the presence of GTP and observed equivalent particles [Figure 3.3b] albeit at lower occurrence and requiring higher $GBP1_F$ concentrations. To gain more insight into the molecular architecture of these homo-oligomeric assemblies, we prepared cryo-EM samples of $GBP1_F$ in the presence of GDP·AlF_3 [Supplementary Data Figure 3.16] and performed 2D class averaging [Figure 3.3a,c]. Additional electron cryotomograms of $GBP1_F$ micelles revealed that these are 3D micelles and not 2D disc-like structures [Supplementary Data Figure 3.17, Supplementary Data Movie SM3]. The GBP1 assemblies in these tomograms and the 2D averages appear highly ordered. The increased detail of cryo-EM micrographs of individual flower-like particles allowed us to discern spherical densities at the particle periphery connected to spokes that extend radially towards the center. We ascribe the spherical densities (4.5 nm ± 0.7 nm in diameter, n = 50) to the LG domains and the spokes to the α-helical stalks. We next quantified the dimension of the observed structures to correlate the observed features to our high-resolution model of the GBP1-dimer. If two oppositely oriented GBP1 dimers assemble through interactions at the C-terminus of their respective MDs, the resulting assembly is expected to span 28 nm [see Figure Figure 3.1i].

Instead, we found the rim-to-rim diameter of the assemblies to be 58.1 nm ± 1.2 nm (n = 33), suggesting that additional structural elements need to make up the remaining distance. To map the location of the MD within the flower-like assembly, we incubated $GBP1_F$ with GDP·AlF_3 in the presence of Nb74. Negative stain images of this sample contained flower-like particles that contained an additional spherical density at approximately 8 nm radial distance to the peripheral LG domain [Figure 3.3d-f]. This estimate is in agreement with the relative distance of Nb74 bound to the MD and the LG domain as determined in our cryo-EM structure of the Nb74-bound GBP1 dimer [Figure 3.1h-i]. The overall particle radius of 29 nm is consistent with a GBP1 containing a fully unlatched α12 helix [compare Figure 3.1a,i]. This leads us to conclude that the remaining

density of the petal towards the particle center must originate from the C-terminal part of the MD and the GED. The particle center in both negative stain (5.6 nm ± 0.8 nm in diameter (n=27)) and cryo-EM micrographs (6.3 nm ± 1.1 nm in diameter (n=22)) displays higher contrast than the peripheral LG domain and MD/GED spokes of the petal. Since the diameter of the particles is incompatible with a fully extended conformation of the entire GED, we hypothesise that this density corresponds to a cluster of α13 helices of the GED and the exposed farnesyl anchors [Figure 3.3g].

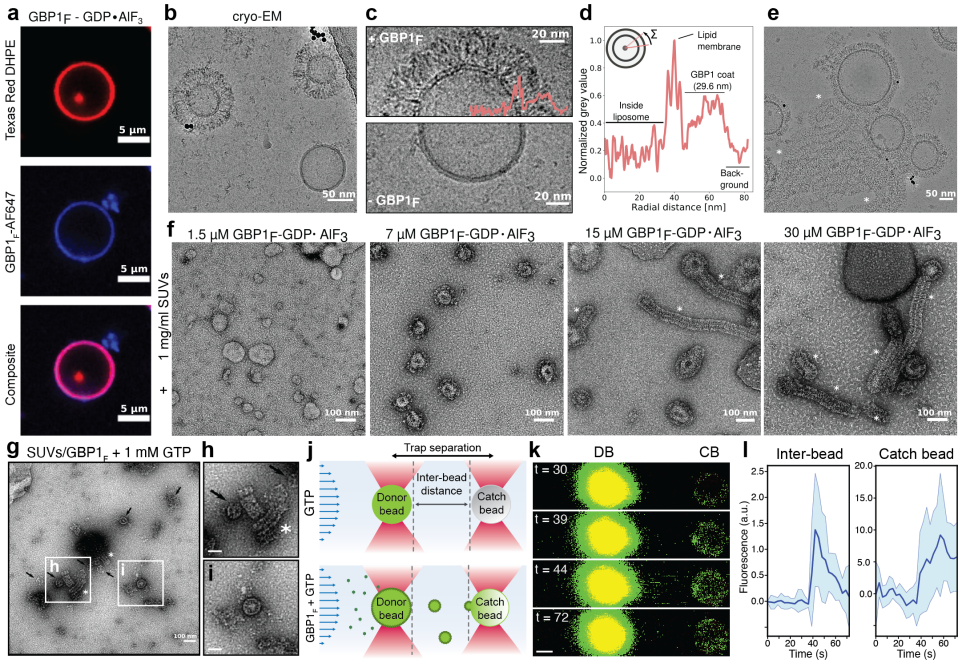

Figure 3.4: Coatomer formation and membrane remodeling capability of GBP1. (a) Confocal fluorescence imaging of Alexa647-labelled GBP1$_F$ binding to DHPE-texas red-labelled BPLE GUVs in the presence of GDP·AlF$_3$. (b) Cryo-EM micrograph of GBP1$_F$-GDP·AlF$_3$ binding to BPLE liposomes. (c) Close-up of BPLE SUVs with or without GBP1$_F$-GDP·AlF$_3$ coat. (d) Radially averaged intensity profile across a GBP1$_F$-coated SUV (e) Cryo-EM micrographs of tubular protrusions (asterisks) formed on GBP1-coated SUVs. (f) GBP1 coatomer formation is concentration dependent. A visible coat starts to form at GBP1$_F$ concentrations of 7 µM. At a concentration of 15 µM and higher, GBP1-coated tubular protrusions (asterisk) become visible and are the dominant structures at concentrations exceeding 30 µM. (g-i) In the presence of GTP, GBP1$_F$ remodels SUVs into spherical micelles (arrows) and short filaments (asterisks). Scale bar in (h-i): 50 nm. (j) Dual-trap membrane fragmentation assay: A donor bead coated with rhodamine 6G-labeled membrane is held in place by an optical trap in a flow cell operating at constant pressure. A second, uncoated "catch" bead is held in an additional optical trap at 6 µm distance of the donor bead. Lower panel: GBP1$_F$-dependent membrane scission/fragmentation would result in membrane transfer from the bead-supported donor membrane to the catch bead. The schematic transfer of membrane vesicles is shown for illustrative purposes only and the precise structure of membrane fragments and GBP1$_F$ scaffold is unclear. (k) Representative confocal fluorescence images illustrating GBP1$_F$-dependent lipid transfer from the donor bead (DB) to the catch bead (CB). Scale bar: 1 µm. (l) Integrated fluorescence intensity time traces of the inter-bead space and the catch bead in the presence of GBP1$_F$ and GTP. Solid lines represent mean fluorescence intensities of 18 experiments and shaded areas represent 95% confidence intervals.

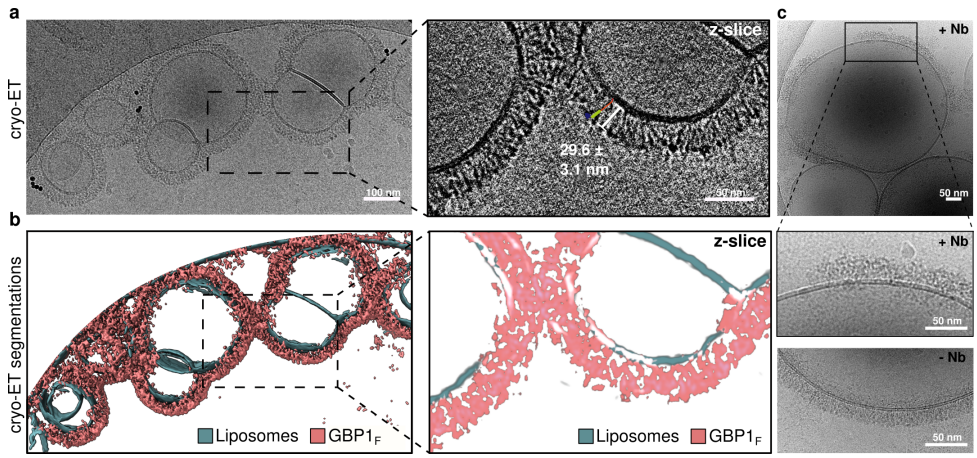

Figure 3.5: Electron cryo-tomography of GBP1 coatomers (a) Electron cryo-tomogram of GBP1-coated liposomes. Projected z-stack of reconstructed tomogram and close-up of an individual z-slice showing discernible repetitive subunits. (b) Segmented tomogram from (a); GBP1: pink, membranes: green. (c) Cryo-EM micrograph of $GBP1_F$-coated liposomes in the presence of Nb74. The close-up shows a comparison to $GBP1_F$-coated liposomes in the absence of Nb74 (lower panel). The presence of Nb74 results in only partially coated liposomes with a higher degree of structural disorder.

$GBP1_F$ forms dense coatomers on liposomes and scaffolds tubular membrane protrusions

Fluorescently labelled $GBP1_F$ ($GBP1_F$-Q577C-AF647) uniformly stains brain polar lipid extract (BPLE)-derived giant unilamellar vesicles (GUVs), suggesting homogeneous GBP1 coverage based on fluorescence [Figure 3.4a]. To determine at the structural level if the GBP1 conformation observed in the lipid-free $GBP1_F$ micelles is relevant for GBP1 association with membranes, we mixed BPLE-derived small unilamellar vesicles (SUVs) with $GBP1_F$-GDP·AlF_3 or $GBP1_F$-GTP for TEM analysis. Cryo-EM micrographs of these samples showed SUVs densely covered with a proteinaceous coat of 29.6 nm (± 3.1 nm, n=47) radial extension [Figure 3.4b-d], consistent with the dimensions of the extended $GBP1_F$ conformation observed in the lipid-free GBP1 micelles. Strikingly, we observe either fully coated SUVs or SUVs devoid of any GBP1 coat [Figure 3.4b,c], suggesting that cooperativity in membrane association may affect efficacy of GBP1 coating potential. On a subset of SUVs, we observed extended tubular protrusions of 59.8 nm (± 2.4 nm, n=37) diameter scaffolded by GBP1 in an arrangement indistinguishable from that on spherical liposomes at the level of detail discernible from these images. Cryo-EM micrographs of such structures in unsupported ice revealed these protrusions to be highly flexible [Figure 3.4e], precluding 2D averaging. The formation of protrusions was highly concentration dependent, transitioning from uniformly coated SUVs to scaffolded tubule extrusion beyond a certain threshold concentration [Figure 3.4f]. 2D class averages and associated power spectra of negatively stained protrusions show repetitive features that are consistent with overall dimensions of laterally associated GBP1 molecules [Supplementary Figure 3.18, Figure 3.1i]. The micrographs did not allow us to uniquely discrim-

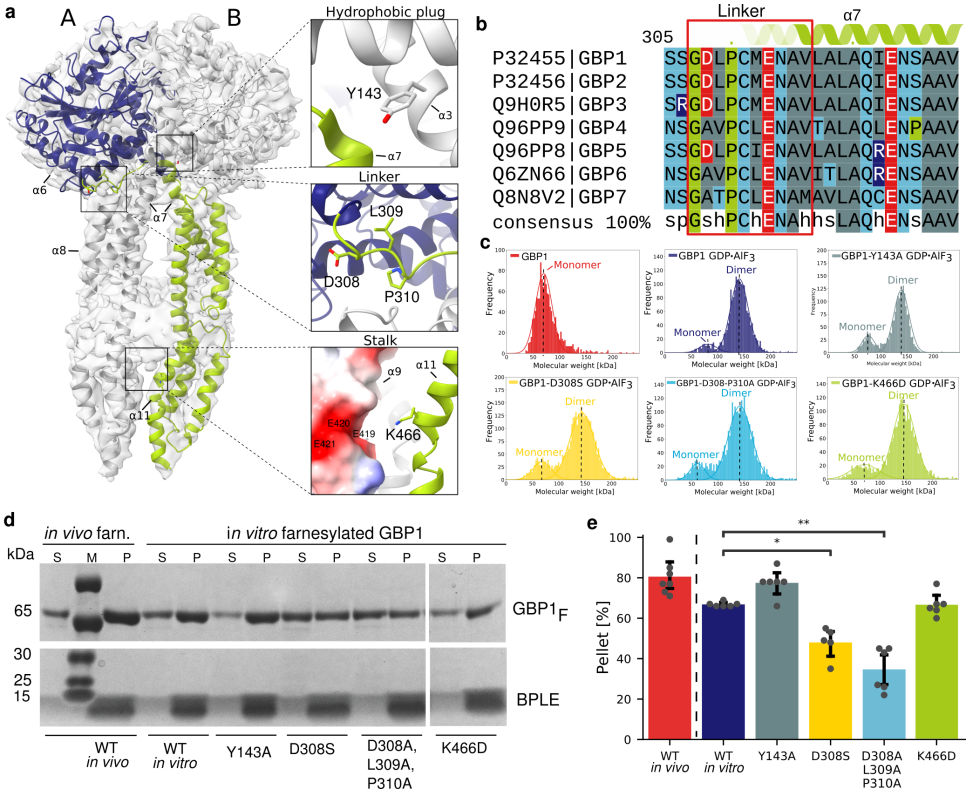

Figure 3.6: Effect of GBP1 variants on membrane association. (a) Schematic overview of the GBP1 dimer highlighting individual point mutation sites of tested variants. (b) Multiple sequence alignment of all human GBP paralogs zooming in on the linker region (307-316) between α6 and α7. The overall linker region is highly conserved; D308 is conserved across all GBPs containing prenylation motifs (+GBP3). (c) Mass photometry spectra of nucleotide-free GBP1, GBP1-GDP·AlF_3 and GDP·AlF_3-stabilised GBP1 variants. The determined molecular weights are indicated and show that the point mutations did not affect the ability of the GBP1 variants to dimerise. (d) Representative SDS-PAGE analysis of co-sedimentation assay of $GBP1_F$ variants with BPLE liposomes. S: Supernatant, P: Pellet (e) Quantitative analysis of the co-sedimentation assay. The sum of densitometric intensities of protein in the pellet and supernatant fractions was used to determine the relative percentage of GBP1 in each fraction. The mean intensity and standard deviation are displayed. Statistical significance was determined using Welch's t-test with Bonferroni correction (*: P≤ 0.05; **: P≤ 0.01)

inate whether the protrusions contain membrane or are formed by excess GBP1 through aggregation of exposed farnesyl anchors similar to GBP1 micelle formation. To test these possibilities we also performed concentration series experiments with $GBP1_F$ in the absence of lipids. Under these conditions, we observed increased formation of micellar assemblies but no formation of tubular structures, suggesting that tubule formation by GBP1 involves extrusion of membrane material [Supplementary Data Figure 3.19].

GTP hydrolysis promotes GBP1-dependent membrane fragmentation

We next tested whether GBP1 scaffolding of membrane protrusions persists in conditions that allow active GTP turnover. Importantly, for conditions containing GTP we exclusively observe short tubular membrane stubs scaffolded by a GBP1 coat while coated SUVs were absent in our micrographs, suggesting that GTP hydrolysis drives GBP1-dependent scission or fragmentation of liposomes [Figure 3.4g-i, Figure 3.21]. Consistent with the higher GBP1 concentrations required for formation of micelllar assemblies in the absence of lipids, we observed weaker binding to GUVs for equimolar levels of GBP_F in the presence of GTP compared to GDP·AlF_3 [Figure 3.4a, Supplementary Data Figure 3.20], providing additional support for a threshold-dependent activity of GBP1.

To probe the consequences of GTP-dependent GBP1 coatomer formation on membranes in real time, we made use of a dual-trap optical tweezer assay coupled to confocal fluorescence imaging. Two 2 µm silica beads were held in optical traps at 6 µm trap separation within a laminar flow cell operated at constant pressure. One bead coated with a bilayer membrane containing rhodamine 6G-labelled lipids served as a membrane donor, whereas the second uncoated "catch" bead served to sequester lipid material released from the donor bead [Figure 3.4j]. We monitored lipid transfer from the donor bead to the catch bead via fluorescence using confocal microscopy [Figure 3.4k, Supplementary Data Movie SM2]. In the absence of $GBP1_F$, fluorescence in the inter-bead space and on the catch bead remained at constant baseline level [Figure 3.4l]. We then dispensed $GBP1_F$ into the flow channel in close proximity to the donor bead and in the presence of GTP. If GTP-dependent membrane scaffolding by $GBP1_F$ results in membrane fragmentation/ scission, membrane fragments released from the donor bead will be sequestered by the catch bead under continuous flow. Indeed, we found lipid fluorescence in the inter-bead space and on the catch bead to increase ~2-fold and ~7-fold, respectively, approximately 30 seconds after addition of $GBP1_F$ (n=18) [Figure 3.4l]. This suggests that lipid material is released from the donor bead in a $GBP1_F$-dependent manner. Altogether our data indicate that GBP1 scaffolding can promote severing of bilayer membranes and lipid release under conditions that permit GTP hydrolysis.

In tomographic reconstructions of GBP1 assemblies on SUVs we observe that GBP1 covers the entire SUV by assembling into three-dimensional coatomers, which appear to be stabilised by tight lateral association of GBP1 subunits [Figure 3.5a-b, Supplementary Data Movie SM3 and SM4]. The partially regular appearance of the GBP1 coat in individual z-slices from these tomograms is indicative of short range order of the GBP1 coat, and appears to be mediated primarily via interactions of adjacent LG domains.

To test this hypothesis, we also acquired cryo-EM micrographs of GBP1-coated SUVs in the presence of Nb74, which through its interactions with the MD domain may sterically affect the lateral association of GBP1 dimers in a dense coatomer [Figure 3.1h,i]. Indeed, for these conditions we frequently observed SUVs that were only partially coated and showed signs of structural disorder in the protein coat [Figure 3.5c], supporting an important role of an unperturbed GBP1 dimer conformation in coatomer assembly.

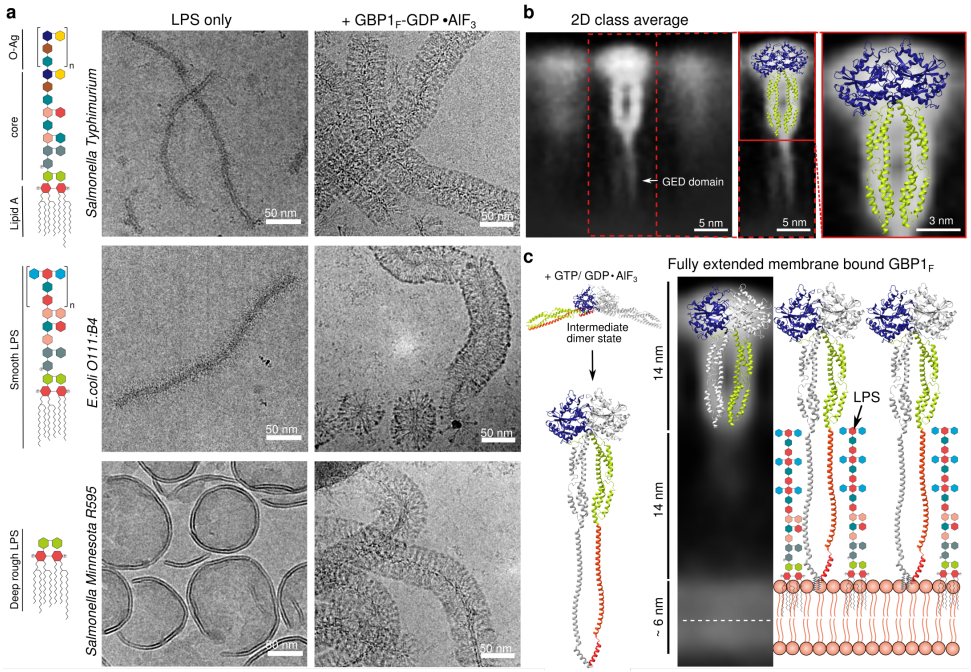

Figure 3.7: GBP1$_F$ coat formation on LPS micelles of bacterial pathogens (a) Schematic representation of complex O-antigen containing LPS molecules from *S. enterica* sv. Typhimurium, smooth LPS *E.coli* O111:B4 and deep rough LPS from *S. enterica* sv. Minnesota R595 (green: 2-keto-3-deoxyoctonic acid; grey: L-glycerol-D-manno-heptose; blue-green: galactose; pink: glucose; red: 2-amino-2-deoxyglucose; light blue: Colitose; brown: Rhamnose, yellow: Abequose, darkblue: Mannose). Cryo-EM micrographs of the three types of LPS in the absence (left column) and presence of GBP1$_F$-GDP·AlF$_3$ (right column). (b) Selected 2D class average of GBP1$_F$ bound to *E.coli* O111:B4 LPS. Leftmost panels: The extended GEDs projecting toward the membrane surface are visible in the average (white arrow). The atomic model of the GDP·AlF$_3$-stabilised GBP1 dimer is superposed onto the projected density. (c) Schematic of nucleotide-dependent activation of GBP1 for membrane binding. Hypothetical encounter complex for initial dimerisation (based on PDB ID 1dg3/2b92), formation of the cross-over conformation of GBP1 dimers upon nucleotide binding with extended GED, and 1D model of the GBP1 coatomer on membranes. The radial extension of O-antigen containing LPS is shown for comparison.

The cross-over conformation of the GBP1 dimer is critical for membrane association

We next asked whether the cross-over arrangement of the nucleotide-activated GBP1 dimer is required for membrane association. To test this hypothesis, we sought to identify mutants that disrupt the interfaces stabilising this extended conformation but retain the ability to form dimers by association through the LG domains. First, we analysed sequence conservation in the α6-α7 region forming the loop structure in the cross-over conformation, the MD-LG interface, the electrostatic zipper motif and the C-terminal contact site of the MD, and designed point mutants to weaken conserved motifs and interactions [Figure 3.6a-b; Supplementary Data Figure 3.22 and Figure 3.23]. The main interface in the GBP1 dimer is formed between the LG domains of both monomers, con-

tributing 2138 Å^2 (62%) of the total buried surface area of the dimer interface as inferred from our structure. We therefore expected the different variants to retain their ability to form dimers via the LG domain and to perform GTP hydrolysis [Figure 3.6c, Supplementary Data Figure 3.24], but to possibly disrupt the parallel arrangement of the MDs and affect the conformation-dependent ability of GBP1 to associate with membranes. To test this hypothesis, we mixed brain polar lipid extract SUVs with GBP1$_F$ variants activated by GDP·AlF$_3$ and performed co-sedimentation assays followed by quantitative SDS-PAGE analysis of pellet and supernatant fractions. Of four variants tested, two mutants in the cross-over region showed a 33% (D308S; p<0.05) and 44% (D308S/L309A/-P310A; p<0.01) reduction in the membrane-bound fraction compared to the WT control [Figure 3.6d-e]. These bulk observations are supported by negative stain imaging of SUVs incubated with the two GBP1 variants [Supplementary Data Figure 3.25], showing substantially decreased coatomer formation on individual SUVs but no complete disruption. For variants affecting the LG-MD and MD-MD interface we found no significant effect [Figure 3.6e, Supplementary Data Figure 3.26], suggesting that the ability to form the cross-over arrangement is a determining factor for efficient membrane recruitment of GBP1.

GBP1 dimers form the essential unit of GBP coatomers on LPS micelles

Apart from targeting intracellular membranes, GBP1 has been reported to directly associate with lipopolysaccharides (LPS), a glycosylated lipid component of the outer membrane in gram-negative bacteria. LPS consists of a lipid A moiety mediating the integration in the membrane leaflet, a core region of non-repetitive oligosaccharides and the O-antigen consisting of an extended and branched chain of repetitive oligosaccharides. The LPS composition can vary greatly between bacterial strains.

To determine whether GBP1 coatomer formation is dependent on the specific oligosaccharide structure of LPS, we incubated nucleotide-activated GBP1$_F$ with three different LPS chemotypes from bacterial pathogens differing in the presence of inner and outer core sugars and O-antigen components; *Salmonella Typhimurium* LPS containing extended O-antigen (LPS-ST), smooth LPS from *Escherichia coli* O111:B4 (LPS-EB) and deep rough LPS from *S. enterica* sv. Minnesota R595 consisting of only the lipid A core [Figure 3.7a]. Outer-core and O-Ag containing LPS forms elongated bilamellar micelles, whereas deep rough LPS displays semi-vesicular morphology. For all three cases we observe formation of dense and elongated GBP1 coatomers on remodelled LPS micelles, extending ~28 nm from the central lipid bilayer and sandwiching a parallel layer of continuous density with ~5-7 nm cross-section, compatible with the estimated thickness of a micellar bilayer and fuzzy contributions of oligosaccharide residues [Figure 3.7a]. These dimensions are in agreement with those determined from GBP1 coatomers on brain polar lipid SUVs, suggesting the overall modes of assembly in these coatomers are equivalent. As GBP1 forms equivalent coatomers on all LPS forms tested, we conclude that the primary association with LPS membranes is mediated by insertion of the C-terminal farnesyl anchor in the lipid layer, but our image data preclude quantitative conclusions on potential affinity differences for certain types of LPS over others. Analogous to micellar GBP1 assemblies and coatomers on lipid SUVs that we use as model system for endogenous membranes, the coat on LPS micelles appears highly ordered with

GBP1 molecules assembling in register as concluded from side and top views of coated LPS micelles [Supplementary Data Figure 3.27]. To analyse the detailed mode of GBP1 assembly within the coatomers, we performed 2D class averaging of individual rims of GBP1-coated LPS micelles [Figure 3.7b]. 2D class averages of the GBP1 coat revealed low-resolution densities compatible with our high-resolution GBP1 dimer structure viewed in projection, suggesting that GBP1 dimers form the repeating unit in mature coatomers. In some of the classes, we also observed rod-like density extending from the MD towards the LPS lipid surface, supporting a model in which an extended α12 of the GED reaches out for association with the membrane [Figure 3.7b].

Together, our results support a model in which nucleotide binding by GBP1 unlatches the C-terminal all-α-helical MD and GED from the LG domain, leading to a swing-like conformational transition of the MD that re-associates with the LG of the adjacent monomer and forms a parallel arrangement of extended GEDs for association with membranes [Figure 3.7c]. Interestingly, the dimensions of an extended GED are compatible with the lateral dimensions of extended bacterial LPS O-antigen (LPS-ST: 10.3 ± 3 nm, (n=23), LPS-EB: 13.1 ± 2.1 nm (n=11), both measured in negative stain-EM), suggesting that these may be a functional adaption to allow intercalation between the dense O-antigen and core oligosaccharide decoration of the LPS layer and coatomer formation on LPS-containing membranes.

3.3. Discussion

GBPs have recently emerged as important effector molecules in cell-autonomous immunity against intracellular bacteria, and GBP1 forms the central organising unit of this cellular response. The main antimicrobial function of GBP1 has been ascribed to its ability to coat the membrane of pathogen-containing compartments or the outer membrane of gram-negative cytosolic bacteria, where it appears to form a multivalent signaling platform for the activation of the non-canonical inflammasome [16, 17, 20, 21]. Coat formation is dependent on nucleotide binding and self-assembly of GBP1. While the functional consequences for GBP1 in intracellular immunity have been firmly established by these studies, the mechanistic underpinnings of these functions remain currently unclear.

Our cryo-EM and cryo-ET data show that the ultrastructure of GBP1 coatomers on lipid and LPS membranes consists of ordered arrays of GBP1 dimers with their α-helical MDs and GEDs protruding in parallel towards the membrane surface. The molecular envelope of the repeating unit that we infer from these data is consistent with our high-resolution cryo-EM structure of the full-length GDP·AlF_3-stabilised GBP1 dimer, displaying a cross-over arrangement of the MD and extended GEDs anchored to the membrane. We found membrane association of GBP1 to be critically dependent on the ability to form cross-over dimers. This cross-over conformation GBP1 is consistent with a recent crystallographic structure of a truncated GBP5 dimer [42] and resembles that of atlastins [43], which are related but functionally different members of the dynamin-like protein (DLP) superfamily of large membrane-associated GTPases. Interestingly, GBPs and atlastins appear to share a set of key structural features stabilising this conformation: a conserved linker region that mediates the MD cross-over, an extended hydrophobic interaction region that latches the MD onto the LG domain of the opposing monomer,

and a series of weak interactions holding together the C-terminal α-helices of the MD. While the atlastins and other dynamin-like proteins associate with membranes through C-terminal amphipathic helices, GBPs are unique among the DLPs in the requirement of isoprenylation for membrane binding. Another distinguishing feature of GBPs is the long, extended α-helical effector domain. While the LG domains and MDs of the GBP1 dimer unit appear rigid, the GED appears to exhibit substantial flexibility. Our data provide important clues for these specialisations. Assembling densely packed coatomers on outer membranes of gram-negative bacteria spiked with extended LPS oligosaccharide chains requires elongated flexible elements that can intercalate between the O-antigen of complex LPS cores. Intriguingly, the dimensions of the extended GED are consistent with the estimated length of LPS chains with extended O-antigen [44], suggesting that the isoprenylated GEDs can act as flexible anchors that allow GBP1 to breach the LPS permeability barrier and assemble densely packed coatomers that are stabilised through interactions between the LG domains of neighbouring dimers.

We found GBP1 coat formation to occur in an all-or-none fashion, with the fraction of coated liposomes strongly dependent on GBP1 concentration. This indicates that coatomer formation is a cooperative process, where successful formation of a GBP coat is dependent on a critical threshold concentration. Cooperativity is a hallmark of processes that require a sharp transition in their biological response, for example by digital activation. The antimicrobial function of GBPs is induced through activation of the interferon pathway that massively upregulates expression of interferon-stimulated genes (ISGs). Interestingly, GBPs are among the most strongly induced ISGs, with basal transcription levels elevated up to three orders of magnitude upon interferon induction [12, 45]. A thresholded response to self-assembly may provide GBPs with the ability to prevent coating of intracellular membranes at cellular concentrations under homeostatic conditions and to only activate this function in the presence of infection.

Several recent studies linked GBP1 coatomer formation to the activation of the non-canonical inflammasome pathway, involving recruitment of caspase-4 to the GBP coat and induction of inflammatory cell death (pyroptosis) [16, 20, 21]. Pyroptosis is dependent on cleavage of gasdermin D by caspase-4, which in turn is activated by binding to the lipid A component of LPS [46, 47]. Caspase-4 dependent pyroptosis is abrogated in the absence of GBP1, suggesting that caspase-4 cannot bind lipid A on bacterial outer membranes by itself. How does GBP1 facilitate access to lipid A components? Our data show that high GBP1 concentrations lead to tubulation of lipid membranes and LPS micelles, indicating that GBP1 has membrane remodelling activity. The tip of membrane tubules forms a region of maximum curvature, which could facilitate access to the membrane-embedded acyl chains of lipid A otherwise shielded by the dense oligosaccharide chains of LPS and therefore inaccessible to the ligand-binding CARD domain of caspase-4. A recent study reporting tomographic data on GBP1 coatomer suggested the coat consists of GBP1 monomers [48], which is inconsistent with the GBP1 dimer units observed in our cryo-EM and cryo-ET data reported here and with previous biochemical studies that established homodimer formation as a prerequisite for membrane association of GBP1 [34]. Interestingly, LPS and GBP1-dependent retrieval of caspase-4 in cellular pull-downs requires GDP-AlFx [21], confirming the functional relevance of the GBP1 dimer conformation in the membrane-bound oligomers under conditions mim-

icking the transition-state of GTP hydrolysis. Local remodelling of bacterial membranes by GBP1 oligomers may therefore provide platforms for caspase-4 recruitment and activation and reconciles observations displaying discontinuous GBP1-dependent recruitment of caspase-4 on cytosol-invasive Gram-negative bacteria [21].

All structural data in our study has been acquired using GBP1 arrested in an activated, but non-hydrolysing state. In its native cellular environment GBP1 can bind and hydrolyse GTP, likely leading to further structural rearrangements throughout the hydrolysis cycle. This raises the question of the functional consequences that these structural changes impose on GBP1-coated membranes. Unlike for the transition-state stabilised GBP1 coatomers, we do not observe coated liposomes in the presence of GTP. Instead, we observed fragmented GBP1-decorated membranes (short filaments) or flower-like assemblies resembling, but distinctly different from the micellar structure observed for $GBP1_F$-GDP·AlF_3 in the absence of lipids. While our present data precludes quantitative conclusions, our observations are indicative of the ability of GBP1 to fragment membranes. How the GBP1 coatomer and GTP-dependent conformational changes relate to this property will be important questions for further studies. Importantly, the concentrations required for GBP1 remodelling activity in the presence of GTP were at least 8-fold increased compared to the situation with GBP1-GDP·AlF_3. Since the concentration of "activated" GBP1 in the presence of GTP will always be lower than that for the non-hydrolysable GTP analog GDP·AlF_3 at equimolar concentrations, this observation is consistent with a threshold-dependent response of GBP1 activity.

Our data firmly establish nucleotide-dependent GBP1 dimers as the assembling unit for GBP coatomer formation. Important questions, for example how the GBP1 coat is stabilised, how GBP1 recruits and integrates non-prenylated GBP family members into the coatomer, and how these heterotypic interactions affect the functionality of the GBP coat remain unsolved.

Acknowledgements

We thank Roland Kieffer and Jeremie Capulade for help with fluorescence imaging, Mario Avellaneda and Florian Wruck for setting up the initial optical trapping experiments and Wiel Evers for cryo-EM data collection. We acknowledge Instruct-ERIC (PID7267), part of the European Strategy Forum on Research Infrastructures (ESFRI), and the Research Foundation - Flanders (FWO) for their support and use of resources, as well as Alison Lundqvist for technical assistance during nanobody discovery. Cryo-EM data collection benefited from access to the Netherlands Centre for Electron Nanoscopy (NeCEN) with financial support from the Dutch Roadmap Grant NEMI (NWO.GWI.184.034.014). This work was supported by the European Research Council (ERC-StG-852880 to AJ), the Dutch Research Council (NWO.STU.018-2.007 to AJ) and the Kavli Institute of Nanoscience Delft.

Contributions

TK, CP and EG purified proteins. TK performed fluorescence imaging, biophysical experiments and prepared cryo-EM samples. TK and AJ collected cryo-EM data. TK, SH and AJ processed cryo-EM data; TK and AJ analysed cryo-EM data and built the atomic model. CP and TK performed mutagenesis and co-sedimentation assays. TK and CT performed cryo-EM of LPS-bound GBP1 coatomers. LG performed, and LG and SJ analysed optical trapping experiments. EP and JS initiated nanobody generation. TK and AJ wrote the manuscript; all authors commented on the final draft. AJ conceptualised and supervised the study.

Data

The refined atomic model of the pseudo-symmetric GBP1 dimer has been deposited in the Protein Data Bank under accession code 8CQB and will become available upon publication. The primary cryo-EM density and the LocScale map of the pseudo-symmetric GBP1 dimer will become available in the Electron Microscopy Data Bank (EMDB). Raw micrographs will be deposited in the Electron Microscopy Public Image Archive (EMPIAR) and raw tilt series will become available on Zenodo.

3.4. Materials and Methods

Plasmid construction

GBP1

Codon-optimised synthetic DNA encoding human GBP1 (UniProt accession P32455) was cloned into the NcoI/NotI linearised pETM14 vector containing a N-terminal His_6 tag and 3C cleavage site, yielding pETM14-GBP1.

GBP1 variants

Expression vectors containing GBP1 variants were generated from pETM14-GBP1 by quickchange mutagenesis using appropriate oligos [Supplementary Table 3.7]. Mutations were confirmed by DNA sequencing (Macrogen Europe B.V., Amsterdam, Netherlands).

pCDFDuet-FNTA-FNTB

A co-expression vector for farnesyl transferase (FTase) was constructed using the pCDF-Duet1 (Novagen) vector backbone. FNTA inserts were PCR-amplified with AJLO-023 and AJLO-024 from pANT7-FNTA-cGST (DNASU HsCD00630808). To allow subcloning into MCS1 of pCDF-Duet1, BsmBI sites compatible with NcoI and NotI overhangs were inserted at the 5'- and 3'-ends of FNTA. The BsmBI-digested FNTA fragment was cloned into NcoI/NotI digested pCDF-Duet1, yielding pCDF-Duet-FNTA. For cloning of FNTB into MCS2 of pCDF-Duet-FNTA, FNTB was PCR-amplified from pANT7-FNTB-cGST (DNASU HsCD00077919) using AJLO-25 and AJLO-026 [Supplementary Table 3.7] to create a 5'-NdeI site and a 3'-BsmBI site compatible with XhoI overhang. An internal NdeI site in pANT7-FNTB-cGST was removed by Quickchange mutagenesis with AJLO-027 and AJLO-028. The NdeI/BsmBI-digested FNTB fragment was cloned into NdeI/XhoI-digested pCDF-Duet-FNTA, yielding the FTase co-expression vector pCDF-Duet-FNTA/-FNTB.

pCDFDuet-His6-FNTA-FNTB

The pJET1.2 constructs containing FNTA or FNTB were obtained by amplification of AJLD0007 or AJLD0022 [Supplementary Table 3.8] using AJLO-023 - AJLO-026 [Supplementary Table 3.7], following the manufacturer recommendations. The pCDFDuet- His6-FNTA-FNTB (AJLD0063) vector was obtained by Gibson assembly. The DNA fragments originated from AJLD0052, AJLD0053 and AJLV0038 using primers AJLO-076 - AJLO-078, AJLO-083 and AJLO-090 - AJLO-093 [Supplementary Table 3.7]. Successful cloning was confirmed at all stages by DNA sequencing (Macrogen Europe B.V., Amsterdam, Netherlands).

Protein expression and purification

GBP1 and GBP1-variants

Proteins were expressed in *E.coli* BL21(DE3) [Supplementary Table 3.1] using auto- induction in lactose-containing media. Pre-cultures were grown in LB-medium o/n at 37°C. For protein expression, ZYP5052 medium was inoculated at 1/50 (v/v) with preculture and cells were grown at 37°C and 180 rpm for 3-4 h before lowering the temperature to 20°C for 15-20 h. Cells were harvested by centrifugation at 4°C and 4000 rpm and

the cell pellet was resuspended in lysis buffer (50 mM HEPES pH 7.8, 500 mM NaCl, 0.1% Triton X-100) on ice. The cells were disrupted by three successive freeze-thaw cycles. To digest genomic DNA, 1-10 ug/ml DNAseI was added and incubated on a rotating wheel for 1-2 hours at 4°C. To separate cell debris, the lysate was centrifuged at 20,000 x g for 40 min at 4°C. The supernatant was applied to TALON (Takara) affinity resin. The bound fraction was washed with 20 column volumes (cv) of wash-buffer (50 mM sodium phosphate, 300 mM NaCl, 10 mM imidazole, pH 7.4) and eluted in the same buffer containing 150 mM imidazole. The eluent was dialysed into 3C cleavage buffer (50 mM HEPES pH 7.4, 150 mM NaCl, 0.5 mM DTT) and incubated with 1:100 mol/mol 3C protease o/n at 4 °C. Following cleavage, the proteins were further purified via size exclusion chromatography using a GE Superdex200 Increase 10/300 GL column (GE Healthcare) in running buffer (50 mM HEPES pH 7.4, 150 mM NaCl, 0.5 mM DTT).

Farnesyl transferase
His-FNTA-FNTB was expressed as described before for GBP1. After harvesting, the cell pellet was placed on ice and resuspended in lysis buffer (50 mM HEPES pH 7.8, 150 mM NaCl, 0.1% Triton X-100). A reduced salt concentration of 150 mM was necessary to avoid disassembly of the FNTA/FNTB . After separating the cell debris, the supernatant was applied to Ni-NTA (GE Healthcare) affinity resin. The bound fraction was washed with 20 column volumes (cv) of wash-buffer (50 mM HEPES pH 7.8, 150 mM NaCl, 0.5 mM DTT, 10-30 mM imidazole) and eluted in the same buffer containing 250 mM imidazole. The proteins were further purified via size exclusion chromatography using a Superdex200 Increase 10/300 GL column (GE Healthcare) in running buffer (50 mM HEPES pH 7.4, 150 mM NaCl, 0.5 mM DTT).

In vivo farnesylation of GBP1

Co-translational farnesylation of GBP1 was performed essentially as described [41]. *E.coli* BL21(DE3) cells were co-transformed with pETM14-GBP1 and pCDFDuet1-FNTA-FNTB plasmids. The expression and initial purification of GBP1 was performed as described for pETM14-GBP1. To separate non-farnesylated and farnesylated GBP1 ($GBP1_F$), an additional hydrophobic interaction chromatography (HIC) step was performed.

Briefly, NH_4SO_4 was added to the protein solution in 3C cleavage buffer to a final concentration of 1 M. The solution was bound to a HiTrap Butyl HP column (GE Healthcare), washed with 30 cv of high salt buffer (1.5 M NH_4SO_4, 50 mM Tris-HCl pH 8, 2 mM $MgCl_2$, 2 mM DTT) before elution over 20 cv with a linear gradient into low salt buffer (50 mM Tris-HCl pH 8, 2 mM $MgCl_2$, 2 mM DTT). Fractions containing the $GBP1_F$ were pooled and further purified by size exclusion chromatography on a Superdex200 Increase 10/300 GL column (GE Healthcare) in running buffer (50 mM HEPES pH 7.4, 150 mM NaCl, 0.5 mM DTT).

In vitro farnesylation of GBP1

In vitro prenylation of GBP1 was adapted from [49]. In brief, 5 µM purified GBP1 was incubated with 5 µM FTase for farnesylation and supplemented with 25 µM farnesyl pyrophosphate (FPP) (Cayman) in prenylation buffer (50 mM HEPES pH 7.2, 50 mM NaCl, 5 mM DTT, 5 mM $MgCl_2$, 20 µM GDP). The reaction mixtures was incubated for 60 min

at room temperature and dialysed o/n at 4° into running buffer.

Preparation of GDP·AlF_3-stabilised GBP1 dimers

15 µM of GBP1 was incubated with 200 µM GDP, 10 mM NaF, 300 µM $AlCl_3$, 5 mM $MgCl_2$ and 1 mM DTT for 10 min at RT.

Nanobody generation, selection and purification

Nanobody generation

Llamas have been immunised either with purified monomeric GBP1, farnesylated GBP1 or GDP·AlF_3-stabilised dimeric GBP1. From each llama a blood sample was taken and the peripheral blood lymphocytes were isolated followed by the purification of RNA and synthesis of cDNA. Nanobody coding sequences were then PCR-amplified and cloned into a phage display library, creating libraries with > 10^8 independent clones.

Nanobody selection

For phage display selections, farnesylated, monomeric or GDP·AlF_3-stabilised dimeric GBP1 was solid phase coated in 50 mM HEPES pH 7.4, 150 mM NaCl, 0.5 mM DTT and selections were performed in the same buffer. To detect the presence of GBP1-specific nanobodies, the His-tag was detected by an anti-His monoclonal antibody followed by the addition of an anti-mouse-antibody conjugated to alkaline phosphatase. As a substrate for alkaline phosphatase conjugates, 2 mg/ml of 4-Nitrophenyl phosphate disodium salt hexahydrate (pNPP) was used. In total 78 clones were found positive on the dimeric GBP1-GDP·AlF_3, 26 on $GBP1_F$ and 33 clones on monomeric GBP1. We selected Nanobodies from different families and performed a SEC-MALS analysis to investigate the binding behaviour. Nanobody 74 was chosen because it binds to GBP1 in a 1:1 ratio without breaking the GDP·AlF_3-stabilised GBP1 dimer apart.

Expression and purification

Nanobody 74 (Nb74) was expressed in *E.coli* WK6 (su-) cells. Pre-cultures were grown overnight in LB medium containing 100 µg/ml ampicillin, 2 % glucose and 1 mM $MgCl_2$. TB medium (2.4 % yeast extract, 2 % tryptone, 0.4 % glycerol, 17 mM KH_2PO_4, 72 mM K_2HPO_4), supplemented with 100 µg/ml ampicillin, 0.1 % glucose and 2 mM $MgCl_2$ was inoculated with a 1:50 (v/v) dilution of the pre-culture and cells were grown at 37 °C with 190 rpm. Protein expression was induced with 1 mM IPTG at an OD_{600nm} between 0.7-1.2, before lowering the temperature to 25 °C for 18 hours of expression. Cells were harvested by centrifugation at 4 °C and 4000 x g for 20 min. For lysis, by osmotic shock, a pellet of a 1 l culture (with OD600nm = 25) was resuspended with 10 ml TES buffer (0.2 M Tris pH 8, 0.5 mM EDTA, 0.5 M sucrose) for 2 hours on a rotating wheel. Next, 30 ml TES/4 buffer (TES buffer, four times diluted in H_2O) was added and left on a rotating wheel for 1 h.

The resuspended cell lysate was centrifuged for 30 min at 8000 x g and the supernatant was kept. Approximately 1 ml of Ni-NTA agarose (Qiagen) was utilised for purification of the lysate resulting from 1 l culture. Pre-equilibrated Ni-NTA agarose beads, in 50 mM sodium phosphate, 1 M NaCl, pH 7, were added to the supernatant and left to incubate on a rotating wheel for 1 h at room temperature. Following incubation the beads

were washed with 20 ml 50 mM sodium phosphate, 1 M NaCl, 10 mM imidazole, pH 7 and protein was eluted with 2.5 ml 50 mM sodium phosphate, 0.15 M NaCl, 0.3 M imidazole, pH 7. The elution fractions were dialysed (Spectra/Por 3, 3.5 kDa cut-off) for 3 days against 50 mM HEPES, 0.15 M NaCl pH 7.5 and subsequently concentrated (Amicon, 3 kDa cut-off) to concentrations between 150 µM to 500 µM prior to storage at –80 °C.

Biophysical analysis

SEC-MALS

The oligomerisation states of GBP1 at 15 µM in the presence and absence of GTP and nucleotide analogs were estimated using analytical size exclusion chromatography coupled to multi-angle light scattering (SEC-MALS). Purified protein samples were resolved on a Superdex200 Increase 10/300 GL column (GE Healthcare) connected to a high-performance liquid chromatography (HPLC) unit (1260 Infinity II, Agilent) running in series with an online UV detector (1260 Infinity II VWD, Agilent), an 8-angle static light scattering detector (DAWN HELEOS 8+; Wyatt Technology), and a refractometer (Optilab T-rEX; Wyatt Technology).

For SEC-MALS measurements, proteins were diluted to a final concentration of 15 µM in SEC buffer (50 mM HEPES pH 7.4, 150 mM NaCl, 0.5 mM TCEP or DTT) with or without the GTP transition state mimic or with 1 mM of GTP, GDP, GMP and 0.5 mM of GppCp, GTPγS or GppNHp and incubated for 5 - 10 min at RT prior to injection. On the basis of the measured Rayleigh scattering at different angles and the established differential refractive index increment of value of 0.185 ml*g^{-1} for proteins in solution with respect to the change in protein concentration (dn/dc), weight-averaged molar masses for each species were calculated using ASTRA software (Wyatt Technology; v.7.3.1).

Mass photometry

GBP1-WT and GBP1 variants were purified as described before. The data was collected on a Refeyn OneMP instrument using the AcquireMP software (version 2.3 and 2.4). Silicon gaskets (Culture Well Reusable gaskets, Grace Biolabs) were adhered to clean cover slips (High Precision cover slips, No. 1.5, 24 × 50 mm, Marienfeld). For measurements, samples were diluted in 50 mM HEPES pH 7.5, 150 mM NaCl to final concentrations between 12.5 nM to 75 nM. Data was acquired and analysed using DiscoverMP (version 2.3 and 2.4), using the smallest acquisition window and default settings.

GTPase activity assay

To determine the GTPase activity of GBP1 the GTPase-Glo™ Assay (Promega) was utilised [50], using the protocol for intrinsic GTPase activity. Briefly, 5 µl of 5 µM GBP1 (WT or variants) in running buffer was added per well to a 384 well plate. 5 µl of 2 x GTP solution containing 10 µM GTP and 1 mM DTT was added to the same well. The reaction was incubated at RT for 60 min. 10 µl of reconstituted GTPase-Glo reagent was added to the reaction and incubated for 30 min at RT while shaking. Finally, 20 µl of detection reagent was added and after another incubation step of 10 min the luminescence was measured using a micro plate reader (Synergy^{TM}H1, BioTek). BSA was used as a negative control and measurements were performed in triplicates.

Liposome preparation

SUV preparation

1 mg of brain polar lipid extract (BPLE, Avanti Polar Lipids) and 1,2-dioleoyl-sn-glycero-3-phosphocholine (DOPC, Avanti Polar Lipids), purchased as chloroform solutions were each dried under a gentle N2 stream. The resulting lipid film was further dried in a desiccator connected to a vacuum pump for 1 h. To hydrate the lipid film, 1 ml of 50 mM HEPES (pH 7.5), 150 mM NaCl was used. Small unilamellar vesicles (SUVs) were prepared with an Avanti Mini Extruder (Avanti Polar Lipids) with hydrophilic polycarbonate membranes with a pore size of 0.1 µm. The solution of swollen lipid was filled into one of the syringes and monodisperse emulsions of SUVs were produced by passing this mixture through the membrane at least 11 times. The SUVs were stored at 4 °C until further use.

GUV preparation

Per experimental condition, 30 µl of 10 mg/ml BPLE (Avanti Polar Lipids), was added to 10 µl of 0.1 mg/mL Texas Red 1,2-Dihexadecanoyl-sn-Glycero-3-Phosphoethanolamine, Triethylammonium (Texas red DHPE, Invitrogen) and 1 % (v/v) DSPE-PEG (2000)-biotin (Sigma Aldrich). 30 µl of this solution was carefully aspirated and spread onto a Polyvinyl alcohol (PVA) coated glass cover slide (5 % PVA was prepared in water, dried on a 22x22 mm cover slide for 30 min at 50 °C), prior to an additional 30 min in a desiccator connected to a vacuum pump. To the dried lipid film 250 µl of inside buffer (50 mM HEPES (pH 7.5), 150 mM NaCl, 50 mM sucrose) were added and lipids were allowed to swell in the dark for 15 min with gentle shaking. The giant unilamellar vesicles (GUVs) were collected and freshly used.

Confocal fluorescence microscopy

Preparation of the imaging chamber

Glass coverslips (22x40 mm) were attached, with UV resin, to a home-made pre-drilled piece of plexiglass, to form the imaging chambers. The chambers were flushed with 2 mg/mL BSA-biotin, containing 3 moles of biotin per mole of BSA (BioVision). After removal of Biotin, the chambers were washed with buffer (50 mM HEPES (pH 7.5), 150 mM NaCl) and incubated further 5 minutes with 1 mg/mL Avidin (Thermo Fisher) prior to addition of the GUVs for imaging.

Maleimide labelling of $GBP1_F$-Q577C

Alexa Fluor 647 (Thermo Fisher) dissolved in DMSO to a final concentration of 10 mM was added dropwise to the protein until a 20x molar excess was achieved. Prior to addition of the fluorophore, the protein was reduced for 5 min with 0.5 mM TCEP. After addition, the sample was incubated 2 h at room temperature. Separation of the labelled protein from excess dye was performed according to the manufacturer using a desalting column (5 ml, HiTrap Desalting, Cytiva) in 50 mM HEPES pH 7.4, 150 mM NaCl and 0.5 mM.

$GBP1_F$-GDP·AlF_3

The GTP transition state mimic was prepared as described before. 20 µl of Texas red DHPE labelled GUVs were mixed with 5 µl protein solution consisting of 18.5 µM $GBP1_F$-

GDP·AlF_3 and 1.5 µM of $GBP1_F$-Q577C-GDP·AlF_3, labelled with Alexa 647-C2-maleimide, resulting in a final protein concentration of 4 µM. The mixture was incubated at 30 °C for 30 minutes prior to imaging.

GTP-activated GBP1
20 µl of GUVs were mixed with 5 µl protein solution consisting of 18.5 µM $GBP1_F$ and 1.5 µM of $GBP1_F$-Q577C, labelled with Alexa 647-maleimide. 5 µl of 10 mM GTP was added to the well directly prior to imaging.

Confocal microscopy
Imaging was performed on a Nikon A1R confocal microscope using a Nikon SR Apo TIRF 100x oil/1.49 NA objective. The excitation wavelength of the lasers was 561 nm (for Texas Red DHPE) and 640 nm (for GBP1-AF647). Images were processed with Fiji software.

Dual trap bead-supported membrane transfer assay

Bead-supported bilayer preparation
Lipid bilayer coated silica beads were prepared by mixing lipids in chloroform in the desired molar ratios: 84.69 mol% DOPC (850375, Avanti), 15 mol% DOPS (840035, Avanti), 0.15 mol% 18:1 Liss Rhodamine PE (810150, Avanti), 0.16 mol% Biotin lipids DSPE-PEG (2000) Biotin (880129, Avanti).

Lipids were dried to a thin film on the walls of a flask. After removal of residual chloroform, the flask was wrapped in aluminum foil and placed in a desiccator overnight. Lipids were resuspended in 1 mL deionised H_2O (dH_2O) to a final lipid concentration of 1 mg/ml, then resuspended for 30 min in a 37°C water bath and subsequently subjected to three freeze-thaw cycles. The lipid solution was extruded 21x using an Avestin-LF-1 extruder with a 100 nm membrane. 10 µL of the lipid solution was added to 89.5 µL H_2O containing NaCl and 0.5 µL of a 5% solids solution of 2 µm silica microparticles (Sigma Aldrich) to a final concentration of 0.1 mM lipids and 1 mM NaCl, followed by incubation on a lab rotator at room temperature for 45 min. Finally, 30 µL of the solution was diluted into 270 µL GBP buffer (50 mM HEPES pH 7.5, 150 mM NaCl, 5 mM $MgCl_2$ and 0.5 mM DTT). For the catching bead, 10 µL of a 200 mM NaCl solution was mixed with 1 µL NTV-DNA 3.5 kDa and 2 µL antiDIG-beads (QDIGP-20-2 ProSciTech), followed by incubation for 30 min on a lab rotator at 4°C and finally diluted in 290 µL GBP buffer.

Optical trapping and confocal microscopy
Optical trapping experiments were performed in a LUMICKS C-Trap. One bead containing bead-supported bilayer and one uncoated bead were successively trapped in one of the LUMICKS C-Trap lasers. The bead pairs were then moved far downstream close to the upper wall of the flow chamber to ensure straight, laminar flow upon switching of the running solution. The bead pairs were flushed at least 30 seconds with GBP-1 buffer + 1 mM GTP at 0.1 bar before dispensing sample containing GBP-1 buffer + 100 µM GBP-1 + 1 mM GTP into the flow chamber. A 532 nm laser operated at 8 mW was used to excite 18:1 Liss Rhodamine PE and confocal fluorescence images were acquired in a 14.15x3.35 µm window at 50 nm pixel size to measure Liss Rhodamine PE lipid fluoroescence. The red channel (638 nm) was used to visualise the beads and as internal control

for potential dirt particles in the flow channel. Prior to adding GBP1$_F$, the beads were flushed for at least 30 seconds with GBP1 buffer supplemented with 1 mM GTP. The time of solute arrival at the first bead was calibrated with a fluorescent dye in separate experiments and estimated to 9 s. To determine fluorescence intensity time traces, the z-axis profile of the inter-bead space and the catch bead was selected in ImageJ and the total relative fluorescence of each frame was processed in Origin. For baseline correction the average fluorescence across 30 seconds prior to addition of GBP1$_F$ was subtracted from each data set, resulting in a baseline of 0 A.U. All curves were averaged with the "Average multiple curves" option in Origin and the resulting average time traces with the 95% confidence interval were plotted using Python's matplotlib library.

Liposome co-sedimentation assays

Wild-type GBP1 and GBP1 variants were *in vitro* farnesylated as described above. Experiments were also performed with *in vivo* farnesylated GBP1 for comparison. The GTP transition state mimic was prepared as described before. GBP1-WT or GBP1 variants were diluted to 2 µM and mixed with 1 mg/ml BPLE SUV liposomes in SEC buffer to a final volume of 100 µl. Samples were incubated for 60 min at RT, followed by ultracentrifugation (Beckman Coulter Optima L-90K, Rotor: 42.2 Ti) at 222,654 x g for 20 min at 4°C. The pellet and supernatant fractions were separated as quickly and gently as possible prior to analysis, whereby 15 µl were loaded onto a 4-12 % SurePAGE Bis-Tris gel for separation by SDS-PAGE.

The lanes of interest were identified and the bands automatically detected using the Gel doc Image Lab software (v. 6.1.0.07). After automatic background subtraction, the sum of intensities of the protein present in the pellet and supernatant fractions was used to determine the relative percentage of GBP1 in each fraction. The pelletation assay was performed five to seven times to compute fractional average intensities and standard deviations.

Negative staining EM

3.5 µL of protein or lipid solution was applied onto a freshly glow-discharged carbon-coated copper mesh grid (Quantifoil). After 1 min, grids were washed twice with 12 µL buffer (50 mM HEPES pH 7.4, 150 mM NaCl, 0.5 mM DTT) followed by staining with 3.5 µL of 2 % (w/v) uranyl acetate at room temperature. At each step, excess sample, wash solution and stain were blotted with filter paper and finally grids were air dried for 15 min. Grids were imaged on a JEM 1400Plus TEM (JEOL) operated at 120 kV and recorded on a bottom-mounted TVIPS F416 CMOS camera.

To observe micelle formation, 0.5 - 2 mg/ml of GBP1$_F$-GDP·AlF_3 or 8 mg/ml of GBP1$_F$ with 1 mM of GTP was applied onto a carbon grid. The incubation time for GBP1$_F$-GDP·AlF_3 was 10 min at RT and 2 min at RT for GTP respectively. To analyse membrane binding of GBP1$_F$, 1 mg/ml of GBP1$_F$ was added together with all other components to form the GTP-transition state mimic (see above). SUVs were added in a 1:10 dilution (10 mg/ml, d = 100 nm and incubated for 10 min at RT. For filament formation to occur, samples needed to incubate o/n at 4°C, 30 min at 30°C or the concentration needed to increase to 2 mg/ml following an incubation step of 10 min at RT.

Single particle imaging

GBP1-GDP·AlF_3 dataset

A total of 3.0 µL of 0.7 mg/ml GBP1-GDP·AlF_3 was applied to glow-discharged Quantifoil grids (QF-1.2/1.3, 300-mesh holey carbon on copper) on a Leica GP2 vitrification robot at 99 % humidity and a temperature of 22 °C. The sample was blotted for 4 s from the carbon side of the grid and immediately flash-cooled in liquid ethane. Micrographs were acquired on a FEI Titan Krios (Thermo Fisher Scientific) operated at 300 kV. Images were recorded on a K2 Summit direct electron detector (Gatan) with a pixel size of 1.09 Å. Image acquisition was performed with EPU Software (Thermo Fisher Scientific), and micrographs were collected at an underfocus varying between –3.5 µm and –0.5 µm. We collected a total of 48 frames accumulating to a total exposure of 60 $e^-/Å^2$. In total, 1,193 micrographs were acquired. Data acquisition parameters are summarised in Supplementary Table 3.3.

GBP1-GDP·AlF_3-Nb74 dataset

GBP1 was incubated in a 1:1 molar ratio with Nb74 for 70 min at RT, before adding GDP·AlF_3 and incubating additionally for 10 min at RT. A total of 3.0 µL of 0.7 mg/ml GBP1-GDP·AlF_3 bound to Nb74 was applied to glow-discharged Quantifoil grids (QF-1.2/1.3, 300-mesh holey carbon on copper) on a GP2 vitrification robot at 99 % humidity and 22 °C. The sample was blotted for 4 s from the carbon side of the grid and immediately flash-cooled in liquid ethane. Micrographs were acquired on a FEI Titan Krios (Thermo Fisher Scientific) operated at 300 kV. Images were recorded on a K3 Summit direct electron detector (Gatan) at a magnification of 105kx, corresponding to a pixel size of 0.834 Å at the specimen level. Image acquisition was performed with EPU 2.8.1 Software (Thermo Fisher Scientific), and micrographs were collected at an underfocus varying between –2.2 µm and –0.6 µm. We collected a total of 50 frames accumulating to a total electron exposure of 60 $e^-/Å^2$. In total, 5,214 micrographs were acquired.

$GBP1_F$-GDP·AlF_3

A total of 3.0 µL of 1 mg/ml $GBP1_F$-GDP·AlF_3 was applied to glow-discharged Quantifoil grids (QF-1.2/1.3, 300-mesh holey carbon on copper) on a Leica GP2 vitrification robot at 97 % humidity and 20 °C. The sample was blotted for 4 s from the carbon side of the grid and immediately flash-cooled in liquid ethane. Grids were imaged on a JEM 3200FSC TEM (JEOL) operated at 300 kV. Images were recorded on a K2 Summit direct electron detector (Gatan). Two different datasets were acquired one at a magnification of 30kx, corresponding to a pixel size of 1.22 Å at the specimen level and the other one at a magnification of 15kx, corresponding to a pixel size of 2.449 Å. Image acquisition was performed with SerialEM [51], and micrographs were collected at an underfocus varying between –3 µm and –1 µm. We collected a total of 60 frames accumulating to a total electron exposure of 48.37 $e^-/Å^2$ (for the dataset at 30kx) or to a total electron exposure of 12.92 $e^-/Å^2$ (for the dataset at 15kx). In total, 395 (dataset at 30kx) or 606 (dataset at 15kx) micrographs were acquired.

$GBP1_F$-GDP·AlF_3 with LPS from *E.coli* O111:B4 (LPS-EB), *Salmonella Minnesota* R595 (LPS-SM) or *Salmonella Typhimurium* (LPS-ST)
1 mg/ml $GBP1_F$-GDP·AlF_3 was mixed with 0.22 mg/ml LPS-EB (InvivoGen), LPS-SM (InvivoGen) or LPS-ST (Enzo) and incubated for 30 min at 30 °C. 3.0 µL of the mixture were applied on to glow-discharged Quantifoil grids (QF-1.2/1.3, 200-mesh holey carbon on copper) on a Leica GP2 vitrification robot at 98 % humidity and 22 °C. The sample was blotted for 4 s from the carbon side of the grid and immediately flash-cooled in liquid ethane. Grids were imaged on a JEM 3200FSC TEM (JEOL) operated at 300 kV. Images were recorded on a K2 Summit direct electron detector (Gatan) using automated image acquisition in SerialEM [51]. Data collection statistics for each dataset are summarised in Supplementary Table 3.6.

Single-particle image processing

GBP1-GDP·AlF_3-Nb74

The GBP1-GDP·AlF_3-Nb74 dataset was processed using cryoSPARC v3.3.2 [52]. The in-built patch-motion correction [53] routine in cryoSPARC was used to correct for stage drift and beam-induced specimen movement over the acquired frames. 5,208 micrographs were selected for further processing and patched contrast transfer function (CTF) determination [54] was performed in cryoSPARC. Using a blob-based particle picker, 2,171,521 particles were extracted and cleaned via multiple rounds of 2D classification, each consisting of 50 - 100 classes. Classes only containing the LG domain of the protein were actively sorted out as they did not yield a full 3D reconstruction [Supplementary Data Figure 3.28]. Selected 2D classes comprising 119,071 particles were used to train a Topaz model [55], which was then used to extract a total of 6,539,167 particles. Following particle extraction, four iterative rounds of 2D classification were performed and 2D class averages were selected displaying secondary structure features. 500,186 particles were used to perform *ab initio* reconstruction to generate five different models. Three classes were selected for heterogeneous refinements without imposing symmetry or imposing C2 symmetry. A single class with 187,161 particles was selected and used for non-uniform refinement [56] either without imposing symmetry or with imposed C2 symmetry [Supplementary Data Figure 3.11]. Per-particle defocus and global CTF refinement improved the resolution to 3.7 Å (Table 3.4). Local resolution was estimated in cryoSPARC [57] and visualised in ChimeraX [58]. Map sharpening was done in cryoSPARC by applying the overall B-factor estimated from Guinier plots. For flexible refinement, the final particle stack of the cryo-EM density was clipped to 256 pixel, fourier-cropped to 96 pixel (pixel size 2.2240 A) and used as input for cryoSPARC v4.1.1 3D Flexible Refinement ([59]) with 4 latent dimensions. Morphs of the density along the four dimensions of the latent space were generated to display different modes of flexibility and were displayed in ChimeraX [58].

GBP1-GDP·AlF_3

1,193 movies of GBP1-GDP·AlF_3 were processed in cryoSPARC v3.1 [52]. Patch-motion correction and patched CTF estimation were followed by manual particle picking. Those manual picks were used to train a Topaz model [55] from which 240,487 particles were extracted. After multiple rounds of 2D classification, particles assigned to classes dis-

playing secondary structure were used as an input to perform *ab initio* reconstruction to generate 5 different models (67,197 particles). Three classes were used for heterogeneous refinement imposing C2 symmetry. A final non-uniform refinement [56] consisting of 35,715 particles resulted in a 4.9 Å resolution structure that only covered the LG domain of GBP1.

GBP1-GDP$_F$·AlF$_3$
Images of GBP1-GDP$_F$·AlF$_3$ micelles were processed in cryoSPARC v3.1.0 [52]. Patch-motion correction and patched CTF estimation were followed by manual particle picking and 2D classification.

GBP1-GDP$_F$·AlF$_3$ with LPS-EB
The dataset was processed using cryoSPARC v3.3.2 [52]. After patch-motion correction and patched CTF estimation, the particle segments were generated from traced filaments using the cryoSPARC filament tracer. After multiple rounds of 2D classification, classes displaying clear molecular features were used as templates for the cryoSPARC template picker. Extracted particles were again subjected to multiple rounds of 2D classification.

Atomic model building

Atomic models of the GTPase Domain of human GBP1-GDP·AlF$_3$ (PDB ID 2b92) [37] and the C-terminal stalk (aa 320 - 483) of GBP1 (PDB ID 1dg3) [35] were rigid body-fitted into the cryo-EM density. Manual model building was performed in Coot 0.9.5 [60] followed by real-space refinement against one of the half maps in Phenix 1.13 [61]. The second half map was used as a test map for assessment of overfitting. Ligand geometry and restraints for GDP·AlF$_3$ were generated using the electronic Ligand Builder and Optimisation Workbench (eLBOW) [62] implemented in Phenix. Secondary structure restraints were used throughout the refinement. A locally sharpened and filtered map was generated using the hybrid version of LocScale [39], which integrates reference based sharpening for modelled regions [63] with generalised scattering properties of biological macromolecules for unmodelled regions approximated by pseudo-atoms [40]. The atomic displacement factors of the combined model were refined using 10 Refmac [64] iterations as implemented in servalcat [65] with the keywords 'refi bonly'. Prior to refinement, all the atomic displacement factors were set to 40 Å^2.

Tomography

GBP1$_F$-GDP·AlF$_3$ with liposomes
For the dataset of GBP1$_F$-GDP·AlF$_3$ together with liposomes, a total of 3.5 µL of 1 mg/ml GBP1$_F$-GDP·AlF$_3$ containing freshly extruded liposomes (1 mg/ml of BPLE, Avanti, d = 100 nm) and 10 nm gold fiducials (1:5 (v/v)) was applied to glow-discharged Quantifoil grids (QF-1.2/1.3, 200-mesh holey carbon on copper, Quantifoil) on a Leica GP2 vitrification robot (Leica) at 98 % humidity and 20 °C. The sample was blotted for 4 s from the carbon side of the grid and immediately flash-cooled in liquid ethane. Grids were imaged on a JEM 3200FSC TEM (JEOL) operated at 300 kV. Images were recorded on a K2 Summit direct electron detector (Gatan) at a magnification of 12kx, corresponding

to a pixel size of 3.075 Å at the specimen level. Image acquisition was performed with SerialEM [51], and micrographs were collected at a nominal defocus of –5 µm or –4 µm. Bidirectional tilt series were acquired from 0° to -60° and from 0° to 60° with a 2° increment. We collected tilt series of 61 micrographs each consisting of 10 frames and a total electron exposure of 93.94 $e^-/Å^2$ for tomogram-33 and tomogram-39 (1.54 $e^-/Å^2$ per tilt increment). For tomogram-50, we collected a tilt series of 61 micrographs consisting of 20 frames and a total electron exposure of 100.04 $e^-/Å^2$ (1.54 $e^-/Å^2$ per tilt increment). Micrographs were motion-corrected with MotionCor2 [53] and dose-weighted according to their accumulated electron exposure [66]. CTF correction was performed using ctfphaseflip from the IMOD package [67] and the tilt series was aligned using patch tracking and reconstructed using weighted back-projection as implemented in Etomo from the IMOD package. Segmentation of lipid membranes and protein coat was performed with tomoseg as part of the EMAN2 package [68] on reconstructed tomograms binned by a factor of 2. Segmented tomograms were visualised with ChimeraX [58].

Bioinformatic analysis

Multiple sequence alignment

The sequence of hGBP1 - hGBP7 (UniProt: P32455, P32456, Q9H0R5, Q96PP9, Q96PP8, Q6ZN66, Q8N8V2) were used as input for Clustal Omega [69]. The resulting sequence alignment was displayed and consensus sequences computed in MView [70].

Sequence conservation

The sequence of hGBP1 (UniProt: P32455) was used as input for the ConSurf Server [71] to search the UniRef90 database with the HMMer [72] using one iteration. The resulting sequence alignment was displayed and consensus sequences computed in MView [70]. The conservation was mapped onto the atomic model using ChimeraX [58].

References

[1] K. Ray, B. Marteyn, P. J. Sansonetti, and C. M. Tang, *Life on the inside: the intracellular lifestyle of cytosolic bacteria,* Nature Reviews Microbiology **7**, 333 (2009).

[2] F. Randow, J. D. MacMicking, and L. C. James, *Cellular self-defense: how cell-autonomous immunity protects against pathogens,* Science **340**, 701 (2013).

[3] F. Randow, *How cells deploy ubiquitin and autophagy to defend their cytosol from bacterial invasion,* Autophagy **7**, 304 (2011).

[4] B.-H. Kim, A. R. Shenoy, P. Kumar, R. Das, S. Tiwari, and J. D. MacMicking, *A family of ifn-γ–inducible 65-kd gtpases protects against bacterial infection,* Science **332**, 717 (2011).

[5] J. D. MacMicking, *Cell-autonomous effector mechanisms against mycobacterium tuberculosis,* Cold Spring Harbor perspectives in medicine **4**, a018507 (2014).

[6] E. Meunier, M. S. Dick, R. F. Dreier, N. Schürmann, D. K. Broz, S. Warming, M. Roose-Girma, D. Bumann, N. Kayagaki, K. Takeda, *et al., Caspase-11 activation requires lysis of pathogen-containing vacuoles by ifn-induced gtpases,* Nature **509**, 366 (2014).

[7] E. Meunier, P. Wallet, R. F. Dreier, S. Costanzo, L. Anton, S. Rühl, S. Dussurgey, M. S. Dick, A. Kistner, M. Rigard, *et al., Guanylate-binding proteins promote activation of the aim2 inflammasome during infection with francisella novicida,* Nature immunology **16**, 476 (2015).

[8] A. Casadevall, *Evolution of intracellular pathogens,* Annual Review of Microbiology **62**, 19 (2008).

[9] P. J. Sansonetti, A. Ryter, P. Clerc, A. Maurelli, and J. Mounier, *Multiplication of shigella flexneri within hela cells: lysis of the phagocytic vacuole and plasmid-mediated contact hemolysis,* Infection and immunity **51**, 461 (1986).

[10] N. Teysseire, J. Boudier, and D. Raoult, *Rickettsia conorii entry into vero cells,* Infection and immunity **63**, 366 (1995).

[11] K. E. Beauregard, K.-D. Lee, R. J. Collier, and J. A. Swanson, *ph-dependent perforation of macrophage phagosomes by listeriolysin o from listeria monocytogenes,* The Journal of experimental medicine **186**, 1159 (1997).

[12] Y. Cheng, R. J. Colonno, and F. H. Yin, *Interferon induction of fibroblast proteins with guanylate binding activity.* Journal of Biological Chemistry **258**, 7746 (1983).

[13] U. Boehm, L. Guethlein, T. Klamp, K. Ozbek, A. Schaub, A. Fütterer, K. Pfeffer, and J. C. Howard, *Two families of gtpases dominate the complex cellular response to ifn-γ,* The Journal of Immunology **161**, 6715 (1998).

[14] S. L. Anderson, J. M. Carton, J. Lou, L. Xing, and B. Y. Rubin, *Interferon-induced guanylate binding protein-1 (gbp-1) mediates an antiviral effect against vesicular stomatitis virus and encephalomyocarditis virus,* Virology **256**, 8 (1999).

[15] C. Krapp, D. Hotter, A. Gawanbacht, P. J. McLaren, S. F. Kluge, C. M. Stürzel, K. Mack, E. Reith, S. Engelhart, A. Ciuffi, *et al.*, *Guanylate binding protein (gbp) 5 is an interferon-inducible inhibitor of hiv-1 infectivity,* Cell host & microbe **19**, 504 (2016).

[16] M. Kutsch, L. Sistemich, C. F. Lesser, M. B. Goldberg, C. Herrmann, and J. Coers, *Direct binding of polymeric gbp1 to lps disrupts bacterial cell envelope functions,* The EMBO journal **39**, e104926 (2020).

[17] D. Fisch, B. Clough, M.-C. Domart, V. Encheva, H. Bando, A. P. Snijders, L. M. Collinson, M. Yamamoto, A. R. Shenoy, and E.-M. Frickel, *Human gbp1 differentially targets salmonella and toxoplasma to license recognition of microbial ligands and caspase-mediated death,* Cell reports **32**, 108008 (2020).

[18] E. Kravets, D. Degrandi, Q. Ma, T.-O. Peulen, V. Kluempers, S. Felekyan, R. Kuehnemuth, S. Weidtkamp-Peters, C. A. Seidel, and K. Pfeffer, *Guanylate binding proteins directly attack toxoplasma gondii via supramolecular complexes,* Elife **5**, e11479 (2016).

[19] P. Li, W. Jiang, Q. Yu, W. Liu, P. Zhou, J. Li, J. Xu, B. Xu, F. Wang, and F. Shao, *Ubiquitination and degradation of gbps by a shigella effector to suppress host defence,* Nature **551**, 378 (2017).

[20] J. C. Santos, D. Boucher, L. K. Schneider, B. Demarco, M. Dilucca, K. Shkarina, R. Heilig, K. W. Chen, R. Y. Lim, and P. Broz, *Human gbp1 binds lps to initiate assembly of a caspase-4 activating platform on cytosolic bacteria,* Nature communications **11**, 1 (2020).

[21] M. P. Wandel, B.-H. Kim, E.-S. Park, K. B. Boyle, K. Nayak, B. Lagrange, A. Herod, T. Henry, M. Zilbauer, J. Rohde, *et al.*, *Guanylate-binding proteins convert cytosolic bacteria into caspase-4 signaling platforms,* Nature immunology **21**, 880 (2020).

[22] J. R. Jimah and J. E. Hinshaw, *Structural insights into the mechanism of dynamin superfamily proteins,* Trends in Cell Biology **29**, 257 (2019).

[23] Y. Cheng, C. Patterson, and P. Staeheli, *Interferon-induced guanylate-binding proteins lack an n (t) kxd consensus motif and bind gmp in addition to gdp and gtp,* Molecular and cellular biology **11**, 4717 (1991).

[24] G. J. Praefcke, M. Geyer, M. Schwemmle, H. R. Kalbitzer, and C. Herrmann, *Nucleotide-binding characteristics of human guanylate-binding protein 1 (hgbp1) and identification of the third gtp-binding motif,* Journal of molecular biology **292**, 321 (1999).

[25] S. Kunzelmann, G. J. Praefcke, and C. Herrmann, *Transient kinetic investigation of gtp hydrolysis catalyzed by interferon-γ-induced hgbp1 (human guanylate binding protein 1),* Journal of Biological Chemistry **281**, 28627 (2006).

[26] M. Schwemmle and P. Staeheli, *The interferon-induced 67-kda guanylate-binding protein (hgbp1) is a gtpase that converts gtp to gmp,* Journal of Biological Chemistry **269**, 11299 (1994).

[27] R. Neun, M. F. Richter, P. Staeheli, and M. Schwemmle, *Gtpase properties of the interferon-induced human guanylate-binding protein 2,* FEBS letters **390**, 69 (1996).

[28] A. Xavier, M. A. Al-Zeer, T. F. Meyer, and O. Daumke, *hgbp1 coordinates chlamydia restriction and inflammasome activation through sequential gtp hydrolysis,* Cell reports **31**, 107667 (2020).

[29] N. Britzen-Laurent, M. Bauer, V. Berton, N. Fischer, A. Syguda, S. Reipschläger, E. Naschberger, C. Herrmann, and M. Stürzl, *Intracellular trafficking of guanylate-binding proteins is regulated by heterodimerization in a hierarchical manner,* PloS one **5**, e14246 (2010).

[30] J. Shi, Y. Zhao, Y. Wang, W. Gao, J. Ding, P. Li, L. Hu, and F. Shao, *Inflammatory caspases are innate immune receptors for intracellular lps,* Nature **514**, 187 (2014).

[31] D. E. Nantais, M. Schwemmle, J. T. Stickney, D. J. Vestal, and J. E. Buss, *Prenylation of an interferon-γ-induced gtp-binding protein: the human guanylate binding protein, hugbp1,* Journal of leukocyte biology **60**, 423 (1996).

[32] C. Ji, S. Du, P. Li, Q. Zhu, X. Yang, C. Long, J. Yu, F. Shao, and J. Xiao, *Structural mechanism for guanylate-binding proteins (gbps) targeting by the shigella e3 ligase ipah9. 8,* PLoS pathogens **15**, e1007876 (2019).

[33] S. Shydlovskyi, A. Y. Zienert, S. Ince, C. Dovengerds, A. Hohendahl, J. M. Dargazanli, A. Blum, S. D. Günther, N. Kladt, M. Stürzl, *et al.*, *Nucleotide-dependent farnesyl switch orchestrates polymerization and membrane binding of human guanylate-binding protein 1,* Proceedings of the National Academy of Sciences **114**, E5559 (2017).

[34] L. Sistemich, L. Dimitrov Stanchev, M. Kutsch, A. Roux, T. Guenther Pomorski, and C. Herrmann, *Structural requirements for membrane binding of human guanylate-binding protein 1,* The FEBS Journal **288**, 4098 (2021).

[35] B. Prakash, G. J. Praefcke, L. Renault, A. Wittinghofer, and C. Herrmann, *Structure of human guanylate-binding protein 1 representing a unique class of gtp-binding proteins,* Nature **403**, 567 (2000).

[36] T. Vöpel, C. S. Hengstenberg, T.-O. Peulen, Y. Ajaj, C. A. Seidel, C. Herrmann, and J. P. Klare, *Triphosphate induced dimerization of human guanylate binding protein 1 involves association of the c-terminal helices: a joint double electron–electron resonance and fret study,* Biochemistry **53**, 4590 (2014).

[37] A. Ghosh, G. J. Praefcke, L. Renault, A. Wittinghofer, and C. Herrmann, *How guanylate-binding proteins achieve assembly-stimulated processive cleavage of gtp to gmp,* Nature **440**, 101 (2006).

[38] E. Pardon, T. Laeremans, S. Triest, S. G. Rasmussen, A. Wohlkönig, A. Ruf, S. Muyldermans, W. G. Hol, B. K. Kobilka, and J. Steyaert, *A general protocol for the generation of nanobodies for structural biology,* Nature protocols **9**, 674 (2014).

[39] A. J. Jakobi and A. Bharadwaj, *LocScale – reference-based local sharpening of cryo-EM maps,* (2022).

[40] A. Bharadwaj and A. J. Jakobi, *Electron scattering properties of biological macromolecules and their use for cryo-em map sharpening,* Faraday discussions (2022).

[41] J. M. Fres, S. Müller, and G. J. Praefcke, *Purification of the caax-modified, dynamin-related large gtpase hgbp1 by coexpression with farnesyltransferase [s],* Journal of lipid research **51**, 2454 (2010).

[42] W. Cui, E. Braun, W. Wang, J. Tang, Y. Zheng, B. Slater, N. Li, C. Chen, Q. Liu, B. Wang, *et al.*, *Structural basis for gtp-induced dimerization and antiviral function of guanylate-binding proteins,* Proceedings of the National Academy of Sciences **118** (2021).

[43] L. J. Byrnes, A. Singh, K. Szeto, N. M. Benvin, J. P. O'donnell, W. R. Zipfel, and H. Sondermann, *Structural basis for conformational switching and gtp loading of the large g protein atlastin,* The EMBO journal **32**, 369 (2013).

[44] N. Kato, *Crystallization and electron microscopy of bacterial lipopolysaccharide (lps),* Micron **24**, 91 (1993).

[45] C. R. Bolen, S. Ding, M. D. Robek, and S. H. Kleinstein, *Dynamic expression profiling of type i and type iii interferon-stimulated hepatocytes reveals a stable hierarchy of gene expression,* Hepatology **59**, 1262 (2014).

[46] J. Shi, Y. Zhao, Y. Wang, W. Gao, J. Ding, P. Li, L. Hu, and F. Shao, *Inflammatory caspases are innate immune receptors for intracellular lps,* Nature **514**, 187—192 (2014).

[47] J. Shi, Y. Zhao, K. Wang, X. Shi, Y. Wang, H. Huang, Y. Zhuang, T. Cai, F. Wang, and F. Shao, *Cleavage of gsdmd by inflammatory caspases determines pyroptotic cell death,* Nature **526**, 660—665 (2015).

[48] S. Zhu, C. J. Bradfield, A. Mamińska, E.-S. Park, B.-H. Kim, P. Kumar, S. Huang, Y. Zhang, J. Bewersdorf, and J. D. MacMicking, *Cryo-et of a human gbp coatomer governing cell-autonomous innate immunity to infection,* bioRxiv (2021), 10.1101/2021.08.26.457804.

[49] B. Dursina, R. Reents, C. Delon, Y. Wu, M. Kulharia, M. Thutewohl, A. Veligodsky, A. Kalinin, V. Evstifeev, D. Ciobanu, *et al.*, *Identification and specificity profiling of protein prenyltransferase inhibitors using new fluorescent phosphoisoprenoids,* Journal of the American Chemical Society **128**, 2822 (2006).

[50] S. Mondal, K. Hsiao, and S. A. Goueli, *A homogenous bioluminescent system for measuring gtpase, gap and gef activities,* in *Cancer Research*, Vol. 75 (2015).

[51] D. N. Mastronarde, *Automated electron microscope tomography using robust prediction of specimen movements,* Journal of structural biology **152**, 36 (2005).

[52] A. Punjani, J. L. Rubinstein, D. J. Fleet, and M. A. Brubaker, *cryosparc: algorithms for rapid unsupervised cryo-em structure determination,* Nature methods **14**, 290 (2017).

[53] S. Q. Zheng, E. Palovcak, J.-P. Armache, K. A. Verba, Y. Cheng, and D. A. Agard, *Motioncor2: anisotropic correction of beam-induced motion for improved cryo-electron microscopy,* Nature methods **14**, 331 (2017).

[54] A. Rohou and N. Grigorieff, *Ctffind4: Fast and accurate defocus estimation from electron micrographs,* Journal of structural biology **192**, 216 (2015).

[55] T. Bepler, A. Morin, M. Rapp, J. Brasch, L. Shapiro, A. J. Noble, and B. Berger, *Positive-unlabeled convolutional neural networks for particle picking in cryo-electron micrographs,* Nature methods **16**, 1153 (2019).

[56] A. Punjani, H. Zhang, and D. J. Fleet, *Non-uniform refinement: adaptive regularization improves single-particle cryo-em reconstruction,* Nature methods **17**, 1214 (2020).

[57] G. Cardone, J. B. Heymann, and A. C. Steven, *One number does not fit all: mapping local variations in resolution in cryo-em reconstructions,* Journal of structural biology **184**, 226 (2013).

[58] T. D. Goddard, C. C. Huang, E. C. Meng, E. F. Pettersen, G. S. Couch, J. H. Morris, and T. E. Ferrin, *Ucsf chimerax: Meeting modern challenges in visualization and analysis,* Protein Science **27**, 14 (2018).

[59] A. Punjani and D. J. Fleet, *3d flexible refinement: structure and motion of flexible proteins from cryo-em,* BioRxiv (2021).

[60] P. Emsley, B. Lohkamp, W. G. Scott, and K. Cowtan, *Features and development of coot,* Acta Crystallographica Section D: Biological Crystallography **66**, 486 (2010).

[61] P. D. Adams, P. V. Afonine, G. Bunkóczi, V. B. Chen, I. W. Davis, N. Echols, J. J. Headd, L.-W. Hung, G. J. Kapral, R. W. Grosse-Kunstleve, *et al.*, *Phenix: a comprehensive python-based system for macromolecular structure solution,* Acta Crystallographica Section D: Biological Crystallography **66**, 213 (2010).

[62] N. W. Moriarty, R. W. Grosse-Kunstleve, and P. D. Adams, *electronic Ligand Builder and Optimization Workbench (eLBOW): a tool for ligand coordinate and restraint generation,* Acta Crystallographica Section D **65**, 1074 (2009).

[63] A. J. Jakobi, M. Wilmanns, and C. Sachse, *Model-based local density sharpening of cryo-em maps,* Elife **6**, e27131 (2017).

[64] G. N. Murshudov, P. Skubák, A. A. Lebedev, N. S. Pannu, R. A. Steiner, R. A. Nicholls, M. D. Winn, F. Long, and A. A. Vagin, *Refmac5 for the refinement of macromolecular crystal structures,* Acta Crystallographica Section D: Biological Crystallography **67**, 355 (2011).

[65] K. Yamashita, C. M. Palmer, T. Burnley, and G. N. Murshudov, *Cryo-em single-particle structure refinement and map calculation using servalcat,* Acta Crystallographica Section D: Structural Biology **77** (2021).

[66] T. Grant and N. Grigorieff, *Measuring the optimal exposure for single particle cryo-em using a 2.6 å reconstruction of rotavirus vp6,* elife **4**, e06980 (2015).

[67] D. N. Mastronarde and S. R. Held, *Automated tilt series alignment and tomographic reconstruction in imod,* Journal of structural biology **197**, 102 (2017).

[68] M. Chen, W. Dai, S. Y. Sun, D. Jonasch, C. Y. He, M. F. Schmid, W. Chiu, and S. J. Ludtke, *Convolutional neural networks for automated annotation of cellular cryo-electron tomograms,* Nature methods **14**, 983 (2017).

[69] F. Madeira, Y. M. Park, J. Lee, N. Buso, T. Gur, N. Madhusoodanan, P. Basutkar, A. R. Tivey, S. C. Potter, R. D. Finn, *et al., The embl-ebi search and sequence analysis tools apis in 2019,* Nucleic acids research **47**, W636 (2019).

[70] N. P. Brown, C. Leroy, and C. Sander, *Mview: a web-compatible database search or multiple alignment viewer.* Bioinformatics (Oxford, England) **14**, 380 (1998).

[71] H. Ashkenazy, S. Abadi, E. Martz, O. Chay, I. Mayrose, T. Pupko, and N. Ben-Tal, *Consurf 2016: an improved methodology to estimate and visualize evolutionary conservation in macromolecules,* Nucleic acids research **44**, W344 (2016).

[72] R. D. Finn, J. Clements, and S. R. Eddy, *Hmmer web server: interactive sequence similarity searching,* Nucleic acids research **39**, W29 (2011).

[73] F. Studier and B. A. Moffatt, *Use of bacteriophage t7 rna polymerase to direct selective high-level expression of cloned genes,* Journal of Molecular Biology **189**, 113 (1986).

[74] R. Zell and H.-J. Fritz, *Dna mismatch-repair in escherichia coli counteracting the hydrolytic deamination of 5-methyl-cytosine residues.* The EMBO Journal **6**, 1809 (1987).

[75] A. Dümmler, A.-M. Lawrence, and A. De Marco, *Simplified screening for the detection of soluble fusion constructs expressed in e. coli using a modular set of vectors,* Microbial cell factories **4**, 1 (2005).

3.5. Supplementary

Table 3.1: Bacterial host strains used in this manuscript.

Strain	Description	Reference
E.coli DH5α	Cloning host	Invitrogen
E.coli BL21(DE3)	Expression host	Thermo Fisher Scientific [73]
E.coli WK6	Expression host for Nanobodies	Zell & Fritz, 1987 [74]

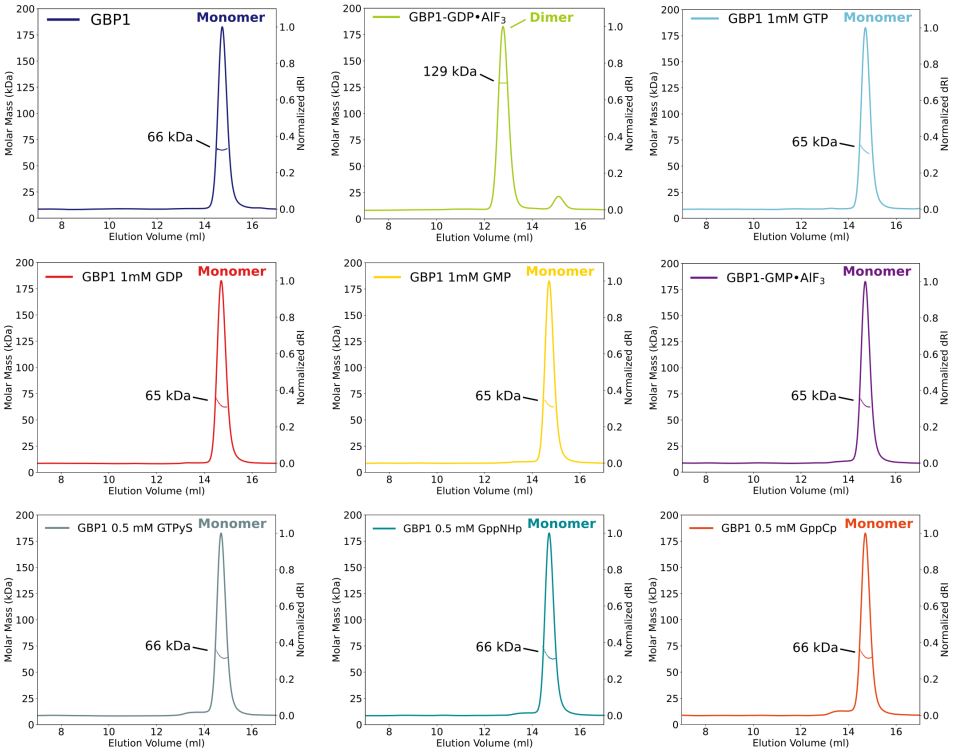

Figure 3.8: Individual SEC-MALS experiments for GBP1 with different guanine nucleotides. In the presence of GTP, GDP, GMP, GMP·AlF_3, GTPγS, Guanosine-5'-[(β,γ)-imido]triphosphate (GppNHp) and Guanosine-5'-[(β,γ)-methyleno]triphosphate (GppCp) GBP1 appears monomeric, while a GBP1 dimer peak emerges in the presence of GDP·AlF_3. The experimentally determined molecular weight is plotted across the chromatographic peak and is reported in kDa.

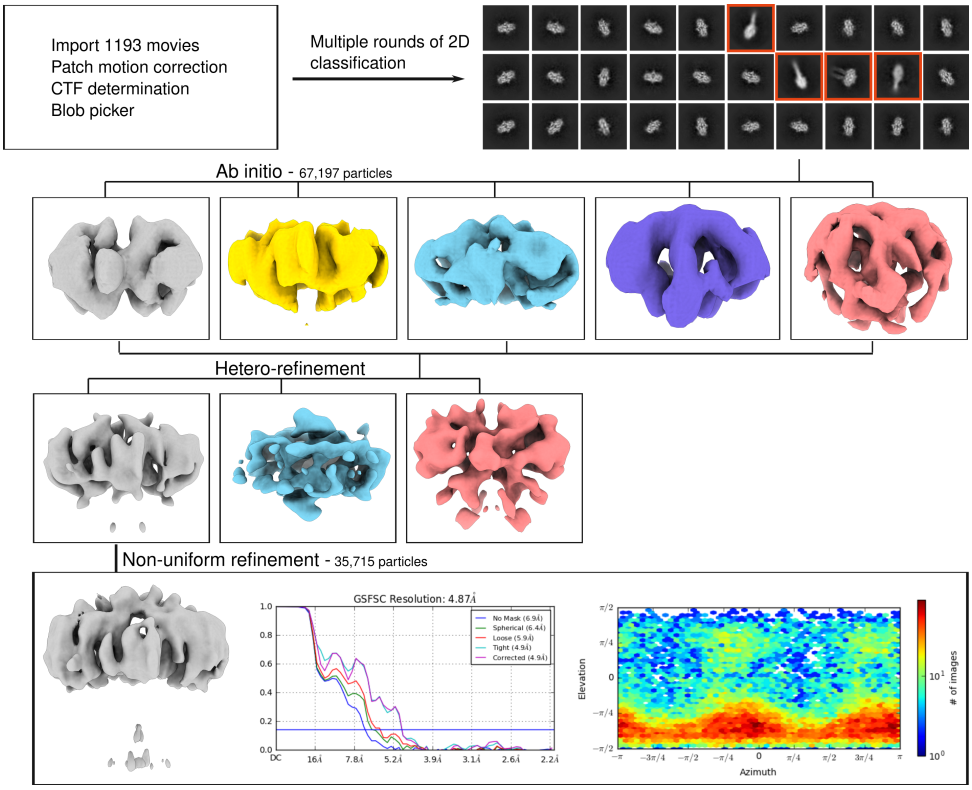

Figure 3.9: Image processing for GBP1-GDP·AlF$_3$. Single-particle analysis processing workflow GBP1-GDP·AlF$_3$ converged on the LG domain dimer. A majority of 2D classes (92% of all particles) showed a top view representative of the LG domain dimer. A subset of 2D classes also comprised the MD domain of both monomers (red boxes).

Table 3.2: Summary of SEC-MALS measurements.

	Average molecular weight [kDa]	No of measurements
GBP1	66.4 ± 2.1 kDa	n = 17
GBP1-GDP·AlF$_3$	134.6 kDa ± 4.1 kDa	n = 16
GBP1$_F$	66.1 kDa ± 0.3 kDa	n = 7
GBP1$_F$-GDP·AlF$_3$	67.6 kDa ± 1.7 kDa	n = 8
GBP1-Nb74	79.9 kDa ± 3.0 kDa	n = 2
GBP1-GDP·AlF$_3$-Nb74	154.8 kDa ± 4.8 kDa	n = 6
GBP1$_F$-Nb74	81.9 kDa	n = 1
GBP1$_F$-GDP·AlF$_3$-Nb74	81.9 kDa ± 3.5 kDa	n = 3

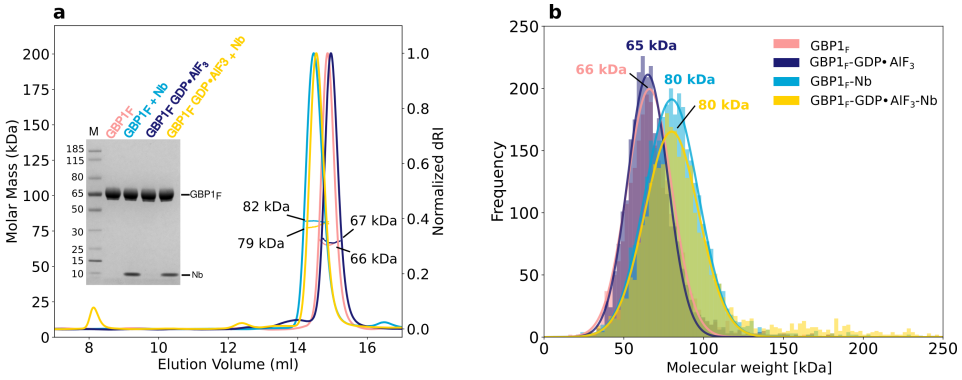

Figure 3.10: GBP1$_F$ - Nb74 interaction. (a) SEC-MALS experiments showing that farnesylated GBP1 (GBP1$_F$) appears primarily monomeric in the absence and in the presence of GDP·AlF$_3$ (M_W = 66 kDa and 67 kDa). Nb74 binds GBP1$_F$ with 1:1 stochiometry both in the absence and in the presence of GDP·AlF$_3$. For conditions containing GDP·AlF$_3$, we frequently observed an additional peak close to the void volume of the SEC column corresponding to higher molecular weight species. The inset shows SDS-PAGE analysis of the SEC-MALS input. (b) Mass photometry analysis confirming that GBP1$_F$ is monomeric in the presence of GDP·AlF$_3$ and the 1:1 stochiometry of Nb74 binding to GBP1$_F$. Note that rare events corresponding to large GBP1$_F$ assemblies such as those observed by SEC-MALS may not be detected in the chosen field-of-view for the experiments shown.

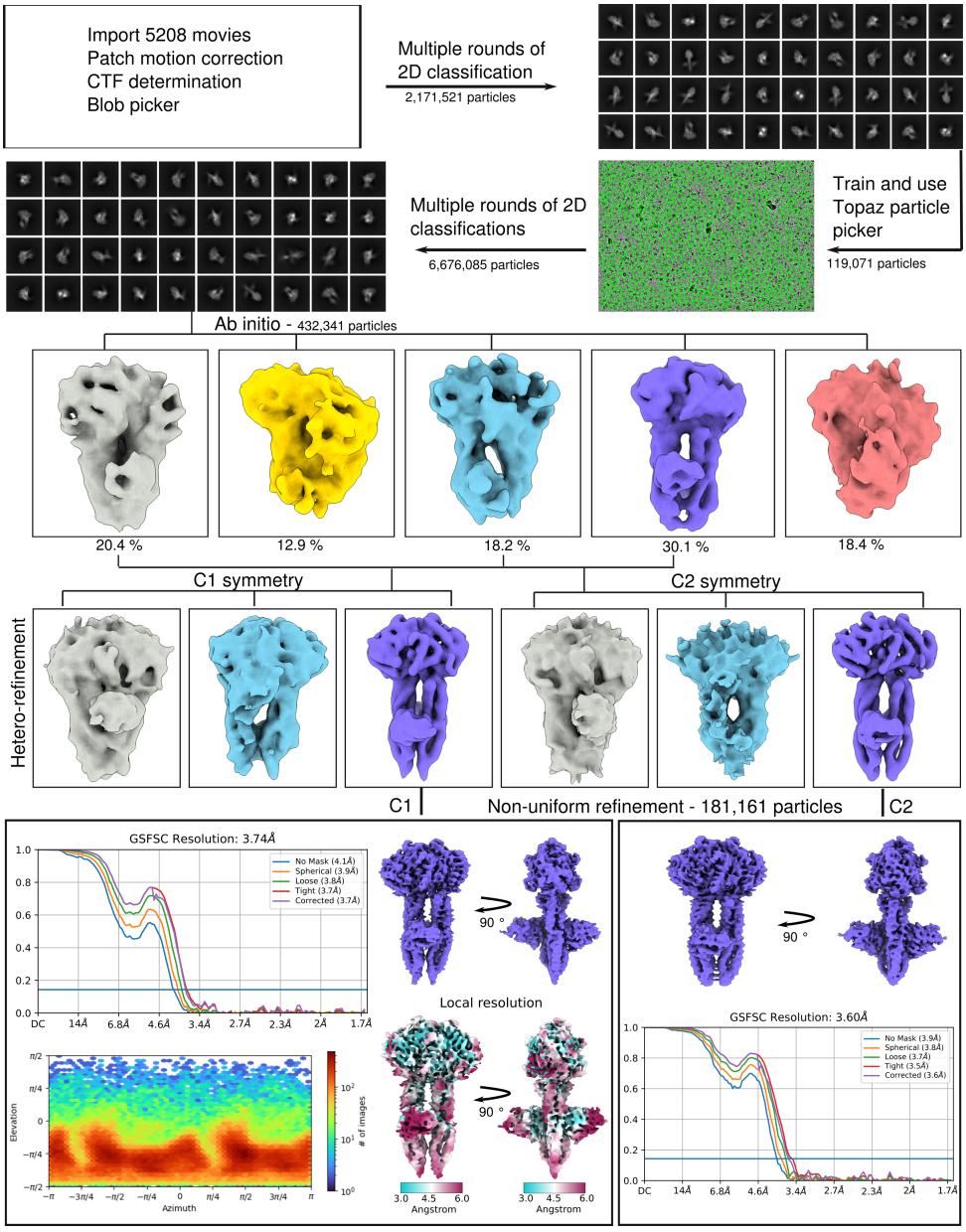

Figure 3.11: Image processing and structure determination of GBP1-GDP·AlF$_3$-Nb74. The processing workflow is displayed for both the C1 reconstruction and for the reconstruction with C2 symmetry imposed.

Table 3.3: Summary of cryo-EM data collection and data processing.

	GBP1-GDP·AlF_3	**GBP1-GDP·AlF_3-Nb74**	**$GBP1_F$-GDP·AlF_3**
Data collection			
Microscope	TFS Titan Krios	TFS Titan Krios	JEOL JEM3200FSC
Voltage (kV)	300	300	300
Detector	Quantum-K2	Quantum-K3	Quantum-K2
Energy filter	Gatan Bio-quantum	Gatan Bioquantum	In-column omega filter
Micrographs collected (no.)	1193	5208	395 / 606
Pixel size (Å)	1.09	0.834	1.22 / 2.449
Electron exposure (e-/Å^2)	60	60	48 / 13
Frame number	48	50	60
Exposure time (s)	10	2.2	12
Defocus range (μm)	-0.5 to -3.5	-0.6 to -2.2	-1.0 to -3.0
Data processing			
Symmetry imposed	C2	C1 or C2	
B-factor (Å^2)	231.1	158.3 (C1), 168.4 (C2)	
Final number of particles	35,715	181,161	
Final map resolution (Å)	4.9	3.7 (C1), 3.6 (C2)	
Map resolution range (Å)	*	3.0 - 6.0	

* Due to strong preferred orientation, the map resolution range for GBP1-GDP·AlF_3 is not conclusive.

Table 3.4: Summary of model refinement/validation statistics for the cryo-EM structure of GBP1-GDP·AlF_3-Nb74.

	GBP1-GDP·AlF_3-Nb74
Model refinement	**PDB 8cqb**
Initial model used (PDB code)	1f5n and 2b92
Primary sequence (Uniprot ID)	P32455
Model resolution	
FSC map-model (0.5)**	3.97 (4.06 unmasked)
Map sharpening B-factor ($Å^2$)	-158.3
Model composition	
Non-hydrogen atoms	7688
Protein residues	956
Nucleotides	2
Ligands	4
B-factors	
Overall ($Å^2$)	74.77
Protein ($Å^2$)	75.13
Ligand ($Å^2$)	52.60
Validation	
MolProbity score	0.94
Clashscore	5.28
RMSD	
Bond lengths (Å)	0.005
Bond angles (°)	0.993
Rotamer outliers (%)	1.29
Ramachandran plot	
Favored (%)	93.49
Allowed (%)	6.09
Disallowed (%)	0.42

** Map-model FSC computed against globally sharpened map

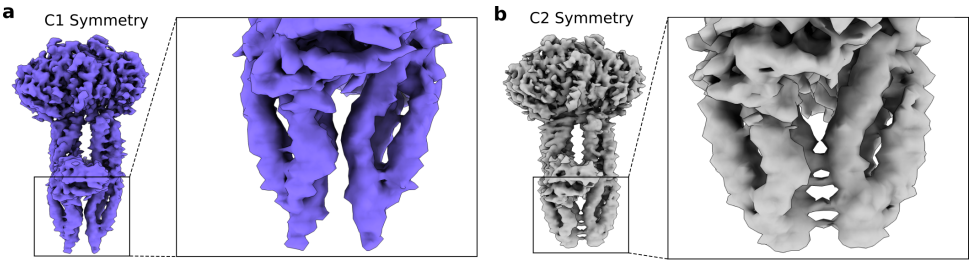

Figure 3.12: Comparison of a cryo-EM map of GBP1-GDP·AlF$_3$-Nb74. (a) without imposed symmetry (C1) or (b) with C2 symmetry imposed. Imposing strict C2 symmetry resulted in symmetrisation artefacts arising at the C-terminal part of the MD domain.

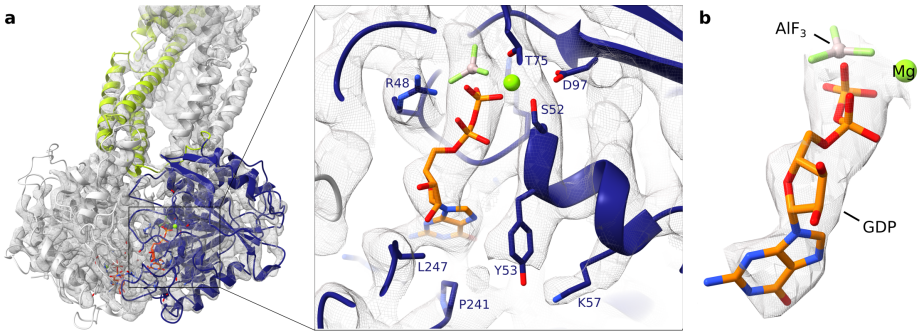

Figure 3.13: Guanine nucleotide binding site. (a) Location of one of the two GDP·AlF$_3$ ligands at the GBP1 dimer interface and close-up of the catalytic site with the ligand in stick representation superposed onto the cryo-EM density. The catalyic arginine R48 and residues in close proximity to the ligand are also highlighted in stick representation. (b) GDP·AlF$_3$ ligand displayed with cropped cryo-EM density.

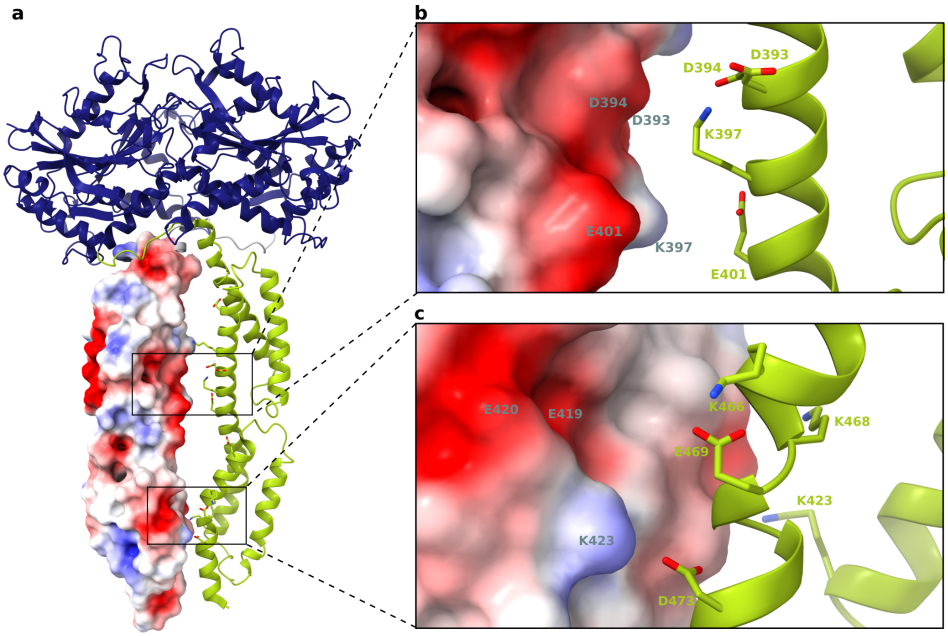

Figure 3.14: Overview of charged residues in the C-terminal helical domain (CTHD) of the GBP1 dimer. (a) Charged residues at the interface between the CTHDs are displayed as sticks for one of the monomers. The CTHD of the other monomer is displayed in surface representation with its mapped electrostatic potential. Note that the resolution of the EM density map in this region did not allow unambiguous modelling of their side chain conformations and only preferential rotamers are shown without reference to potential interactions. (b) and (c) Close-up of the MD interfaces between two GBP1 monomers in the dimer. Residues with opposing charges can be found on both sides of the interface, potentially stabilising the two parallel middle domains of the GBP1 dimer by electrostatic interactions.

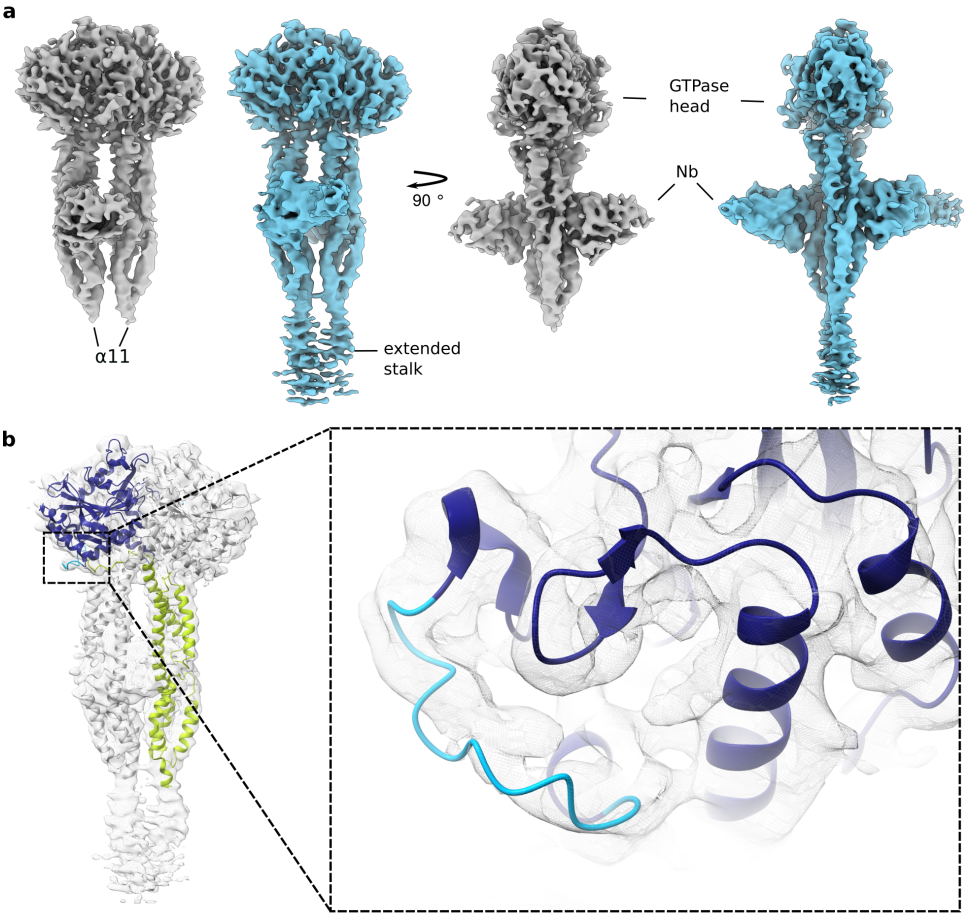

Figure 3.15: LocScale map of the GBP1–Nb74 dimer. (a) Locally sharpened density maps (LocScale2 [39]) reveal additional density protruding from helix α11 consistent with a flexible GED. (b) The locally sharpened map also allowed tracing the α3-α3' loop (residues 156 to 167), highlighted in light blue.

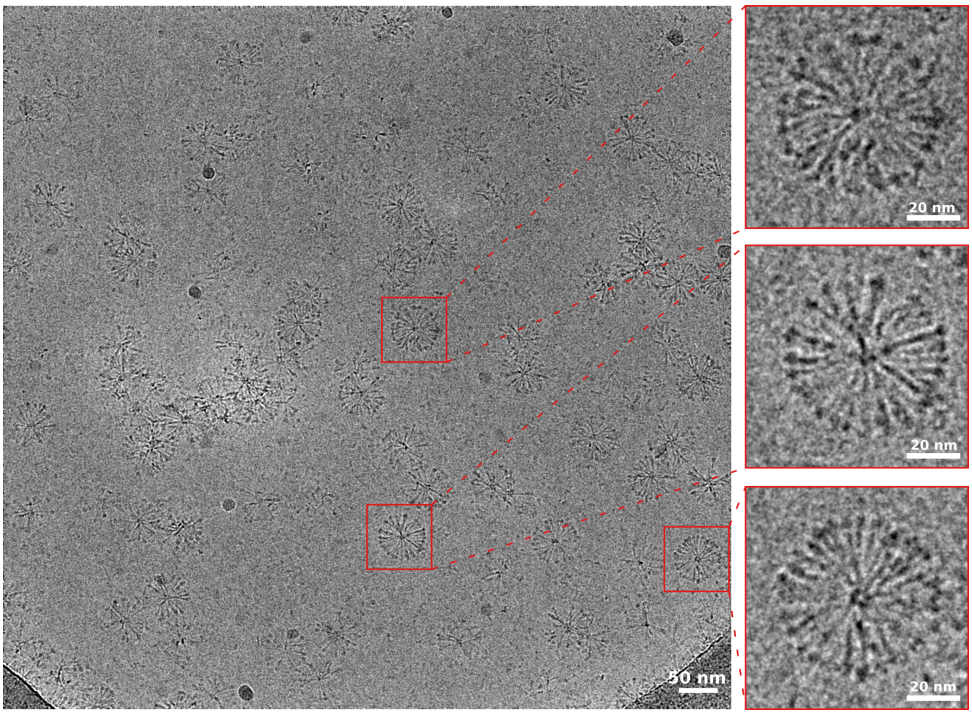

Figure 3.16: Representative cryo-EM micrograph of GBP1$_F$ in the presence of GDP·AlF$_3$. In the absence of lipids, farnesylated GBP1$_F$ oligomerises into flower-like assemblies.

Table 3.5: Summary of data collection parameters of cryo-electron tomograms.

	Tomogram 33 and Tomogram 39	**Tomogram 50**
Content	GBP1$_F$-GDP·AlF$_3$ + BPLE liposomes	GBP1$_F$-GDP·AlF$_3$ + BPLE liposomes
Pixel size (Å)	3.075	3.075
Total electron exposure (e-/Å^2)	93.94 (1.54 per increment)	100.04 (1.64 per increment)
Tilt range (°)	-60 to 60	-60 to 60
Increment (°)	2	2
Acquisition scheme	Bidirectional	Bidirectional
Frame number	10 per increment	20 per increment
Exposure time per increment (s)	2.0	3.0
Defocus (µm)	-5.0	-4.0

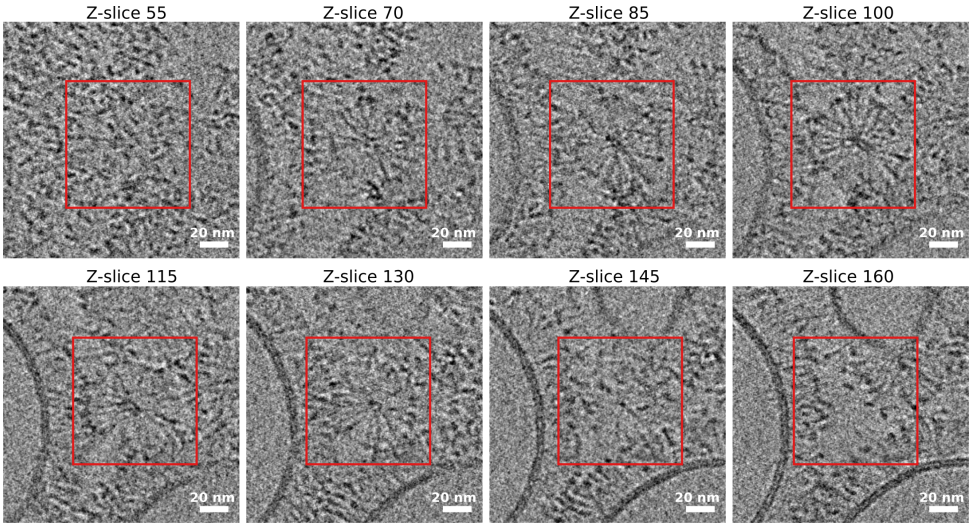

Figure 3.17: Tomographic z-stack of spherical, micellar GBP1$_F$ assemblies. Slices through the z-stack show the varying diameter of GBP1$_F$-GDP·AlF$_3$ assemblies consistent with a spherical geometry. Associated movie: Supplementary Data movie SM3.

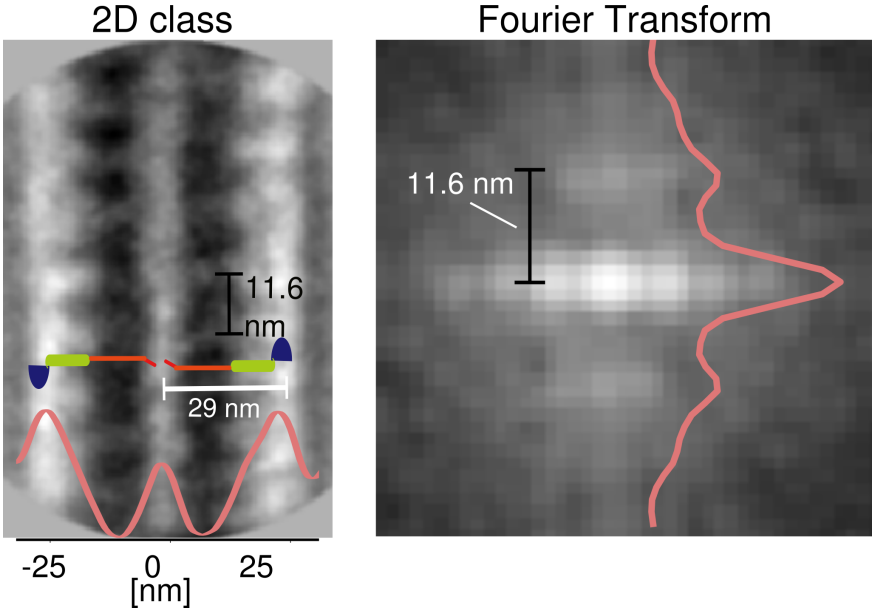

Figure 3.18: GBP1$_F$-GDP·AlF$_3$ tubular protrusion. 2D class average of negatively stained GBP1$_F$-GDP·AlF$_3$ tubular protrusion (left panel). The computed power spectrum shows a principal layer line at 0.086 Å^{-1}, corresponding to a periodicity of 11.6 nm along the filament axis (right panel).

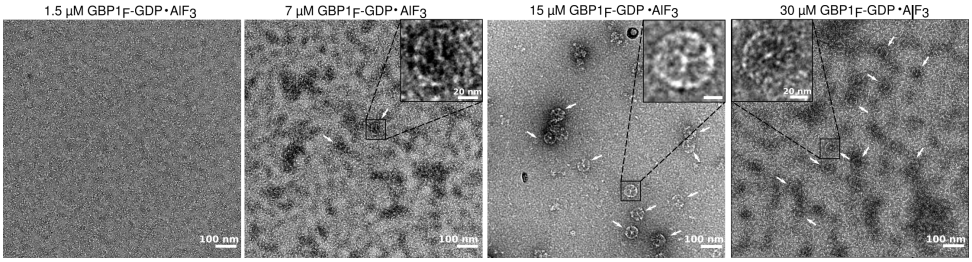

Figure 3.19: Micelle formation of GBP1$_F$-GDP·AlF$_3$ is concentration dependent. Formation of micellar assemblies of GBP1$_F$-GDP·AlF$_3$ (white arrows) starts beyond a threshold concentration of around 7 µM.

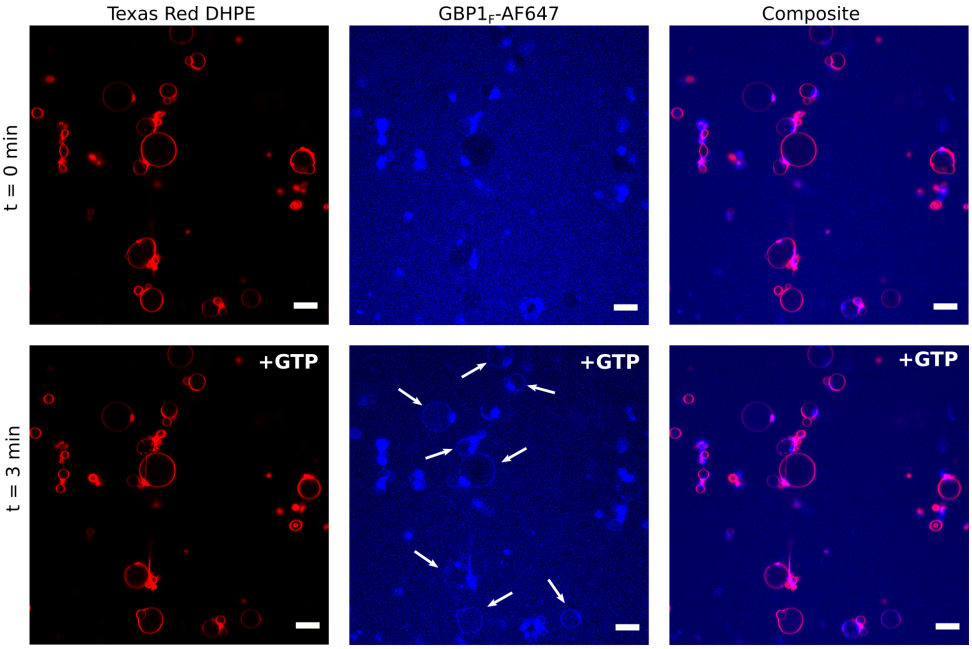

Figure 3.20: Confocal fluorescence imaging of GBP1$_F$ on GUVs. GBP1$_F$-Q577C-AF647 shows weak binding to texas red-DHPE labelled GUVs 3 min after the addition of 1 mM GTP (white arrows). Scale bars correspond to 5 µm.

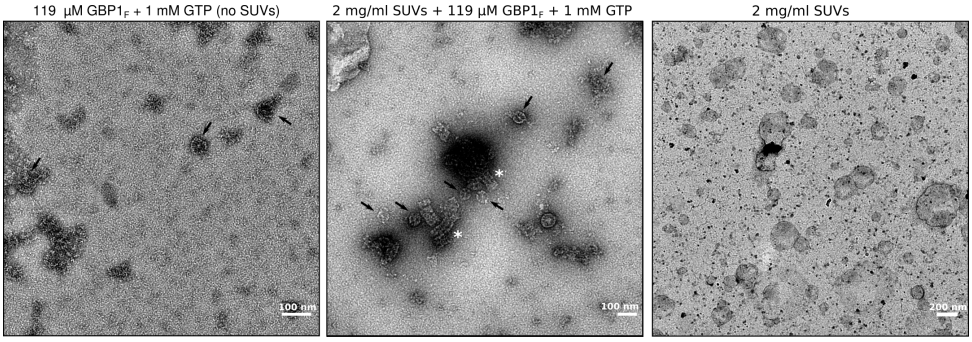

Figure 3.21: GTP-induced assembly of GBP1$_F$ micelles and membrane fragmentation. Micelle formation of GBP1$_F$ (black arrows) was observed after addition of 1 mM GTP to a highly concentrated GBP1$_F$ solution (119 µM) in the absence of lipids (left panel). Upon addition of 2 mg/ml SUVs, GBP1$_F$ remodelled SUVs into spherical micelles (middle panel; arrows) and short filaments (white asterisks). A sample containing 2 mg/ml of SUVs without GBP1$_F$ is shown for comparison (right panel).

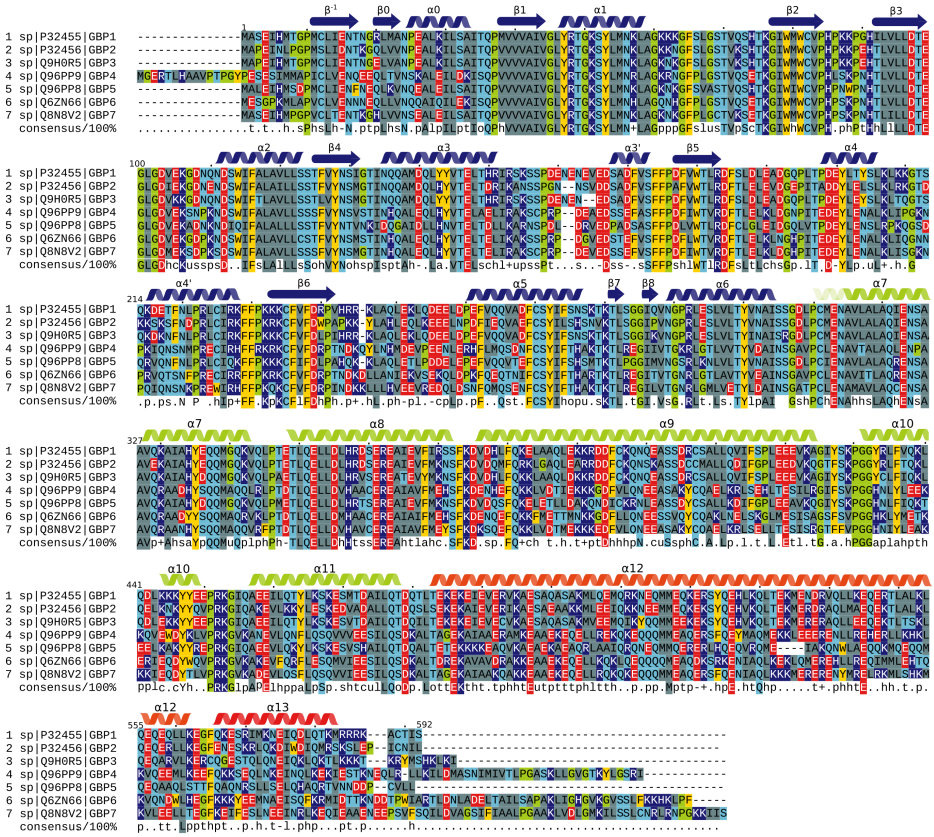

Figure 3.22: Multiple sequence alignment (MSA) of human GBP1-GBP7. Primary sequences of GBP1 - GBP7 (UniProt: P32455, P32456, Q9H0R5, Q96PP9, Q96PP8, Q6ZN66, Q8N8V2) were used as input for Clustal Omega [69]. Secondary structure elements for GBP1 [35] are displayed for guidance. The colour of the alpha-helices and beta-sheets correspond to the domain architecture of GBP1 shown in Figure 3.1a and used throughout the main text (blue: Large GTPase domain, green: Middle domain (MD), orange/red: GTPase effector domain). Residues are coloured by physicochemical property of the side chain (grey: hydrophobic, light blue: polar, red: negatively charged, dark blue: positively charged, yellow: aromatic, green: special cases). The consensus sequence (100 %) is shown below the alignment together with conserved physicochemical classes (l: aliphatic, a: aromatic, c: charged, h: hydrophobic, -: negative, p: polar, +: positive, s: small, u: tiny, t: turnlike).

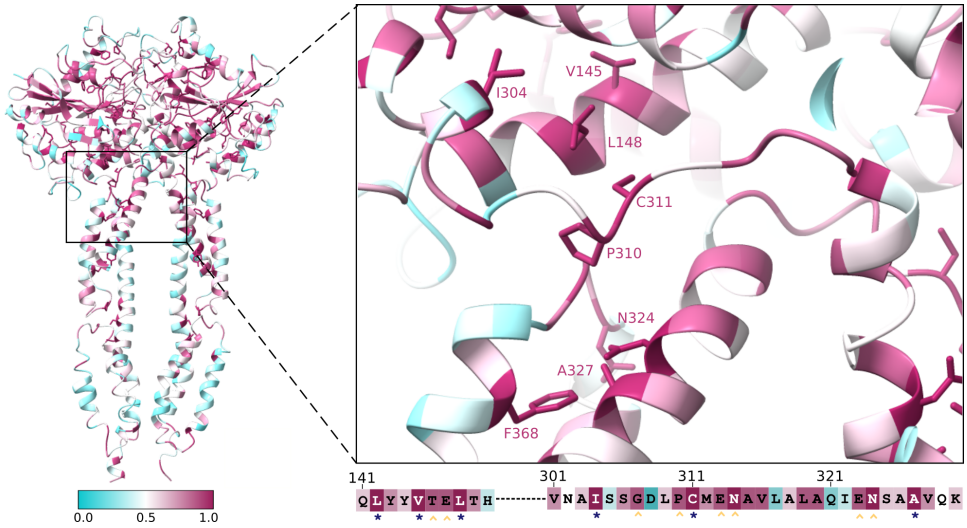

Figure 3.23: Sequence conservation mapped onto the structure of the GBP1-GDP·AlF$_3$-dimer. Highly conserved regions are displayed in magenta whereas less conserved areas are shown in cyan. Residues with a conservation higher than 95 % are shown in stick representation. Right panel: Close-up of the cross-over linker region. The primary sequence of highly conserved stretches is displayed below (blue asterisk: highly conserved and buried residue, yellow circumflex: highly conserved and exposed residue).

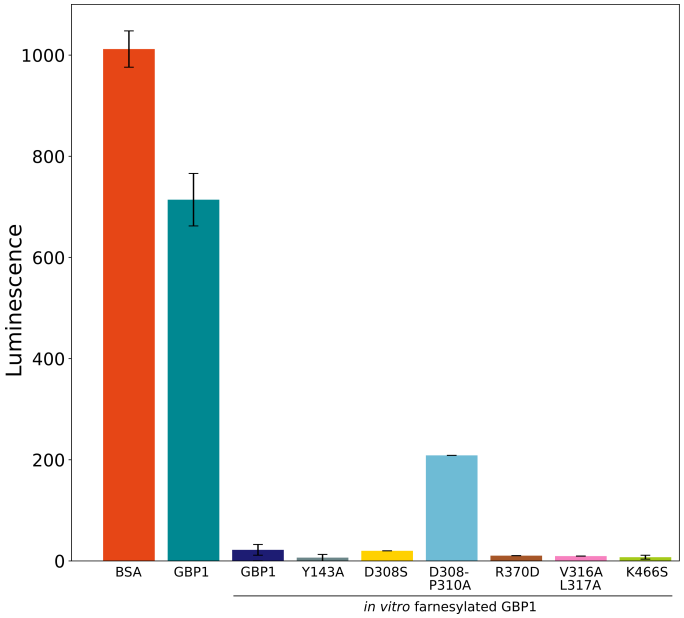

Figure 3.24: GTPase activity assay of GBP1. GTPase activity of non-farnesylated GBP1 and in vitro farnesylated GBP1 WT and GBP1 variants was determined using the GTPase-Glo™ Assay (Promega). Low luminescence signal corresponds to high GTPase activity. Bovine serum albumin (BSA) was used as a negative control (n=5).

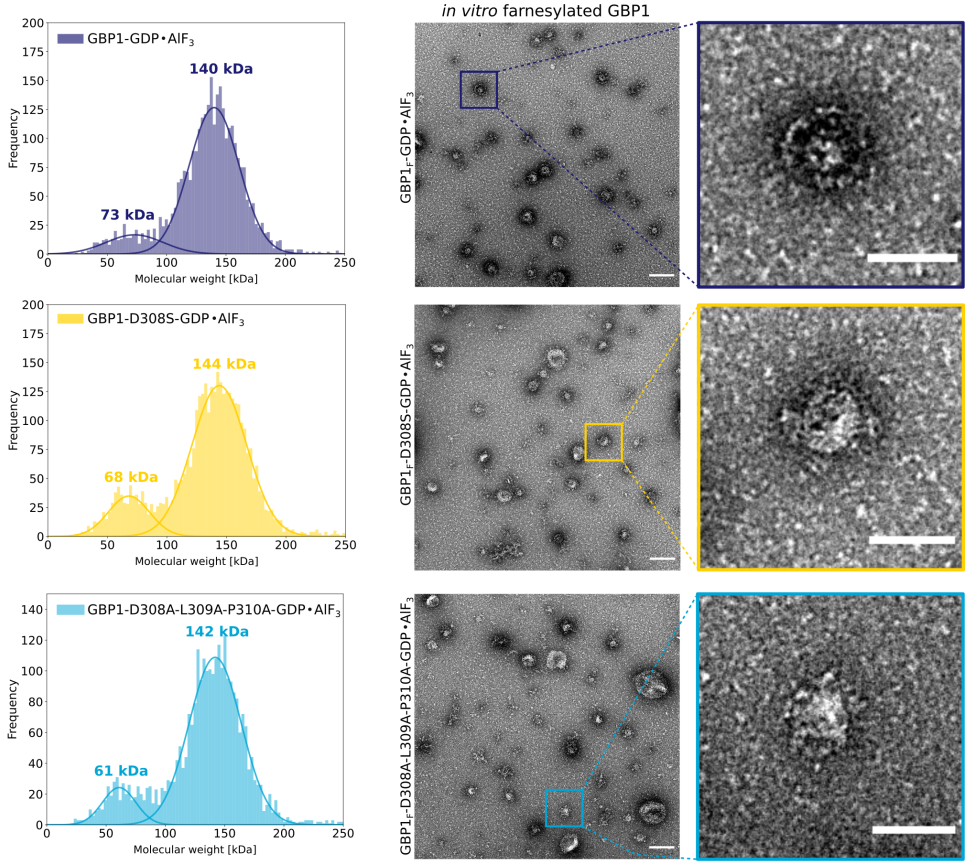

Figure 3.25: Effect of GBP1 variants on dimerisation and of GBP1$_F$ variants on membrane binding. Left panel: Individual mass photometry spectra revealing that variants D308S and D308A-L309A-P310A do not influence the ability of GBP1 to form dimers. Right panel: Negative stain EM of GBP1$_F$, GBP1$_F$-D308S and GBP1$_F$-D308A-L309A-P310A bound to SUVs. A reduction in membrane binding for GBP1$_F$-D308S and GBP1$_F$-D308A-L309A-P310A is observed, but the capability to bind to membranes is not entirely lost. Scale bars correspond to 200 nm in the left column and 100 nm in the right column.

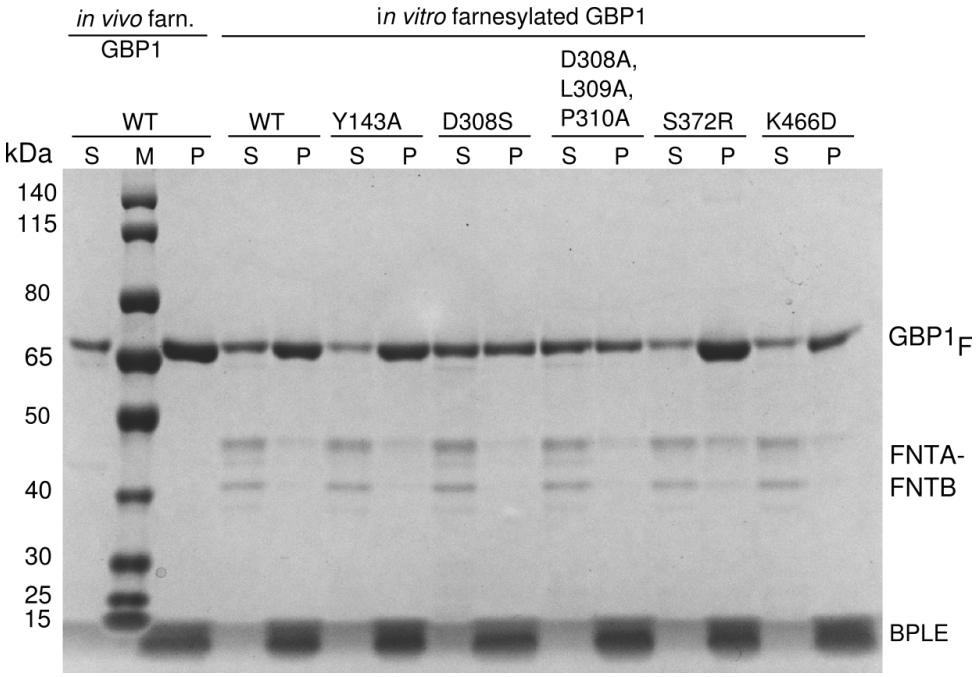

Figure 3.26: SDS-PAGE analysis of co-sedimentation assays. Representative uncropped SDS-PAGE gel from Figure 3.6 showing the result of a co-sedimentation assay of $GBP1_F$ variants with BPLE-derived liposomes liposomes. S: Supernatant, P: Pellet

Table 3.6: Summary of data collection parameters of LPS-datasets

	LPS-EB	LPS-EB-GBP1-GDP·AlF$_3$	LPS-SM	LPS-SM-GBP1$_F$-GDP·AlF$_3$	LPS-ST	LPS-ST-GBP1$_F$-GDP·AlF$_3$
Micrographs collected (no.)	488	561	118	515	79	437
Pixel size (Å)	1.288	1.288	2.449	1.288	1.891	1.891
Electron exposure (e-/Å^2)	46.68	48.01	16.15	43.01	32.02	26.53
Frame number	50	50	50	50	60	48
Exposure time (s)	15	15	15	15	15	12
Defocus range (µm)	-1.0 to -3.5	-1.0 to -3.0	-1.0 to -3.5	-1.0 to -3.5	-1.0 to -3.5	-1.0 to -3.5

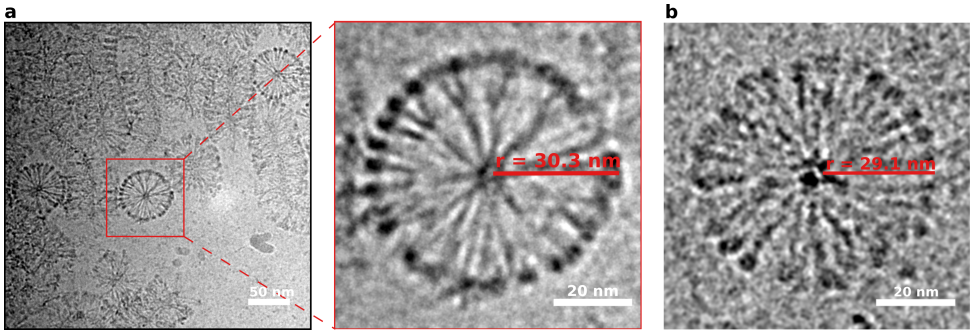

Figure 3.27: Top views of filaments formed by GBP1$_F$ on LPS-EB. (a) Putative top views of GBP1$_F$-decorated LPS micelles are indicative of a highly ordered coat. The diameter of these projections was determined to be 60 nm. (b) For comparison, a GBP1$_F$ micelle with a diameter of 58 nm is shown.

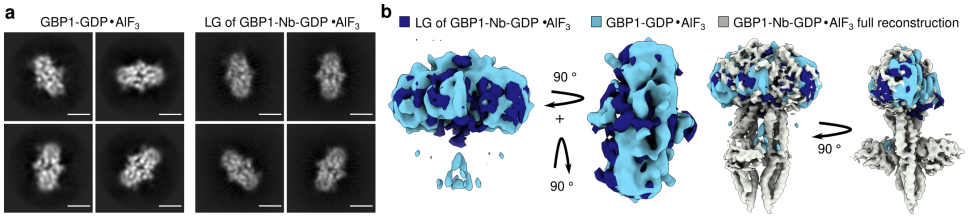

Figure 3.28: Comparison of 3D reconstructions of the LG dimer-like particles from the GBP1-GDP·AlF$_3$ and GBP1-GDP·AlF$_3$-Nb datasets. (a) 2D classes representative for projections of the LG domains of the GBP1 dimer from both datasets. Scale bar corresponds to 4 nm. (b) 3D reconstructions based on particles from 2D classes in (a) displaying density consistent with a dimeric LG domain. Rightmost panels: Comparison of both maps to the 3D reconstruction of GBP1-GDP·AlF$_3$-Nb dataset using all particles.

Table 3.7: Primer sequences used in this manuscript (f indicating the forward primer and r the reverse primer).

AJ LO-	Description	Sequence
002	hGBP1-f	GGTCTCCCATGGCGAGCGAGATCCACATG
004	hGBP1-r	GGTCTCCGGCCGCTTATTAGCTG
023	FNTA-f	CGTCTCCCATGGCGGCCACCGAGGG
024	FNTA-r	CGTCTCCGGCCGCTTATTATTGCTGTACATTTGTTGG TGAGTC
025	FNTB-f	CATATGGCTTCTCCGAGTTCTTTCACC
026	FNTA-r	CGTCTCCTCGATTATTAGTCGGTTGCAGGCTCTGCCG
027	FNTB-QC-f	TTGACTGCTGCGTATGTGGGTGCAAGGTGTGGA
028	FNTB-QC-r	TCCACACCTTGCACCCACATACGCAGCAGTCAA
074	GBP1-Q577C-f	CATTTTGGTCTGCAGGTCTGCAATCTCGTTTTTCATGAT
075	GBP1-Q577C-r	ATCATGAAAAACGAGATTGCAGACCTGCAGACCAAAATG
076	FNTA-His6-Gib-f	TTTTGTTTAACTTTAATAAGGAGATATACCATGCATCATCAT CACCACCAC
077	FNTA-His6-Gib-r	ACTTAAGCATTATGCGGCCTTATTGCTGTACATTTGTTGGT GAG
078	pCDFDuet1-Gib-spacer-f	CTCACCAACAAATGTACAGCAATAAGGCCGCATAATGCT TAAGT
083	pCDFDuet1-Gib-r	GTGGTGGTGATGATGATGCATGGTATATCTCCTTATTAAA GTTAAACAAAA
090	pCDFDuet1-Gib-f	GAGCCTGCAACCGACTAATAATCGAGTCTGGTAAAGAAA CCG
091	pCDFDuet1-Gib-spacer-r	AAAGAACTCGGAGAAGCCATTATGTATATCTCCTTCTTAT ACTTAACTAATATA CTAAG
092	pANT-FNTB-Gib-f	CTTAGTATATTAGTTAAGTATAAGAAGGAGATATACATAAT GGCTTCTCCGAGT TCTTT
093	pANT-FNTB-Gib-r	CGGTTTCTTTACCAGACTCGATTATTAGTCGGTTGCAG GCTC
138	GBP1-Y143A-f	GCGATGGATCAGCTGGCGTATGTTACCGAACTGAC
139	GBP1-Y143A-r	GGTCAGTTCGGTAACATACGCCAGCTGATCCATCGC
146	GBP1-D308S-r	CGCGTTCTCCATGCACGGCAGGCTACCGCTGCTAATCGC
147	GBP1-D308S-f	GCGATTAGCAGCGGTAGCCTGCCGTGCATGGAGAACGCG
152	GBP1-V316A-L317A-r	GCTGTTTTCGATTTGCGCCAGCGCCGCGGCCGCGTTCTC CATGCACGG
153	GBP1-V316A-L317A-f	CCGTGCATGGAGAACGCGGCCGCGGCGCTGGCGCAAATC GAAAACAGC
164	GBP1-K466D-r	GGTCATGCTTTCCTTGCTATCCAGGTAGGTCTGCAGAATCTC
165	GBP1-K466D-f	GAGATTCTGCAGACCTACCTGGATAGCAAGGAAAGCATGACC
184	GBP1-D308A-P310A-r	CGCGTTCTCCATGCACGCGGCGGCGCCGCTGCTAATCGC
185	GBP1-D308A-P310A-f	GCGATTAGCAGCGGCGCCGCCGCGTGCATGGAGAACGCG
291	GBP1-R370D-r	GTGATCAACGTCTTTAAAGCTGCTATCAATGAACACCTC
292	GBP1-R370D-f	GAGGTGTTCATTGATAGCAGCTTTAAAGACGTTGATCAC

Table 3.8: Vectors and constructs used in this manuscript.

Name	Description	Source/ Reference
AJLV-0009	pETM14: *E.coli* expression vector (KanR)	[75]
AJLV-0038	pCDFDuet: *E.coli* expression vector (SmR)	Merck Millipore (Novagen)
AJLV-0040	pJET1.2/blunt: Positive selection cloning vector (AmpR)	Thermo Fisher Scientific
AJLD-0001	Subcloning vector pUC57 with synthetic gene of hGBP1 optimised for *E.coli* expression (AmpR)	GenScript
AJLD-0007	GST-tagged-FNTA *in vitro* expression vector pANT7 (AmpR)	DNASU clone HsCD00630808
AJLD-0008	GST-tagged-FNTB *in vitro* expression vector pANT7 (AmpR)	DNASU clone HsCD00733069
AJLD-0022	NdeI site removed from pANT7-FNTB-cGST (AmpR)	Derived from AJLD0008
AJLD-0030	pETM14-hGBP1: *E.coli* expression vector (KanR)	Derived from AJLV-0009 and AJLD0001
AJLD-0031	pCDF-Duet-FNTA: Intermediate vector for cloning purposes (SmR)	Derived from AJLV0038 and AJLD0007
AJLD-0035	pCDFDuet-FNTA-FNTB: *E.coli* co-expression vector for *in vivo* farnesylation of hGBP1 (SmR)	Derived from AJLV0038 and AJLD0022
AJLD-0052	pJET1.2 His6-FNTA: Intermediate vector for cloning purposes (AmpR)	Derived from AJLV0040 and AJLD0007
AJLD-0053	pJET1.2 FNTB (NdeI removed): Intermediate vector for cloning purposes (AmpR)	Derived from AJLV0040 and AJLD0022
AJLD-0056	pETM14-hGBP1-Q577C: *E.coli* expression vector (KanR), point mutation for site-specific labelling	Derived from AJLD0030
AJLD-0063	pCDFDuet-His-FNTA-FNTB: *E.coli* co-expression vector (SmR) to express His-FNTA-FNTB	Derived from AJLV0038, AJLD0052, AJLD0053
AJLD-0074	pMES4y-CA16697: C-His6-tagged nanobody (Nb74) raised against farnesylated GBP1	Instruct-ERIC (PID7267)
AJLD-0147	pETM14-hGBP1-Y143A: *E.coli* expression vector (KanR) with point mutation	Derived from AJLD0030
AJLD-0150	pETM14-hGBP1-L316A-V317A: *E.coli* expression vector (KanR) with point mutation	Derived from AJLD0030
AJLD-0151	pETM14-hGBP1-D308S: *E.coli* expression vector (KanR) with point mutation	Derived from AJLD0030
AJLD-0153	pETM14-hGBP1-D308A-L309A-P310A: *E.coli* expression vector (KanR) with point mutation	Derived from AJLD0030
AJLD-0158	pETM14-hGBP1-K466D: *E.coli* expression vector (KanR) with point mutation	derived from AJLD0030
AJLD-0244	pUC57-hGBP1-R370D: Subcloning vector with point mutation	Derived from AJLD0001
AJLD-0247	pETM14-hGBP1-R370D: *E.coli* expression vector (KanR) with point mutation	Derived from AJLD0244 and AJLV0009

4

Studying the effect of GBP prenylation on self-oligomerisation and coat formation.

Out of the seven human guanylate binding proteins, three are prenylated. A prenylation is a posttranslational modification that involves the attachment of either a C15 farnesyl group or a C20 geranylgeranyl group to the C-terminal cysteine of a protein. By increasing the hydrophobicity of a protein, a prenylation can facilitate membrane interactions. Despite the fact that GBP1, GBP2 and GBP5 have been shown to be prenylated in vivo, GBP1 has been identified to be the first GBP1 member on pathogens as well as pathogen containing vacuoles initiating the binding of other members of the GBP family. While GBP1 gets farnesylated, GBP2 and GBP5 are geranylgeranylated. To better understand what drives the self-assembly of GBPs and what properties are responsible for coat formation on membranes, we used biophysical methods and electron microscopy techniques to study farnesylated GBP1 and geranylgeranylated GBP2 as well as a GBP2 mutant enabling its farnesylation. We showed for the first time that geranylgeranylated GBP2 forms similar micelle like structures as farnesylated GBP1. At the same time, geranylgeranylated GBP2 and a farnesylated GBP2 mutant failed to coat membranes, highlighting that it is more than the type of prenylation responsible for coat formation on membranes.

This chapter has not been published. Contributions to the work were made by Tanja Kuhm, Cecilia de Agrela Pinto, Adja Zoumaro-Djayoon and Arjen J. Jakobi

4.1. Introduction

Guanylate binding proteins belong to a group of interferon inducible large GTPases that play a crucial role in targeting intracellular pathogens [1–5]. Humans have seven different GBPs with a high degree of sequence homology. Nevertheless, the different GBPs have been shown to exhibit distinct sub-cellular locations within the cells [6], as well as different functions within the process of cell-autonomous immunity for instance in caspase-4 recruitment and activation [4, 5, 7].

Out of the seven human GBPs, GBP1, GBP2 and GBP5 are prenylated on a C-terminal cysteine [6, 8]. Prenylation is a posttranslational modification that involves the attachment of either a C15 farnesyl group or a C20 geranylgeranyl group to the C-terminal cysteine of a protein [9]. The reaction is catalysed by either a farnesyl transferase (FTase) or a geranylgeranyl transferase (GGTase). Both enzymes are hetero-dimers consisting of either a farnesyl-protein transferase alpha and beta subunit (FNTA and FNTB, respectively) for the FTase or of FNTA and protein geranylgeranyl transferase type I subunit beta (PGGT1B) for the GGTase. Those transferases recognise an amino acid sequence called CaaX-box at the C-terminus of the target protein whose specific sequence determines the type of prenylation [10]. The C in the CaaX-box corresponds to the cysteine to which the prenyl group will be covalently attached, followed by two aliphatic amino acids (a) and a C-terminal residue (X) which determines specificity for FTase or GGTase. Farnesyltransferases preferentially bind the CaaX-box, if the X corresponds to a methionine, serine, glutamine, alanine or cysteine and geranylgeranyl transferases preferentially bind the CaaX box with X corresponding to a leucine or a glutamic acid. The C-terminal amino acid sequence of GBP1 is CTIS enabling farnesylation whereas the C-terminus of GBP2 (CNIL) and GBP5 (CVLL) are preferentially geranylgeranylated. The prenylation of a protein increases its hydrophobicity and can therefore be responsible for changes in the sub-cellular location of proteins and can facilitate membrane interactions [6]. Despite the fact that GBP1, GBP2 and GBP5 all have been shown to be prenylated *in vivo* [6], GBP1 has been identified to be the first GBP1 member on pathogens as well as pathogen containing vacuoles initiating the binding of other members of the GBP family including non-prenylated members [3–5, 7, 11, 12]. Multiple groups have proposed that a triple arginine motif (RRR584-586) at the C-terminus of GBP1 together with its farnesylation is necessary for the recruitment to membranes [13, 14]. Neither GBP2 nor GBP5 have this polybasic motif nearby their C-terminus.

Another difference between the members of the human GBPs lies in their GTPase activity. For GBP1, GMP is the major product of GTP hydrolysis (90%), whereas GBP2 hydrolyses GTP mainly to GDP (85%-90%) and only 10%-15% are further hydrolysed to GMP [15, 16]. A point mutation in GBP1 (G68A) that has been shown to inhibit the GDP to GMP hydrolysis step, without interfering with the hydrolysis from GTP to GDP [17] was unable to target *F. novicida* [12]. This highlights that additionally to the prenylation moiety and the adjacent polybasic stretch, also the GDPase activity of GBP1 can have an influence on the targeting of specific intracellular pathogens.

Additionally to membrane binding, the farnesylation of GBP1 has also been shown to facilitate self-assembly resulting in micellar structures as discussed in chapter 3. Whether

other prenylated members such as GBP2 are also able to self-assemble in the absence of lipids is still unknown.

In this study, we therefore investigated the differences between GBP1 and GBP2 in regards to their self-assembly properties as well as the abilities of geranylgeranylated GBP2 to interact with brain polar lipid extract derived small unilamellar vesicles and LPS-EB. To investigate the effect of farnesylation and geranylgeranylation, we created a GBP2-CTIS construct that can be farnesylated *in vitro*. The effects of prenylated GBP2 as well as GBP2-CTIS on its ability to dimerise and oligomerise were analysed using biophysical assays and electron microscopy. Finally, we investigated the effects of prenylation on the GTPase activity of GBP2 and compare the results to GBP1. With this study we showed for the first time that geranylgeranylated GBP2 ($GBP2_G$) is able to form micellar structures *in vitro* that are similar to earlier observed $GBP1_F$ micelles. In accordance with literature from studies performed *in vivo*, we did not observe coat formation by $GBP2_G$ or GBP2-$CTIS_F$, confirming that coat formation of GBPs is not exclusively dependent on the type of prenylation.

4.2. Results

4.2.1. Purification of prenyltransferases and GBP2 constructs

In order to study the ability of geranylgeranylated GBP2 to self-assemble and bind membranes, we expressed and purified full-length GBP2 as well as the corresponding human geranyl-transferase from *E.coli* (Figure 4.1a).

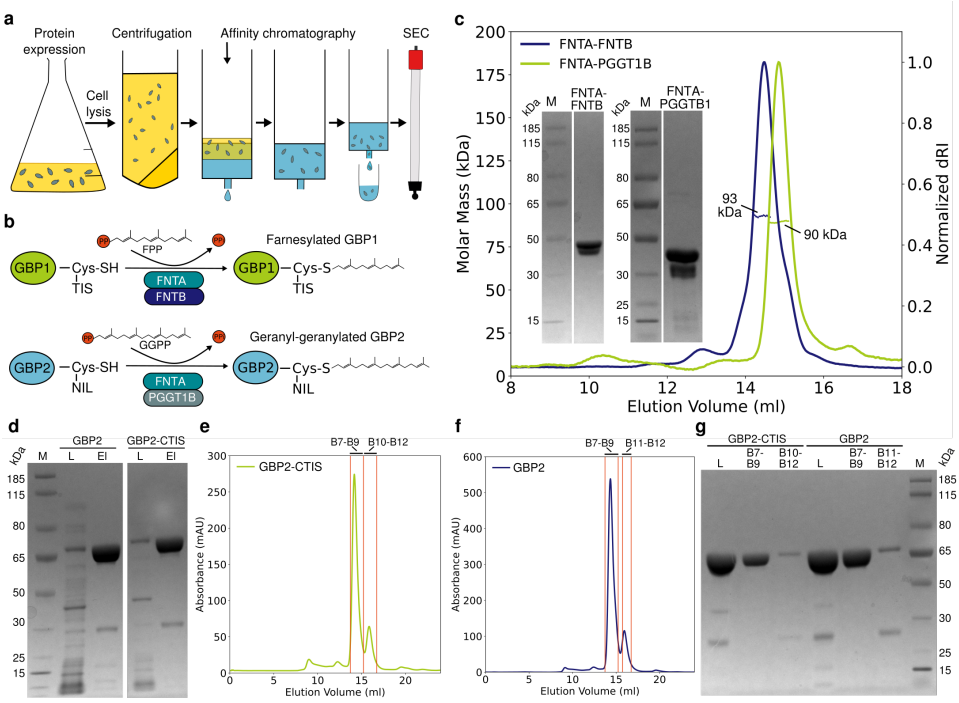

Figure 4.1: Purification of prenyl-transferases and GBP2 variants. (a) Schematic representation of protein expression and purification workflow. (b) GBP1 is farnesylated on its C-terminal cysteine by FNTA-FNTB, whereas GBP2 is geranylgeranylated by FNTA-PGGT1B. (c) SEC-MALS experiments demonstrating complex formation of FNTA-FNTB or FNTA-PGGT1B, resulting in a molecular weight of 93 kDa for FNTA-FNTB and of 90 kDa for FNTA-PGGT1B. Inset: SDS-PAGE analysis showing individual components of the complexes (MW_{FNTA} = 44.4 kDa, MW_{FNTB} = 48.8 kDa, MW_{PGGT1B} = 42.4 kDa). (d) SDS-PAGE analysis of an IMAC purification of GBP2 and GBP2-CTIS (L: Load, El: Elution). GBP2 and GBP2-CTIS showing high abundance of protein at the expected molecular weight around 67 kDa. (e) SEC elution profile of GBP2-CTIS (f) and GBP2. (g) SDS-PAGE of SEC runs in (e-f). Fraction B7-B9 were pooled, concentrated and used for further experiments.

To clarify whether the observations were dependent on the type of prenyl modification, we also created a GBP2 construct in which we swapped the native GBP2 CaaX box sequence CNIL (GBP2), which is typically geranylgeranylated, for CTIS (from GBP1) enabling farnesylation (Figure 4.1b) [6, 10]. Successful purification and complex formation of FNTA-FNTB and FNTA-PGGT1B to perform *in vitro* farnesylation and *in vitro* geranylgeranylation was confirmed by SDS-PAGE and SEC-MALS (Figure 4.1c). For FNTA-FNTB we determined a molecular weight of 93 kDa which is in accordance with its theoretical

molecular weight of 93.2 kDa. FNTA-PGGT1B eluted with an experimentally determined molecular weight of 90 kDa which is close to its theoretical molecular weight of 86.7 kDa. Both GBP2 and GBP2-CTIS expressed well and were purified via ion metal affinity chromatography, followed by a size exclusion chromatography (Figure 4.1d-f). The purity of the sample was verified by SDS-PAGE (Figure 4.1g).

4.2.2. Confirmation of GBP2 prenylation via LC-MS

To confirm *in vitro* geranylgeranylation of GBP2 and *in vitro* farnesylation of GBP2-CTIS, we used liquid chromatography-mass spectrometry (LC-MS). Trypsin digested and acidified peptides were run over a reverse phase chromatography column and the eluent was sprayed into the mass spectrometer. Fragments of GBP2 containing the C-terminal cysteine with geranylgeranyl modification eluted at a retention time around 11.7 min (Figure 4.2a and Supplementary Figure 4.10). The mass difference associated with the cysteine was determined to be 272.3 Da which is in excellent agreement with the theoretical weight of a geranylgeranylation moiety of 273.5 Da (Figure 4.2a). We were unable to detect fragments without the geranylgeranyl modification indicating that the majority of GBP2 protein was geranylgeranylated. Fragments originating from *in vitro* farnesylated GBP2-CTIS eluted at a retention time of 11 min and had an additional mass of 204.2 Da associated on its C-terminal cysteine corresponding to the theoretical molecular weight of a farnesyl moiety of 205.4 Da (Figure 4.2b and Supplementary Figure 4.11). These results confirmed that we can selectively prenylate GBP2 and GBP2-CTIS *in vitro*.

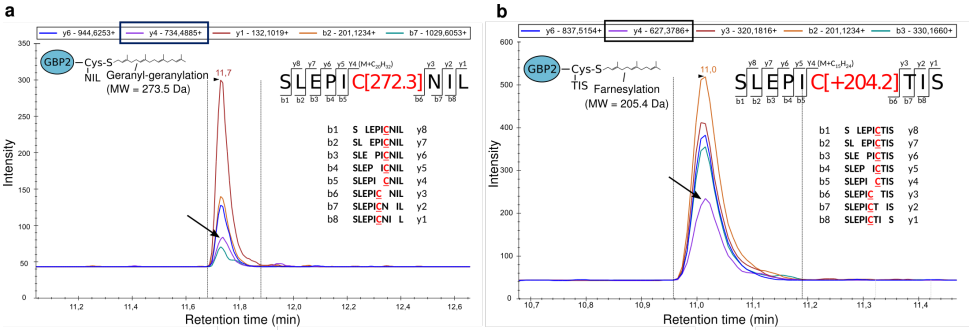

Figure 4.2: LC-MS analysis of GBP2 prenylation. LC-MS chromatogram (intensity vs retention time) of (a) $GBP2_G$ and (b) $GBP2\text{-}CTIS_F$. The y4 fragment containing the prenylation is highlighted with an arrow. The full chromatograms are shown in Supplementary Figure 4.10 and Supplementary Figure 4.11.

4.2.3. Prenylation of GBP2 influences the SEC-MALS profiles of the nucleotide activated state.

In chapter 3 we have demonstrated that prenylation of GBP1 in combination with nucleotide activation leads to the formation of dimers that further assemble into high-order micellar assemblies. Intriguingly, dimer peaks of farnesylated GBP1 are absent in its SEC-MALS profiles, presumably because the micellar assemblies do not enter the SEC column (Supplementary Figure 4.12 and [18]). Similar to GBP1, GBP2 dimerises in the presence of GDP·AlF_3, causing a shift of its molecular weight from 64 kDa (monomer) to

125 kDa (dimer) (Figure 4.3a) in the SEC-MALS profile.

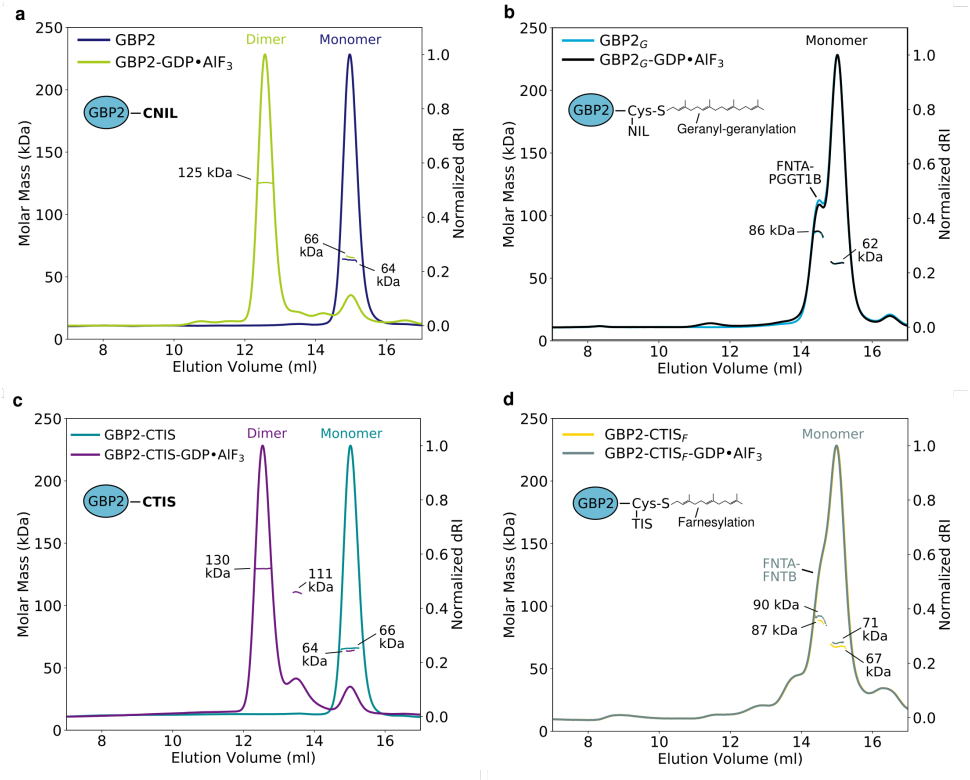

Figure 4.3: SEC-MALS analysis of prenylated GBP2. (a) SEC-MALS experiments of WT GBP2 with its original C-terminal CNIL sequence showed GBP2 dimerisation when GDP·AlF_3 was added. (b) *In vitro* geranylgeranylated GBP2 eluted in a peak corresponding to its monomeric form when GDP·AlF_3 was added (MW ~62 kDa). The peak at 86 kDa corresponds to the geranyl-transferase FNTA-PGGT1B from the prenylation reaction. (c) GBP2-CTIS containing the C-terminal sequence of GBP1 (CTIS) was able to dimerise when adding GDP·AlF_3. (d) As described in (b), *in vitro* farnesylated GBP2 eluted in a peak corresponding to its monomeric form when GDP·AlF_3 was added (MW ~68 kDa). The peak at 90 kDa corresponds to the farnesyl-transferase FNTA-FNTB.

To test whether geranylgeranylation of GBP2 influences the dimerisation observed with SEC-MALS experiments, we used *in vitro* geranylgeranylated GBP2. As for $GBP1_F$, $GBP2_G$ only displayed in a monomer peak with a molecular weight of 62 kDa when GDP·AlF_3 was added. We observed an additional peak of 86 kDa, consistent with the FNTA-GGT1 complex that was still present from *in vitro* geranylgeranylation (Figure 4.3b). To test whether the exchange of the CaaX-box from the original GBP2 amino acid sequence CNIL to CTIS affected its ability to dimerise, we repeated the same experiment with farnesylated and non-farnesylated GBP2-CTIS. We observed that GBP2-CTIS dimerised upon GDP·AlF_3 addition, shifting the molecular weight from 66 kDa to 130 kDa (Figure 4.3c). Similar to geranylgeranylated GBP2 and farnesylated GBP1, farnesylated GBP2-CTIS resulted in a monomer peak at 67 kDa/71 kDa and a second peak of the farnesyl transferase FNTA-FNTB around 90 kDa (Figure 4.3d). In analogy to our observa-

tions with GBP1 (chapter 3), we hypothesise that the prenylation of GBP2 promotes the assembly of dimers into higher-order structures which cannot migrate through the size exclusion column.

4.2.4. Geranylgeranylated GBP2 forms micellar structures upon nucleotide binding.

Negatively stained electron microscopy images of nucleotide-activated farnesylated GBP1 revealed micellar structures with a diameter of ~58 nm (chapter 3, [19]). To test whether geranylgeranylated GBP2 would also be able to form similar structures, we acquired negatively stained electron microscopy images of $GBP2_G$ in the presence of GDP·AlF_3.

Indeed, we observed circular particles of $GBP2_G$ (Figure 4.4a, red arrows). The observed particles had comparable features to the earlier described $GBP1_F$ micelles in chapter 3. The overall particle diameter determined from negative stain EM was between 56 nm and 77 nm. The $GBP2_G$ micelles seem to be less regular and less dense compared to those observed for $GBP1_F$, making it more difficult to determine the diameter accurately. Nevertheless, the distribution of diameters is in a range comparable to the average particle diameter of ~58 nm observed for $GBP1_F$ micelles (chapter 3). Similar to $GBP1_F$ micelles, we could identify spherical densities at the outer rim of the micelle with an overall diameter of 4 nm, connected to spokes that extend towards a dense center with a diameter of around 10 nm (Figure 4.4b), suggesting that their overall architecture is preserved. To obtain higher resolution detail, we acquired cryo-EM micrographs of $GBP2_G$ in the presence of GDP·AlF_3. Analogous to the negative stain images, we observed micellar structures of around 62 nm in diameter (Figure 4.4c), comparable to the particle diameter of ~58 nm observed for $GBP1_F$ micelles. For visualisation purposes, we denoised some of the cryo-EM micrographs containing $GBP2_G$ micelles using Topaz-Denoise (Figure 4.4d). Consistent with the negative stain images, the observed micelles appeared partly disordered, but key features were similar to those observed for $GBP1_F$ micelles (Figure 4.4e,f).

By taking previous observations for farnesylated GBP1 into account, and the high-sequence similarity between GBP1 and GBP2, it is likely that the observed spherical densities at the outer rim of the micelles correspond to the LG-domain of GBP2. The overall rim-to-rim diameter of the structures around 60 nm further implies that $GBP2_G$, similar to $GBP1_F$, is able to form an outstretched conformation with an extended GED domain where the geranylgeranylated α13 of the GED cluster at the center of the micelle (Figure 4.4f).

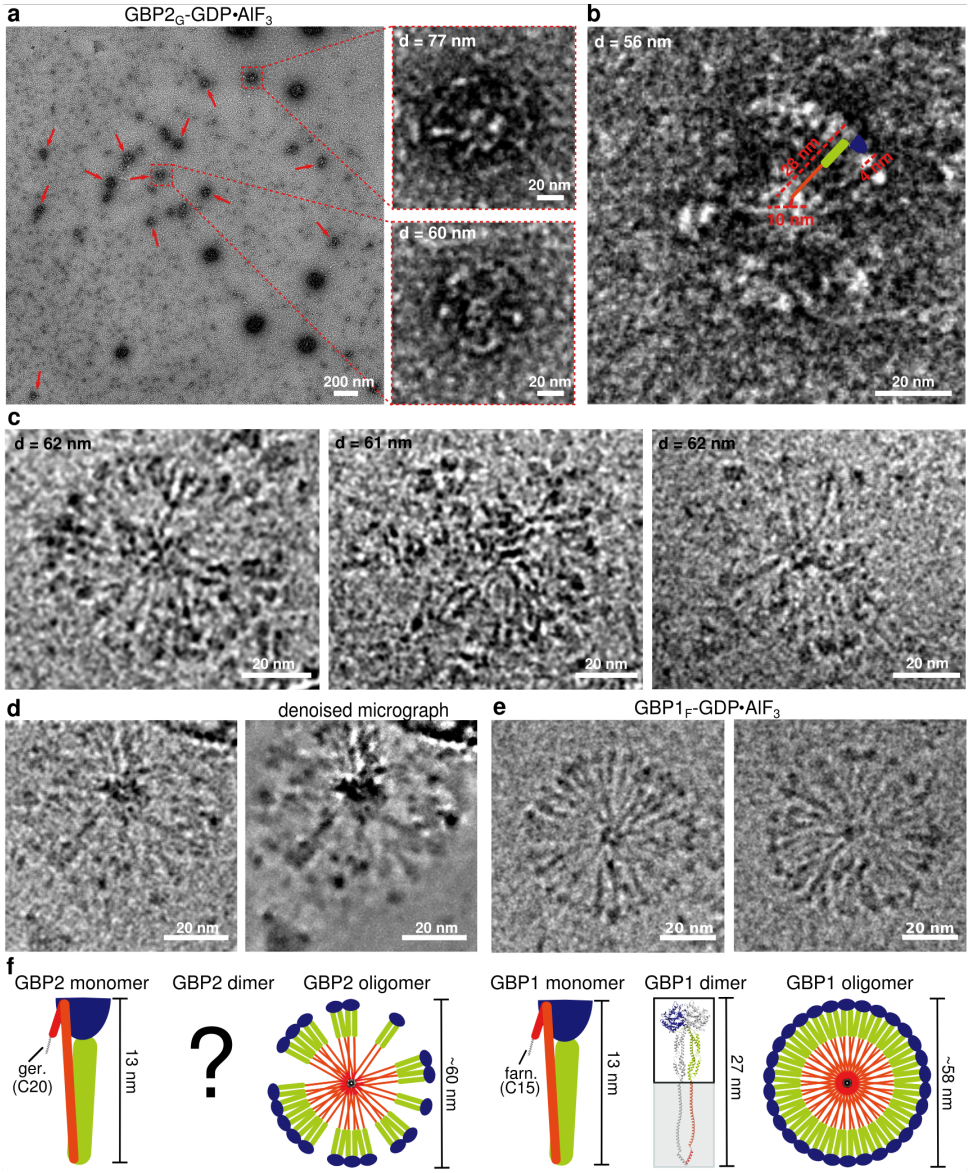

Figure 4.4: Micellar self-assembly by GBP2$_G$-GDP·AlF$_3$. (a) Negative stain image of GBP2$_G$-GDP·AlF$_3$ show micellar structures with varying diameters between 56 nm and 77 nm. (b) Close up of GBP2$_G$ micelle with an overall diameter of 56 nm, a dense particle center of 10 nm in diameter and spherical densities of 4 nm in diameter at the perimeter. (c) Cryo-EM image of GBP2$_G$ micelles with a diameter between 61 nm and 62 nm. (d) Topaz-Denoise was used to remove high-frequency noise of cryo-EM micrographs to better visualise GBP2$_G$ micelles. (e) Cryo-EM image of GBP1$_F$ micelles shown as comparison. (f) Schematic representation of different oligomeric states of GBP1 and GBP2. The cryo-EM structure of the GDP·AlF$_3$ stabilised dimer of GBP1 only resolved the LG-domain and middle domain (chapter 3).

4.2.5. Geranylgeranylated GBP2 does not coat SUVs or LPS

Following the observation that geranylgeranylated GBP2 was able to form micellar structures when activated with nucleotides, we next wanted to study potential coat formation of GBP2$_G$ using an *in vitro* reconstituted membrane system. Although GBP2 has been shown to be prenylated *in vivo* [6], the formation of GBP2 coats on intracellular or pathogen membranes on its own has not been observed yet. Instead GBP2 has been shown to associate with membranes in a hierarchical manner being recruited to a preformed GBP1$_F$ membrane coat [4, 5, 7].

To test whether GBP2$_G$ behaves similar in an *in vitro* system, we used negative stain microscopy of nucleotide activated GBP2$_G$ incubated with small unilamellar vesicles (SUVs) derived from brain polar lipid extract (BPLE). We did not observe coat formation around SUVs, which we concluded from SUVs appearing similar to SUV images without GBP2$_G$ present (Figure 4.5a, c). To test whether GBP2$_G$ can coat O-antigen containing LPS-EB as a surrogate for gram-negative membranes of intracellular pathogens, we again performed negative stain experiments. Unlike GBP1$_F$, which forms a discernible coat around LPS micelles (Figure 4.5d, left panel), we observed GBP2$_G$ to mainly form undefined aggregates as well as occasional GBP2$_G$ micelles (Figure 4.5d, right panel and close-up).

The LPS itself appeared uncoated and similar to LPS that was imaged without the addition of protein (Figure 4.5b), suggesting that GBP2$_G$ does not interact with LPS at all. To further investigate this point, we resorted to a system containing deep rough LPS from *S. enterica* sv. Minnesota R595 (LPS-SM), for which we had previously observed strong differences in micellar morphology in the presence or absence of GBP1$_F$ (chapter 1 and Figure 4.5e, left and middle panel). Instead, for GBP2$_G$ we only observed naked LPS-SM eggshells (Figure 4.5e, right panel).

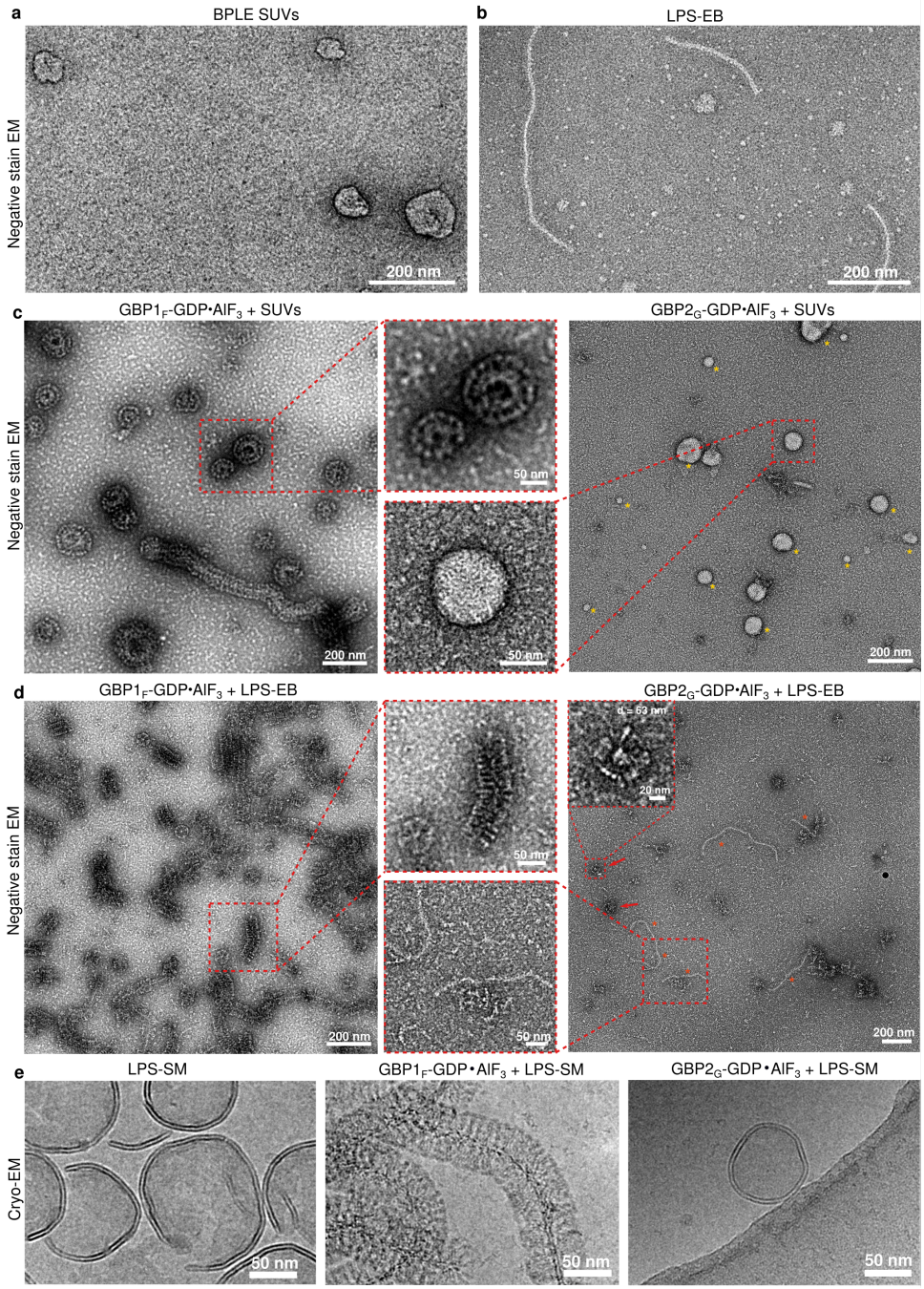

Figure 4.5: Nucleotide activated GBP2$_G$ does not form a dense coat on SUVs or LPS. (a) Negative stain images of bare BPLE SUVs and (b) LPS-EB. (c) Negative stain images comparing GBP1$_F$ and GBP2$_G$ on BPLE SUVs. Yellow asterisks indicate bare BPLE-SUVs. (d) Negative stain images comparing GBP1$_F$ and GBP2$_G$ on LPS-EB. Orange asterisks indicate bare LPS-EB, red arrows point at GBP2$_G$ micelles. (e) Cryo-EM micrographs of deep rough LPS from *S. enterica* sv. Minnesota R595 (LPS-SM) and LPS-SM coated with GBP1$_F$ adapted from chapter 3 (left and middle panel) are compared with LPS-SM incubated with GBP2$_G$ (right panel).

The previous experiments demonstrated that GBP2$_G$ lacks the ability to form membrane coats. To investigate the possibility that GBP2$_G$ may form smaller or less ordered associations with membranes that may be difficult to discern with the limited resolution of negative stain EM, we imaged GBP$_G$ in the presence of BPLE SUVs using cryo-EM. For better comparison, we first acquired cryo-EM micrographs of uncoated SUVs (Figure 4.6a) as well as of GBP1$_F$-coated SUVs (Figure 4.6b). Cryo-EM micrographs confirmed our observation from negative stain-EM that nucleotide activated GBP2$_G$ is unable to form a dense coat on SUVs (Figure 4.6c) when using similar protein concentrations as for GBP1$_F$ (22 µM for GBP2$_G$ in Figure 4.4c and 15 µM for GBP1$_F$ in Figure 4.4b). Detailed comparative analysis of SUV membranes in the presence and absence of GBP2$_G$ showed additional densities associated with the membrane (resulting in membranes appearing less smooth) only when GBP2$_G$ was present, suggesting GBP2$_G$ may sparsely decorate rather than fully coat SUV membranes (compare Figure 4.6a and c; Figure 4.6d).

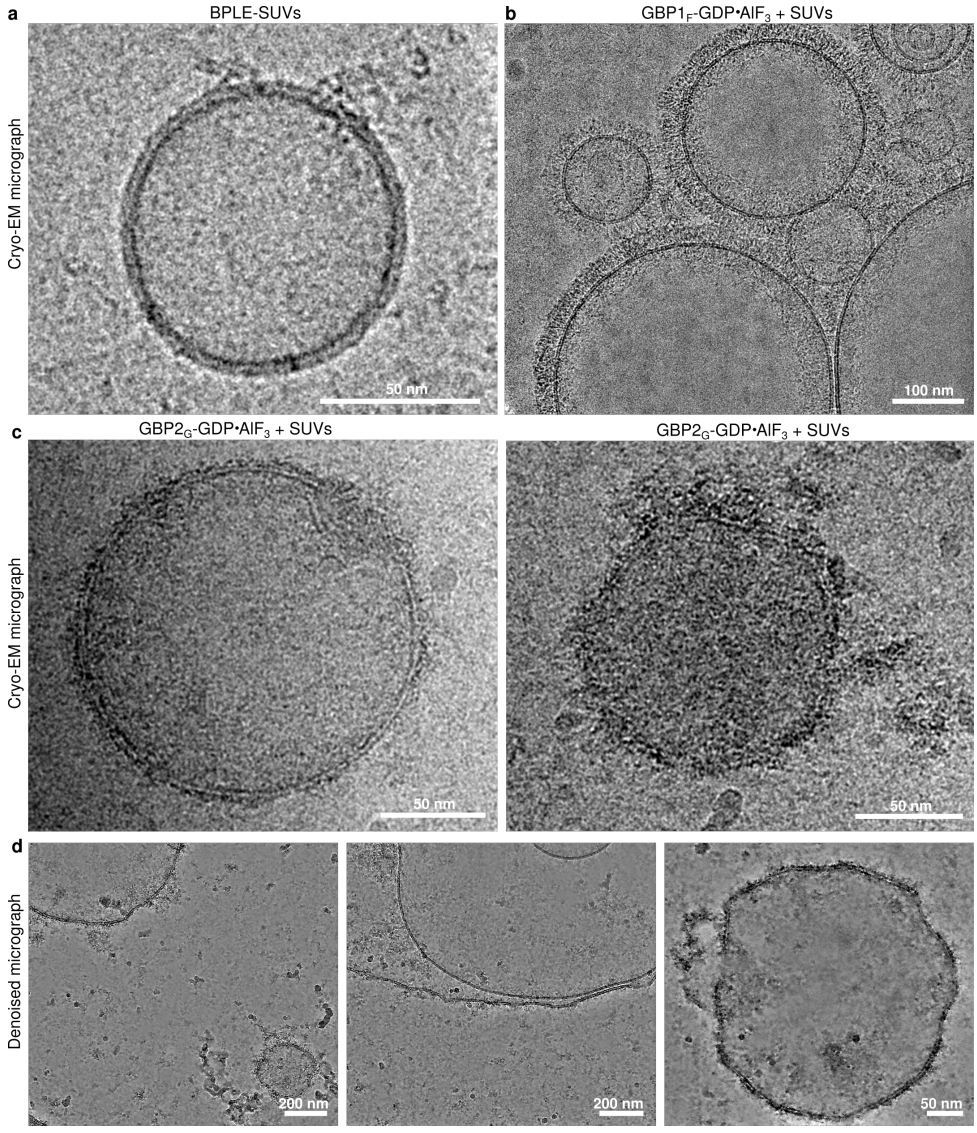

Figure 4.6: Cryo-EM micrographs of nucleotide activated GBP2$_G$ on SUVs. (a) Cryo-EM micrograph of a BPLE SUV. (b) GBP1$_F$-GDP·AlF$_3$ incubated with SUVs, imaged by cryo-EM. (c) Cryo-EM micrographs of GBP2$_G$-GDP·AlF$_3$ on SUVs. (d) Topaz-denoised micrographs of GBP2$_G$-GDP·AlF$_3$ on SUVs [20].

4.2.6. Farnesylated GBP2-CTIS does not form micelles or coatomers.

Our previous experiments showed that unlike GBP1$_F$, GBP2$_G$ does not form dense membrane coats. To understand whether coat formation is linked to farnesylation and not prenylation in general, we repeated our membrane binding experiments with farnesylated GBP2-CTIS. As shown above, farnesylated GBP2-CTIS behaves similarly to GPB2$_G$ in SEC-MALS experiments (Figure 4.3b and c).

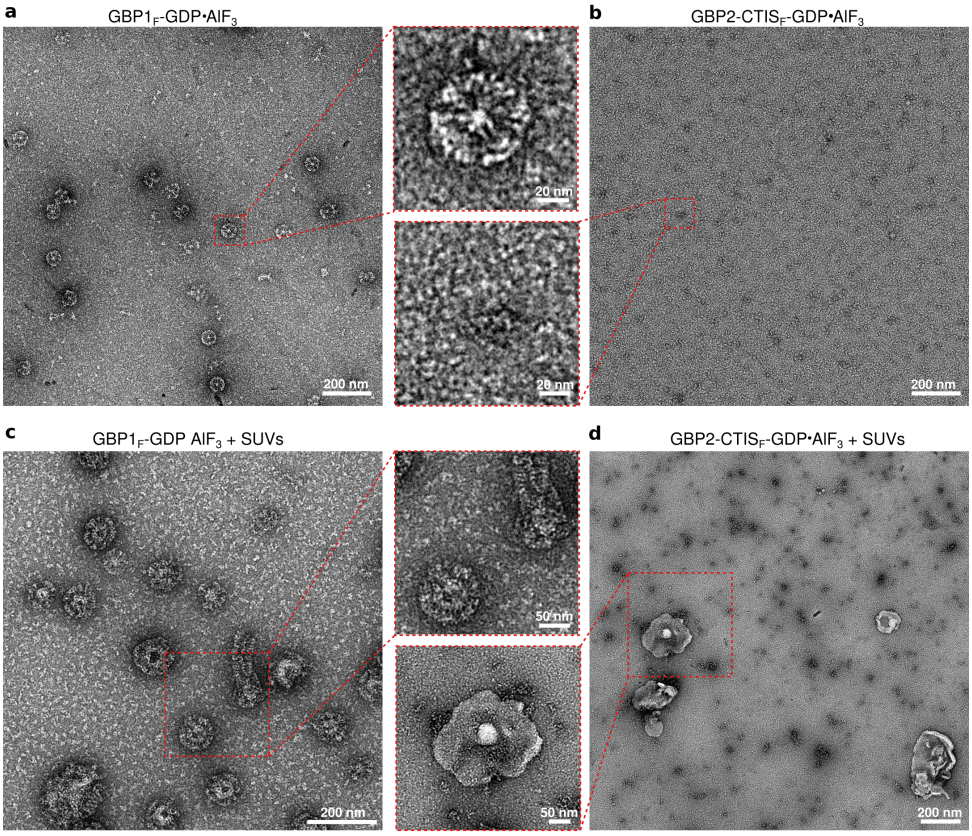

Figure 4.7: Comparison of micellar self-assembly and membrane coatomer formation by GBP1$_F$ and GBP2-CTIS$_F$. (a) Negative stain image of GBP1$_F$-GDP·AlF$_3$ showing formation of flower-like GBP1 micelles with a diameter of 58 nm. (b) Negative stain image of GBP2-CTIS$_F$-GDP·AlF$_3$ does not show any distinct morphological features. (c) Negative stain image of GBP1$_F$-GDP·AlF$_3$ binding to BPLE liposomes. Coated SUVs and tubular protrusions can be observed. (d) Membrane binding is not visible for GBP2-CTIS$_F$-GDP·AlF$_3$.

To test whether nucleotide-activated farnesylated GBP2-CTIS forms micellar assemblies similar to GBP1$_F$ and GBP2$_G$ we imaged farnesylated GBP2-CTIS by negative stain EM. Surprisingly, we did not observe micelles (Figure 4.7 compare a and b). Rather, in some areas, we observed unstructured aggregation of GBP2-CTIS$_F$ (Supplementary Figure 4.13, red arrows). Since GBP2$_G$ can form micellar assemblies similar to GBP1$_F$, this observation suggests that prenylation per se is not sufficient for GBP self-assembly, but that a combination of primary sequence and native prenylation motif determine the

self-assembly properties of prenylated GBPs. Likewise, farnesylated GBP2 did not coat SUVs in contrast to GBP1$_F$ (Figure 4.7c and d), again highlighting that coatomer formation is dependent on GBP1-specific properties.

4.2.7. A triple arginine motif (RRR584-586) at the C-terminus of GBP1 is required for membrane binding.

In an attempt to identify the GBP1-specific sequence motifs facilitating tight association with membranes, we investigated the C-terminal primary sequence of GBP1 and GBP2 (Figure 4.8a). Multiple groups have previously proposed that a triple arginine motif (RRR584-586) at the C-terminus of GBP1 together with its farnesyl moiety is a necessary requirement for the recruitment to gram-negative bacterial membranes [2, 13, 14]. To rule out that defective dimerisation of this mutant may prevent membrane binding, we purified the GBP1-R584-586A mutant to perform SEC-MALS experiments. These results showed that GBP1-R584-586A dimerised in the presence of GDP·AlF$_3$, resulting in an elution peak with a molecular weight around 130 kDa (Figure 4.8b).

To test whether farnesylated GBP1-R584-586A was still able to bind to LPS-EB and BPLE SUVs *in vitro*, we activated the protein with GDP·AlF$_3$ prior to incubation with LPS or SUVs and imaged the sample using negative stain electron microscopy. As described before (chapter 3) GBP1$_F$ forms a coat around LPS-EB micelles (Figure 4.8c, top left). Binding to LPS-EB was completely disrupted for farnesylated GBP1-R584-586A (Figure 4.8c, top panel, middle and right). To our surprise, GBP1-R584-586A$_F$ formed ordered, straight tubes by self-polymerisation which we never observed before. We also performed the same experiments with BPLE-derived SUVs instead of LPS-EB. As described in detail in chapter 3, we observe a dense coat of GBP1$_F$ on SUVs as well as membrane protrusions (Figure 4.8c, bottom panel, left). In contrast, GBP1-R584-586A$_F$ was unable to bind to BPLE-SUVs. Instead GBP1-R584-586A$_F$ again self-interacted, forming short filaments.

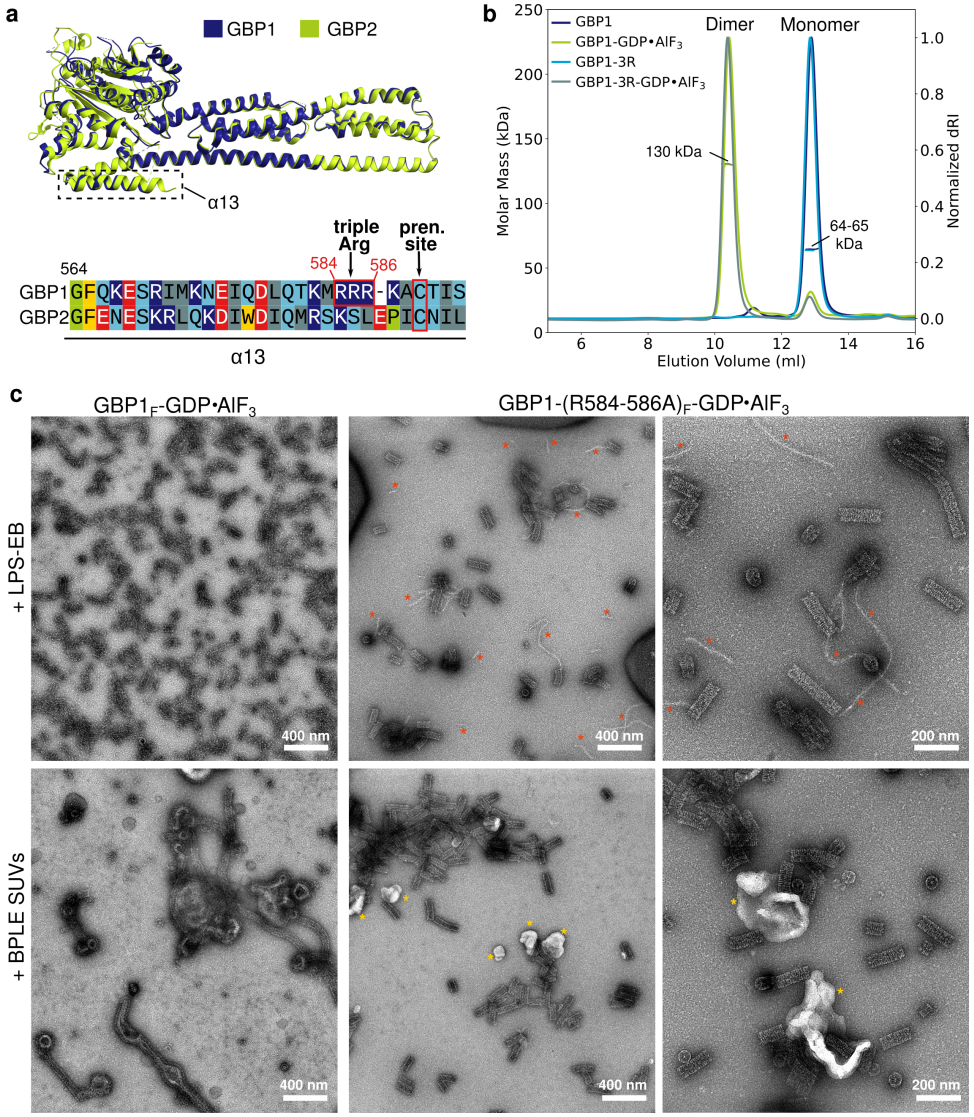

Figure 4.8: Functional analysis of the RRR584-586 motif of GBP1. (a) Structural comparison of monomeric GBP1 and GBP2. The crystal structures of GBP1 (PDB ID: 1dg3 [21]) and GBP2 (PDB ID: 7e58 [22]) in its monomeric form are overlayed to display the high degree of structural similarity. The C-terminal α-helix 13 is highlighted and a sequence alignment is shown, highlighting the RRR584-586 motif in GBP1 and the prenylation site at the C-terminal cysteine. (b) SEC-MALS experiments of GBP1-R584-586A. (c) Negative stain micrographs of activated $GBP1_F$ and $GBP1\text{-}R584\text{-}586A_F$ incubated with LPS-EB or BPLE-SUVs. Orange and yellow asterisks indicate bare LPS-EB or bare BPLE-SUVs, respectively.

4.2.8. Farnesylation of GBP2-CTIS increases its GTPase activity.

As the formation of micelles and coatomers of GBP1 is dependent on its GTPase activity, we wanted to test whether our purified GBP constructs are all active and how the prenylation affects this activity. To determine the GTPase activity we used the GTPase-Glo™ Assay (Promega) [23], with BSA as a negative control. In this assay, a low luminescence signal corresponds to highly active proteins. For GBP1, we observed a strong increase in activity, when the protein was farnesylated. GBP1 has been described to be able to hydrolyse GTP in a cooperative manner [21, 24]. This cooperative mechanism of GTP hydrolysis is most likely linked to multimerisation of GBP1. As we have shown farnesylated GBP1 to self-oligomerise into micellar assemblies, it is tempting to speculate that these assemblies are responsible for the higher GTPase activity observed (Figure 4.9, compare dark-blue with red or yellow).

Non-prenylated GBP2 as well as non-prenylated GBP2-CTIS was 9-fold more active than non-prenylated GBP1, again highlighting how subtle primary sequence differences between GBP1 and GBP2 can have a notable effect. Surprisingly, we observed a decrease in activity when GBP2 was geranylgeranylated compared to an increase in activity when GBP2-CTIS was farnesylated. This was particularly surprising, since we did not observe ordered oligomerisation states for GBP2-CTIS$_F$ with negative stain-EM. With our current data we are unable to explain these differences, but they show that that the type of prenylation could play an important role in regulating the activity of GBPs.

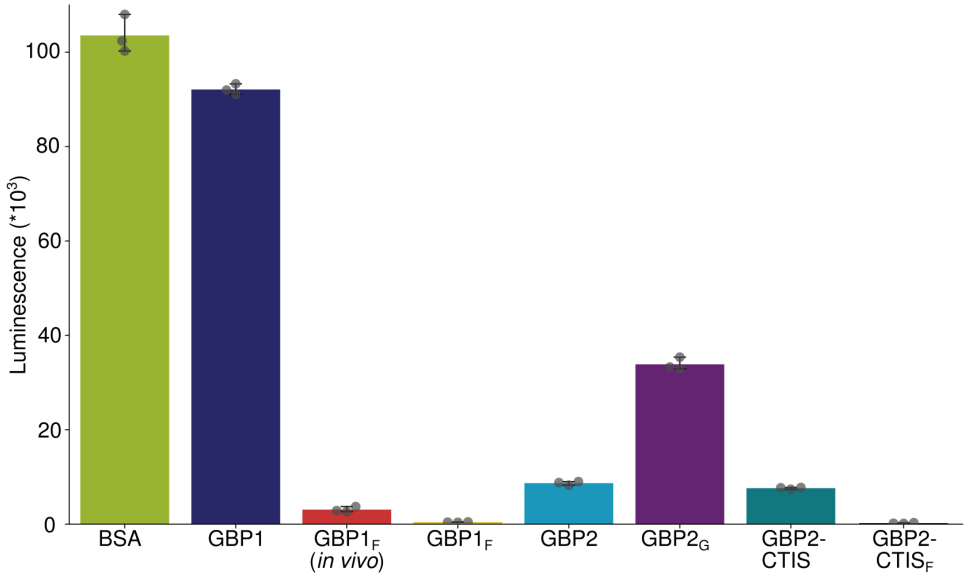

Figure 4.9: The effect of prenylation of GBP1 and GBP2 on its GTPase activity GTPase activity of non-farnesylated GBP1, *in vivo* farnesylated GBP1 and *in vitro* farnesylated GBP1 was compared to GBP2 in its non-prenylated or geranylgeranylated form as well as to farnesylated and non-farnesylated GBP2-CTIS using the GTPase-Glo™ Assay (Promega). Low luminescence signal corresponds to high GTPase activity. Bovine serum albumin (BSA) was used as a negative control (n=3).

4.3. Discussion

Both GBP1 and GBP2 have been shown to be prenylated *in vivo* [6]. Although GBP1 and GBP2 share a high degree of homology, *in vivo* experiment have shown that both proteins have different sub-cellular locations. While farnesylated GBP1 forms oligomers associating at the plasma membrane, $GBP2_G$ was found at the perinuclear membrane [6]. Important to note is that GBPs are able to influence the location of other GBP members including the recruitment of non-prenylated family members to membranes [6].

Although GBP2 is prenylated and can generally associate with membranes *in vivo*, it is not found to associate with pathogen-associated vacuoles or bacterial membranes in the absence of GBP1. Instead, GBP2 requires a pre-formed GBP1 coat to be recruited to these membranes [4, 5, 7]. The precise reason for $GBP1_F$'s preferential recruitment is not completely resolved. To investigate differences originating from the type of prenylation, we created a GBP2-CTIS mutant that we were able to farnesylate *in vitro*. It is worth noting that *in vivo* many prenylated proteins are further processed after the addition of the prenylation. In a first step, the amino acids on the C-terminus subsequent of the prenylated cysteine are proteolytically removed followed by a methylation of the prenylated cysteine [9, 25, 26]. Both of these processes are absent in our *in vitro* system and could potentially influence membrane binding properties.

In our study, we wanted to investigate the effect of GBP2 prenylation on the ability of GBP2 to oligomerise and to form coatomers on SUVs as well as on LPS micelles *in vitro*. We observed that prenylation of GBP2 affected its ability to dimerise and similar to $GBP1_F$, we were able to observe GDP·AlF_3 induced $GBP2_G$ micelles. Although the micelles were less frequent compared to $GBP1_F$ and seemed incomplete, the overall diameter of 60 nm suggests that GBP2 can form a similar outstretched conformation with the geranylgeranyl moiety pointing to the inside of the micelle and the LG-domains located on the periphery. Recently, another group has used dynamic light scattering (DLS) experiments to show that GDP·AlF_3-stabilised $GBP2_G$ is able to self-assemble [27]. Our electron microscopy data confirm this observation and establish that the observed self-assembly is functionally linked to the formation of $GBP2_G$ micelles [27].

While we did observe self-assembly into micellar structures similar to $GBP1_F$, it was challenging to decisively establish association with SUVs or LPS membranes since unlike the highly dense coatomers observed for $GBP1_F$ we could not identify similar structure for $GBP2_G$. Consistent with literature showing that GBP1 is required for recruitment of GBP2 to incracellular bacterial membranes, [4, 5, 7], we do not observe GBP2 binding to LPS *in vitro*. Contrary to these observations, a recent study reported direct interaction of $GBP2_G$ with LPS by analysing the altered mobility of GDP·AlF_3 activated $GBP1_F$ and $GBP2_G$ in the presence of LPS using native PAGE [27]. However, $GBP2_G$ needed a roughly 100 times higher LPS concentration to show the same shift in mobility as $GBP1_F$ indicating a substantially lower affinity towards LPS [27]. Our experiments were performed at LPS and protein concentrations established from our LPS-binding experiments with $GBP1_F$. It is thus possible that LPS binding of GBP2 could be observed with electron microscopy if using higher concentration of GBP2 or LPS. Furthermore, since gram-negative pathogens display broad variation in their abundance and composition of LPS on the outer membrane, the affinity between GBPs and LPS could also be dependent on the specific type of LPS. In support of this, another study recently showed that when co-

infecting cells with *F. novicida* and *S. flexneri*, GBP1 preferentially targeted *S. flexneri* [12]. It will thus be interesting to extend the studies into the interaction between farnesylated GBP1 and geranylgeranylated GBP2 with different types of membranes.

We found that a farnesylated variant of GBP2 (GBP2-CTIS) is unable to form micelles and coatomers on SUVs *in vitro*. The functional dependence and interchangeability of GBP1 and GBP2 in intracellular pathogen defense was recently also tested by creating GBP1:GBP2 chimeras *in vivo* [12]. These studies showed that both GBP1 (containing a farnesyl) and GBP1-CNIL (containing a geranylgeranyl) were recruited to *F. novicida*, while GBP2 and GBP2-CTIS were not [12]. Consistent with our *in vivo* observations, this suggests other molecular features in addition to the type of prenyl modification contribute to determining membrane targeting. Interestingly, the exchange of farnesyl for geranylgeranyl modification in GBP1-CNIL increased recruitment to *F. novicida* whereas no difference was observed for *S. flexneri* [12]. These comparative studies suggest that geranylgeranyl and farnesyl-modifications may contribute to regulating specificity for certain LPS sub-types. Additionally, the same group was able to show that by exchanging the last 14 amino acids of GBP2 to those of GBP1 (including the triple arginine (RRR584-586) motif), they could restore binding to *S. flexneri* but not to *F. novicida*, again highlighting the intricate interplay between LPS composition and prenylation type [12] for pathogen specificity of GBPs.

The polybasic motif (RRR584–586) of GBP1 was shown to be required for coat formation on pathogen membranes [2, 12, 27, 28]. Building on these observations, we here showed for the first time *in vitro* that binding to both LPS-EB and to BPLE-SUVs was completely abrogated when all three arginines of this motif were mutated to alanines (GBP1-R584-586A). To our surprise, GBP1-R584-586A$_F$ in the absence of membranes formed straight and ordered filamentous structures which is in stark contrast to the micellar assemblies observed for the wild-type protein. This might explain that puncta formation, but no coat formation on bacteria has been observed for this mutant using fluorescence microscopy [2] . The absence of the polybasic motif in GBP2 could explain why farnesylated GBP2-CTIS cannot form membrane coats. Introducing the RRR584-586 motif into a GBP2-construct as well as creating a GBP1 mutant with a C-terminus that can be geranylgeranylated will be next steps to better understand the precise molecular requirements triggering coat formation of GBPs.

The farnesylation of GBP1 increased the GTPase activity (in our case 9-fold), which we linked to the formation of self-assembled GBP1$_F$ micelles as previously hypothesized [19]. To our surprise both non-prenylated GBP2 and non-prenylated GBP2-CTIS on their own already display a much higher GTPase activity compared to non-prenylated GBP1. Important to note is that while both GBP1 and GBP2 exhibit GTPase activity, they differ in their reaction products and nucleotide affinities. While GBP1 is able to hydrolyse GTP to GMP, the main reaction product of GBP2 is GDP [15, 16]. At the same time, it has been noted for GBP1 before that the product of GTP hydrolysis could change depending on the state of prenylation, from producing mainly GMP (85%) when being non-prenylated to 30% of GMP when being farnesylated [29]. It has also been reported that GBP1$_F$ hydrolysis consists of a slow initial phase followed by a fast hydrolysis phase which correlated with the observation of turbidity indicating polymerisation [19].

Since both GBP2 and GBP2-CTIS displayed the same GTPase activity, the exchange of

the C-terminal CNIL to CTIS motif does not seem to affect the hydrolysis rate of unmodified GBP2. Intriguingly, geranylgeranylation of GBP2 decreased, whereas farnesylation increased its GTPase activity. This observation was surprising since farnesylated GBP2-CTIS does not seem to self-assemble, contrasting the hypothesis that the cooperative effect in GTP-hydrolysis observed for GBPs is linked to their ability to oligomerise beyond the dimer state. In support of this, farnesylated GBP1 and farnesylated GBP2-CTIS display comparable GTPase activity, highlighting that the type of prenylation potentially affects GTPase activity of GBPs. One alternative possibility could be that the higher GTPase activity of farnesylated GBP2-CTIS over geranylgeranylated GBP2 is related to a favored extended conformation of the GED. However, the absence of GBP2-CTIS$_F$ oligomers in our experiments is yet another factor that remains unsolved. It should be noted, that our current GTPase assays are end-point measurements that cannot capture reaction rates and cooperativity effects. More detailed studies using kinetic monitoring of GTPase activity will be required to deduce a mechanistic model for the observations described here.

4.4. Conclusions and Outlook

In this study we successfully geranylgeranylated GBP2 as well as farnesylated GBP2-CTIS *in vitro* to study the ability of GBP2 to self-assemble and to interact with LPS and SUVs. While prenylation prevented dimerisation for both GBP2$_G$ and GBP2-CTIS$_F$, only GBP2$_G$ was able to form nucleotide activated micelles. Coat formation on either SUVs or LPS was not observed for both constructs highlighting the importance of additional features in GBP1 responsible for coat formation.

In a first step, constructs containing the last 14 amino acids of GBP1 including the RRR584-586 motif close to the CaaX motif could be tested to see whether this enables GBP2-CTIS to associate with membranes *in vitro* [12]. For GBP2, we could introduce the RRR584-586 motif, leaving the C-terminus with its geranylgeranylation site intact. In case those constructs lead to coat formation, this would enable the ultrastructure determination of GBP2$_G$ on LPS, investigating whether the coat is formed by GBP2-dimers. Further research also needs to clarify, whether the type of prenylation determines the affinity or preference for certain types of LPS or membranes. The GTPase activity assay performed in this study gives indications that the type of prenylation might also have an effect on the GTPase activity of GBPs. Additional experiments need to elucidate whether this could be a potential mechanistic effect used by the cells to up or down regulate the GTPase activity of GBPs. It has been shown with fluorescence experiments that GBPs are able to form large oligomers on the membranes of pathogens functioning as a signalling platform for other players such as caspase-4 [4, 5]. Ultimately, the goal will be to visualise those signalling platforms with high resolution cryo-electron microscopy to determine the ultrastructure of the complex.

Author contributions

TK and CP purified proteins, TK conducted biophysical experiments, performed GTPase activity assays, prepared negative stain and cryo-EM samples and collected cryo-EM data. AZD performed LS-MS measurements and analyzed the results. TK wrote the

chapter. AJ revised the chapter as well as conceptualised and supervised the study.

Acknowledgements
We thank Wiel Evers for help with cryo-EM data collection. This work was supported by the European Research Council (ERC-StG-852880 to AJ), the Dutch Research Council (NWO.STU.018-2.007 to AJ) and the Kavli Institute of Nanoscience Delft.

4.5. Materials and Methods

Plasmid construction

GBP1 and GBP2
Codon-optimised synthetic DNA encoding human GBP1 (UniProt accession P32455) and human GBP2 (UniProt accession P32456) was cloned into the NcoI/NotI linearised pETM14 vector containing an N-terminal His_6 tag and 3C cleavage site, yielding pETM14-GBP1 or pETM14-GBP2.

GBP2-CTIS
In order to test a GBP2 variant containing the CTIS motif from GBP1 enabling its farnesylation, we generated a pETM14-GBP2-CTIS construct by quickchange mutagenesis using the appropriate oligos (AJLO-116 and AJLO-117, Supplementary table 4.2). Mutations were confirmed by DNA sequencing (Macrogen Europe B.V., Amsterdam, Netherlands).

pCDFDuet-His6-FNTA-FNTB
The pJET1.2 constructs containing FNTA or FNTB were obtained by amplification of AJLD-007 or AJLD-022 (Supplementary table 4.3) using AJLO-023 - AJLO-026 (Supplementary table 4.2), following the manufacturer recommendations. The pCDFDuet-His6-FNTA-FNTB (AJLD-063) vector was obtained by Gibson assembly. The DNA fragments originated from AJLD-052, AJLD-053 and AJLV-038 using primers AJLO-076 - AJLO-078, AJLO-083 and AJLO-090 - AJLO-093 (Supplementary table 4.2). Successful cloning was confirmed at all stages by DNA sequencing (Macrogen Europe B.V., Amsterdam, Netherlands).

pCDFDuet-His6-FNTA-PGGT1B
The pCDFDuet-His6FNTA-PGGT1B (AJLD-061) vector was obtained by Gibson assembly. The DNA fragments originated from AJLD-052, AJLD-054 and AJLV-038 using primers AJLO-076 - AJLO-078, AJLO-080, AJLO-081, AJLO-083 and AJLO-090 - AJLO-091 (Supplementary table 4.2). Successful cloning was confirmed at all stages by DNA sequencing (Macrogen Europe B.V., Amsterdam, Netherlands).

Protein expression and purification

GBP1, hGBP1-R584-586A, GBP2, GBP2-CTIS
Protein expression was performed as described in chapter 2. For completeness: Proteins were expressed in *E.coli* BL21(DE3) (Supplementary Table 4.1) using auto induction in

lactose-containing media. Pre-cultures were grown in LB-medium o/n at 37 °C. For protein expression, ZYP5052 medium was inoculated at 1/50 (v/v) with pre-culture and cells were grown at 37 °C at 180 rpm for 3-4 h before lowering the temperature to 20 °C for 15-20 h. Cells were harvested by centrifugation at 4 °C and 4000 rpm and the cell pellet was resuspended in lysis buffer (50 mM HEPES pH 7.8, 500 mM NaCl, 0.1 % Triton X-100) on ice. The cells were disrupted by three successive freeze-thaw cycles. To digest genomic DNA, 1-10 ug/ml DNAseI was added and incubated on a rotating wheel for 1-2 hours at 4 °C. To separate cell debris, the lysate was centrifuged at 20,000 x g for 40 min at 4 °C. The supernatant was applied to TALON (Takara) affinity resin. The bound fraction was washed with 20 column volumes (cv) of wash-buffer (50 mM sodium phosphate, 300 mM NaCl, 10 mM imidazole, pH 7.4) and eluted in the same buffer containing 150 mM imidazole. The eluent was dialysed into 3C cleavage buffer (50 mM HEPES pH 7.4, 150 mM NaCl, 0.5 mM DTT) and incubated with 1:100 mol/mol 3C protease o/n at 4 °C. Following cleavage, the proteins were further purified via size exclusion chromatography using a GE Superdex-200 Increase 10/300 GL column (GE Healthcare) in running buffer (50 mM HEPES pH 7.4, 150 mM NaCl, 0.5 mM DTT).

FNTA-FNTB and FNTA-PGGT1B

Protein expression was performed as described for GBP1. To prevent the FNTA-FNTB or FNTA-PGGT1B complex from falling apart, the salt concentration in the lysis buffer was reduced to 150 mM NaCl. Protein purification was performed with Ni-NTA beads keeping the NaCl concentration at 150 mM, followed by a purification step via size exclusion chromatography using a GE Superdex200 Increase 10/300 GL column in running buffer.

Preparation of GDP·AlF_3-stabilised GBP1/GBP2 or GBP2-CTIS dimers

15 µM of full length GBP1/GBP2 or GBP2-CTIS was incubated with 200 µM GDP, 10 mM NaF, 300 µM $AlCl_3$, 5 mM $MgCl_2$ and 1 mM DTT for 10 min at RT.

In vitro prenylation of GBP1, GBP2 or GBP2-CTIS

In vitro prenylation of GBP1 and GBP2 was adapted from [30]. In brief, 5 µM purified GBP1 or GBP2 was incubated with 5 µM FNTA-FNTB for farnesylation or with 5 µM FNTA-PGGT1B for geranylgeranylation and supplemented with 25 µM farnesyl pyrophosphate (FPP) or geranyl pyrophosphate (GPP) (both from Cayman) in prenylation buffer (50 mM HEPES pH 7.2, 50 mM NaCl, 5 mM DTT, 5 mM $MgCl_2$, 20 µM GDP). The reaction mixtures was incubated for 60 min at room temperature and dialysed o/n at 4 °C into running buffer (50 mM HEPES pH 7.4, 150 mM NaCl, 0.5 mM DTT).

Liquid chromatography–mass spectrometry (LC–MS)

Sample preparation

For the trypsin digestion, 20 µL of digestion buffer (25 mM Tris buffer (pH 8.1) supplemented with 1 mM $CaCl_2$ and 5 mM TCEP) was added to 10 µM - 25 µM of proteins. Alkylation of cysteine residues was performed by adding 3 µL of 50 mM iodoacetamide followed by 15 min of incubation in darkness. Digestion was performed by adding 10 µL of 0.2 mg/ml Trypsin Gold (Promega) followed by overnight incubation at 37 °C. Samples

were centrifuged at 15000 rpm for 15 min, and 10 µL of the reaction volume was injected in an LC-MS system.

LC-MS Method

The LC-MS analysis were performed using an Agilent LC/MS system consisting of a high pressure liquid chromatography set-up coupled to a triple-quadrupole (QQQ) mass spectrometer (G6460C) equipped with a standard electrospray ionisation (ESI) source. Both systems were operated through MassHunter data acquisition software (version 10.1). The tryptic digested peptides were acidified with 25 mM FA and delivered to a CSH C18 guard-column and a CSH C18 column (Waters) (2.1 mm by 50 mm, 1.7 µm pore size) at 40 °C with a flow rate of 0.5 ml/min using the following binary gradient: 5% B (ACN, 25 mM FA), ramp to 95% B in 8 min followed by a 2 min hold at 95% B, 2 min ramp back to 5% B and 3 min re-equilibration (A, MilliQ, 25 mM FA). Next, peptides were eluted from the column and the eluent was sprayed into the mass spectrometer operated in data-dependent mode, as in dynamic multiple-reaction monitoring (dMRM) mode using transitions. The transitions were generated from protein sequences with Skyline [31]. The modified peptides were selected from in silico digested tryptic peptides based on prior knowledge of the medication location in their sequences. Non-modified peptides were selected based on their length (7-25 amino acids). Each MRM transition was optimised for the fragmentor voltage and collision energy. The dMRM was acquired in positive mode with a cycle time of 500 ms.

Biophysical analysis

SEC-MALS

Proteins were analysed using analytical size exclusion chromatography coupled to multi-angle light scattering (SEC-MALS). Purified protein samples were resolved on a Superdex-200 Increase 10/300 GL column (GE Healthcare) connected to a high-performance liquid chromatography (HPLC) unit (1260 Infinity II, Agilent) running in series with an online UV detector (1260 Infinity II VWD, Agilent), an 8-angle static light scattering detector (DAWN HELEOS 8+; Wyatt Technology), and a refractometer (Optilab T-rEX; Wyatt Technology). For SEC-MALS measurements, proteins were diluted to a final concentration of 15 µM in SEC buffer (50 mM HEPES pH 7.4, 150 mM NaCl, 0.5 mM TCEP or DTT) with or without the GTP transition state mimic. On the basis of the measured Rayleigh scattering at different angles and the established differential refractive index increment value of 0.185 ml*g^{-1} for proteins in solution with respect to the change in protein concentration (dn/dc), weight-averaged molar masses for each species were calculated using ASTRA software (Wyatt Technology; v.7.3.1).

Liposome preparation

SUV preparation

1 mg of brain polar lipid extract (BPLE, Avanti Polar Lipids) was purchased as chloroform solution and dried under a gentle N2 stream. The resulting lipid film was further dried in a desiccator connected to a vacuum pump for 1 h. To hydrate the lipid film, 1 ml of 50 mM HEPES (pH 7.5), 150 mM NaCl was used. Small unilamellar vesicles (SUVs) were prepared with an Avanti Mini Extruder (Avanti Polar Lipids) with hydrophilic poly-

carbonate membranes with a pore size of 0.1 µm. The solution of swollen lipid was filled into one of the syringes and monodisperse emulsions of SUVs were produced by passing this mixture through the membrane at least 11 times. The SUVs were stored at 4 °C until further use.

Negative staining EM

3.5 µL of protein or lipid solution was applied onto a freshly glow-discharged carbon-coated copper mesh grid (Quantifoil). After 1 min, grids were washed twice with 12 µL buffer (50 mM HEPES pH 7.4, 150 mM NaCl, 0.5 mM DTT) followed by staining with 3.5 µL of 2 % (w/v) uranyl acetate at room temperature. At each step, excess sample, wash solution and stain were blotted with filter paper and finally grids were air dried for 15 min. Grids were imaged on a JEM 1400Plus TEM (JEOL) operated at 120 kV and recorded on a bottom-mounted TVIPS F416 CMOS camera.

Single particle cryo-EM

$GBP2_G$-GDP·AlF_3 + SUVs dataset

The transition state of $GBP2_G$ was obtained as described before. It should be noted that the sample still contains FNTA-PGGT1B from the *in vitro* geranylgeranylation of GBP2. SUVs were added in a final concentration of 1 mg/ml and incubated with $GBP2_G$-GDP·AlF_3 for 45 min at 30 °C followed by 2h at 4 °C. A total of 3.0 µL of 1.5 mg/ml $GBP2_G$-GDP·AlF_3 + SUVs was applied to glow-discharged Quantifoil grids (QF-1.2/1.3, 300-mesh holey carbon on copper) on a Leica GP2 vitrification robot at 98 % humidity and a temperature of 20 °C. The sample was blotted for 4 s from the carbon side of the grid and immediately flash-cooled in liquid ethane. Micrographs were acquired on a JEM 3200FSC TEM (JEOL) operated at 300 kV. Images were recorded on a K2 Summit direct electron detector (Gatan) at a magnification of 20kx, corresponding to a pixel size of 1.891 Å at the specimen level. Image acquisition was performed with SerialEM, and micrographs were collected at an underfocus varying between –3 µm and –1 µm. We collected a total of 60 frames accumulating to a total electron exposure of 20.18 $e^-/Å^2$. In total, 740 micrographs were acquired. Topaz-Denoise was used to increase the signal to noise ratio of the cryo-EM micrographs [20].

$GBP2_G$-GDP·AlF_3 + LPS-SM dataset

The transition state of $GBP2_G$ was obtained as described before. It should be noted that the sample still contains FNTA-PGGT1B from the *in vitro* geranylgeranylation of GBP2. Deep rough LPS from *S. enterica* sv. Minnesota R595 (LPS-SM) was added in a final concentration of 0.5 mg/ml and incubated with 2 mg/ml $GBP2_G$-GDP·AlF_3 for 30 min at 30 °C followed by 2h at 4 °C. The vitrification process was performed as described previously. Micrographs were acquired on a JEM 3200FSC TEM (JEOL) operated at 300 kV. Images were recorded on a K2 Summit direct electron detector (Gatan) at a magnification of 15kx, corresponding to a pixel size of 2.449 Å at the specimen level. Image acquisition was performed with SerialEM, and micrographs were collected at an underfocus varying between –4 µm and –1 µm. We collected a total of 60 frames accumulating to a total electron exposure of 11.52 $e^-/Å^2$.

$GBP1_F$-GDP·AlF_3 + SUVs dataset
1 mg/ml $GBP1_F$-GDP·AlF_3 was mixed with 1 mg/ml BPLE SUVs and incubated for 30 min at 30 °C. 3.5 µL of the mixture were applied on to glow-discharged Quantifoil grids (QF-1.2/1.3, 200-mesh holey carbon on copper) on a Leica GP2 vitrification robot at 98 % humidity and 20 °C. The sample was blotted for 4 s from the carbon side of the grid and immediately flash-cooled in liquid ethane. Grids were imaged on a JEM 3200FSC TEM (JEOL) operated at 300 kV. Images were recorded on a K2 Summit direct electron detector (Gatan) at a magnification of 20kx, corresponding to a pixel size of 1.891 Å at the specimen level. Image acquisition was performed with SerialEM [32], and micrographs were collected at an underfocus varying between –3 µm and –1 µm. We collected a total of 100 frames accumulating to a total electron exposure of 43 $e^-/Å^2$.

GTPase activity assay

To determine the GTPase activity of GBP1 the GTPase-Glo™ Assay (Promega) was utilised [23], using the protocol for intrinsic GTPase activity. Briefly, 5 µl of 5 µM protein in GTPase buffer was added per well to a 384 well plate. 5 µl of 2 x GTP solution containing 10 µM GTP and 1 mM DTT was added to the same well. The reaction was incubated at RT for 75 min. 10 µl of reconstituted GTPase-Glo reagent was added to the reaction and incubated for 30 min at RT while shaking. Finally, 20 µl of detection reagent was added and after another incubation step of 15 min the luminescence was measured using a micro plate reader (Synergy^{TM}H1, BioTek). BSA was used as a negative control and measurements were performed in triplicates.

References

[1] Y. Cheng, R. J. Colonno, and F. H. Yin, *Interferon induction of fibroblast proteins with guanylate binding activity.* Journal of Biological Chemistry **258**, 7746 (1983).

[2] M. Kutsch, L. Sistemich, C. F. Lesser, M. B. Goldberg, C. Herrmann, and J. Coers, *Direct binding of polymeric gbp1 to lps disrupts bacterial cell envelope functions,* The EMBO journal **39**, e104926 (2020).

[3] D. Fisch, B. Clough, M.-C. Domart, V. Encheva, H. Bando, A. P. Snijders, L. M. Collinson, M. Yamamoto, A. R. Shenoy, and E.-M. Frickel, *Human gbp1 differentially targets salmonella and toxoplasma to license recognition of microbial ligands and caspase-mediated death,* Cell reports **32**, 108008 (2020).

[4] J. C. Santos, D. Boucher, L. K. Schneider, B. Demarco, M. Dilucca, K. Shkarina, R. Heilig, K. W. Chen, R. Y. Lim, and P. Broz, *Human gbp1 binds lps to initiate assembly of a caspase-4 activating platform on cytosolic bacteria,* Nature communications **11**, 3276 (2020).

[5] M. P. Wandel, B.-H. Kim, E.-S. Park, K. B. Boyle, K. Nayak, B. Lagrange, A. Herod, T. Henry, M. Zilbauer, J. Rohde, *et al.*, *Guanylate-binding proteins convert cytosolic bacteria into caspase-4 signaling platforms,* Nature immunology **21**, 880 (2020).

[6] N. Britzen-Laurent, M. Bauer, V. Berton, N. Fischer, A. Syguda, S. Reipschläger, E. Naschberger, C. Herrmann, and M. Stürzl, *Intracellular trafficking of guanylate-binding proteins is regulated by heterodimerization in a hierarchical manner,* PloS one **5**, e14246 (2010).

[7] S. Zhu, C. J. Bradfield, A. Mamińska, E.-S. Park, B.-H. Kim, P. Kumar, S. Huang, Y. Zhang, J. Bewersdorf, and J. D. MacMicking, *Cryo-et of a human gbp coatomer governing cell-autonomous innate immunity to infection,* Biorxiv , 2021 (2021).

[8] D. E. Nantais, M. Schwemmle, J. T. Stickney, D. J. Vestal, and J. E. Buss, *Prenylation of an interferon-γ-induced gtp-binding protein: the human guanylate binding protein, hugbp1,* Journal of leukocyte biology **60**, 423 (1996).

[9] S. Clarke, *Protein isoprenylation and methylation at carboxyl-terminal cysteine residues,* Annual review of biochemistry **61**, 355 (1992).

[10] S. L. Moores, M. D. Schaber, S. D. Mosser, E. Rands, M. B. O'Hara, V. M. Garsky, M. S. Marshall, D. L. Pompliano, and J. Gibbs, *Sequence dependence of protein isoprenylation,* Journal of Biological Chemistry **266**, 14603 (1991).

[11] D. Fisch, H. Bando, B. Clough, V. Hornung, M. Yamamoto, A. R. Shenoy, and E.-M. Frickel, *Human gbp 1 is a microbe-specific gatekeeper of macrophage apoptosis and pyroptosis,* The EMBO journal **38**, e100926 (2019).

[12] S. V. Valeva, M. Degabriel, F. Michal, G. Gay, J. R. Rohde, F. Randow, B. Lagrange, and T. Henry, *Comparative study of gbp recruitment on two cytosol-dwelling pathogens, francisella novicida and shigella flexneri highlights differences in gbp repertoire and in gbp1 motif requirements,* Pathogens and Disease **81**, ftad005 (2023).

[13] A. S. Piro, D. Hernandez, S. Luoma, E. M. Feeley, R. Finethy, A. Yirga, E. M. Frickel, C. F. Lesser, and J. Coers, *Detection of cytosolic shigella flexneri via a c-terminal triple-arginine motif of gbp1 inhibits actin-based motility,* MBio **8**, 10 (2017).

[14] K. M. Kohler, M. Kutsch, A. S. Piro, G. D. Wallace, J. Coers, and M. F. Barber, *A rapidly evolving polybasic motif modulates bacterial detection by guanylate binding proteins,* MBio **11**, 10 (2020).

[15] R. Neun, M. F. Richter, P. Staeheli, and M. Schwemmle, *Gtpase properties of the interferon-induced human guanylate-binding protein 2,* FEBS letters **390**, 69 (1996).

[16] A. Ghosh, G. J. Praefcke, L. Renault, A. Wittinghofer, and C. Herrmann, *How guanylate-binding proteins achieve assembly-stimulated processive cleavage of gtp to gmp,* Nature **440**, 101 (2006).

[17] A. Xavier, M. A. Al-Zeer, T. F. Meyer, and O. Daumke, *hgbp1 coordinates chlamydia restriction and inflammasome activation through sequential gtp hydrolysis,* Cell reports **31** (2020).

[18] C. Lorenz, S. Ince, T. Zhang, A. Cousin, R. Batra-Safferling, L. Nagel-Steger, C. Herrmann, and A. M. Stadler, *Farnesylation of human guanylate-binding protein 1 as safety mechanism preventing structural rearrangements and uninduced dimerization,* The FEBS journal **287**, 496 (2020).

[19] S. Shydlovskyi, A. Y. Zienert, S. Ince, C. Dovengerds, A. Hohendahl, J. M. Dargazanli, A. Blum, S. D. Günther, N. Kladt, M. Stürzl, *et al.*, *Nucleotide-dependent farnesyl switch orchestrates polymerization and membrane binding of human guanylate-binding protein 1,* Proceedings of the National Academy of Sciences **114**, E5559 (2017).

[20] T. Bepler, K. Kelley, A. J. Noble, and B. Berger, *Topaz-denoise: general deep denoising models for cryoem and cryoet,* Nature communications **11**, 5208 (2020).

[21] B. Prakash, G. J. Praefcke, L. Renault, A. Wittinghofer, and C. Herrmann, *Structure of human guanylate-binding protein 1 representing a unique class of gtp-binding proteins,* Nature **403**, 567 (2000).

[22] W. Cui, E. Braun, W. Wang, J. Tang, Y. Zheng, B. Slater, N. Li, C. Chen, Q. Liu, B. Wang, *et al.*, *Structural basis for gtp-induced dimerization and antiviral function of guanylate-binding proteins,* Proceedings of the National Academy of Sciences **118**, e2022269118 (2021).

[23] S. Mondal, K. Hsiao, and S. A. Goueli, *A homogenous bioluminescent system for measuring gtpase, gap and gef activities,* in *Cancer Research*, Vol. 75 (2015).

[24] G. J. Praefcke, S. Kloep, U. Benscheid, H. Lilie, B. Prakash, and C. Herrmann, *Identification of residues in the human guanylate-binding protein 1 critical for nucleotide binding and cooperative gtp hydrolysis,* Journal of molecular biology **344**, 257 (2004).

[25] M. R. Philips, M. H. Pillinger, R. Staud, C. Volker, M. G. Rosenfeld, G. Weissmann, and J. B. Stock, *Carboxyl methylation of ras-related proteins during signal transduction in neutrophils,* Science **259**, 977 (1993).

[26] V. L. Boyartchuk, M. N. Ashby, and J. Rine, *Modulation of ras and a-factor function by carboxyl-terminal proteolysis,* Science **275**, 1796 (1997).

[27] M. S. Dickinson, M. Kutsch, L. Sistemich, D. Hernandez, A. S. Piro, D. Needham, C. F. Lesser, C. Herrmann, and J. Coers, *Lps-aggregating proteins gbp1 and gbp2 are each sufficient to enhance caspase-4 activation both in cellulo and in vitro,* Proceedings of the National Academy of Sciences **120**, e2216028120 (2023).

[28] M. P. Wandel, C. Pathe, E. I. Werner, C. J. Ellison, K. B. Boyle, A. von der Malsburg, J. Rohde, and F. Randow, *Gbps inhibit motility of shigella flexneri but are targeted for degradation by the bacterial ubiquitin ligase ipah9. 8,* Cell host & microbe **22**, 507 (2017).

[29] J. M. Fres, S. Müller, and G. J. Praefcke, *Purification of the caax-modified, dynamin-related large gtpase hgbp1 by coexpression with farnesyltransferase [s],* Journal of lipid research **51**, 2454 (2010).

[30] B. Dursina, R. Reents, C. Delon, Y. Wu, M. Kulharia, M. Thutewohl, A. Veligodsky, A. Kalinin, V. Evstifeev, D. Ciobanu, *et al.*, *Identification and specificity profiling of protein prenyltransferase inhibitors using new fluorescent phosphoisoprenoids,* Journal of the American Chemical Society **128**, 2822 (2006).

[31] B. MacLean, D. M. Tomazela, N. Shulman, M. Chambers, G. L. Finney, B. Frewen, R. Kern, D. L. Tabb, D. C. Liebler, and M. J. MacCoss, *Skyline: an open source document editor for creating and analyzing targeted proteomics experiments,* Bioinformatics **26**, 966 (2010).

[32] D. N. Mastronarde, *Automated electron microscope tomography using robust prediction of specimen movements,* Journal of structural biology **152**, 36 (2005).

[33] F. Studier and B. A. Moffatt, *Use of bacteriophage t7 rna polymerase to direct selective high-level expression of cloned genes,* Journal of Molecular Biology **189**, 113 (1986).

[34] A. Dümmler, A.-M. Lawrence, and A. De Marco, *Simplified screening for the detection of soluble fusion constructs expressed in e. coli using a modular set of vectors,* Microbial cell factories **4**, 1 (2005).

4.6. Supplementary

Table 4.1: Bacterial host strains used in this chapter.

Strain	Description	Reference
E.coli DH5α	Cloning host	Invitrogen
E.coli BL21(DE3)	Expression host for GBPs	Thermo Fisher Scientific [33]

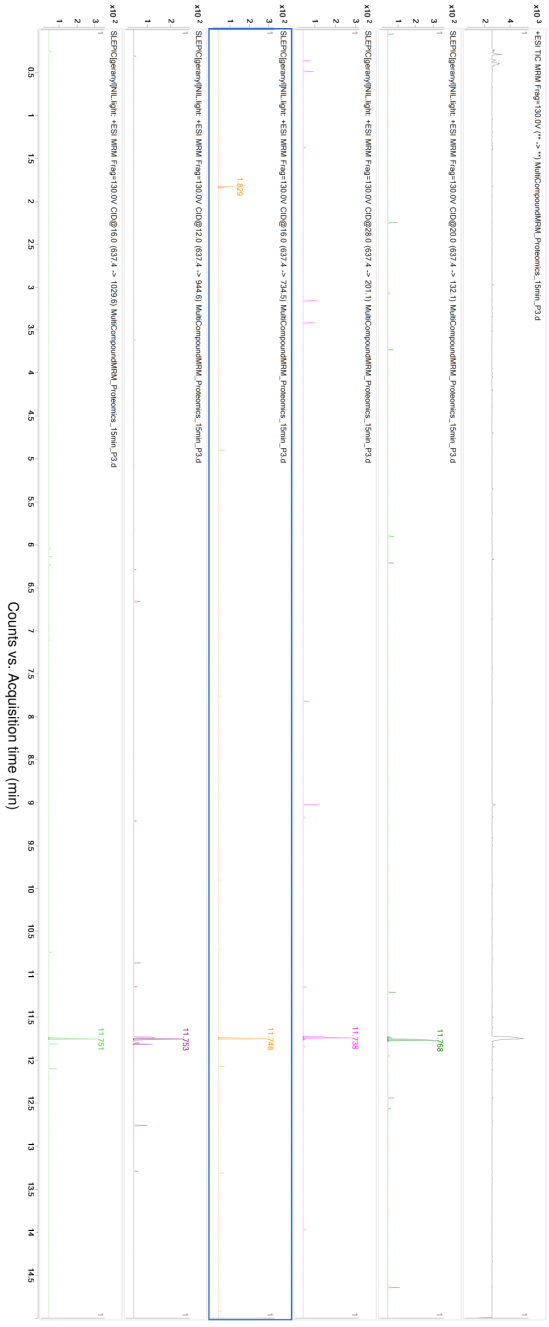

Figure 4.10: Full LC-MS chromatogram (intensity vs retention time) of GBP2$_G$.

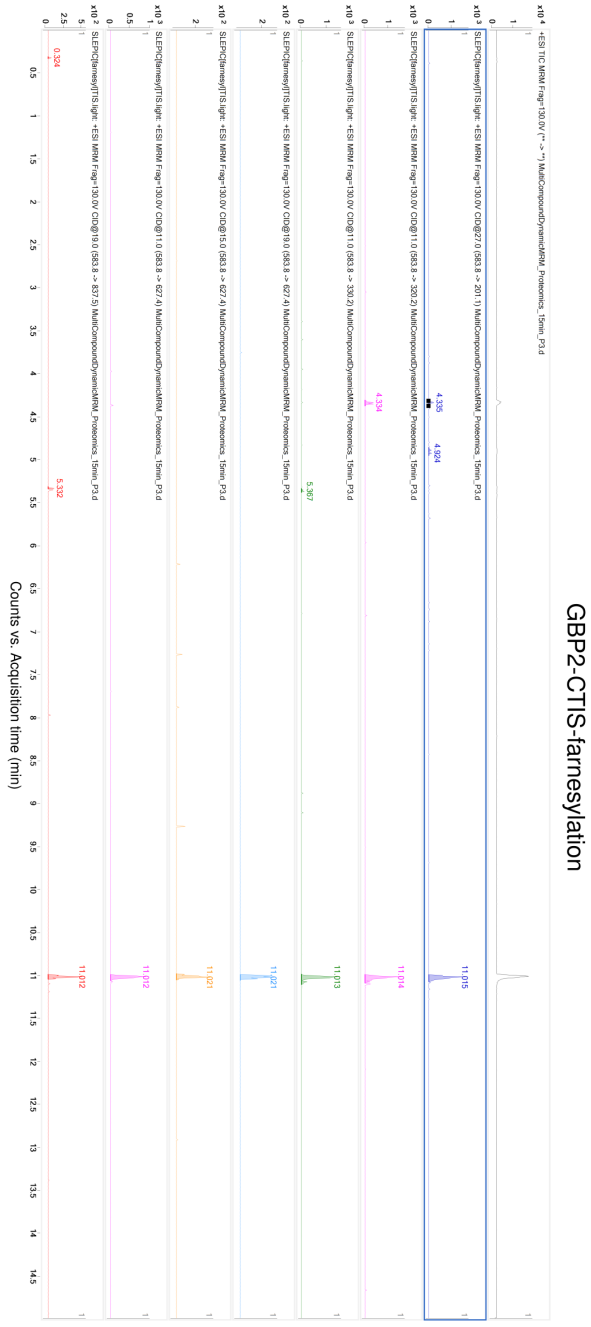

Figure 4.11: Full LC-MS chromatogram (intensity vs retention time) of GBP2-CTIS$_F$.

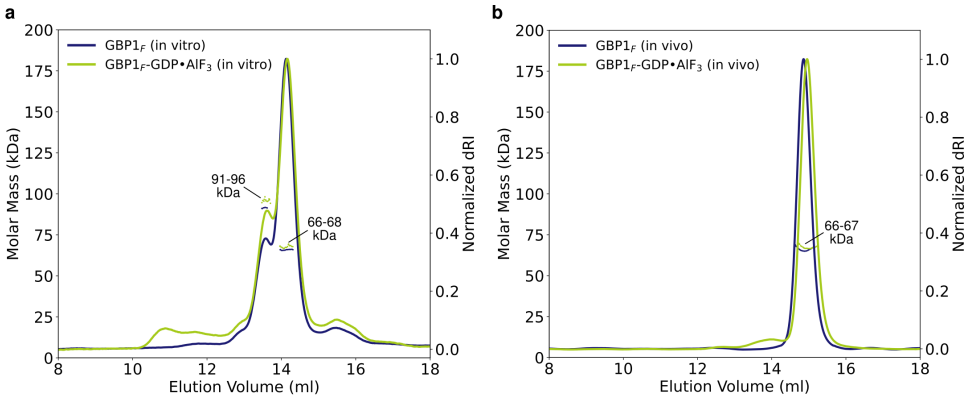

Figure 4.12: SEC-MALS experiments of *in vitro* and *in vivo* farnesylated GBP1. SEC-MALS experiments reveal that prenylated GBP1 stays monomeric (MW = 66 - 68 kDa) when GDP·AlF_3 is added independent on whether farnesylation was achieved *in vitro* (a) or *in vivo* (b). The *in vitro* farnesylated GBP1 sample still contains FNTA-FNTB with a determined molecular weight between 91 and 96 kDa.

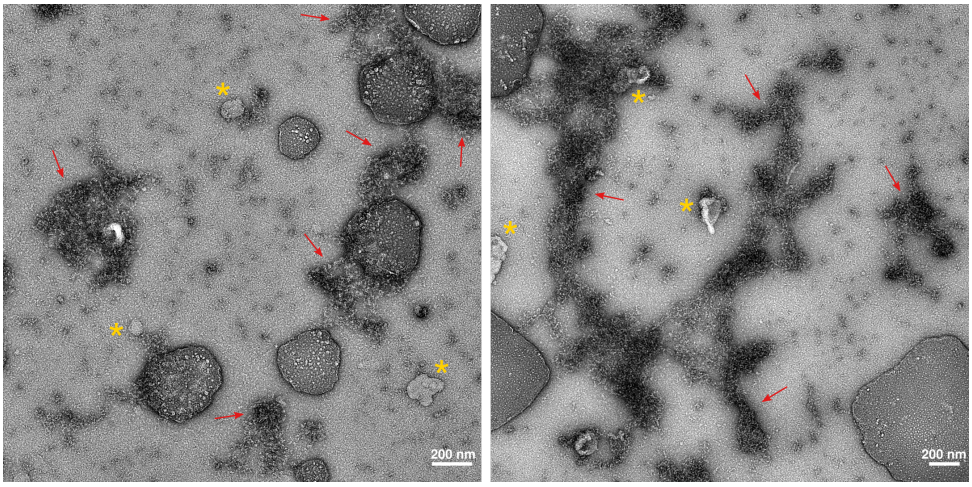

Figure 4.13: GBP2-CTIS$_F$ aggregates visualised with negative stain EM. Negative stain images show GBP2-CTIS$_F$ aggregations (red arrows) as well as non coated SUVs (yellow asterisk).

Table 4.2: Primer sequences used in this manuscript.

Oligo name	Description	Sequence
AJLO-002	pUC57-hGBP1-fw	ggtctcccatggcgagcgagatccacatg
AJLO-004	pUC57-hGBP1-rev	ggtctccggccgcttattagctg
AJLO-006	pUC57-hGBP2-fw	ggtctcccatggcgccggaaatcaacctgc
AJLO-007	pUC57-hGBP2-rev	ggtctccggccgcttattacagaatg
AJLO-023	FNTA-fw	cgtctcccatggcggccaccgaggg
AJLO-024	FNTA-rev	cgtctccggccgcttattattgctgtacatttgttggtgagtc
AJLO-025	FNTB-fw	catatggcttctccgagttctttcacc
AJLO-026	FNTA-rev	cgtctcctcgattattagtcggttgcaggctctgccg
AJLO-076	FNTA-His6-Gib-fw	ttttgtttaactttaataaggagatataccatgcatcatcatcaccaccac
AJLO-077	FNTA-His6-Gib-rev	acttaagcattatgcggccttattgctgtacatttgttggtgag
AJLO-078	pCDFDuet1-Gib-spacer-fw	ctcaccaacaaatgtacagcaataaggccgcataatgcttaagt
AJLO-080	GGT1-Gib-fw	cttagtatattagttaagtataagaaggagatatacatatatggcggccactgaggat
AJLO-081	GGT1-Gib-rev	cggtttctttaccagactcgattattcttatgtggagatatgtacattctct
AJLO-083	pCDFDuet1-Gib-rev	gtggtggtgatgatgatgcatggtatatctccttattaaagttaaacaaaa
AJLO-090	pCDFDuet1-Gib-fw	gagcctgcaaccgactaataatcgagtctggtaaagaaaccg
AJLO-091	pCDFDuet1-Gib-spacer-rev	aaagaactcggagaagccattatgtatatctccttcttatacttaactaatatactaag
AJLO-092	pANT-FNTB-Gib-fw	cttagtatattagttaagtataagaaggagatatacataatggcttctccgagttcttt
AJLO-093	pANT-FNTB-Gib-rev	cggtttctttaccagactcgattattagtcggttgcaggctc
AJLO-116	QC hGBP2-CTIS-rev	gcctggagccgatctgcaccatcagctaataagcggccgcactc
AJLO-117	QC hGBP2-CTIS-fwd	gtgcggccgcttattagctgatggtgcagatcggctccaggc

Table 4.3: Vectors and Constructs used in this manuscript.

Name	Description	Source/ Reference
AJLV-009	pETM14: *E.coli* expression vector (KanR)	[34]
AJLV-038	pCDFDuet: *E.coli* expression vector (SmR)	Merck Millipore (Novagen)
AJLV-040	pJET1.2/blunt: Positive selection cloning vector (AmpR)	Thermo Fisher Scientific
AJLD-001	pUC57-hGBP1: Subcloning vector pUC57 with synthetic gene of hGBP1 optimised for *E.coli* expression (AmpR)	GenScript
AJLD-002	pUC57-hGBP2: Subcloning vector pUC57 with synthetic gene of hGBP2 optimised for *E.coli* expression (AmpR)	GenScript
AJLD-007	GST-tagged-FNTA *in vitro* expression vector pANT7 (AmpR)	DNASU clone HsCD00630808
AJLD-008	GST-tagged-FNTB *in vitro* expression vector pANT7 (AmpR)	DNASU clone HsCD00733069
AJLD-022	NdeI site removed from pANT7-FNTB-cGST (AmpR)	derived from AJLD-008
AJLD-030	pETM14-hGBP1: *E.coli* expression vector (KanR) with hGBP1	Derived from AJLV-009 and AJLD-001
AJLD-036	pETM14-hGBP2: *E.coli* expression vector (KanR) with hGBP2	Derived from AJLV-009 and AJLD-002
AJLD-052	pJET1.2 His6-FNTA: Intermediate vector for cloning purposes (AmpR)	Derived from AJLV-040 and AJLD-007
AJLD-053	pJET1.2 FNTB (NdeI removed): Intermediate vector for cloning purposes (AmpR)	Derived from AJLV-040 and AJLD-022
AJLD-054	pJET1.2-PGGT1B: Intermediate vector for cloning purposes (AmpR)	Derived from AJLV-040 and AJLD-060
AJLD-060	pENTR223.1-PGGT1B: sub-cloning vector containing PGGT1B (SmR)	DNASU clone ID HsCD00082643
AJLD-061	pCDFDuet-His-FNTA-PGGT1B: *E.coli* co-expression vector (SmR) to express His-FNTA-PGGT1B	Derived from AJLV-038, AJLD-052 and AJLD-054
AJLD-063	pCDFDuet-His-FNTA-FNTB: *E.coli* co-expression vector (SmR) to express His-FNTA-FNTB	Derived from AJLV-038, AJLD-052 and AJLD-053
AJLD-084	pETM14-hGBP2-CTIS: *E.coli* expression vector (KanR)	derived from AJLD-036
AJLD-250	pETM14-hGBP1-R584-586A: *E.coli* expression vector (KanR)	GenScript

5

Conclusions and Outlook

Developments to target small and flexible proteins with cryo-EM

In this thesis, we investigated the oligomerization ability of guanylate binding protein 1 (GBP1), an interferon-inducible GTPase that has been shown to have an antimicrobial activity by targeting membranes of intracellular pathogens or pathogen containing compartments. We were able to solve the cryo-EM structure of the full-length human GBP1 dimer in its guanine nucleotide-bound state and resolve the molecular ultrastructure of GBP1 coatomer assemblies on liposomes and bacterial lipopolysaccharide membranes, providing a framework to interrogate the molecular basis for GBP1 effector functions in intracellular immunity. In chapter 3, we also discuss the problems we encountered when trying to solve the cryo-EM structure of the nucleotide stabilized GBP1-dimer. With its molecular weight of 130 kDa the GBP1-dimer is considered small for structure determination using cryo-EM. In order to prevent damage of biological samples, an extremely low electron dose is used, resulting in a low signal to noise ratio. In order to accurately align and average individual particles, enough signal is necessary. The low contrast of small proteins makes this alignment process challenging and it is thus more difficult to obtain a high resolution 3D reconstruction. The additional flexibility of the C-terminal domain of GBP1 and the strong observed preferred particle orientation made the GBP1-dimer a challenging project for structure determination. As further discussed in chapter 3, the use of nanobodies (Nbs) that had been raised against GBP1 decreased protein flexibility and improved particle distribution.

While the small size of Nbs has been previously highlighted as advantage multiple times, having a binding partner with a larger molecular mass can be beneficial when performing cryo-EM on small proteins. By increasing the overall molecular mass, particles can be more easily detected and aligned accurately enabling structure determination of small proteins or increasing their resolution. One development to increase the molecular mass of small proteins was the creation of so called megabodies [1]. Megabodies comprise a nanobody coupled to a scaffold protein, resulting in an overall molecular weight of ~56 kDa or ~100 kDa (as compared to the 15 kDa of a Nb by itself), without affecting antigen specificity or affinity [1] (Figure 5.1a). The increase in molecular weight enables more accurate particle picking of the megabody-antigen complex, due to the increased signal to noise ratio and facilitates the alignment necessary for averaging. Another advantage of using megabodies for cryo-EM structure determination is that they can help to achieve a more heterogeneous particle distribution by changing the propensities of the molecular surface [1]. The megabody can further stabilize the protein, thereby preventing it from unfolding.

Another approach to increase the size of Nbs is the assembly into a so called Legobody [2]. Hereby, the Nb is bound to two scaffolds, a Fab fragment of an antibody raised against the Nb and a maltose binding protein fused to a part of protein A which is able to bind the Nb [2] (Figure 5.1b). The overall construct has a molecular weight of 120 kDa and was shown to facilitate cryo-EM structure determination of two small proteins with a molecular weight of around 22 kDa which otherwise would have been too small to be resolved by cryo-EM. The additional size and particular shape of the Legobody facilitates particle alignment as described previously for the megabodies.

To tackle the problem of flexibility and heterogeneity in cryo-EM, there were various

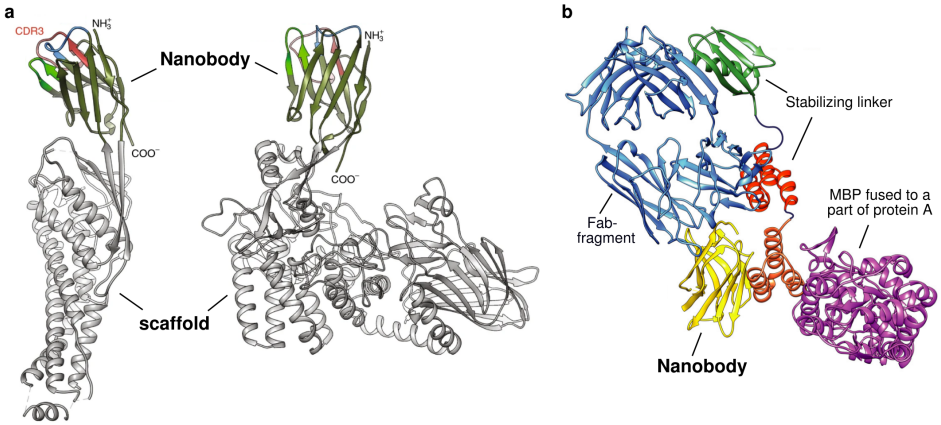

Figure 5.1: Overview of the megabody and legobody assembly. (a) Structural representation of two megabodies consisting of a Nb coupled to a scaffold protein. The image is adapted from [1]. (b) Structural representation of a legobody adapted from [2].

improvements in software throughout the last years. Typically, 3D reconstruction methods in cryo-EM result in a single rigid 3D structure, where moving parts of the protein are blurred out and poorly resolved. New algorithms can take flexibility into account and infer a model of the particle flexibility from the 2D images [3–5]. We made use of this to visualize the flexibility of the α-helical middle domain of GBP1 in chapter 3.

Nanobodies have the potential to link structural data with functional data.

Since their discovery in 1993 [6], Nbs have become a versatile tool in various applications such as molecular imaging, as nanobody-mediated drug delivery system or as tools in structural biology [7]. A powerful application to link structural data with functional data is to use Nbs as fluorescently labelled intrabodies inside cells [8]. As shown in chapter 2, we were able to identify Nbs that would only bind to dimeric GBP1 and not to its monomeric form, as well as Nbs that would prevent dimerisation. With those Nbs, we found a way to differentiate between oligomeric states of GBP1 as well as to actively interfere with the dimerisation and coat formation of GBP1 to study the biological implications on downstream effectors of GBP1 in regards to pathogen restriction and pyroptosis. If the observed specificity of multiple described Nbs for GBP1 holds true for the other GBP homologs (GBP3-GBP7), it could be a powerful tool to study earlier described hetero-dimers of GBP [9]. With the here identified Nbs we created a toolbox for future biochemical and cell biological studies of GBPs.

Alternatives of Nb generations without requiring animal immunization

One disadvantage of Nbs is that the generation often involves animal immunization, which in addition to requiring living animals is costly and time consuming. Another option to generate Nbs is from synthetic libraries or naïve libraries [10–12] which are especially useful when working with toxic, harmful or contagious material that cannot

be injected into an animal or when working with DNA which might fail to trigger an immune response [13]. To create a naïve library blood is taken from a non-immunized animal making use of the natural diversity of the animal's immune system [14]. For a synthetic library, a scaffold structure is chosen and the sequences at the complementary determining regions are randomised [13]. The disadvantage of naïve libraries lies in the fact that they require large amounts of blood from animals and in order to obtain Nbs that bind the target with high affinities an affinity improvement step might be necessary [13, 14]. Additionally, the immune system was not specifically triggered and therefore no over-expression of the target specific Nbs occurred. Nbs generated synthetically on the other hand can result in stability problems and exhibit more issues regarding proper folding of the Nbs [15].

Improvements towards a publicly accessible Nb database

Despite the various areas of application and huge potential Nbs possess, it is not traceable how many Nbs have been generated up to date. Databases to monitor Nbs are sparse and not well managed, which is especially surprising considering that Nb generation most of the time involves animal immunization which additionally to the need of using living animals is timely and costly. First attempts to collect Nb sequences in a general databank have been made by the Institute collection and analysis of Nbs (iCAN) [16] and the Single Domain Antibody Database (sdAB-DB) [17]. A newer attempt from the integrated Nb database for immunoinformatics (INDI) identified 18.000 sequences originating from either manually curating publications, from structures in the protein databank or from the NCBI GenBank (August 2021) [18]. As this is most likely only a small fraction of all discovered Nb sequences, it highlights the importance of standardized databases for Nb sequences, to avoid repetitive immunization of animals with the same antigen and to benefit a broader scientific community.

Structural biology in times of structure prediction methods

Within the last years, the field of structural biology has undergone some drastic changes with the introduction of structure prediction methods such as AlphaFold2 or RoseTTAFold [19, 20]. Those structure predictions provided results that were very close to experimentally determined structures, which has been considered a massive developmental progress. With the ability to use the AlphaFold algorithm and by having a large collection of pre-calculated protein structures in the AlphaFold Database at the European Bioinformatics Institute, the availability of predicted protein structures has massively increased [19, 21, 22]. Despite the advantages coming from such a fast AI-driven structure determination, there are still some major considerations. First of all, AlphaFold only predicts the polypeptide part of the protein, unable to predict ligands, ions or posttranslational modifications. Moreover, AlphaFold displays difficulties when predicting larger proteins or protein complexes. In the case of the full length GBP1-dimer, AlphaFold failed to correctly predict the cross-over arrangement of the middle domain and C-terminal α-helical domain which we determined experimentally, once more highlighting the demand for experimental structural biology.

Finally, the results from AlphaFold do not represent the different states a protein can adopt, but rather represents one fold. The strength on the other hand is that it enables

structural biologists to use AlphaFold as a tool, setting the starting point for further experimental work, to understand the proteins mechanism as well as its role in a cellular environment. Especially docking protein-structure predictions into molecular envelopes obtained from cryo-electron tomography has a lot of potential to get further insights of large multi-protein assemblies.

Advances in sample preparation for cryo-EM

While there have been impressive advances in the field of structure prediction, sample preparation for cryo-EM has remained largely unchanged over the years and sample preparation often keeps being the bottleneck in the cryo-EM workflow. Common problems in sample preparation are related to the ice thickness and originate from the fact that reproducing a certain ice thickness can be challenging. Other issues arise from the interaction of proteins with the air-water interface which can result in preferred particle orientation, but also in protein denaturation and protein aggregation [23]. Solutions to circumvent the above described challenges, include the addition of binding partners, the addition of detergents or the use of thin support films. Recently there have also been technical advances circumventing the blotting step in sample preparation which is difficult to precisely control. Those technical advances include the development to spray picoliter-sized droplets of solution onto a grid before rapidly plunge-freezing the grids (Spotiton) [24–26]. Another development are nanofluidic chips, that contain nanochannels with a uniform thickness, eliminating the issue of proteins to potentially interact with the air-water interface and the advantage of very small picoliter sample volumes [27]. Combining those methods with the potential to perform a more efficient grid screening, could benefit challenging projects such as ours to accelerate EM grid preparation with thin ice and a good coverage of particle orientation, enabling 3D structure determination.

One big potential in cryo-EM lies in the possibility to perform time-resolved structural studies that are in the millisecond range. While the actual freezing process is quite fast, the steps of sample deposition and blotting usually take multiple seconds limiting achievable time-resolution cryo-EM [28]. There are however multiple attempts to make time-resolved cryo-EM feasible. In the case of GBP1, this could enable us to follow the structural changes induced by GTP hydrolysis as well as coat formation on membranes and potential membrane deformations. One approach is to mix two solutions together either before applying them on an EM-grid or directly on the grid, while the second approach is to use flash-photolysis [26, 29–32]. Flash-photolysis uses molecules that can be light activated (such as a caged form of GTP), which are illuminated by a light source just before plunge freezing the EM grid.

Understanding the antimicrobial mechanism of GBPs

Recent progress has been made to resolve the ability of GBP1 to directly bind to LPS, initiating the binding of other members of the GBP family as well as caspase-4 and creating a signalling platform [33–36]. In chapter 3 we add to this knowledge by describing the ultrastructure of the GBP1 coat on SUVs as well as on different types of LPS using cryo-EM. Despite this progress, the mechanistic implications of coat formation are still unknown. GBP1-induced membrane rupture has not been shown for gram negative bacte-

ria yet, but we observed membrane tubulation and membrane deformation as described in chapter 3, which could be a more indirect way of destabilizing membranes. Additionally, tubulation might enable the presentation or liberation of LPS molecules to cytosolic binding partners such as caspase-4 [37, 38], that are otherwise unable to interact with the lipid-A part of the LPS. Quantitative methods measuring LPS release as well as time resolved high resolution experiments resolving different time steps of GTP-hydrolysis and its effect on membranes will hopefully give important clues on the mechanism underlying GBP1 coat formation.

One remaining mystery is how GBPs are able to interact with a very broad range of membranes, including the membranes of protozoan such as *Toxoplasma gondii*, gram negative bacteria but also to host-derived pathogen containing vacuoles. How are GBPs able to target such a broad range of membranes, without targeting their own hostmembranes? The identification of patterns enabling the GBPs to differentiate self from non-self will be of major interest. So far, there is also no explanation why it could be useful that GBP1 contains a farnesylation moiety while GBP2 and GBP5 are geranylgeranylated. In chapter 4 we study what kind of effect the type of prenylation has on self-oligomerization processes as well as its interaction with membranes *in vitro*. Systems studying GBPs *in vivo* have shown that despite their prenylation, GBP2 and GBP5 are unable to coat gram-negative bacteria or *Toxoplasma gondii* by themselves [34, 39]. Studying different types of parasites might give some indications on whether geranylgeranylation preferentially interacts with certain types of membranes or types of LPS. First hints in this direction have emerged from studies with *F. novicida* and *S. flexneri*, where a mutant allowing geranylgeranylation of GBP1 showed an increased recruitment to *F. novicida* compared to farnesylated GBP1 [40]. Additionally, determining the affinity between farnesylated and geranylgeranylated GBPs and different types of membranes might give some insights on why there are GBPs with either a farnesyl or a geranylgeranyl moiety. Studying the effect of prenylation on the GTPase activity of GBPs more systematically might also help to understand the impact different types of prenylation can have on the GTPase activity for example whether this could be a potential mechanistic effect used by the cells to up or down regulate the GTPase activity of GBPs.

The ultimate goal will be to mechanistically study the signalling platform including multiple GBP members as well as caspase-4 on biological membranes and to resolve this structure with cryo-EM and cryo-ET. One major difficulty will result from the fact that the different GBPs are similar in molecular weight, potentially adopting a comparable fold. Ideally we would like to use our earlier described Nb toolbox (chapter 2) to help us differentiate different GBP members as well as specifically label them fluorescently to follow the assembly of the complex. For this purpose using a correlated light and electron microscopy (CLEM) approach could be extremely powerful enabling high resolution imaging in a cellular context.

.

References

[1] T. Uchański, S. Masiulis, B. Fischer, V. Kalichuk, U. López-Sánchez, E. Zarkadas, M. Weckener, A. Sente, P. Ward, A. Wohlkönig, *et al., Megabodies expand the nanobody toolkit for protein structure determination by single-particle cryo-em,* Nature methods **18**, 60 (2021).

[2] X. Wu and T. A. Rapoport, *Cryo-em structure determination of small proteins by nanobody-binding scaffolds (legobodies),* Proceedings of the National Academy of Sciences **118**, e2115001118 (2021).

[3] E. D. Zhong, T. Bepler, B. Berger, and J. H. Davis, *Cryodrgn: reconstruction of heterogeneous cryo-em structures using neural networks,* Nature methods **18**, 176 (2021).

[4] L. F. Kinman, B. M. Powell, E. D. Zhong, B. Berger, and J. H. Davis, *Uncovering structural ensembles from single-particle cryo-em data using cryodrgn,* Nature Protocols **18**, 319 (2023).

[5] A. Punjani and D. J. Fleet, *3dflex: determining structure and motion of flexible proteins from cryo-em,* Nature Methods , 1 (2023).

[6] C. Hamers-Casterman, T. Atarhouch, S. a. Muyldermans, G. Robinson, C. Hammers, E. B. Songa, N. Bendahman, and R. Hammers, *Naturally occurring antibodies devoid of light chains,* Nature **363**, 446 (1993).

[7] G. Bao, M. Tang, J. Zhao, and X. Zhu, *Nanobody: a promising toolkit for molecular imaging and disease therapy,* EJNMMI research **11**, 1 (2021).

[8] M. A. De Beer and B. N. Giepmans, *Nanobody-based probes for subcellular protein identification and visualization,* Frontiers in cellular neuroscience **14**, 573278 (2020).

[9] N. Britzen-Laurent, M. Bauer, V. Berton, N. Fischer, A. Syguda, S. Reipschläger, E. Naschberger, C. Herrmann, and M. Stürzl, *Intracellular trafficking of guanylate-binding proteins is regulated by heterodimerization in a hierarchical manner,* PloS one **5**, e14246 (2010).

[10] A. Olichon and A. de Marco, *Preparation of a naïve library of camelid single domain antibodies,* Single Domain Antibodies: Methods and Protocols , 65 (2012).

[11] J. Yan, G. Li, Y. Hu, W. Ou, and Y. Wan, *Construction of a synthetic phage-displayed nanobody library with cdr3 regions randomized by trinucleotide cassettes for diagnostic applications,* Journal of translational medicine **12**, 1 (2014).

[12] J. S. Sabir, A. Atef, F. M. El-Domyati, S. Edris, N. Hajrah, A. M. Alzohairy, and A. Bahieldin, *Construction of naïve camelids vhh repertoire in phage display-based library,* Comptes Rendus Biologies **337**, 244 (2014).

[13] S. Muyldermans, *A guide to: generation and design of nanobodies,* The FEBS journal **288**, 2084 (2021).

[14] B. Liu and D. Yang, *Easily established and multifunctional synthetic nanobody libraries as research tools,* International Journal of Molecular Sciences **23**, 1482 (2022).

[15] Q. Su, W. Shi, X. Huang, S. Yin, X. Yang, and X. Lu, *Recent advances of nanobody applications in diagnosis and detection,* MedComm–Biomaterials and Applications **2**, e54 (2023).

[16] J. Zuo, J. Li, R. Zhang, L. Xu, H. Chen, X. Jia, Z. Su, L. Zhao, X. Huang, and W. Xie, *Institute collection and analysis of nanobodies (ican): a comprehensive database and analysis platform for nanobodies,* BMC genomics **18**, 1 (2017).

[17] E. E. Wilton, M. P. Opyr, S. Kailasam, R. F. Kothe, and H.-J. Wieden, *sdab-db: the single domain antibody database,* (2018).

[18] P. Deszyński, J. Młokosiewicz, A. Volanakis, I. Jaszczyszyn, N. Castellana, S. Bonissone, R. Ganesan, and K. Krawczyk, *Indi—integrated nanobody database for immunoinformatics,* Nucleic Acids Research **50**, D1273 (2022).

[19] J. Jumper, R. Evans, A. Pritzel, T. Green, M. Figurnov, O. Ronneberger, K. Tunyasuvunakool, R. Bates, A. Žídek, A. Potapenko, *et al.*, *Highly accurate protein structure prediction with alphafold,* Nature **596**, 583 (2021).

[20] M. Baek, F. DiMaio, I. Anishchenko, J. Dauparas, S. Ovchinnikov, G. R. Lee, J. Wang, Q. Cong, L. N. Kinch, R. D. Schaeffer, *et al.*, *Accurate prediction of protein structures and interactions using a three-track neural network,* Science **373**, 871 (2021).

[21] M. Mirdita, K. Schütze, Y. Moriwaki, L. Heo, S. Ovchinnikov, and M. Steinegger, *Colabfold: making protein folding accessible to all,* Nature methods **19**, 679 (2022).

[22] R. J. Read, E. N. Baker, C. S. Bond, E. F. Garman, and M. J. van Raaij, *Alphafold and the future of structural biology,* (2023).

[23] R. Danev, H. Yanagisawa, and M. Kikkawa, *Cryo-electron microscopy methodology: current aspects and future directions,* Trends in biochemical sciences **44**, 837 (2019).

[24] T. Jain, P. Sheehan, J. Crum, B. Carragher, and C. S. Potter, *Spotiton: a prototype for an integrated inkjet dispense and vitrification system for cryo-tem,* Journal of structural biology **179**, 68 (2012).

[25] M. C. Darrow, J. P. Moore, R. J. Walker, K. Doering, and R. S. King, *Chameleon: next generation sample preparation for cryoem based on spotiton,* Microscopy and Microanalysis **25**, 994 (2019).

[26] V. P. Dandey, W. C. Budell, H. Wei, D. Bobe, K. Maruthi, M. Kopylov, E. T. Eng, P. A. Kahn, J. E. Hinshaw, N. Kundu, *et al.*, *Time-resolved cryo-em using spotiton,* Nature methods **17**, 897 (2020).

[27] S. T. Huber, E. Sarajlic, R. Huijink, F. Weis, W. H. Evers, and A. J. Jakobi, *Nanofluidic chips for cryo-em structure determination from picoliter sample volumes,* Elife **11**, e72629 (2022).

[28] J. Dubochet, M. Adrian, J.-J. Chang, J.-C. Homo, J. Lepault, A. W. McDowall, and P. Schultz, *Cryo-electron microscopy of vitrified specimens,* Quarterly reviews of biophysics **21**, 129 (1988).

[29] J. Frank, *Time-resolved cryo-electron microscopy: Recent progress,* Journal of structural biology **200**, 303 (2017).

[30] T. R. Shaikh, D. Barnard, X. Meng, and T. Wagenknecht, *Implementation of a flash-photolysis system for time-resolved cryo-electron microscopy,* Journal of structural biology **165**, 184 (2009).

[31] M.-E. Mäeots, B. Lee, A. Nans, S.-G. Jeong, M. M. Esfahani, S. Ding, D. J. Smith, C.-S. Lee, S. S. Lee, M. Peter, *et al.*, *Modular microfluidics enables kinetic insight from time-resolved cryo-em,* Nature communications **11**, 3465 (2020).

[32] S. Torino, M. Dhurandhar, A. Stroobants, R. Claessens, and R. G. Efremov, *Time-resolved cryo-em using a combination of droplet microfluidics with on-demand jetting,* Nature Methods **20**, 1400 (2023).

[33] D. Fisch, B. Clough, M.-C. Domart, V. Encheva, H. Bando, A. P. Snijders, L. M. Collinson, M. Yamamoto, A. R. Shenoy, and E.-M. Frickel, *Human gbp1 differentially targets salmonella and toxoplasma to license recognition of microbial ligands and caspase-mediated death,* Cell reports **32**, 108008 (2020).

[34] M. Kutsch, L. Sistemich, C. F. Lesser, M. B. Goldberg, C. Herrmann, and J. Coers, *Direct binding of polymeric gbp1 to lps disrupts bacterial cell envelope functions,* The EMBO journal **39**, e104926 (2020).

[35] J. C. Santos, D. Boucher, L. K. Schneider, B. Demarco, M. Dilucca, K. Shkarina, R. Heilig, K. W. Chen, R. Y. Lim, and P. Broz, *Human gbp1 binds lps to initiate assembly of a caspase-4 activating platform on cytosolic bacteria,* Nature communications **11**, 1 (2020).

[36] M. P. Wandel, B.-H. Kim, E.-S. Park, K. B. Boyle, K. Nayak, B. Lagrange, A. Herod, T. Henry, M. Zilbauer, J. Rohde, *et al.*, *Guanylate-binding proteins convert cytosolic bacteria into caspase-4 signaling platforms,* Nature immunology **21**, 880 (2020).

[37] J. Shi, Y. Zhao, Y. Wang, W. Gao, J. Ding, P. Li, L. Hu, and F. Shao, *Inflammatory caspases are innate immune receptors for intracellular lps,* Nature **514**, 187 (2014).

[38] J. Shi, Y. Zhao, K. Wang, X. Shi, Y. Wang, H. Huang, Y. Zhuang, T. Cai, F. Wang, and F. Shao, *Cleavage of gsdmd by inflammatory caspases determines pyroptotic cell death,* Nature **526**, 660 (2015).

[39] D. Fisch, B. Clough, R. Khan, L. Healy, and E.-M. Frickel, *Toxoplasma-proximal and distal control by gbps in human macrophages,* Pathogens and disease **79**, ftab058 (2021).

[40] S. V. Valeva, M. Degabriel, F. Michal, G. Gay, J. R. Rohde, F. Randow, B. Lagrange, and T. Henry, *Comparative study of gbp recruitment on two cytosol-dwelling pathogens, francisella novicida and shigella flexneri highlights differences in gbp repertoire and in gbp1 motif requirements,* Pathogens and Disease **81**, ftad005 (2023).

Summary

Mammalian cells have acquired a repertoire of defense strategies to deal with intracellular pathogens summarized as cell-autonomous immunity. In this thesis we studied one family of interferon inducible effector proteins involved in this process called guanylate binding proteins (GBPs). GBPs have been shown to combat a broad variety of pathogens including bacteria, viruses and protozoa. Due to their important antimicrobial role we used a structural approach to better understand the underlying oligomerization properties of GBPs, their organization on membranes as well as the functional implication originating from membrane binding.

In **Chapter 1** we introduced the general concept of cell-autonomous immunity, a process that describes the ability of an individual cell to defend itself against invading pathogens. We moved on describing key effector proteins involved in this process called guanylate binding proteins. Their structure and function was discussed in detail as they were the main protein of interest in this thesis. After we emphasized the ability of GBPs to hydrolyse GTP and to bind to membranes, we highlighted their location within the cell and especially their antimicrobial functions. We closed this chapter by introducing the main technique used in this thesis namely cryogenic electron microscopy and we explained what nanobodies (Nbs) are and how they can be useful for the structural characterization of proteins.

In **Chapter 2** we explained the production and characterization of conformational specific Nbs that were derived by immunizing llamas with either monomeric GBP1, farnesylated GBP1 or nucleotide stabilized dimeric GBP1. We described different nanobodies that can be used as tools to determine the structure of the GBP1-dimer as well as nanobodies that were able to disrupt GBP1-dimer formation and GBP1-coat formation. We further showed in this chapter that some of the identified nanobodies bind to GBP1 while being unable to interact with GBP2. To further understand this specificity, we compared GBP1 and GBP2 on a sequence level and structural level and determined the putative interfaces between GBP1 and two of the nanobodies using cryo-electron microscopy. With the characterization of those conformational specific nanobodies raised against GBP1, we set the groundwork for future research. Using those nanobodies within cells will potentially enable us to determine the localization of certain conformational states of GBP1 as well as the effects caused by disrupting GBP1-dimer formation or GBP1-coat formation on downstream effector molecules.

In **Chapter 3** we used one of the nanobodies characterized in chapter 2 to help us solve the cryo-EM structure of the nucleotide stabilized GBP1 dimer. Previous attempts solving the structure of the GBP1-dimer without a nanobody present failed due to strong preferred particle orientation of the GBP1-dimer and a high degree of structural flexibility.

We showed that the GBP1-dimer adopts a cross-over shape of its middle domain resulting in an outstretched conformation with potentially isoprenylated carboxyl-termini of the GBP1 dimer pointing into the same direction. This was especially interesting as it explained how farnesylated GBP1 formed a dense coat on SUVs and different types of LPS-micelles which we imaged using cryo electron microscopy. Additionally, we observed that farnesylated GBP1 formed tubular membrane protrusions, a potential mechanism for GBP1 to destabilize membranes.

In **Chapter 4** we expanded our view from GBP1 to GBP2 and took a closer look at the differences of their self-assembly properties and abilities to coat membranes. We successfully geranyl-geranylated GBP2 ($GBP2_G$) *in vitro* as well as farnesylated a GBP2-CTIS mutant. This enabled us to study whether the observed results originated from the type of prenylation or from GBP specific characteristics. While we showed that $GBP2_G$ forms similar micelle like structures as farnesylated GBP1, there was no coat formation observed for $GBP2_G$ or farnesylated GBP2-CTIS. Despite highlighting that additionally to the type of prenylation, GBP1 possesses certain characteristics enabling coat formation that GBP2 seems to lack, we also revealed that the type of prenylation had an effect on the GTPase activity of GBP2.

To conclude the thesis, in **Chapter 5** we put our findings into a broader context. We discussed the current state of research, highlighted ongoing developments in the field and made suggestions for future experiments.

Samenvatting

Dierlijke cellen hebben een repertoire aan verdedigingsstrategieën ontwikkeld om intracellulaire pathogenen af te wenden. Samengevat is dit de cel-autonome immuniteit. In dit proefschrift onderzochten wij één van de interferon induceerbare eiwit families genaamd "guanylate binding proteins"(GBPs). Het is aangetoond dat GBPs verschillende pathogenen tegengaan, waaronder bacteriën, virussen en protozoa. Vanwege hun belangrijke antimicrobiële rol onderzochten wij met een structuur-gerichte aanpak de onderliggende oligomerisatie eigenschappen van GBPs, hun organisatie op het membraan en de functionele implicaties die voortkomen uit membraan binding.

In **Hoofdstuk 1** introduceerden we het algemene concept van cell-autonome immuniteit, een process dat beschrijft hoe een cel zich kan verdedigen tegen binnengedrongen pathogenen. Daarna beschreven we de belangrijkste eiwitten in dit proces, de "guanylate binding proteins". We hebben de structuur en functie van deze eiwitten, de focus van dit onderzoek, in detail uiteengezet. Eerst benadrukten we hoe GBPs GTP kunnen hydrolyseren en membranen kunnen binden, vervolgens lichtten we hun locatie binnen de cel en in het bijzonder hun antimicrobiële functie uit. We sloten het hoofstuk af met een introductie van de belangrijkste techniek gebruikt in dit proefschrift, cryo-electronen microscopie, en we lichtten toe wat nanolichamen ('nanobodies', Nbs) zijn en hoe deze nuttig kunnen zijn voor het characteriseren van de structuur van eiwitten.

In **Hoofdstuk 2** legden we de productie en characterisatie van conformatie-specifieke Nbs uit die worden gewonnen door lama's met monomerisch GBP1, gefarnesyleerd GBP1, of nucleotide-gestabiliseerd dimerisch GBP1 te immunizeren. We beschreven verschillende nanolichamen die gebruikt kunnen worden om de structuur van de GBP1 dimeer te bepalen en nanolichamen die in staat zijn de dimerisatie en vachtvorming van GBP1 te verstoren. Daarnaast toonden we in dit hoofdstuk aan dat sommige geïdentificeerde nanolichamen in staat zijn GBP1 te binden, maar geen interactie vertoonden met GBP2. Om deze specificiteit verder te begrijpen vergeleken we GBP1 en GBP2 op sequentieniveau en structuurniveau en bepaalden we het vermoedelijke bindingsraakvlak tussen GBP1 en twee van de nanolichamen door middel van cryo-electronen microscopie. Met de characterisatie van deze conformatie-specifieke nanolichamen tegen GBP1 hebben we het fundament gelegd voor toekomstig onderzoek. Het gebruik van deze nanolichamen stelt ons mogelijk in staat om de localisatie van zekere conformationele toestanden van GBP1 te bepalen en de effecten te bestuderen van het verstoren van GBP1 dimerisatie en vachtvorming op effectormoleculen.

In **Hoofdstuk 3** benuttigden we één van de nanolichamen beschreven in hoofdstuk 2

Dank aan Maarten Joosten voor het vertalen van deze samenvatting.

om de cryo-EM structuur van de nucleotide-gestabiliseerd dimerisch GBP1 op te lossen. Eerdere pogingen om de structuur op te lossen zonder nanolichaam mislukten vanwege de sterke preferentiële oriëntatie van de GBP1 dimeer en een hoog gehalte aan structurele flexibiliteit. Wij waren in staat aan te tonen dat de GBP1 dimeer een gekruisde vorm aanneemt in het middelste domein, wat resulteert in een uitgestrekte conformatie met mogelijke geïsoprenyleerde carboxyl-uiteinden van de GBP1 dimeer in dezelfde richting gericht. Dit is in het bijzonder interessant omdat het uitlegt hoe GBP1 in staat is een dichte vacht te vormen rondom SUVs en verschillende typen LPS-micellen die we hebben bekeken met behulp van cryo-electronen microscopie. Daarnaast observeerden we dat gefarnesyleerd GBP1 in staat is om buisvormige membraanuitstulpingen te vormen, een potentiëel machanisme voor GBP1 om membranen te destabiliseren.

In **Hoofdstuk 4** breidden we onze blik uit van GBP1 tot GBP2 en namen een dichtere kijk op de verschillen in hoe deze eiwitten zichzelf monteren en een vacht vormen rondom membranen. We slaagden erin GBP2 *in vitro* te geranyl-geranyleren ($GBP2_G$) en om een GBP2-CTIS mutant te farnesyleren. Dit maakte het mogelijk om te bestuderen of de eerder geobserveerde resultaten voortkwamen uit het type prenylatie of uit de GBP-specifieke eigenschappen. Hoewel het ons lukte om aan te tonen dat $GBP2_G$ vergelijkbare micelstructuren vormt als gefarnelyseerd GBP1, konden we geen vachtvorming observeren voor $GBP2_G$ of gefarnelyseerd GBP2-CTIS. Ondanks dat we uitlichtten dat naast het type prenylatie, GPB1 eigenschappen bezit die vachtvorming mogelijk maken die GBP2 niet lijkt te delen, waren we in staat om aan te tonen dat het type prenylatie een effect had op de GTPase activiteit van GBP2.

Ter afronding van het proefschrift plaatsten we in **Hoofdstuk 5** onze bevindingen in een bredere context. We zetten de huidige staat van onderzoek uiteen, lichtten de voortdurende ontwikkelingen toe in het veld en maakten suggesties voor toekomstige experimenten.

List of Publications

Preprints

2023 Kuhm T., Pinto C., Gross L., Huber S. T., Taisne C., Giannopoulou E. A., Pardon E., Steyaert J., Tans S. J.,Jakobi A. J.
Structural basis of membrane targeting and coatomer assembly by human GBP1.
bioRxiv (2023)
https://doi.org/10.1101/2023.03.28.534355
Accepted in Nature Structural & Molecular Biology

Journal articles

2020 Jakobi A. J., Huber S. T., Mortensen S. A. , Schultz S. W. , Palara A., Kuhm T., Shrestha B. K., Lamark T., Hagen W. J. H., Wilmanns M., Johansen T., Brech A., Sachse C.
Structural basis of p62/SQSTM1 helical filaments and their role in cellular cargo uptake.
Nat Commun. 2020 Jan 23;11(1):440, 2020.
https://doi.org/10.1038/s41467-020-14343-8

2018 Huber S. T., Kuhm T., Sachse C.
Automated tracing of helical assemblies from electron cryo-micrographs.
Journal of structural biology 202(1): 1–12, 2018.
https://doi.org/10.1016/j.jsb.2017.11.013

Book chapter

2019 Tarafder, A. K., Guesdon, A., Kuhm, T. and Sachse, C.
Recombinant expression, purification, and assembly of p62 filaments.
Autophagy: Methods in Molecular Biology, vol 1880, 3–15, 2019.
https://doi.org/10.1007/978-1-4939-8873-0_1